Investigation of homo-FRET and rotational mobility via time-resolved fluorescence microscopy to probe the fluorophore's environment

Teijeiro Gonzalez, Yurema

Awarding institution:
King's College London

Investigation of homo-FRET and rotational mobility via time-resolved fluorescence microscopy to probe the fluorophore's environment

Yurema Teijeiro González

King's College London

Supervisors: Prof. Klaus Suhling and Dr. Amelle Zair

A dissertation submitted in partial fulfilment

of the requirements for the degree of

Doctor of Philosophy

October 2019

Department of Physics

King's College London

Declaration

I, Yurema Teijeiro González, confirm that the work presented in this thesis is my own. Where information has been derived from other sources, I confirm that this has been indicated in the work.

The author would like to clarify the following points:

- Figure 1.17 was the result of a collaborative work, where the main collaborator was cited when relevant (Chapter 1).
- Figure 2.1 was elaborated by PhD Alessandro Crnjar, as a part of a collaboration (Chapter 2).
- The cell work presented in Chapter 2 was part of a collaboration with Dr. Elena Ortiz Zapater and Prof. Maddy Parsons.

Abstract

The aim of this thesis is the development of a multi-modal fluorescence microscopy setup, with the main objective of maximising the amount of information from a single limited photon budget. Fluorescence in an image can be characterised by position, intensity, lifetime, wavelength and polarisation. The more of these parameters are measured, the more information about the probe's environment is gained. Here, I show how position, intensity, lifetime and polarisation can be measured in a single experiment. The time-resolved polarisation in particular can give information about rotational diffusion, and homo-FRET. Several fluorescence microscopy techniques were combined in a based Time-Correlated Single Photon Counting (TCSPC) framework: Fluorescence Lifetime IMaging (FLIM), time-resolved Fluorescence Anisotropy IMaging (tr-FAIM) and Fluorescence Recovery After Photobleaching (FRAP). The set-up was built in-house and calibrated with rhodamine 6G (R6G) solutions in water/glycerol mixtures and further tested in single lipid bilayers (SLBs) with the environmentally-sensitive dye di-4-ANEPPDHQ. With this multimodal fluorescence microscopy setup the hydrodynamic radius of the fluorescence probe can be calculated without any a priori viscosity knowledge when the solution is isotropic and homogeneously distributed.

Protein dimerisation in cells triggers many biological processes such as cell signalling, which is crucial for the right functioning of the cell itself. For this reason, protein dimerisation was also investigated by firstly studying two enhanced green fluorescence protein (EGFP) constructs - monomer & dimer - in buffer/glycerol so-

lution mixtures. Time-resolved fluorescence anisotropy measurements were taken for both EGFP constructs and the Förster Resonance Energy Transfer (FRET) from the EGFP dimer was extracted by fitting the time-resolved fluorescence anisotropy data with a stretched exponential model, whose FRET energy values were encountered within the range provided by the molecular dynamic (MD) simulation results. As a real example, the protein homo-dimerisation of Coxsackievirus and Adenovirus Receptor (CAR) tagged with GFP within the cell membrane of Human Bronchial Epithelial (HBE) cells was investigated, where CAR arranges itself as a dimer. Steady-state anisotropy information revealed the distinction of different cell stages from the disruption of the CAR-GFP dimer configuration via the infection of cells with adenovirus.

Lastly, the amount of photons needed in time-resolved fluorescence anisotropy measurements is investigated. An expression for the uncertainty associated with the rotational correlation time θ, based on the Perrin equation, is derived. The validation of this expression is undertaken by comparison with experimental data. Some simulations provide information in regards to the optimal boundary conditions that must be set in the experiment to achieve low rotational correlation time uncertainties $\Delta\theta$. As part of imaging, the distribution of the rotational correlation time θ across an isotropic and homogeneous solution is investigated, based on the fluorescence lifetime τ, steady-state anisotropy r distributions and the application of the Perrin equation.

Publications

Research articles

- J. Berrout, E. Kyriakopoulou, L. Moparthi, A. S. Hogea, L. Berrout, C. Ivan, M. Lorger, J. Boyle, C. Peers, S. Muench, J. E. Gomez, X. Hu, C. Hurst, T. Hall, S. Umamaheswaran, L. Wesley, M. Gagea, M. Shires, I. Manfield, M. A. Knowles, S. Davies, K. Suhling, **Y. Teijeiro-Gonzalez**, N. Carragher, K. Macleod, N. J. Abbott, G. A. Calin, N. Gamper, P. M. Zygmunt, and Z. Timsah, "TRPA1-FGFR2 binding event is a regulatory oncogenic driver modulated by miRNA-142-3p," Nature Communications, vol. 8, no. 1, 2017.

- S. Bourke, **Y. Teijeiro-Gonzalez**, F. Dona, M. Panamarova, K. Suhling, U. Eggert, L. A. Dailey, P. Zammit and M. Green, "Cellular Imaging using Emission-Tuneable Conjugated Polymer Nanoparticles." RSC Advances, vol. 9, 2019.

Conference proceedings

- **Y. Teijeiro-Gonzalez**, A. Le Marois, A. M. Economou, L. M. Hirvonen, J. A. Levitt, A. J. Beavil, R. L. Beavil, A. Crnjar, C. Molteni, E. Ortiz-Zapater, M. Parsons, and K. Suhling, "Fluorescence recovery after photobleaching (FRAP) with simultaneous fluorescence lifetime and time-resolved fluorescence anisotropy imaging (FLIM and tr-FAIM)," Proc. SPIE 10883, Three-Dimensional and Multidimensional Microscopy: Image Acquisition and Processing XXVI, 108830A (2019); doi: 10.1117/12.2508692.

- K. Suhling, **Y. Teijeiro-Gonzalez**, I. E. Steinmark, A. L. James, A. M. Economou, G. Yahioglu, A. Le Marois, L. M. Hirvonen, J. Nedbal, J. A. Levitt, P.-H. Chung, C. A. Dreiss, A. J. Beavil, R. L. Beavil, E. Ortiz-Zapater, C. D. Lorenz, M. Parsons, A. Crnjar, B. Cornell and C. Molteni, "Fluorescence Lifetime Imaging for viscosity and diffusion measurements," Proc. SPIE 10882, Multiphoton Microscopy in the Biomedical Sciences XIX; 1088210 (2019); doi:10.1117/12.2508744.

Conference presentations

Y. Teijeiro-Gonzalez, A. Le Marois, K. Suhling, "Time-Correlated Single Photon Counting-based FLIM, FRAP and FAIM to investigate intracellular dynamics and their environments", was presented at:

- Focus on Microscopy (FOM) in Bordeaux (France), April 2017 - Poster presentation.

Y. Teijeiro-Gonzalez, A. Le Marois, L. M. Hirvonen, J. A. Levitt, K. Suhling, "Time-Correlated Single Photon Counting-based FLIM, FRAP and tr-FAIM to investigate the dynamics of heterogeneous systems", was presented at:

- 11th FLIM Workshop in Berlin (Germany), July 2017 - Short talk and poster presentation.

- FluoroFest Workshop in Glasgow (UK), April 2017 - Poster presentation.

Y. Teijeiro-Gonzalez, J. A. Levitt, A. J. Beavil, R. L. Beavil and K. Suhling, "Towards exploring the dynamics in living cells by combining different techniques based on time-correlated single photon counting", was presented at:

- Focus on Microscopy (FOM) in Singapore, March 2018 - Poster presentation.

Y. Teijeiro-Gonzalez, A. Le Marois, A. M. Economou, L. M. Hirvonen, J. A. Levitt, A. J. Beavil, R. L. Beavil, A. Crnjar, C. Molteni, E. Ortiz-Zapater, M.

Parsons and K. Suhling, "Simultaneous Fluorescence Recovery after photobleaching (FRAP) with Fluorescence Lifetime (FLIM) and time-resolved Fluorescence Anisotropy IMaging (tr-FAIM)", was presented at:

- 12th Annual Advanced Imaging Methods Workshop (AIM) in Berkeley (California, USA), January 2019 - Poster presentation.
- Photonics West in San Francisco (California, USA), February 2019 - Oral presentation.

Y. Teijeiro-Gonzalez, A. Le Marois, A. M. Economou, L. M. Hirvonen, J. A. Levitt, A. J. Beavil, R. L. Beavil, A. Crnjar, C. Molteni, E. Ortiz-Zapater, M. Parsons and K. Suhling, "Advancing Fluorescence Microscopy: Simultaneous Fluorescence Lifetime and Anisotropy IMaging (FLIM FAIM) and Fluorescence Recovery After Photobleaching (FRAP)", was presented at:

- Frontiers in Imaging in Janelia Farm (VA, USA), May 2019 - Short talk and poster presentation.

Acknowledgements

The author would like to thank King's College London for funding of her Graduate Teaching Assistant PhD studentship.

I would like to greatly thank my first supervisor Prof. Klaus Suhling for the PhD opportunity, all the knowledge I have gained from him over the duration of my PhD, all his inspiring conversations till late evenings and all his support at the toughest times. I also would like to thank my second supervisor Dr. Amelle Zair, for always showing interest about my well-being and my work. I really enjoyed having a chat with you either in English or Spanish. Also, thanks to Dr. Susan Cox for introducing me into the fluorescence microscopy field, whose input was almost crucial for my future decision of going for a PhD. Also, I would like to thank my PhD examiners, Prof. David Birch and Dr. James McGinty, for their good job and valuable input.

I would like to thank my group, the current and past colleagues, for all the help received from the beginning till the end of my PhD: Dr. James Levitt, Dr. Liisa Hirvonen, Dr. Alix Le Marois, Dr. Jakub Nedbal, Ida Emilie Steinmark, Iveta Ivanova and Augoustina Maria Economou. Special thanks to Dr. Alix Le Marois for her crucial boost at the very beginning of this journey. Thank you also to Dr. Jakub Nedbal for proof reading this thesis and for his wise tips, and thank you to my student Augoustina Maria Economou for her excellent performance and contribution to part of the work presented in this thesis.

I also would like to thank all the people I collaborated with, from the ones I was able to learn some valuable scientific knowledge: Prof. Maddy Parsons, Dr. Elena Zapater-Ortiz, Dr. Thomas Gensch, Dr. Zahra Timsah, Dr. Alix Le Marois, Dr. Struan Bourke, Dr. Nishanthan Srikantha, Dr. Stephane Chretien, Victoria Gonzalez Sabater Budilov, Prof. Carla Molteni, Alessandro Crnjar. Thank you all for your professionalism and enthusiasm!

MASSIVE THANKS to all my friends and colleagues at King's College London and all that people that made my life at uni and London simply GREAT: Margoth, Ale, David, Sreedevi, Claudio, Josu, Laia, Marciano, Miao, Iveta, Jorge, Pablo (the Mexican), Tarso, Andrea, Struan, Leo, Esther, Miguel^2, Giuseppe, Matt, Ali, Dries, Krzysiek, Thomas^2, Celeste, Eva, Paco, Chris Lorenz, Miss Aggeliki, Joy, Arjun, Pablo (the pilot), Hector, Cristina (NPL), Till, German, Paola, Toby (NPL), Lidia, Christos, Monica, Quique, Simon and many others!

The author feels very grateful to have always counted on the continuous support of her closest friends from childhood to uni times. I simply love you: Eli, Ana la ama, Mariner, Lucia, Neich, Nuri, Mariser, Nere, Miguel Montero, Guti, Sandra^2, Carla, Cris, Mary, Yai and Olayer. You are the real survivors!

Thank you so much to my family, specially to my parents who have played a key role on the person I am nowadays and supported me in every single decision I have made in my life. I will never be grateful enough to all the good received from you! THANK YOU. I also would like to thank my grandparents, uncle, closest cousins (Marina, Fran and Sella), anty, godmother, etc. Your love and support throughout my entire life have always accompanied me. Lastly but not least, thanks to my life partner Maciek, who has fully supported me during my PhD journey and taught me so much during these years throughout his encouragement, love and growth mindset.

Thank you all!!!

Acronyms

ACF Auto-Correlation Function.

Ad5FK Adenovirus Ad5 Fibre-knob.

ADC Analog-to-Digital Converter.

AFM Atomic Force Microscopy.

APP Amyloid Precursor Protein.

BS Beam Splitter.

BSA Bovine Serum Albumin.

CAR Coxsackievirus and Adenovirus Receptor.

CCD Charge-Coupled Device.

CFD Constant Fraction Discriminator.

CHO Chinese Hamster Ovary.

CMOS Complementary Metal-Oxide Semiconductor.

CW Continuous Wave.

di-4-ANEPPDHQ 2-di-butylaminonaphthylethylpyridinium propyl-2-hydroxy-3-dimethyl-hydroxyethyl quaternary ammonium cation.

DMEM Dulbecco's Modified Eagle Medium.

DMSO Dimethyl Sulfoxide.

DOPC di-oleyl-phosphatidycholine.

DRLP Dichroic Long Pass.

EGFP Enhanced Green Fluorescence Protein.

EGFR Epidermal Growth Factor Receptor.

FCS Fluorescence Correlation Spectroscopy.

FITC Fluorescein Isothiocyanate.

FLIM Fluorescence Lifetime IMaging.

FOV Field of View.

FPALM Fluorescence Photo-Activated Localisation Microscopy.

FPFA Fluorescence Polarisation and Fluctuation Analysis.

FRAP Fluorescence Recovery After Photobleaching.

FRET Förster Resonance Energy Transfer.

GFP Green Fluorescence Protein.

GPI-APs Glycosyl-Phosphatidylinositol-Anchored Proteins.

GUVs Giant Unilamellar Vesicles.

HBE Human Bronchial Epithelial.

HIV Human Immunodeficiency Virus.

IRF Instrument Response Function.

LUVs Large Unilamellar Vesicles.

MD Molecular Dynamic.

MEM Maximum Entropy Method.

ML Maximum Likelihood.

NA Numerical Aperture.

NAD Nicotinamide Adenine Dinucleotide.

ND Neutral Density.

NL-LS Non-Linear Least Squares.

OD Optical Density.

PALM Photo-Activated Localisation Microscopy.

PBS Phosphate-Buffered Saline.

PCA Principal Component Analysis.

PEG Polyethylene Glycol.

PGA Programmable Gain Amplifier.

PLIM Phosphorescence Lifetime IMaging.

PMTs Photomultiplier Tubes.

PSF Point Spread Function.

R6G Rhodamine 6G.

RFP Red Fluorescence Protein.

ROI Region of Interest.

RT Room Temperature.

SED Stokes-Einstein-Debye.

SIM Structured Illumination Microscopy.

SLBs Single Lipid Bilayers.

SNR Signal-to-Noise Ratio.

STED Stimulated Emission Depletion.

STORM Stochastic Optical Reconstruction Microscopy.

SUVs Small Unilamellar Vesicles.

TAC Time-to-Amplitude Converter.

TCSPC Time-Correlated Single Photon Counting.

TG2 Transglutaminase type 2.

TIRFLIM Total Internal Reflection Fluorescence Lifetime IMaging.

tr-FAIM time-resolved Fluorescence Anisotropy IMaging.

UV Ultraviolet.

WD Window Discriminator.

YFP Yellow Fluorescence Protein.

Contents

1 Fluorescence photophysics, lifetime and polarisation 1

1.1 Brief introduction to fluorescence microscopy and basic concepts . . 1

1.1.1 Fluorescence microscopy in biology 1

1.1.2 What emits fluorescence? 3

1.1.3 Excitation and absorption spectra - The Lambert-Beer law . 4

1.1.4 What is fluorescence? 5

1.1.5 Emission spectrum 8

1.1.6 Fluorescence lifetime 9

1.1.7 Fluorescence polarisation or anisotropy 12

1.2 Förster Resonance Energy Transfer 24

1.2.1 What is Förster Resonance Energy Transfer? 24

1.2.2 Excitation probability of an isolated molecule 27

1.2.3 Homo-FRET 28

1.2.4 Hetero-FRET 33

1.3 Time-resolved fluorescence microscopy 37

1.3.1 Time-correlated single photon counting (TCSPC) 37

1.3.2 Fluorescence lifetime imaging (FLIM) 40

1.3.3 Time-resolved fluorescence anisotropy imaging (tr-FAIM) . 41

1.4 Fluorescence recovery after photobleaching (FRAP) 42

1.5 Overview of the experimental setup 44

1.5.1 Experimental setup, fluorescence microscopy modalities and excitation optical paths 45
1.5.2 Which setup modalities are used per chapter and what for? . 49
1.5.3 Instrument response function: definition and acquisition . . 51
1.5.4 G-factor: definition and acquisition 52
1.6 Data analysis procedures for FLIM, tr-FAIM and FRAP 53
1.6.1 Estimation procedures for FLIM and tr-FAIM 54
1.6.2 Time-resolved fluorescence anisotropy data fit approaches . 56
1.6.3 FRAP data analysis methods 60
1.7 Förster Resonance Energy Transfer Applications 68
1.7.1 What is special about Förster Resonance Energy Transfer? . 68
1.7.2 Detection of homo-FRET via (tr-)FAIM 69
1.7.3 Detection of hetero-FRET via FLIM 70
1.8 Summary and Conclusion 73

2 Exploring the stretched exponential decay model as a FRET indicator for EGFP dimers 74

2.1 Motivation 74
2.2 Introduction 75
2.2.1 Green Fluorescent Protein 75
2.2.2 Investigating homo-FRET via the application of the stretched exponential model to the time-resolved fluorescence anisotropy data 76
2.2.3 Coxsackievirus and Adenovirus Receptor (CAR) 79
2.2.4 What is studied in this chapter? 80
2.3 Materials & Methods 81
2.3.1 Sample preparation 81
2.3.2 Fluorescence Polarisation Equipment 83

2.3.3 Fluorescence Polarisation Data Analysis 84
2.3.4 Refractive Index Measurements 87
2.3.5 Fluorescence Recovery After Photobleaching (FRAP) Equipment 87
2.3.6 FRAP Data Analysis 88
2.3.7 Polarisation-Resolved Excitation and Emission Spectra . . . 90
2.3.8 Molecular Dynamic Simulations 90
2.4 Results and discussion 93
2.4.1 The EGFP Fluorescence Lifetime Versus Environmental Refractive Index 93
2.4.2 Time-Resolved Fluorescence Anisotropy Measurements . . 95
2.4.3 Molecular Dynamic (MD) simulations 106
2.4.4 FRAP: lateral diffusion of the two EGFP constructs 116
2.4.5 Red-edge failure of homo-FRET between EGFPs in varying viscosity solutions 119
2.4.6 Preliminary results of Fluorescence lifetime studies of GFP-CAR in live and fixed cells 120
2.4.7 Preliminary results of Time-resolved and Steady-State Fluorescence Anisotropy studies of GFP-CAR in live and fixed cells 123
2.5 Summary & Conclusion 129

3 Development of a Multi-Modal Confocal Fluorescence Microscopy Technique based on Time-Correlated Single Photon Counting 132

3.1 Motivation 132
3.2 Introduction 133
3.2.1 Combining FRAP, FLIM and tr-FAIM - F^3 microscopy . . . 133
3.2.2 Structure and Biological Importance of Cell Membranes . . 134

3.2.3 Artificial Cell Membranes - Single Lipid Bilayers (SLBs) . 136
3.2.4 F^3 microscopy on SLBs 137
3.2.5 Literature Review on the Study of Supported Lipid Bilayers SLBs and other Similar Lipid Systems with Fluorescence Techniques & Environmentally-Sensitive Dyes 139
3.3 Materials & Methods 146
3.3.1 Samples preparation 146
3.3.2 F^3 Setup & Acquisition Procedure 147
3.3.3 F^3 data analysis 149
3.3.4 Translational and Rotational Diffusion 154
3.4 Results & Discussion 158
3.4.1 Setup Calibration with Rhodamine 6G 158
3.4.2 F^3 applied to Di-4-ANEPPDHQ in DOPC SLBs at RT . . . 171
3.5 Summary & Conclusion 182

4 Investigation of the Rotational Correlation Time Uncertainty and Distribution from Time-Resolved Fluorescence Anisotropy Data 189
4.1 Motivation 189
4.2 Introduction 189
4.3 Estimation of the Rotational Correlation Time Uncertainty from a Single Decay 192
4.3.1 Description of Theoretical Uncertainty Equations 192
4.3.2 Materials & Methods 199
4.3.3 Results & Discussion 202
4.4 Rotational Correlation Time Distribution from Image 215
4.4.1 Materials & Methods 215
4.4.2 Results & Discussion 219
4.5 Summary & Conclusion 225

5 Conclusions and future directions 228

Appendices 235

A Single Lipid Bilayers Preparation 235

B Dependence of Rotational Correlation Time Uncertainty with Time Resolution: Cross Sections 239

C Evolution of the Rotational Correlation Time Distribution with the Steady-State Anisotropy Standard Deviation 246

D Evolution of the Rotational Correlation Time Distribution with the Steady-State Anisotropy Standard Deviation for a r_0 Normal Distribution 250

E Mode Dependence with the Fluorescence Lifetime Standard Deviation 252

F Mode Dependence with the Steady-State Anisotropy 253

Bibliography 254

List of Tables

2.1 Average fluorescence lifetime and inverse, for EGFP monomer and dimer, per refractive index and viscosity composition sample. 95

2.2 Fit parameters from anisotropy decay per EGFP monomer sample composition. 99

2.3 Fit parameters from anisotropy decay per EGFP dimer sample composition and anisotropy model. 100

2.4 Fit parameters from stretched exponential anisotropy decay fit per EGFP dimer solution viscosity, with δ = 0.5 and free. The EGFP fluorescence lifetime is given by the third column. 102

2.5 Experimental molecule concentration c_{exp} and corrected molecule concentration c_{corr} and quantum yield Φ_{corr}, per EGFP varying solution viscosity. 103

2.6 FRET energy efficiencies, donor-acceptor distances and relevant parameters, for bi- and stretched exponential models, per refractive index and viscosity composition sample. 106

2.7 Fit parameters and goodness of fit for monomer and dimer FRAP recovery curves in 50% and 35% glycerol solutions. 116

2.8 EGFP monomer and dimer half-recovery times, mobility fractions, bleach depth percentages and translational diffusion coefficients for two varying viscosity solutions. 118

2.9 Fit parameters and goodness of fit for GFP-CAR total intensity decay per cell condition. 121

2.10 Average fit parameters and goodness of fit of hindered rotation and stretched exponential models per cell condition. 127

3.1 Refractive index and fluorescence lifetime per R6G glycerol-water solution. 160

3.2 Steady-state anisotropy, steady-state anisotropy standard deviation and intensity per R6G water-glycerol solution. 164

3.3 Fit parameters of the integrated time-resolved anisotropy decay per R6G water-glycerol solution. 166

3.4 Parameters extracted from the F^3 FRAP data per R6G glycerol/water solution. 169

3.5 Parameters extracted from the confocal FRAP data per R6G glycerol/water solution. 171

3.6 Hydrodynamic radius of R6G extracted from the combination of the rotational correlation time information and the confocal and F^3 FRAP data. 171

3.7 FLIM and FAIM parameters for di-4-ANEPPDHQ in DOPC SLB at RT. 177

3.8 Average viscosity values of DOPC SLB given by the di-4-ANEPPDHQ rotational diffusion parameters (Table 3.7) and applying the Saffman-Delbruck and Stokes-Einstein-Debye models (equations 3.12 and 3.9, respectively). 178

3.9 Average viscosity values of DOPC SLB given by the di-4-ANEPPDHQ translational diffusion parameters (Table in Figure 3.25) and applying the Saffman-Delbruck and Stokes-Einstein-Debye models (equation 3.13 and second term of equation 2.23, respectively). 180

3.10 Summary of the found R6G hydrodynamic radii R_h per technique and approach. 184

3.11 Mean F^3 parameters for the dye di-4-ANEPPDHQ in DOPC SLBs. 187

4.1 Mean fluorescence lifetime parameters and standard deviations per FAIM data set. 210

4.2 Experimental time-resolved fluorescence anisotropy, steady-state anisotropy and fluorescence lifetime parameters per ROI of the 120 minutes FAIM data set. 212

4.3 Experimental and theoretical $sd(\theta)/\theta$ for N_{exp} and N = 1. The theoretical results are divided in two columns, indicating which G-factor was used for getting the final results. 213

4.4 Calculation of the number of photons N needed to achieve the different θ accuracies in time-resolved fluorescence anisotropy. 226

List of Figures

1.1 Standard sample cuvette with a d path length. I_0 corresponds to the incident optical intensity and I to the transmitted optical intensity. . 5

1.2 Jablonski diagram and illustration of the different positions for absorption, fluorescence and phosphorescence spectra. Figure adapted from reference [19]. 7

1.3 The Stokes shift of the excitation and emission spectrum of a fluorophore in two different cases. In the first one, the excitation and emission are clearly separated from each other, meanwhile in the second one this distinction is more difficult to observe, increasing the background signal. An overlap between excitation and emission spectra occurs because it exists a range of orbitals at different energies. Low energy excitation orbitals (high excitation wavelength) can lead to an overlap of the two spectra. 8

1.4 Transition moments and photoselection. Figure adapted from reference [19]. 13

1.5 Relations between the intensity components (defined in the Cartesian coordinates) after applying the Curie symmetry principle. The first case corresponds to vertically polarised excitation light and the second one to horizontal polarised excitation light. Figure adapted from reference [19]. 14

1.6 Parallel and perpendicular fluorescence intensity components for a random fluorophore in a spherical coordinate system. Figure adapted from reference [20]. 15

1.7 Fluorescence depolarisation due to rotational motions. The absorption and emission transition moments are assumed to be parallel. β corresponds to the initial orientation of the emission transition moment and ω to its evolution due to rotation during the excited state. Figure adapted from reference [19]. 17

1.8 Time-resolved anisotropy decay models from free and hindered rotations. Figure adapted from reference [19]. 22

1.9 TCSPC principle. Figure adapted from reference [36]. 38

1.10 TCSPC classic device diagram. Figure adapted from reference [20]. 39

1.11 Wide-field images of a microscope calibration sample taken with (A) a CMOS camera and (B) a CMOS camera and an intensifier. The blue squares indicate the area in which the average intensity was calculated. A ND filter with an Optical Density (OD) of 0.9 was used. (C) Plot of the signal measured per OD ND filter and setup configuration. Image scale bar: 500 μm. 41

1.12 Example of some data acquired with the confocal-based TCSPC FLIM setup and the basic steps to obtain the FLIM map. (A) Intensity image. Each pixel has one intensity decay. (B) Decay fit per pixel with the convolution of the Instrument Response Function (IRF) with a multi-exponential model. (C) FLIM image. Image scale bar: 10 μm. 42

1.13 Confocal images of a fluorescence sample before bleaching (a), while bleaching (b) and after bleach (c-d). The graph on the right shows the recovery curve due to the bleach of the sample over time, with the different FRAP parameters. 43

1.14 Schematic of the laboratory setup. L refers to lens, P to pinhole, PL to polariser, ND to neutral density, M to mirror, BS to beam splitter, D to dichroic, and PM to photomultiplier. 46

1.15 Diagram of the 472DRLP filter fabricated by Omega Optical, where transmission is plotted against wavelength. 48

1.16 Photographic picture of the laboratory setup. Each one of the numbered elements refer to the nomenclature used in Figure 1.14. 50

1.17 A,B FLIM experiment in HEK 293T cells co-transfected with FGFR2-RFP and Δ5-GFP or Δ10-GFP. Y-axis depicts the fluorescence lifetime frequency. Scale bar is 10 μm. HEK 293T cells that were transfected with an empty GFP vector (upper panel) were utilised as a control to establish the lifetime of GFP. Histograms (shown on the same scale) in (A) indicate lifetime changes in nanoseconds (ns), where a decrease in GFP lifetime (peak shift to the left of the yellow curve) correlates with a potential direct binding event between the two proteins [144]. 71

2.1 Illustration of the dimer configuration plus linker. The chromophore responsible for the fluorescence emission is shown in the enlarged view. The linker joins both proteins and is presented in red. 82

2.2 Schematic of the time-resolved fluorescence polarisation setup. M stands for mirror, P for pinhole, D for dichroic and PL for polariser. 84

2.3 Schematic of the confocal FRAP setup. M stands for mirror, P for pinhole, D for dichroic, L for lens, PM for photomultiplier, ND for neutral density (filter) and PL for polariser. 88

2.4 Representative total intensity decays for (A) monomer and (B) dimer, in a solution of 25% glycerol. For each plot, the data is presented along the IRF, fit and residuals. (C) Inverse of the average fluorescence lifetime against the square of the refractive index, per solution and EGFP construct. The data for both constructs is fitted showing a linear relationship as established by the Strickler-Berg law. 94

2.5 Time-resolved anisotropy decays in different PBS(X1)/glycerol mixtures for (A) EGFP monomer and (B) EGFP dimer. 96

2.6 (A,B) Representative $I_{\parallel}$ and $I_{\perp}$ for monomer and dimer. (C) Representative time-resolved fluorescence anisotropy decay and fit for the EGFP monomer with a mono-exponential model. Time-resolved fluorescence anisotropy decay for EGFP dimer and fitted with a (D) double and (E) stretched exponential models. The solvent is 10% glycerol and 90% buffer. 97

2.7 (A) Rotational correlation time against viscosity for monomer and dimer. The monomer data is fitted with a linear equation, which gives rise to a radius for the monomer of 2.607 $\pm$ 0.005 nm. (B) Initial anisotropy values for monomer and dimer extracted from the single exponential and bi-exponential fits. 98

2.8 Anisotropy decay parameters against sample composition (% glycerol) calculated from two different models: (A) bi-exponential and (B) stretched exponential model. 100

2.9 Stretched exponential model fit parameters and extracted values. (A) δ, (B) molecule concentration c and (C) E_{FRET} against viscosity's solution. 101

2.10 The FRET energy efficiency plotted versus the donor-acceptor separation for the bi-exponential (blue shade plot) and the stretched exponential model (red shade plot). R_0 is plotted with dashed vertical lines for each solution. κ^2=2/3. 105

2.11 (A) Temporal evolution and (B) histogram of the fluorophore separation R. From the histogram fit, the mean value and standard deviation are 4.56 nm and 0.07 nm, respectively. 107

2.12 (A) Temporal evolution and (B) histogram of the relative dipole orientation κ^2 between EGFP monomers. 108

2.13 (A) Temporal evolution and (B) histogram of the FRET energy efficiency E_{FRET}. 111

2.14 E_{FRET} per fluorophore separation and κ^2, extracted from the MD simulations. The FRET energy efficiency was calculated using equation 2.26. 112

2.15 (A) Individual time-resolved anisotropy decays for the EGFP monomer and (B) average with fit. 113

2.16 Individual tr-anisotropy decays for the EGFP dimer, where (A) corresponds to the first monomer and (B) to the second monomer. (C) Final average tr-anisotropy decay for the EGFP dimer with fit. . . . 114

2.17 Representative FRAP data for EGFP monomer in 35% glycerol. (A) corresponds to the FRAP recovery curve and (B) to the different angular-oriented bleach spot profiles of the normalised first postbleach image. Each image has 512x512 pixels with a pixel size of 0.465030 μm. The confocal FRAP images in (A) are just some frames taken from the actual data to give an idea of how it looks like. The scale colours for (A) and (B) images are false. The dimensions of each frame is 238$\times$238 μm^2. 117

2.18 Profile data of the normalised first postbleach image with fit. (A) corresponds to the entire data and (B) it is just a zoomed version of the first one. 118

2.19 Representative FRAP recovery curves for EGFP monomer and dimer in (A) 35% and (B) 50% glycerol. For each curve, a fit is applied and the parameters presented in Table 2.7. 119

2.20 Steady state anisotropy measurements at different excitation wavelengths for EGFP monomer and dimer in PBS(X1). 120

2.21 Confocal images and ROI of representative areas for the (A) control live cells, (B) fixed untreated cells, (C) fixed three-minute treated cells and (D) fixed 20-minute treated cells. The time-resolved fluorescence anisotropy decays were extracted from the ROI highlighted in red dash line. The scale bar corresponds to 50 μm. 122

2.22 (A) Representative parallel, perpendicular and total intensity decays, per measurement. Specifically, this corresponds to a measurement taken from the fixed cells batch after 3 min of Ad5FK uptake. (B) Intensity weighted average fluorescence lifetime per cell condition. LC stands for live cell and FC for fixed cell. On each box, the central mark indicates the median, and the bottom and top edges of the box indicate the 25^{th} and 75^{th} percentiles, respectively. The whiskers extend to the most extreme data points not considered outliers, and the outliers are plotted individually using the '+' symbol. . 123

2.23 Representative parallel, perpendicular and anisotropy decays for the batch of fixed cells 3 min after Ad5FK cell uptake. 124

2.24 (A) Representative parallel, perpendicular and anisotropy decays with fit - hindered rotation model. This data corresponds to the batch of fixed three-minute treated cells. The fit parameters are: r_0 = 0.115 ± 0.002, ϕ = 2.60 ± 0.31 ns and r_∞ = 0.043 ± 0.003. (B) Initial steady state anisotropy r_0, (C) parameter associated to FRET and (D) limiting anisotropy r_∞ for each cell condition. 125

2.25 FRET energy efficiency calculated from the FRET parameter ϕ extracted from the hindered rotational model, per cell condition. . . . 126

2.26 (A) Representative parallel, perpendicular and anisotropy decays with fit - stretched exponential model. This data corresponds to the batch of cells fixed 3 minutes after the Ad5FK uptake. The fit parameters are: r_0 = 0.131 ± 0.003, γ = 0.381 ± 0.016 with δ = 0.5. (B) Initial steady-state anisotropy and (C) γ parameters. 128

2.27 (A) E_{FRET} extracted from the stretched exponential model per cell condition. (B) Experimental steady-state fluorescence anisotropy per cell condition. 128

3.1 Structures of the polarity-sensitive membrane dye (left) laurdan and (right) di-4-ANEPPDHQ (adapted from reference [231, 234]). . . . 139

3.2 Cartoon and fluorescence confocal image of (A) GUV and (B) SLB. The cell membrane composition is DOPC and the used probe for visualisation purposes is di-4-ANEPPDHQ. 147

3.3 (A) F^3 input and (B) output diagrams. The first diagram presents the involved elements during the data acquisition. The second diagram displays the series of images (parallel and perpendicular) acquired during the experiment. L1 and L2 refer to the pulsed and CW lasers, respectively. D refers to detector, MD to module (electronic) and PBS to polarising beam splitter. Figures adapted from reference [201]. 149

3.4 Representative G-factor data correspondent to the pixel position (75,75). (A) Parallel and perpendicular intensity decays after background subtraction. (B) G-factor decay given by the ratio of the two polarisation intensity decays. A mean value for that pixel position of 1.2408 in the selected range (within the magenta lines) is obtained. (C) G-factor map. (D) G-factor histogram and fit with μ = 1.124 and σ = 0.075. Scale bar: 50 μm. 153

3.5 F^3 data acquisition and analysis. The three steps performed during the data acquisition and presented in Figure 3.3A are indicated by colours: pre-bleach in blue, bleach in green and post-bleach in purple. The first raw corresponds to the parallel intensity images per time data point, the second one to the perpendicular intensity images and the last one to the total intensity images. From the former raw, the FRAP data analysis is undertaken. An integration of all the parallel intensity images yields the total parallel intensity one. The same happens with the perpendicular transient. The combination of these two images gives rise to the anisotropy (steady-state and time-resolved) maps. The last element of the last column is the total intensity image, which is the combination and integration of the two previous ones. From this image, the fluorescence lifetime map is calculated. 155

3.6 Emission and Excitation spectra of di-4-ANEPPDHQ in DOPC Lipid Solution. 158

3.7 Representative fluorescence lifetime data of the R6G solution with 98.48 % glycerol and 1.52 % water for 1 pixel. (A) Parallel, perpendicular and total intensity decays. (B) Total intensity fit with parameters I_0 = 245.9331, τ_F = 3.1507 and BG = 0.0347. (C) Fluorescence lifetime map with a pixel size of 1.8601 μm. (D) Fluorescence lifetime map histogram and fit with μ = 3.25 and σ = 0.08 ns. Scale bar: 50 μm. 159

3.8 Inverse of fluorescence lifetime per R6G solution against its quadratic environmental refractive index. 160

3.9 Representative steady-state anisotropy and steady-state anisotropy standard deviation data of the R6G solution with 98.48 % glycerol and 1.52 % water. (A,B) Steady-state anisotropy map and histogram. The fit of the histogram gives arise to μ = 0.27 and σ = 0.045. (C,D) Steady-state anisotropy standard deviation map and histogram. The fit of the histogram yields to the following parameters: μ = 0.03 and σ = 0.001. Scale bar: 50 μm. 163

3.10 Representative intensity data for R6G solution with 98.48 % glycerol and 1.52 % water. (A) Intensity map. (B) Intensity histogram. The fit parameters are: μ = 1060 and σ = 75. Scale bar: 50 μm. . . 164

3.11 (A) Inverse of steady-state anisotropy against inverse of R6G solution viscosity. The data is fitted with a linear relationship, whose fit parameters are: gradient (261.6 $\pm$ 66.9 cP) and intercept (3.294 $\pm$ 0.155). (B) Steady-state anisotropy standard deviation against total number of counts per R6G solution. The values are extracted from the fit parameters of the produced map histograms. (C) Enlarged view of (B). 165

3.12 Representative time-resolved anisotropy data from the integration of all the image pixels signal and for R6G solution in 98.48 % glycerol and 1.52 % water (η = 911.02 cP). (A) Parallel and perpendicular normalised intensity decays. (B) Time-resolved anisotropy decay and fit. (C) Rotational correlation time against viscosity R6G solution, with a gradient of 0.07 $\pm$ 0.01 ns/cP. 166

3.13 (A) Time-resolved fluorescence anisotropy decay and fit, (B) rotational correlation time map and (C) histogram for some representative R6G data (94.67% glycerol). A binning of n = 3 (7$\times$7 pixels) has been applied. The red dots displayed on the map correspond to that rotational correlation time values beyond 200 ns, which was set as a threshold. Scale bar: 50 μm. 167

3.14 Representative data for R6G in 98.48% glycerol and 1.52% water. (A) Corresponds to the FRAP recovery curve and (B) to the different angular-oriented bleach spot profiles of the normalised first postbleach image. Each image has 128$\times$128 pixels with a pixel size of 1.9 μm. The scale colours for (A) and (B) images are false. The dimensions of each frame is 238$\times$238 μm^2. 168

3.15 Profile data of the normalised first postbleach image with fit. 169

3.16 Representative data for R6G in 94.67 % glycerol and 5.33 % water. (A) Corresponds to the FRAP recovery curve and (B) to the different angular-oriented bleach spot profiles of the normalised first postbleach image. Each image has 512$\times$512 pixels with a pixel size of 0.46 μm. The scale colours for (A) and (B) images are false. The dimensions of each frame is 238$\times$238 μm^2. 170

3.17 Profile data of the normalised first postbleach image with fit. 171

3.18 (A) F^3 and (B) confocal trasnlational diffusion coefficients against inverse of R6G solution's viscosity. 172

3.19 (A) F^3 and (B) confocal translational diffusion coefficient against inverse of rotational correlation time for R6G in varying water/glycerol viscosity solutions. 172

3.20 Representative fluorescence lifetime data of di-4-ANEPPDHQ in DOPC SLB at RT. (A) Parallel, perpendicular and total intensity decays. (B) Total intensity fit with τ_F = 2.0285 $\pm$ 0.0219 ns. (C) Fluorescence lifetime map. (D) Fluorescence lifetime map histogram and fit with μ = 2.09 and σ = 0.05 ns. Scale bar: 50 μm. 173

3.21 Representative steady state anisotropy data, its standard deviation and the total amount of counts per pixel of di-4-ANEPPDHQ in DOPC SLB at RT. (A) Steady state anisotropy map (binning with n = 1). (B) Fitted steady state anisotropy distribution with μ = 0.029 and σ = 0.004. (C) total intensity and (D) δr maps. Scale bar: 50 μm.175

3.22 Representation of the supported lipid bilayer system onto the glass surface. The oval shape in orange represents the fluorescence probe, whose dipole orientation goes along its largest axis. The electric field of the excitation laser is shown below in blue. 176

3.23 Representative time-resolved anisotropy decay of di-4-ANEPPDHQ in DOPC SLB at R.T extracted from the entire field of view. The decay is fitted with the hindered rotation model. The fit parameters are: r_0 = 0.09, θ = 2.17 ns and r_∞ = 0.02. 176

3.24 Representative time-resolved anisotropy data of di-4-ANEPPDHQ in DOPC SLB at RT for the pixel position (10,10). (A) Parallel and perpendicular intensity decays with fit. The fit parameters are: $\tau_{F,1}$ = 1.99 ns and $\tau_{F,2}$ = 3.80 ns for the parallel intensity component, and $\tau_{F,1}$ = 2.14 ns and $\tau_{F,2}$ = 3.96 ns for the perpendicular one. (B) Time-resolved anisotropy decay with fit. The fit parameters are: r_0 = 0.10 and θ = 17.47 ns. (C) Rotational correlation time map. The green dots correspond to NaN values. (D) Rotational correlation time histogram. Scale bar: 50 μm. 178

3.25 Representative FRAP recovery curve with fit of di-4-ANEPPDHQ in DOPC SLB at RT along some representative F^3 FRAP images (pixel size = 1.8601 μm). On the bottom the extracted FRAP parameters are displayed. 180

4.1 Normalised variance of τ against T/τ for different time resolutions. The normalised variance decreases with the number of photons N. Figure adapted from reference [282] 195

4.2 3D plots showing the dependence of $\Delta\theta/\theta_{N=1}$ with τ and θ for different time resolutions k and constant time window T. The last case has no dependence with T and k. 204

4.3 2D representation of the dependence of $\Delta\theta/\theta_{N=1}$ with τ and θ for different time channels k and constant time window T. The last case has no dependence with T and k. The minimum $\Delta\theta/\theta$ is found for every single combination of τ and θ and plotted along the condition $\tau/\theta = 1$. 205

4.4 Dependence of minimum $\Delta\theta/\theta_{N=1}$ with τ and k for a fixed θ and time window T. This example is given for T = 50 ns. 207

4.5 FLIM maps with representative parallel and perpendicular intensity decays for the (A) 30 minutes and (B) 120 minutes FAIM data sets. (C,D) Fitted FLIM map and sd(τ) histograms with a Gaussian distribution per FAIM data set. Map scale bars: 50 μm. 210

4.6 Theoretical fluorescence lifetime standard deviation sd(τ) plotted against the experimental sd(τ) per FAIM data set. The data is fitted with a polynomial function of first order: $sd(\tau)_{th}$ = *(1.08* $\pm$ *0.377)*$sd(\tau)_{exp}$ *- (0.002* $\pm$ *0.014).* 211

4.7 (A) Parallel and perpendicular decays for a ROI with N = 1.39×10^6 of the 120 minutes FAIM data set. (B) Time-resolved fluorescence anisotropy decay and fit of the same ROI. 212

4.8 Location of experimental data within the simulated plots given by equation 4.21. The number of time channels k = 1024 and the time window is T = 50 ns. 212

4.9 (A) Plot of the theoretical and experimental sd(θ)/θ values per 120 minutes FAIM data set ROI. The data per G-factor is fitted with a first degree polynomial model. (B) The second graph is an enlarged view of the first one. 215

4.10 (A) Evolution of the rotational correlation time distribution with $sd(r)$ for r = 0.3, τ = 3.7 $\pm$ 0.1 ns and r_0 = 0.4. Rotational correlation time maps and histograms for (B) $sd(r)$ = 0.005 and (C) $sd(r)$ = 0.1. The map scale bars correspond to 25 pixels. 220

4.11 Dependence of the maximum value (θ_{max}) of the rotational correlation time distribution with $sd(r)$ (A) for a fixed r and varying τ and sd(τ), and (B) for a fixed τ and sd(τ) and varying r. All the data sets are fitted with a linear approximation. 222

4.12 Rotational correlation time distribution mode per r, $sd(r)$ and τ $\pm$ $sd(\tau)$. 223

4.13 Rotational correlation time distribution skewness SK per r, $sd(r)$ and $\tau \pm sd(\tau)$. 224

B.1 Dependence of minimum $\Delta\theta/\theta_{N=1}$ with τ and k for a fixed θ and time window T. This example is given for T = 10 ns. 239

B.2 Dependence of minimum $\Delta\theta/\theta_{N=1}$ with τ and k for a fixed θ and time window T. This example is given for T = 50 ns. 240

B.3 Dependence of minimum $\Delta\theta/\theta_{N=1}$ with τ and k for a fixed θ and time window T. This example is given for T = 100 ns. 240

B.4 Dependence of minimum $\Delta\theta/\theta_{N=1}$ with τ and k for a fixed θ and time window T. This example is given for T = 200 ns. 241

B.5 Dependence of minimum $\Delta\theta/\theta_{N=1}$ with τ and k for a fixed θ and time window T. This example is given for T = 500 ns. 241

B.6 Dependence of minimum $\Delta\theta/\theta_{N=1}$ with τ and k for a fixed θ and time window T. This example is given for T = 1000 ns. 242

B.7 Dependence of minimum $\Delta\theta/\theta_{N=1}$ with θ and k for a fixed τ and time window T. This example is given for T = 10 ns. 242

B.8 Dependence of minimum $\Delta\theta/\theta_{N=1}$ with θ and k for a fixed τ and time window T. This example is given for T = 50 ns. 243

B.9 Dependence of minimum $\Delta\theta/\theta_{N=1}$ with θ and k for a fixed τ and time window T. This example is given for T = 100 ns. 243

B.10 Dependence of minimum $\Delta\theta/\theta_{N=1}$ with θ and k for a fixed τ and time window T. This example is given for T = 200 ns. 244

B.11 Dependence of minimum $\Delta\theta/\theta_{N=1}$ with θ and k for a fixed τ and time window T. This example is given for T = 500 ns. 244

B.12 Dependence of minimum $\Delta\theta/\theta_{N=1}$ with θ and k for a fixed τ and time window T. This example is given for T = 1000 ns. 245

C.1 Evolution of the rotational correlation time distribution with $sd(r)$ for τ = 100 $\pm$ (a) 0.1, (b) 1 and (c) 10 ns. The initial anisotropy r_0 is set to 0.4. 247

C.2 Evolution of the rotational correlation time distribution with $sd(r)$ for τ = 3.7 $\pm$ 0.1 ns and for three different steady-state anisotropy values: (a) r = 0.1, (b) r = 0.2 and (c) r = 0.3. The initial anisotropy r_0 is set to 0.4. 248

C.3 Evolution of the rotational correlation time distribution with $sd(r)$ for τ = 100 $\pm$ 0.1 ns and for three different steady-state anisotropy values: (a) r = 0.1, (b) r = 0.2 and (c) r = 0.3. The initial anisotropy r_0 is set to 0.4. 249

D.1 Evolution of the rotational correlation time distribution with $sd(r)$ for τ = 3.7 $\pm$ 0.1 ns and r = 0.1. The initial anisotropy r_0 is set to (a) 0.4 and (b) 0.38 $\pm$ 0.02. 251

E.1 Dependence of the maximum value (θ_{max}) of the rotational correlation time distribution with $sd(r)$ for r = 0.1 and r_0 = 0.4. Varying fluorescence lifetimes and standard deviations are applied: (a) τ = 10 $\pm$ 0.01, 0.1 and 1 ns, and (b) τ = 100 $\pm$ 0.1, 1 and 10 ns. 252

F.1 Dependence of the maximum value (θ_{max}) of the rotational correlation time distribution with $sd(r)$ for r = 0.1, 0.2 and 0.3. The fluorescence lifetime is: (a) τ = 10 $\pm$ 0.1 ns and (b) τ = 100 $\pm$ 0.1 ns. The initial anisotropy r_0 is equal to 0.4 253

Chapter 1

Fluorescence photophysics, lifetime and polarisation

1.1 Brief introduction to fluorescence microscopy and basic concepts

1.1.1 Fluorescence microscopy in biology

Fluorescence microscopy is a widely spread technique [1] that provides information in regards to biological processes at the cellular and subcellular level. It is considered to be a powerful technique due to its several advantages: sub-cellular resolution, its single-molecule sensitivity, its molecular specificity and the real-time data collection from live cells with almost negligible cytotoxicity. Compared to other imaging techniques, such as electron microscopy [2], its resolution is much worse, restricted by the diffraction limit of light, about 200-300 nm in the lateral direction and 500-700 nm in the axial direction. Although electron microscopy provides structural and morphological information about the sample at a nano-scale resolution, the sample is measured in vacuum and must be usually coated with conductive layers or cut into thin sections, which makes this technique incompatible with live-cell imaging. On the other hand, light microscopy allows the observation

of structures inside live samples in real time through specific labelling of any of its cellular components [3].

The fluorescence microscope contains an excitation filter and an emission filter. In epi-fluorescence microscopy this is known as the filter cube, which consists of both excitation and emission filters within a cubic structure. This device was invented by the Dutch medic Johann Sebastiaan Ploem in 1970. The excitation filter transmits only light with the desired wavelength. The emitted light has to pass through the emission filter before it reaches the detector. The emission filter is only transparent for light with a distinct wavelength, like the light emitted by the specimen. The final image shows fluorescing areas which can be observed on a dark background producing a high contrast.

With conventional fluorescence microscopy, due to the diffraction limit of light of around 250 nm in the lateral direction, we are not able to observe structures whose separation is lower than 250 nm. The spatial resolution is given by the Abbe limit, which is roughly $d = \lambda/2$, where λ is the emission wavelength of the illuminating source [4]. This resolution is small compared to most biological cells (1 μm to 100 μm), but large compared to viruses (100 nm), proteins (10 nm) and less complex molecules (1 nm). Therefore, the spatial resolution provided by the conventional fluorescence microscopy is not good enough to study systems with dimensions below the diffraction limit. Super-resolution fluorescence microscopy overcomes this problem, which resolves microscopy images by at least a factor of two over the diffraction of light. There are three major super resolution techniques based on different principles: Stimulated Emission Depletion (STED) [5, 6], Structured Illumination Microscopy (SIM) [7–9], and localization microscopy, where three different techniques can be found: Stochastic Optical Reconstruction Microscopy (STORM) [10], Photo-Activated Localisation Microscopy (PALM) and Fluorescence Photo-Activated Localisation Microscopy (FPALM) [11].

The work presented in this thesis does not require of any high resolution technique, as the features we want to image are well sampled with a conventional fluorescence microscope. This thesis is mainly focused on the simultaneous acquisition of multi-parametric fluorescence properties by utilising time-resolved fluorescence imaging techniques, which will be introduced in the upcoming subsections of this chapter.

1.1.2 What emits fluorescence?

In the life sciences, fluorescence sensing can be performed labelling a sample with fluorescent probes, quantum dots [12], other nanoparticles [13] or genetically encoded proteins [14], and also by imaging autofluorescence [15]. Autofluorescence is the fluorescence of naturally occurring substances, such as clorophyll [16], fluorite and collagen. Most plant and animal tissues show some autofluorescence when excited with Ultraviolet (UV) light. In tissues, the autofluorescence information can provide a guide to the morphology of the tissue and it is due to several fluorophores: collagen and elastin as the components of the connective tissue, tryptophan as a component of most proteins, and Nicotinamide Adenine Dinucleotide (NAD), a coenzyme found in all living cells. In cancer identification, the advantage of the use of autofluorescence lies in no need to apply exogeneous substances, which may potentially be harmful and time consuming [15, 17, 18]. However, when a sample is labelled with fluorescent probes, autofluorescence can lead to some background noise that may cover the main signal partially or entirely.

The aforementioned fluorophores can be divided in three classes: *intrinsic probes; extrinsic covalently bound probes; and extrinsic associating probes* [19]. However, it should be mentioned that the fluorescence tends to occur in the presence of molecules with an aromatic structure, where the degree of electron delocalisation is significant.

1.1.3 Excitation and absorption spectra - The Lambert-Beer law

Excitation from the ground state to an excited state can occur when the excitation light has an energy that corresponds to at least the energetic difference in between both states. Obviously, a minimum of energy is required to make this transition happen. It is important not to confuse the excitation and absorption spectra. An absorption spectrum measures wavelengths at which a molecule absorbs light, while an excitation spectrum determines the wavelengths of light necessary to produce emission or fluorescence from the molecule, at a particular wavelength. We could think of the excitation spectrum as the *fluorescence detected absorption*.

The height of peaks shown in the excitation spectrum is directly proportional to the number of photons absorbed, meanwhile for getting an absorption spectrum, the absorbance of the sample is measured, which is a unitless measure, independent of illumination intensity [19,20]. The *Lambert-Beer law* states how much the intensity of light is reduced when passing through a sample, compared to the incident one I_0 [19,20].

$$I = I_0 10^{-\varepsilon[c]d} \tag{1.1}$$

where ε is the extinction coefficient, $[c]$ is the concentration of the sample and d is the pathlength.

This equation is valid at low concentrations of the absorbing species ($\leq$ 10 mM), where non-multiple scattering (light scattering) takes place. Light scattering is not taken into account in equation 1.1, otherwise an additional term should appear in the exponent.

The absorbance corresponds to the logarithm of the ratio of the incident light and the transmitted one.

$$A = \varepsilon[c]d = log\frac{I_0}{I} \tag{1.2}$$

Absorbance measurements can be difficult to interpret quantitatively when com-

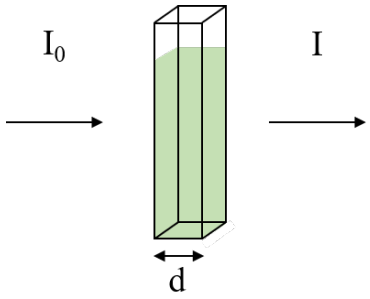

Figure 1.1: Standard sample cuvette with a d path length. I_0 corresponds to the incident optical intensity and I to the transmitted optical intensity.

bined with imaging, due to light-scattering effects and the generally unknown path length, and it is also less sensitive than fluorescence [20]. William E. Moerner received the Nobel Prize in 2014 (shared with Eric Betzig and Stephan W. Hell) for reporting for the first time the optical absorption spectrum of a single molecule (hydrocarbon called pentacene) [21].

1.1.4 What is fluorescence?

Fluorescence is the emission of light from a molecule when a photon is absorbed. This process happens on the nano-second time-scale, whereas, phosphorescence also consists of the emission of light but at a much slower rate due to the different nature of the excited state. Phosphorescence occurs when a photon is emitted due to the transition of the electron from the triplet state to the ground singlet state; fluorescence happens when the electron transition occurs in between the singlet states. The phosphorescence transition is forbidden, that is the reason why the rate process is very slow ($10^{-3} - 100\ s^{-1}$), in comparison to the fluorescence one ($\sim 10^9\ s^{-1}$) [20]. Specifically, fluorescence is the result of a three-stage process that occurs in certain molecules called fluorescent dyes or fluorophores.

1. **First stage**

   In the first stage a photon of energy $h\nu_{ex}$ is supplied by an external source such as a laser or an incandescent lamp to the fluorophore. This creates an

excited electronic single state (S_1').

2. **Second stage**

   During the second stage, the excited state exists for a certain time given by the lifetime of the system in that state. During this time, the fluorophore is subjected to several interactions with the molecular environment and undergoes conformational changes. These two processes give rise to two important consequences. The first one is that the energy of S_1' is partially dissipated, reaching the lowest energy singlet excited state (S_1), from where fluorescence emission is originated, a rule known as *Kasha's rule* [22]. The second one is that not all the molecules initially excited by absorption return to the ground state (S_0) by fluorescence emission. Other processes such as Förster Resonance Energy Transfer (FRET) and intersystem crossing could also depopulate S_1. This will be further explained in the *Jablonski diagram* section.

3. **Third stage**

   In the third and last step, a photon of energy $h\nu_{em}$is emitted, returning the fluorophore to its ground state S_0. Due to the dissipation mentioned above, the energy of this photon is lower, having therefore a longer wavelength than the excitation photon $h\nu_{ex}$. The energy difference between the excitation photon and the emission photon $h(\nu_{ex} - \nu_{em})$ is called the *Stokes shift*.

The Jablonski energy diagram is used to represent the various energy levels involved in the absorption and emission of light by a fluorophore. It shows how the electrons are excited from the ground state to the different excited states and then, how they eventually fall back to the original ground state via different paths with different probabilities. The different de-excitation pathways will be explained by describing Figure 1.2.

S_0, S_1 and S_2 represent the ground state, the first and second excited singlet

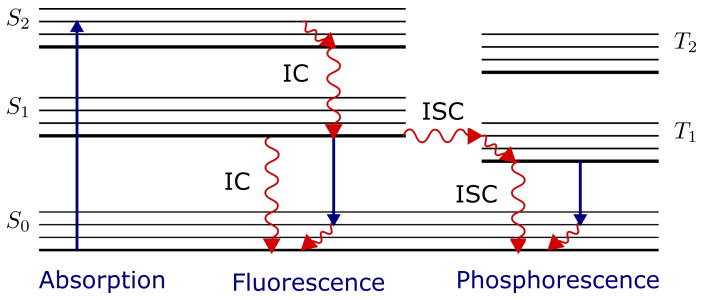

Figure 1.2: Jablonski diagram and illustration of the different positions for absorption, fluorescence and phosphorescence spectra. Figure adapted from reference [19].

energy states, respectively, whereas, T_1 and T_2 represent the first and second excited triplet energy states. If the photon is energetic enough to reach the second excited single energy state S_2 or high vibrational levels of the first excited singlet energy state S_1 (S_1'), the most likely de-excitation pathway will be via non-radiative dissipation to the lowest vibrational energy level for the first excited single state S_1. This phenomenon takes place within the same electronic state and it is known as vibrational relaxation.

Non-radiative dissipation can also happen from S_1 to S_0, but with a much lower efficiency, because of the much larger energy gap that separates both electronic states [19]. This process, occurring between two different electronic states, is known as internal conversion (IC) [22]. We have seen that the fluorescence process corresponds to the relaxation of the electron from the S_1 to the S_0 state, independent on the excitation wavelength [19], but on the molecular structure of the fluorophore and its environment. Another possible de-excitation process is the intersystem crossing from S_1 to T_1, which is followed by other processes. This transition is non-radiative, and it occurs in between two isoenergetic vibrational levels, to end up in the lowest vibrational level of the T_1 state. It ultimately results either in emission of a photon through phosphorescence or in a non-radiative de-excitation, where the last one is the predominant. As mentioned in the previous section, phosphorescence involves a forbidden transition ($T_1 \rightarrow S_0$), and therefore, the radiative rate constant

is very low [19].

1.1.5 Emission spectrum

As mentioned above, after the excitation happens, the molecule relaxes very quickly to the lowest vibrational mode of the excited state S_1 by thermal dissipation. This process occurs in about 10^{-12} s, which allows an independence of the emission spectra with respect to the excitation wavelength [20].

The *Stokes shift* between the emitted and the absorbed light allows a filter to be used in order to block the excitation light, and therefore detect only the fluorescence light. This effect was first described by the scientist George Stokes [23] (Figure 1.3).

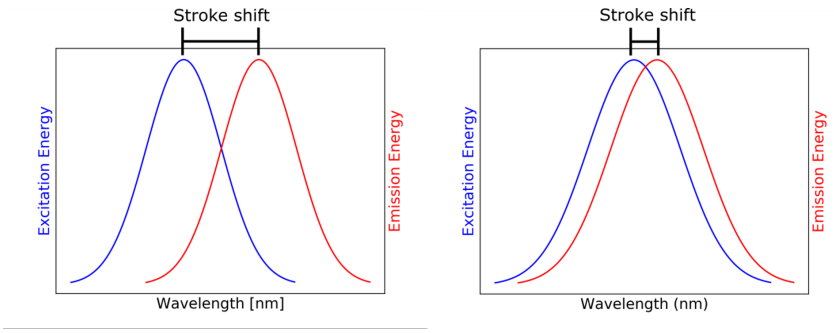

Figure 1.3: The Stokes shift of the excitation and emission spectrum of a fluorophore in two different cases. In the first one, the excitation and emission are clearly separated from each other, meanwhile in the second one this distinction is more difficult to observe, increasing the background signal. An overlap between excitation and emission spectra occurs because it exists a range of orbitals at different energies. Low energy excitation orbitals (high excitation wavelength) can lead to an overlap of the two spectra.

As the electronic transition does not alter much the nuclear configuration, similar spacing of the vibrational energy levels of the ground and excited states are observed, and therefore, a symmetry in the excitation and emission spectra. This is the so-called *mirror image rule*. There are several exceptions to this rule, such as proton dissociation, dimerisation, charge-transfer complex formation, etc. [20, 24].

1.1.6 Fluorescence lifetime

Since the fluorescent probe is excited through absorption of light to the excited state S_1, different processes will start to compete in order to de-excite the molecule to the ground state S_0 via different paths. The rate constant k of the excited state will be the sum of the kinetic constants of all these processes:

$$k = k_r + k_{nr} \tag{1.3}$$

where k_r is the radiative rate constant and k_{nr} is the non-radiative rate constant, which is the sum of the rate constant for internal conversion k_{ic}, and the rate constant for intersystem crossing to the triplet state k_{isc}. The fluorescence emission always occurs from the lowest vibrational level of the first excited state (S_1), which is known as Kasha's rule [22].

The fluorescence lifetime τ is the average time the molecule spends in its excited state S_1 before falling back to its ground state. It is defined as the inverse of the sum of the rate constants for all excited state depopulation processes:

$$\tau = \frac{1}{k_r + k_{nr}} \tag{1.4}$$

The natural or radiative lifetime $\tau_0 = k_r^{-1}$ is related to the fluorescence lifetime τ via the fluorescence quantum yield Φ_F:

$$\Phi = \frac{k_r}{k_r + k_{nr}} = \frac{\tau}{\tau_0} = k_r \tau \tag{1.5}$$

The fluorescence quantum yield Φ gives the ratio of the emitted photons and

the absorbed ones. Its value is always below 1.

$$\Phi = \frac{emitted\ photons}{absorbed\ photons} = \frac{k_r}{k_r + k_{nr}} \tag{1.6}$$

When the fluorescence lifetime τ and the quantum yield Φ of a fluorophore are known, the radiative and non-radiative rate constants (k_r and k_{nr}) can be uniquely determined by combining equations 1.4 and 1.5.

The radiative rate constant k_r depends on the refractive index due to the polarisability of the medium that surrounds the fluorescence emitter, according to the Strickler-Berg formula [25]:

$$k_r = 2.88 \times 10^{-9} n^2 \frac{\int F(\vec{\nu}) d\vec{\nu}}{\int F(\vec{\nu}) \vec{\nu}^{-3} d\vec{\nu}} \int \frac{\varepsilon(\vec{\nu}) d\vec{\nu}}{\vec{\nu}} \tag{1.7}$$

where k_r is the inverse of the natural or radiative lifetime τ_0, n is the refractive index, F is the fluorescence emission, ε is the extinction coefficient and $\vec{\nu}$ is the wavenumber.

Equation 1.7 refers to the natural lifetime, this expression can also be used to assess the dependence of the fluorescence lifetime of the fluorophore with its environmental refractive index as previously presented in the study of several fluorescence emitters [26–30].

After N fluorophores are excited and populate the excited state S_1, they will de-excite to the ground state S_0. The time-dependence of the depopulation of the excited state S_1 can be described by the following rate equation:

$$dN = -(k_r + k_{nr}) N(t) dt \tag{1.8}$$

where t is the time.

Integration of equation 1.8 and taking into account that the fluorescence intensity $I(t)$ is proportional to the number of excited fluorophores $N(t)$:

$$I(t) = I_0 e^{-t/\tau} \tag{1.9}$$

where I_0 is the fluorescence intensity at time $t = 0$ and τ is the fluorescence lifetime defined in equation 1.4. The decay of the fluorescence intensity follows an exponential decay law [31]. The fluorescence lifetime τ refers to the time it takes for the fluorescence intensity to decay from its peak to $e^{-1} \sim 37\%$ of its peak value. If the set of fluorophores are surrounded by several micro-environments, most likely the fluorescence intensity will decay as a linear combination of several fluorescence exponentials. This implies that sub-sets of fluorophores will exhibit different fluorescence lifetimes. Thus, the intensity decay of this population of fluorophores would decay as follows:

$$I(t) = \sum_{i=1}^{N} A_i e^{-t/\tau_i} \tag{1.10}$$

where A_i is the i_{th} amplitude of the intensity decay with τ_i and N is the number of fluorescence components.

The multi-exponential fit of the fluorescence intensity decay of a set of fluorophores does not necessarily mean that the medium in which the fluorescence probes are located is formed by different micro-environments. Some probes have several excited states, which means several depolarisation pathways are likely to exist. This was for instance observed with the Green Fluorescence Protein (GFP) [32–35]. The absorption bands of this protein are located at 400 nm and 475 nm. When the protein is excited with ultraviolet light (UV), the de-excitation occurs via one pathway, which implies a single fluorescence lifetime. However, if the protein is excited with blue light, the depopulation of the excited state occurs via two fluorescence lifetimes (3.4 and 2.7 ns). This means that two excited states are populated

when the protein is excited with blue light.

The intensity-weighted average lifetime is the average of the lifetimes of the decay components weighted by their integral intensities. Thus, the intensity-weighted average lifetime with N components is given by the following equation [36]:

$$\tau_{avg} = \frac{\sum_{i=1}^{N} A_i \tau_i^2}{\sum_{i=1}^{N} A_i \tau_i} \tag{1.11}$$

1.1.7 Fluorescence polarisation or anisotropy

The fluorescence anisotropy theory will be explained in detail, paying special attention to the anisotropy depolarisation of a dye in its excited state due to Brownian motion. Different case scenarios will be presented, where the anisotropy evolution over time for an isotropic freely and hindered rotating fluorophore is described.

1.1.7.1 Definition of fluorescence anisotropy

Anisotropy measurements are based on the principle of photoselection (Figure 1.4). The fluorophore is excited with polarised light. Fluorophores absorb photons in a preferential direction, when their transition dipole is parallel to the one of the excitation light. The probability of absorption by the fluorophore is proportional to $cos^2\beta$, where β is the angle between the dipole moment of the transition (absorption transition moment) and the direction of the polarisation of the excited light. The orientation of the absorption transition moment depends on the electronic state reached through absorption. By contrast, the emission transition moment is the same whatever the reached excited-state is (internal conversion towards S_1) [19]. Therefore, the result of this photoselection is that part of the population of fluorophores is oriented (due to the excitation electric field), and part of the fluorescence emission is polarised.

Emitted light will be measured with a polariser. Two components of the emis-

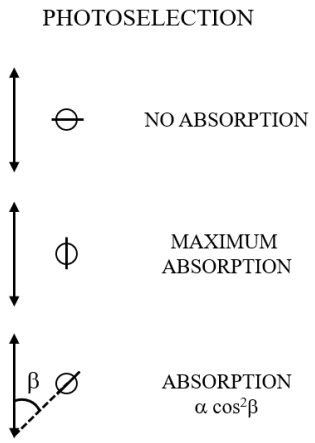

Figure 1.4: Transition moments and photoselection. Figure adapted from reference [19].

sion light will be measured, the parallel and the perpendicular intensity components with respect to the polarisation of the excitation light. The light anisotropy is defined as follows:

$$r = \frac{I_{\parallel} - I_{\perp}}{I_{\parallel} + 2I_{\perp}} = \frac{I_{\parallel} - I_{\perp}}{I_{tot}} \tag{1.12}$$

where $I_{\parallel}$, $I_{\perp}$ are the parallel and perpendicular intensity components of the fluorescence emission and I_{tot} is the total fluorescence intensity. Note that when $I_{\perp} = 0 \rightarrow r = 1$ and when $I_{\parallel} = 0 \rightarrow r = -1/2$. Thus, the anisotropy is within a range $-1/2 \leq r \leq 1$.

The factor 2 for defining the total fluorescence emission comes from applying the Curie symmetry principle [19]. This leads to relations between intensities that is shown in Figure 1.5.

The total emission is given by $I_{tot} = I_x + I_y + I_z$. For the first case, where the excitation light is vertically polarised, the z axis is an axis of symmetry for the emission (parallel axis), therefore, $I_x = I_y$ (perpendicular axis). In the second case, the excitation light is horizontally polarised. This time, the axis of symmetry for the emission will be the x axis (parallel axis). Therefore, by symmetry, $I_y = I_z$ (perpendicular axis). Both cases lead to the final expression for the total fluorescence intensity.

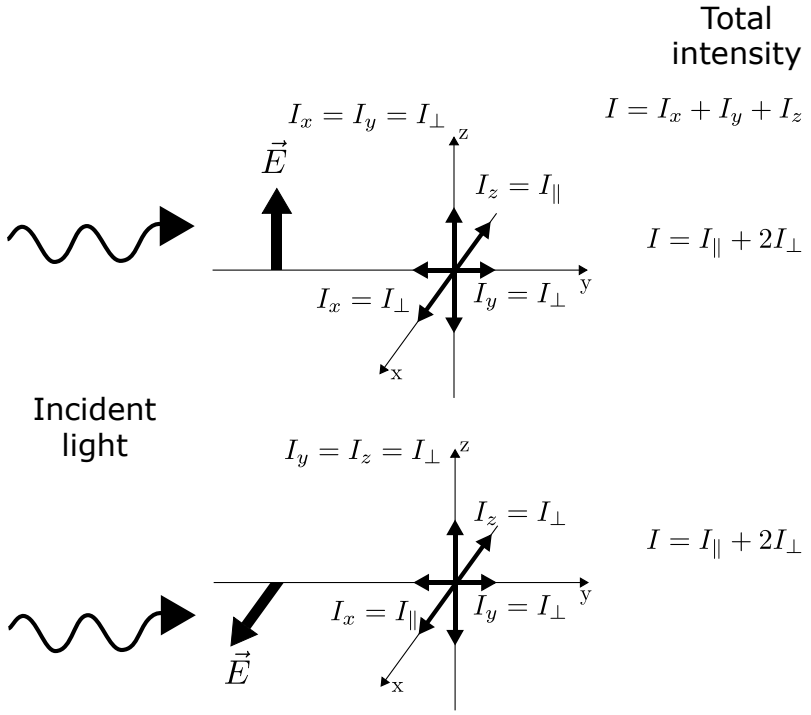

Figure 1.5: Relations between the intensity components (defined in the Cartesian coordinates) after applying the Curie symmetry principle. The first case corresponds to vertically polarised excitation light and the second one to horizontal polarised excitation light. Figure adapted from reference [19].

1.1.7.2 Anisotropy theory - Photoselection and initial anisotropy r_0

The theory for fluorescence anisotropy can be derived considering a a fluorophore oriented at an angle β from the z axis and ϕ from the y axis, as shown in Figure 1.6, with collinear excitation and emission dipoles. The maximum anisotropy will have assigned a specific value due to the effect of the photoselection.

As we can see in Figure 1.6, the parallel intensity component of the fluorescence emission is proportional to $cos^2\beta$ as this corresponds to the projection of the field along the z axis. In the same way, we can observe that the perpendicular component for the fluorescence emission goes with the $sin^2\beta sin^2\phi$. Therefore, the perpendicular and parallel components for the fluorescence intensity are given by:

$$I_\parallel(\beta,\phi) = cos^2\beta \tag{1.13}$$

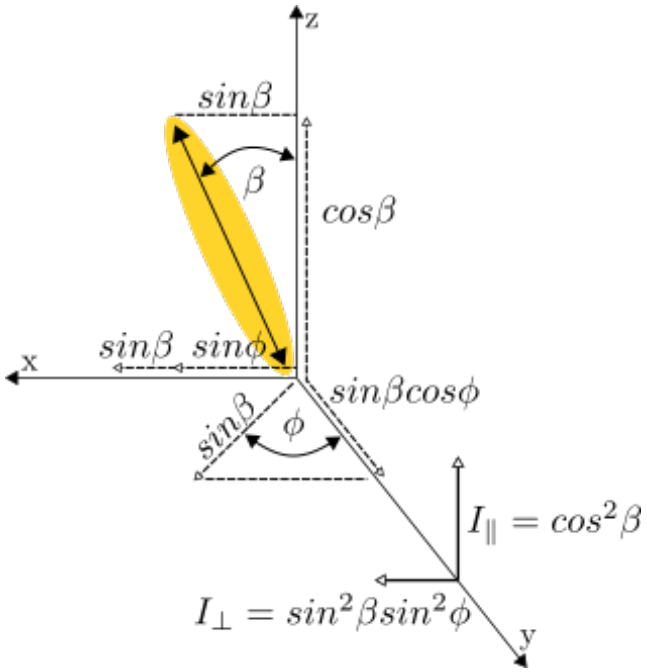

Figure 1.6: Parallel and perpendicular fluorescence intensity components for a random fluorophore in a spherical coordinate system. Figure adapted from reference [20].

$$I_{\perp}(\beta,\phi) = sin^2\beta sin^2\phi \tag{1.14}$$

If we consider an isotropic system, where the dipoles are randomly oriented, the fluorophores will be equally excited regardless of the angle ϕ from the y-axis. That's why we can eliminate the dependence of ϕ in equation 1.14, by calculating its average value.

$$< sin^2\phi >= \frac{\int_0^{2\pi} sin^2\phi d\phi}{\int_0^{2\pi} d\phi} = \frac{1}{2} \tag{1.15}$$

The combination of equations 1.12, 1.13, 1.14 and 1.15 allows us to get to the following expression for the anisotropy:

$$r = \frac{3 < cos^2\beta > -1}{2} \tag{1.16}$$

We can see from equation 1.16 that $r = 1$ at $\beta = 0°$. But due to photoselection, the maximum value of r is lower. If we consider a random orientation of dipole

moments, β has to be averaged. The probability density function of finding an excited molecule with a dipole under the angle β is:

$$p(\beta) = sin\beta cos^2\beta \tag{1.17}$$

So the average value of $< cos^2\beta >$ is:

$$< cos^2\beta >= \frac{\int_0^{\pi/2} cos^2\beta\, p(\beta) d\beta}{\int_0^{\pi/2} p(\beta) d\beta} = \frac{\int_0^{\pi/2} cos^4\beta sin\beta d\beta}{\int_0^{\pi/2} cos^2\beta sin\beta d\beta} = \frac{3}{5} \tag{1.18}$$

If we introduce this result in equation 1.16, we realise that now the maximum value that r can have for an isotropic conformation is $r_0 = 0.4$. It should be noted that this expression is only valid for samples with symmetry along the z-axis and single-photon excitation. These values can exceed 0.4 for multiphoton excitation (e.g. $r_{02} = 4/7$ for two-photon excitation and $r_{03} = 2/3$ for three-photon excitation).

If the excitation and emission dipoles are not collinear, this is not true. In most of the cases, there is an angular displacement in between the dipoles (α). Therefore, the fundamental anisotropy of the fluorophore is modified in the following manner [20]:

$$r_0 = \frac{2}{5}\left(\frac{3cos^2\alpha - 1}{2}\right) \tag{1.19}$$

where r_0 is within the range from -0.2 to 0.4 for single-photon excitation.

1.1.7.3 Anisotropy depolarisation and rotational Brownian motion

The anisotropy of a fluorophore can depolarise due to different depolarisation sources. One of them is the non-collinearity in the excitation and emission dipoles, which introduces this angle α in the anisotropy expression (equation 1.19). Anisotropy depolarisation can also occur if excitation energy is transferred non-radiatively from one fluorophore to another. This is the so-called Förster Resonance Energy Transfer (FRET), which due to its relevance, it will be covered in *Section*

1.2.

The rotational Brownian motion of the fluorophore after excitation is the main cause of fluorescence depolarisation, as long as the excited fluorophore is able to rotate during the excited-state lifetime. The anisotropy of the fluorophore at time $t = 0$ will be gradually depolarised as a function of time by the rotational Brownian motions (Figure 1.7). From this depolarisation, information about the size of the molecule or viscosity of the medium can be obtained. Note that quantitative information can only be obtained if the time-scale of rotational motions is of the order of the excited-state lifetime τ. Moreover, if the rotational motions are rapid with respect to τ ($r \sim 0$) or slow ($r \sim r_0$), inferring any information about the rotational motion via anisotropy measurements is not possible, as the motions occur out of the experimental time window.

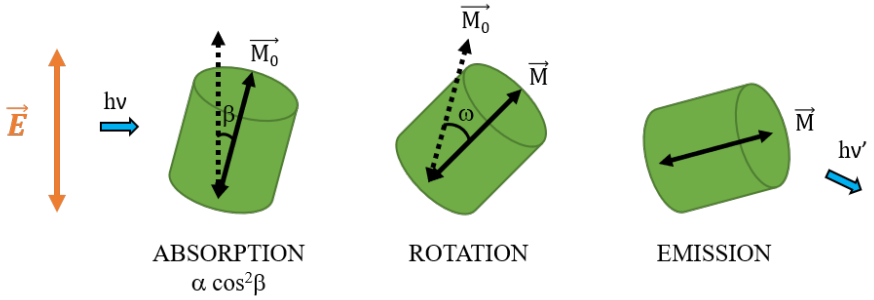

Figure 1.7: Fluorescence depolarisation due to rotational motions. The absorption and emission transition moments are assumed to be parallel. β corresponds to the initial orientation of the emission transition moment and ω to its evolution due to rotation during the excited state. Figure adapted from reference [19].

Depending on how the distribution of the dipoles in the fluorophore is (isotropic or anisotropic) and the medium in which it is encountered, the time-dependent anisotropy curve can adopt different shapes [19]. If the micro-environment in where the fluorophore is, permits it to rotate freely, then this case is of free rotation. In this situation, the anisotropy goes from r_0 to 0, as the final stage implies the random orientation of the fluorophores at long times. By contrast, this is not possible for the case of hindered rotation, where the anisotropy cannot decay

to 0 due to hindered motion. Free rotation of an isotropic system involves a single exponential anisotropy decay, meanwhile several exponential terms conform the one that governs the free anisotropic rotation decay. For the hindered rotation, apart from the fundamental anisotropy (r_0), another term must be introduced. This is the so-called *limiting anisotropy* r_∞. These two cases of free and hindered rotations will now be discussed.

- **Free rotation**

  If we consider the initial emission transition moment of the freely rotating fluorophore is given by β and its evolution over time (from time $t = 0$ to time t) is described by $\omega(t)$, following the same method that led to equation 1.16, the emission anisotropy will be given by:

$$r(t) = \frac{\overline{3cos^2\omega(t)} - 1}{2} \tag{1.20}$$

  The orientation autocorrelation function (ACF) is given by $(\overline{3cos^2\omega(t)})/2$. It represents the probability that the fluorophore with a certain orientation at time $t = 0$ is oriented at ω with respect to its initial orientation. The Legendre polynominal of order 2, $P_2(x)$ is given by $(3x-1)/2$. Thus, sometimes equation 1.20 is written as follows:

$$r(t) = r_0 < P_2[cos\omega(t)] > \tag{1.21}$$

- **Isotropic rotation**

  The rotation of spherical fluorophores is isotropic and the average of $cos^2\omega(t)$ can be calculated considering an orientation distribution function $W(\omega,t)$, which expresses the probability that a fluorophore has an orientation ω at time t, with $\omega = 0$ at time $t = 0$. Therefore, the average $cos^2\omega(t)$ is obtained

as follows:

$$\overline{cos^2\omega(t)} = \int_0^\infty cos^2\omega W(\omega,t) sin\omega d\omega \tag{1.22}$$

The Brownian diffusion equation for a spherical particle is given by:

$$\frac{\partial W(\omega,t)}{\partial t} = D_r \nabla^2 W(\omega,t) \tag{1.23}$$

where D_r is the rotational diffusion coefficient. Equation 1.23 can be rewritten in spherical coordinates:

$$\frac{\partial W}{\partial t} = D_r \frac{1}{sin\omega} \frac{\partial}{\partial \omega}(sin\omega \frac{\partial W}{\partial \omega}) \tag{1.24}$$

If $cos^2\omega(t)$=u and $cos^2\omega(0)$=0, equations 1.22 and 1.24 lead to:

$$u = \frac{1}{3} = [1 + 2e^{(-6D_r t)}] \tag{1.25}$$

Taking into account that the ACF $(3u-1)/2$ is a single exponential, the evolution of the anisotropy over time is given by:

$$r(t) = r_0 e^{-6D_r t} \tag{1.26}$$

The rotational correlation time θ is the time it takes the fluorophore/molecule to rotate 1 radian. The Stokes-Einstein-Debye (SED) equation describes the motion of a Brownian particle in an homogeneous fluid and it is widely used to relate orientational molecular diffusivity quantitatively to viscosity. SED can describe the rotational motion of a fluorescent probe, yielding:

$$\theta = \frac{\eta V}{k_b T} \tag{1.27}$$

where η is the viscosity, k_b is the Boltzmann constant, V is the volume of the

rotating molecule and T is the temperature.

The rotational correlation time θ is related to the rotational diffusion coefficient by $\theta = (6D_r)^{-1}$. Therefore, knowing the rotational correlation time of the rotating probe, the rotational diffusion coefficient can be calculated. The viscosity of the solution that contains the fluorescent probe can be estimated if its volume is known a priori via equation 1.27 [20]. Following the Stokes-Einstein-Debye behaviour and considering a spherical fluorescent probe, its rotational diffusion coefficient is given by:

$$D_r = \frac{1}{6\theta} = \frac{k_b T}{8\eta\pi R_h^3} \tag{1.28}$$

where k_b is the Boltzmann constant and R_h is the hydrodynamic radius of the fluorescent probe.

From the previous equation, the hydrodynamic radius of the probe can be extracted:

$$R_h = \left(\frac{k_b T}{8\eta\pi D_r}\right)^{1/3} \tag{1.29}$$

The anisotropy evolution over time is commonly expressed in terms of the rotational correlation time θ. Combining equations 1.26 and 1.28, the anisotropy of a freely rotating fluorophore in an isotropic medium is given by:

$$r(t) = r_0 e^{-t/\theta} \tag{1.30}$$

where no restriction but the solution's viscosity is present, which allows the free rotation of the probe.

- **Hindered rotation**

The decay of the anisotropy for a fluorophore rotating between two barriers is of special interest. The problem of a fluorophore with restricted rotation in an

ordered lipid bilayer was discussed by Kinosita et al. [37]. If we consider the *'wobble-in-cone'* model, in which the rotations of the fluorophore with a rod-like shape are restricted within a cone and the direction of the absorption and emission transition dipole moments coincide with the long molecular axis, the rotational motions will be described by: a wobbling diffusion constant D_r and a degree of orientation constraint (half-angle of the cone β_0). D_r is defined as the rotational diffusion coefficient around an axis perpendicular to the long molecular axis (these rotations do not affect the emission anisotropy). Kinosita et al.'s analysis leads to [37]:

$$\frac{r(t)}{r_0} = \sum_i A_i e^{(-D_r t/\sigma_i)} \tag{1.31}$$

where D_r is the *wobbling* diffusion constant. The coefficients A_i and σ_i cannot be expressed as closed analytical functions of β. Therefore, Kinosita et al. proposed the following approximate expression for $r(t)/r_0$ [37]:

$$\frac{r(t)}{r_{0,approx.}} = A_\infty + (1 - A_\infty) e^{(-D_r t/<\sigma>)} \tag{1.32}$$

where $A_\infty = r_\infty/r_0$ and $<\sigma> = \sum_{i \neq \infty} A_i \sigma_i/(1 - A_\infty)$.

In contrast to an isotropic system, the anisotropy evolution of a fluorophore rotating within an anisotropic system, such as a lipid bilayer, will not depolarise completely to zero at long times. This will give rise to a final limiting value r_∞. This means that at low viscosities, r_∞/r_0 will not be zero and will provide information about the degree of confinement of orientation of the fluorophore within the membrane. The relationship between this quantity and the half-angle of the cone β_0 is:

$$\frac{r_\infty}{r_0} = <P_2(cos\beta)>^2 = \left[\frac{1}{2} cos\beta_0 (1 + cos\beta_0)\right]^2 \tag{1.33}$$

where β is the orientation angle of the probe with respect to the axis of the bilayer. β_0 is the maximum value of β.

An approximate solution to the anisotropy decay given by Kinosita was given by Lipari and Szabo [38], where they considered the general case for a probe attached to a macromolecule:

$$\frac{r(t)}{r_{0,approx.}} = A_\infty e^{-t/\tau_M} + (1 - A_\infty) e^{[-t(\tau_M^{-1} + \tau_{eff}^{-1})]} \tag{1.34}$$

where $\tau_M = D_M/6$, D_M being the rotational diffusion coefficient of the macromolecule and τ_{eff} is the effective correlation time of D_r:

$$\tau_{eff} = 7\beta_0/24D_r \tag{1.35}$$

In many cases, considering $\tau_M >> \tau_{eff}$ is a good approximation, which leads to the well-known relation for the anisotropy decay with hindered rotation:

$$r(t) = (r_0 - r_\infty)e^{-t/\theta} + r_\infty \tag{1.36}$$

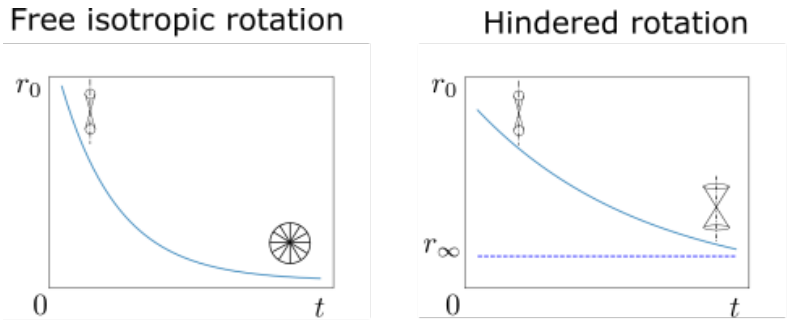

Figure 1.8: Time-resolved anisotropy decay models from free and hindered rotations. Figure adapted from reference [19].

Note that equations 1.28 and 1.29 imply the volumetric shape of the fluorescent probe is spherical. For non-spherical probes the anisotropy evolution is given by a multi-exponential expression. In a homogeneous solution, the SED equation to describe the translational Brownian motion of the fluorescent probe can be also derived. Note that if the probe is not spherical, the SED equations may not describe the system accurately and deviations from the current SED equations may be found. For the description of the Brownian motion of proteins within the cell membrane, Saffman and Delbruck developed a model, in which the protein is considered as a cylinder and to diffuse laterally in a 2-dimensional case scenario [39]. The derivation of the rotational diffusion of the protein is straightforward, but the translational diffusion equation, which is derived for different case scenarios. In *Chapter* 3, both models (SED and Saffman-Delbruck) are applied and discussed for the description of the Brownian motion (rotational and translational) of the environmentally-sensitive dye di-4-ANEPPDHQ in DOPC single lipid bilayers (SLB).

1.1.7.4 Steady-state anisotropy

Steady-state anisotropy measurements are simple and do not require any time-resolved setup and can be calculated from an average of the anisotropy decay $r(t)$, over the intensity $I(t)$:

$$r = \frac{\int_0^\infty I(t)r(t)dt}{\int_0^\infty I(t)dt} \tag{1.37}$$

The integration of equation 1.37 yields the *Perrin equation*, which relates the anisotropy parameters r and r_0 with the fluorescence lifetime τ and the rotational relaxation θ. For the *hindered rotation* case, the limiting anisotropy r_∞ is also present in the Perrin equation. Considering the intensity fluorescence decays as a single exponential model $I(t) \propto e^{-t/\tau}$, the steady-state anisotropy for the two cases studied above (*free isotropic and hindered rotation*) is given by introducing equations 1.30

and 1.36 separately in the steady-state anisotropy equation (1.37) [19].

$$Free\ isotropic\ rotation \Rightarrow r = \frac{r_0}{1+\tau/\theta} \tag{1.38}$$

$$Hindered\ rotation \Rightarrow r = \frac{r_0 - r_\infty}{1+\tau/\theta} + r_\infty \tag{1.39}$$

Much of the molecular information available from fluorescence is lost during the time averaging process, such as the shape of the anisotropy decay, which may be mono-exponential or multi-exponential. The intensity decays also contain information that is lost during the averaging process. Although time-resolved anisotropy measurements are much more powerful that steady-state anisotropy, still the steady-state anisotropy r is widely used to report on the orientation of the transition dipole moments [40–42]. Also, when the number of photons is insufficient to recreate a reliable time-resolved fluorescence anisotropy decay, steady-state anisotropy measurements can still reveal some information in regards to polarisation.

1.2 Förster Resonance Energy Transfer

1.2.1 What is Förster Resonance Energy Transfer?

FRET is a mechanism describing energy transfer between two fluorescence probes. The donor, initially in its electronic excited state, may transfer energy to an acceptor chromophore through non-radiative dipole-dipole coupling. Protein interactions play a key role in most of pathological and physiological processes and these can be studied with FRET.

For FRET to occur successfully, three conditions must be met:

1. Donor and acceptor must be close to one another (few nanometres) for the FRET process to be efficient. This energy transfer efficiency is inversely proportional to the sixth power of the distance between donor and acceptor. This makes FRET extremely sensitive to small changes.

2. The emission spectrum of the donor fluorophore must overlap with the absorption spectrum of the acceptor fluorophore.

3. As the transfer of energy between donor and acceptor happens via intermolecular dipole-dipole coupling, its efficiency depends on the dipole orientation between fluorophores, which comes with κ^2.

In the late 1940's, Theodor Förster explained the relationship between the probability of energy transfer, due to a dipole-dipole interaction, and molecular distance [43]. One of the final expressions for the transfer rate constant is given by the following equation [20]:

$$k_F = \frac{\Phi\kappa^2 9000 ln10}{128\pi^5 n^4 N_A \tau_D R^6} \int_0^\infty F_D(\lambda)\varepsilon_A(\lambda)\lambda^4 d\lambda \tag{1.40}$$

where Φ accounts for the quantum yield of the donor in the absence of acceptor, n is the refractive index of the probe's environment, τ_D is the isolated donor fluorescence lifetime, R corresponds to the distance between donor and acceptor, κ^2 is the dipole orientation between chromophores, N_A is Avogadro's number, $F_D(\lambda)$ is the fluorescence intensity of the donor in the wavelength range λ to $\lambda + \Delta\lambda$. The extinction coefficient of the acceptor at λ is given by $\varepsilon_A(\lambda)$ $[M^{-1}cm^{-1}]$.

The integral involved in equation 1.40 refers to the overlap integral of the absorption and emission spectra of acceptor and donor, respectively. Normally this integral overlap of spectra is denoted as $J(\lambda)$:

$$J(\lambda) = \int_0^\infty F_D(\lambda)\varepsilon_A(\lambda)\lambda^4 d\lambda \tag{1.41}$$

The transfer rate constant can be expressed as a function of distance and consequently FRET can be used to measure molecular distances, sometimes calling the

technique a molecular ruler. Therefore, equation 1.40 can be rewritten as follows:

$$k_F = \frac{1}{\tau_D}\left(\frac{R_0}{R}\right)^6 \tag{1.42}$$

where R_0 accounts for the Förster distance at which the energy efficiency due to FRET is half.

R_0 is therefore:

$$R_0^6 = \frac{\Phi\kappa^2 9000(ln10)}{128\pi^5 n^4 N_A}\int_0^\infty F_D(\lambda)\varepsilon_A(\lambda)\lambda^4 d\lambda \tag{1.43}$$

Equation 1.43 involves many constants, which means the expression can get simplified. If $\varepsilon_A(\lambda)$ is expressed in units of $M^{-1}cm^{-1}$ and λ in nm, then $J(\lambda)$ is in $M^{-1}cm^{-1}nm^4$ units and R_0 is as follows, in Å:

$$R_0 = 0.02108(\kappa^2 n^{-4}\Phi J(\lambda))^{\frac{1}{6}}(nm) \tag{1.44}$$

The FRET energy efficiency accounts for the proportion of photons the donor absorbs and transfers to the acceptor through nonradiative dipole–dipole coupling. It can be then defined as the quantum yield of the energy transfer transition and in combination with equation 1.42:

$$E_{FRET} = \frac{R_0^6}{R^6 + R_0^6} = \frac{1}{\left(\frac{R}{R_0}\right)^6 + 1} \tag{1.45}$$

Therefore, if the distance R and dipole orientation κ^2 between fluorophores is known, along with the donor quantum yield Φ, the solution's refractive index n and the spectral overlap between donor's emission and acceptor's excitation spectra $J(\lambda)$, then the energy efficiency E_{FRET} between fluorophores due to FRET can be calculated.

Equation 1.45 can also be rewritten in terms of the donor's fluorescence lifetime in absence and presence of an acceptor:

$$E_{FRET} = 1 - \frac{\tau_{DA}}{\tau_D} \tag{1.46}$$

where the fluorescence lifetime of the donor in presence of an acceptor is $\tau_{DA} = (k_T + k_r + k_{nr})^{-1}$ and the donor's fluorescence lifetime in absence of an acceptor is $\tau_D = (k_r + k_{nr})^{-1}$.

1.2.2 Excitation probability of an isolated molecule

Let's initially consider a molecule with no interaction with any other molecule. Therefore, no FRET takes place.

- **N = 1 cluster**

  As we have seen in *Section* 1.1.6, if a molecule is excited by irradiation at time t = 0, its excitation probability ρ(t) decays through radiative and non-radiative processes, such as:

  $$\frac{d\rho(t)}{dt} = -\frac{1}{\tau}\rho(t) \longrightarrow \rho(t) = e^{-t/\tau} \tag{1.47}$$

  The quantum yield Φ is defined by the ratio of the number of photons emitted to the number of photons absorbed. It is a measure of the efficiency of photon emission and ranges from 0 to 1. Its value is given by the overall radiation probability:

  $$\Phi = \frac{1}{\tau_0}\int_0^\infty \rho(t)dt = \frac{1}{\tau_0}\int_0^\infty e^{-t/\tau}dt = \frac{\tau}{\tau_0} \tag{1.48}$$

  where τ_0 is the natural fluorescence lifetime:

  $$\tau_0 = \frac{1}{k_r} \tag{1.49}$$

with k_r equal to the radiative rate constant.

If $N \geq 2$ and the FRET conditions for the transfer of energy are met, then the individual intensity decay can be depolarised due to FRET. FRET can happen in between different (hetero-FRET) or identical (homo-FRET) fluorophores. The two FRET cases will be studied in detail. The theory of hetero-FRET for a group of molecules uniformly distributed in solution will be presented, so as the homo-FRET theory, which will be applied for clusters, where a general and unique solution are presented.

1.2.3 Homo-FRET

1.2.3.1 Background and Theory

In the case of energy migration between identical molecules, the excitation probability of each individual molecule will be determined by the uptake or release of the non-radiative energy. Let's consider there is a possibility of transfer of excitation energy from one molecule k to another molecule l. Then, there will be a decay of the excitation probability of the first molecule at a rate proportional to ρ_k and an increase of the same magnitude in that of the second molecule. Considering these processes to occur between pair of molecules, one obtains:

$$\frac{d\rho_k}{dt} = \sum_l F_{kl}[\rho_l(t) - \rho_k(t)] - \frac{1}{\tau}\rho_k(t),\ F_{lk} = F_{kl} \tag{1.50}$$

F_{kl} is the number of transfers $k \to l$ per unit time that would obtain if ρ_k were held constant. If we recall the right side of equation 1.42, the pairwise excitation transfer rate from molecule k to l, or Forster Transfer rate (F_{kl}) is given below:

$$F_{kl} = k_F = \frac{1}{\tau_0}\left(\frac{R_0}{R_{kl}}\right)^6 \tag{1.51}$$

Equation 1.50 implies that the decay of excitation is accompanied by an equi-

libration of the excitation energy among the individual molecules. If the excitation probabilities are summed all over the molecules:

$$\sum_k \rho_k(t) = \sum_k \rho_k(t=0) e^{-t/\tau} \tag{1.52}$$

The whole system decay of excitation remains invariant, which means equation 1.47 also remains valid.

Let's consider now the general case with a cluster of $N \geq 3$ molecules and the unique case of $N = 2$ molecules. The anisotropy decay in the presence of homo-FRET between identical molecules will be given by a simplified model given by Warren et al. [44] of the approach developed by Runnels and Scarlata [45]. In this approach, Runnels et al. [45] showed that the emission anisotropy is mainly sensitive only to the number of interacting molecules below the critical Förster distance, not to the distance between them. Therefore, a configuration of distances between molecules will not be considered in this method, but equal transfer rates between them.

- **General case: N $\geq$ 3 cluster**

  For a population of N identical fluorophores with a fluorescence lifetime τ, the probability a initially excited molecule at time $t = 0$ remains in the excited state at time t is given by:

$$\rho_1(t) = \frac{1}{N}\left(1 + (N-1)e^{-Nk_F t}\right)e^{-t/\tau} \tag{1.53}$$

  where k_F is the homo-FRET rate, τ is the fluorescence lifetime and N the number of fluorophores in the cluster. The probability of the i^{th} molecule to be excited and remain in its excited state is given by:

$$\rho_i(t) = \frac{1}{N}\left(1 - e^{-Nk_F t}\right)e^{-t/\tau} \tag{1.54}$$

Both probabilities are solutions of equation 1.50 for 1 and $(N-1)$ molecules. Now, the probabilities of a photon to be emitted either by the initially excited fluorophore or any other from the cluster $(N-1)$ is given by:

$$p_1(t) = \frac{\rho_1(t)}{\rho_1(t) + (N-1)\rho_i(t)} = \frac{1}{N}\Big(1 + (N-1)e^{-Nk_F t}\Big) \tag{1.55}$$

$$p_i(t) = \frac{(N-1)\rho_i(t)}{\rho_1(t) + (N-1)\rho_i(t)} = \frac{1}{N}(N-1)(1 - e^{-Nk_F t}) \tag{1.56}$$

If the anisotropy of emission by the initially excited molecule is given by r_0 and the rest of the anisotropy emission is given by r_{et}, then the time evolution of anisotropy will be given by the following expression:

$$r(t) = p_1 r_0 + p_i r_{et} = \frac{1}{N}\Big[r_0[1 + (N-1)e^{-Nk_F t}] + r_{et}(N-1)(1 - e^{-Nk_F t})\Big] \tag{1.57}$$

For such a system, Agranovich and Galanin showed that the average anisotropy for emission after a single transfer is $r_{et} = 0.016$ [46].

If the molecules are free to rotate, then the anisotropy evolution will be given by:

$$r(t) = \frac{1}{N}\Big[r_0[1 + (N-1)e^{-Nk_F t}] + r_{et}(N-1)(1 - e^{-Nk_F t})\Big]e^{-t/\theta} \tag{1.58}$$

The molecule is assumed to be spherical with a rotational correlation time given by θ. If the time-resolved fluorescence anisotropy data is fitted with a bi-exponential model, the number of molecules N can be calculated. Let's consider r_1 and θ_1 are associated to the rotational decorrelation of the anisotropy decay, and r_2 and θ_2 to the homo-FRET. Then, along with equation

1.58, r_1 and r_2 can be expressed in terms of r_0 and r_{et}:

$$r_1 = \frac{1}{N}\Big(r_0 + (N-1)r_{et}\Big) \tag{1.59}$$

$$r_2 = \frac{(N-1)}{N}(r_0 - r_{et}) \tag{1.60}$$

By rearranging equations 1.59 and 1.60, the number of molecules N is as follows:

$$N = \frac{r_1 - r_{et} + r_2}{r_1 - r_{et}} = 1 + \frac{r_2}{r_1 - r_{et}} \tag{1.61}$$

The total radiation probabilities of the first excited molecule and the i^{th} molecule from the $(N-1)$ cluster are:

$$\Phi_{1,i}(t) = \frac{1}{\tau_0}\int_0^\infty \rho_{1,i}(t)dt \tag{1.62}$$

This is the same as saying:

$$\Phi_1(t) = \Phi\frac{1+\tau k_F}{1+N\tau k_F} \tag{1.63}$$

$$\Phi_i(t) = \Phi\frac{(N-1)\tau k_F}{1+N\tau k_F} \tag{1.64}$$

where Φ is the overall quantum yield ($\Phi = \Phi_1 + \Phi_i = 1$).

The equation that describes the emission steady-state anisotropy arising from the cluster is given by the following expression:

$$r_{tot} = r_0\frac{\Phi_1}{\Phi} + r_{et}\frac{\Phi_i}{\Phi} \tag{1.65}$$

$$\rightarrow r_{tot} = r_0\frac{1+\tau k_F}{1+N\tau k_F} + r_{et}\frac{(N-1)(\tau k_F)}{1+N\tau k_F} \tag{1.66}$$

- **N = 2 cluster**

The rate constant k_F is expected to decrease rapidly with distance, so the transfer of energy between molecules will occur below a critical distance. If an unexcited second molecule is below this critical distance from an excited molecule. Then, the excitation probabilities of each of them will be given by the solution of equation 1.50 for two identical molecules ($N = 2$):

$$\rho_1(t) = \frac{1}{2}(1 + 2e^{-2k_F t})e^{-t/\tau} \tag{1.67}$$

$$\rho_2(t) = \frac{1}{2}(1 - 2e^{-2k_F t})e^{-t/\tau} \tag{1.68}$$

The total radiation probabilities of the two molecules are:

$$\Phi_{1,2}(t) = \frac{1}{\tau_0}\int_0^\infty \rho_{1,2}(t)dt \tag{1.69}$$

This is the same as saying:

$$\Phi_1(t) = \Phi\frac{1 + \tau k_F}{1 + 2\tau k_F} \tag{1.70}$$

$$\Phi_2(t) = \Phi\frac{\tau k_F}{1 + 2\tau k_F} \tag{1.71}$$

where ϕ is the overall quantum yield ($\Phi = \Phi_1 + \Phi_2 = 1$).

The equation that describes the emission steady-state anisotropy arising from the cluster is given by the following expression:

$$r_{tot} = r_0\frac{\Phi_1}{\Phi} + r_{et}\frac{\Phi_2}{\Phi} \tag{1.72}$$

$$\rightarrow r_{tot} = r_0\Big(\frac{1 + \tau k_F}{1 + 2\tau k_F}\Big) + r_{et}\Big(\frac{\tau k_F}{1 + 2\tau k_F}\Big) \tag{1.73}$$

As derived previously for a cluster of $N \geq 3$ molecules, the evolution of the

anisotropy decay due to homo-FRET or with additional rotation, will be given by replacing N by 2 in equations 1.57 and 1.58:

$$r(t) = \frac{1}{2}\Big[r_0[1+e^{-2k_F t}] + r_{et}(1-e^{-2k_F t})\Big] \tag{1.74}$$

$$r(t) = \frac{1}{2}\Big[r_0[1+e^{-2k_F t}] + r_{et}(1-e^{-2k_F t})\Big]e^{-t/\theta} \tag{1.75}$$

Förster also derived the equations for the transfer of energy between two identical molecules at the time in a solution with a uniform distribution of molecules N [47]. This probability distribution is introduced and explained in great detail in the next section, where the hetero-FRET theoretical background is presented and discussed, giving rise to the well-known *stretched exponential function*. In *Chapter 2*, we will attempt to simplify the homo-FRET formulae derivations from Förster's paper for a low concentrated solution of identical dyes, focusing on the evolution of the time-resolved anisotropy decay.

1.2.4 Hetero-FRET

1.2.4.1 Background and Theory

If the distance between molecules is fixed, then a single distance will determine the FRET efficiency (equation 1.45 or equation 1.46, in terms of the fluorescence lifetime). This case is the most commonly used. However, if a distribution of distances between fluorescent molecules is permitted, the overall FRET rate constant will be given by a contribution of several FRET rate constants, each one associated to a specific separation between molecules. This is the scenario that will be considered in this subsection.

Let's assume a random distribution of dye molecules in solution. It suffices to consider only the nearest neighbour of the excited molecule at low concentrations. One molecule is at the origin (molecule in the excited electronic state) and the rest

of the molecules N are at a distance R + dR from the origin. Only the transfer of energy between the molecule at the origin and the nearest neighbour, at R + dR, is considered at the time. The molecule at the origin will be surrounded by an empty volume $v = 4\pi R^3/3$, and the second is somewhere within a volume dv (= $4\pi R^2$dR). The formulae derivation of this section is based on the work published by Theodor Förster in 1948 [48].

The excitation probability ρ of the molecule at the origin (donor) will decay with the fluorescence lifetime and with an additional quenching term given by the non-radiative transfer between molecules (equation 1.42), at different distances R_k. Therefore, equation 1.47 is rewritten as follows:

$$\frac{d\rho(t)}{dt} = -\frac{1}{\tau}\rho(t) - \frac{1}{\tau}\sum_{k=1}^{N}\left(\frac{R_0}{R_k}\right)^6\rho(t) \longrightarrow \rho(t) = e^{-t/\tau}\prod_{k=1}^{N} e^{-\left(\frac{R_0}{R_k}\right)^6\frac{t}{\tau}} \tag{1.76}$$

If the probability of the acceptor of being in the vicinity of the excited state is $w(R)dR$, then:

$$\rho(t) = e^{-t/\tau}\prod\int_{0}^{R_g} e^{-\left(\frac{R_0}{R_k}\right)^6\frac{t}{\tau}} w(R_k)dR_k = e^{-t/\tau}\left[J(t)\right]^N \tag{1.77}$$

where

$$J(t) = \int_{0}^{R_g} e^{-\left(\frac{R_0}{R_k}\right)^6\frac{t}{\tau}} w(R)dR \tag{1.78}$$

As the volume of the sphere where the donor is, is given by $V = \frac{4}{3}\pi R_g^3$, and if w(R) is considered to follow a uniform distribution over the volume V, then:

$$w(R)dR = \frac{4\pi R^2 dR}{V} \tag{1.79}$$

Therefore, J(t):

$$J(t) = \frac{4\pi}{V} \int_0^{R_g} e^{-\left(\frac{R_0}{R}\right)^6 \frac{t}{\tau}} R^2 dR = \frac{1}{2}\sqrt{\xi_g} \int_{\xi_g}^{\infty} e^{-\xi} \frac{d\xi}{\sqrt{\xi^3}} \tag{1.80}$$

where

$$\xi = \left(\frac{R_0}{R}\right)^6 \frac{t}{\tau} \tag{1.81}$$

$$\xi_g = \left(\frac{R_0}{R_g}\right)^6 \frac{t}{\tau} \tag{1.82}$$

Applying equation 1.82, equation 1.80 is given by a series of increasing powers of $\sqrt{\xi_g}$:

$$\int_{\xi_g}^{\infty} e^{-\xi} \frac{d\xi}{\sqrt{\xi^3}} = \frac{2}{\sqrt{\xi_g}} - 2\sqrt{\pi} - 6\sqrt{\xi_g} + ... \tag{1.83}$$

Neglecting higher powers of $\sqrt{\xi_g}$:

$$J(t) = 1 - \sqrt{\pi \xi_g} \tag{1.84}$$

which yields:

$$\rho(t) = e^{-t/\tau}\left(1 - \sqrt{\pi \xi_g}\right)^N \tag{1.85}$$

In solution, N is assumed to be very large. Therefore, a good approximation is $N \rightarrow \infty$. Thus, applying limits, the result is as follows:

$$\rho(t) = e^{-t/\tau} \lim_{N\to\infty} \left(1 - \frac{1}{N} N\sqrt{\pi \xi_g}\right)^N = e^{-t/\tau - N\sqrt{\pi \xi_g}} = e^{-t/\tau - \frac{\sqrt{\pi} N R_0^3}{R_g^3}\sqrt{t/\tau}} \tag{1.86}$$

Although the decay process on the single molecule is strictly exponential, it cannot be represented by a simple exponential function for the overall number of acceptors N, according to equation 1.86.

As shown before, the fluorescence quantum yield Φ is given by the overall

radiation probability. Since, the number of emission processes per time interval is proportional to this probability, Φ is proportional to their intensity over the entire period of time:

$$\Phi = C \int_0^\infty \rho(t) dt \tag{1.87}$$

where C is a constant. If the extinction is zero (N = 0), then:

$$\Phi = C \int_0^\infty e^{-t/\tau} dt = C\tau \tag{1.88}$$

Therefore, the relative fluorescence yield will be:

$$\frac{\Phi}{\Phi_0} = \frac{1}{\tau} \int_0^\infty \rho dt \tag{1.89}$$

To solve this integral, the following simplifications are applied:

$$s = t/\tau \tag{1.90}$$

$$q = \frac{\sqrt{\pi}}{2} \frac{N R_0^3}{R_g^3} \tag{1.91}$$

This yields:

$$\frac{\Phi}{\Phi_0} = \int_0^\infty \rho(s) ds = \int_0^\infty e^{-s-2q\sqrt{s}} ds = 1 - \sqrt{\pi} q e^{q^2} [1 - \phi(q)] \tag{1.92}$$

where $\phi(q)$ is the Gaussian error integral:

$$\phi(q) = \frac{2}{\sqrt{\pi}} \int_q^\infty e^{-x^2} dx \tag{1.93}$$

According to equation 1.91, q may be rewritten as a function of the molar concentration c of the acceptor molecules ($C \propto N/R_g^3$). Here, the concentration of the

donors is not taken into account. Thus, equation 1.92 is given by:

$$\frac{\Phi}{\Phi_0} = 1 - \sqrt{\pi}(c/c_0)e^{(c/c_0)^2}[1 - \phi((c/c_0))] \tag{1.94}$$

The overall FRET efficiency can be obtained according to:

$$E_{FRET} = 1 - \frac{\Phi}{\Phi_0} = \sqrt{\pi}(c/c_0)e^{(c/c_0)^2}[1 - \phi((c/c_0))] \tag{1.95}$$

The anisotropy decay of the donor can be obtained as previously derived in the *Homo-FRET* section, via the quantum yield of the initially excited molecules. The result is as follows:

$$r(t) = r_0 e^{-2q\sqrt{s}} \tag{1.96}$$

where s and q are defined in equations 1.90 and 1.91.

1.3 Time-resolved fluorescence microscopy

The time-correlated single photon counting (TCSPC) principle will be explained in detail in this section, along with two time-resolved fluorescence microscopy techniques based on TCSPC, that we will utilise for the elaboration of this thesis: Fluorescence lifetime imaging (FLIM) and time-resolved fluorescence anisotropy imaging (tr-FAIM).

1.3.1 Time-correlated single photon counting (TCSPC)

Time-correlated single-photon counting (TCSPC) is a very robust technique for the acquisition of fluorescence lifetime measurements. It has been reported to have the best signal-to-noise ratio of the standard time-resolved imaging methods [49–52], which is key taking into account the limited available photon budget from the fluorescent probe before it bleaches irreversibly [53]. TCSPC is able to record low-level light signals with picosecond resolution and extremely high precision using a

pulsed laser with a fixed repetition rate. Its high sensitivity, well-defined Poisson statistics and easy visualisation of the photon arrival times make TCSPC a widely used technique to measure fluorescence decays [36, 54].

The principle of TCSPC is the detection of single photons and the measurement of their arrival times with respect to the light pulse. TCSPC is a Poisson-based statistical method that requires a repetitive light source (cycles) to acquire enough photons. A vast number of cycles are needed to the accurate detection of a single photon. The photon events are accumulated in time bins, if time-domain TCSPC measurements are performed, and a histogram of counts per time position is constructed. From the resultant intensity histogram a exponential model can be used to fit the intensity data and extract the corresponding fluorescence lifetime components [36] (Figure 1.9).

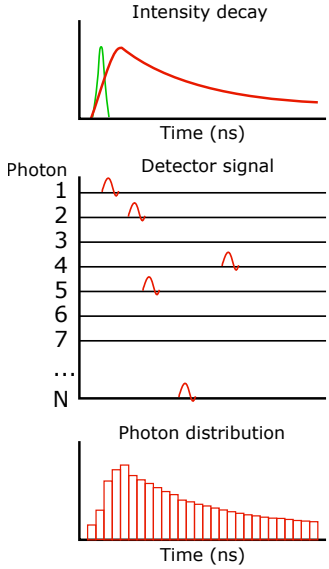

Figure 1.9: TCSPC principle. Figure adapted from reference [36].

TCSPC functions as follows: The sample is excited with a pulsed laser. After many cycles, a single fluorescence photon is collected by the detector and delivered to the TCSPC electronic card. The pulse triggers a Constant Fraction Discriminator (CFD). The purpose of the CFD is to detect and avoid pulse-height induced

timing jitter by thresholding the signal. A second CFD is used to obtain a timing reference pulse from the light source. The output pulses of the CFDs, coming from the light source and the detector, are sent to a Time-to-Amplitude Converter (TAC) which functions as a fast stopwatch with two inputs. A conventional TAC uses a switched current source charging a capacitor. It is activated with the start pulse and stopped with the stop pulse. The final charge of the capacitor represents the arrival time of the photon (pulse) in the start-stop interval. The TAC output is amplified by a Programmable Gain Amplifier (PGA) converted to a numerical value by the Analog-to-Digital Converter (ADC), which digitises the analog arrival time of the photon. False readings are minimised by a Window Discriminator (WD). Its function consists of discriminating readings out of a given range of voltages. The digital value of the arrival time of the photon is allocated with an extremely high precision at a specific memory location with a suitable calibration. This process is repeated after many light source cycles and the photon distribution is built up [36]. A diagram of the TCSPC classic device is shown in Figure 1.10.

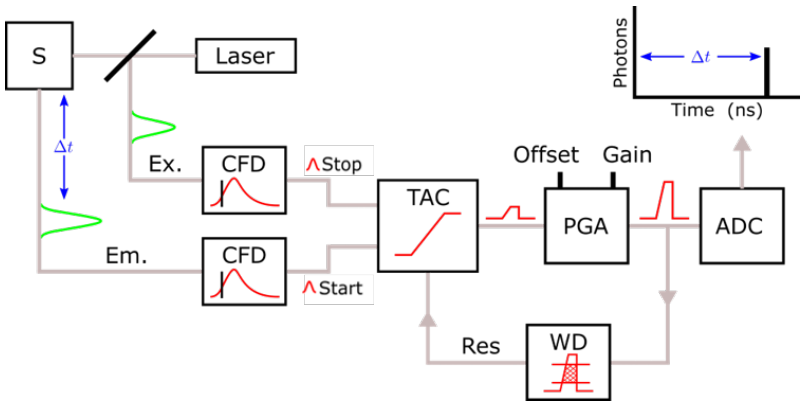

Figure 1.10: TCSPC classic device diagram. Figure adapted from reference [20].

In order to assure accurate TCSPC recordings, the count rate of the detector must not exceed 10% the repetition rate of the excitation source [55]. Otherwise, an accumulation of a large number of photons at short arrival times shows up and distorts the shape of the recorded photon distribution. This is known as the pile-up

effect. Thus, it is important that the light intensity is low enough that the probability to detect more than one photon in one signal period is negligible [36].

1.3.2 Fluorescence lifetime imaging (FLIM)

In the early 1970s [56–58], TCSPC started to be widely used for time-resolved spectroscopy to measure the fluorescence lifetime in solutions. The development of laser scanning confocal microscopes enabled TCSCP-based fluorescence lifetime imaging (FLIM), where the image is created by raster scanning the sample and collecting intensity decays per pixel. Meanwhile in scanning-based TCSPC FLIM, point detectors are utilised to collect the pulse information, wide-field TCSCP requires of a sensitive camera for single photon detection. This can be achieved combining a fast frame rate Charge-Coupled Device (CCD) or Complementary Metal-Oxide Semiconductor (CMOS) camera with an image intensifier, which amplifies the signal and allows single photon detection. Moreover, camera-based wide-field TCSPC is especially suitable for Phosphorescence Lifetime IMaging (PLIM), which fastens the data acquisition in comparison to a scanning-based TCSPC setup. This was done for instance by Hirvonen et al., where she measured the phosphorescence decays of samples containing ruthenium and iridium with an image intensifier with a phosphor screen (P20) [59]. Figure 1.11 shows some wide-field images *we* recorded in the lab using first a CMOS camera (real signal) and then a CMOS camera combined with an intensifier (amplified signal) in order to assess the strength of the signal collected by the camera. The intensity of the illuminating signal coming from the lamp was reduced using Neutral Density (ND) filters before reaching the sample.

FLIM is a powerful technique for probing the local environment of the fluorophore, as the lifetime is largely independent of the local fluorophore concentration. This means FLIM provides an absolute measurement which is less susceptible to artefacts arising from scattered light, non-uniform illumination of the sample, excitation intensity variations and photobleaching, compared to fluorescence inten-

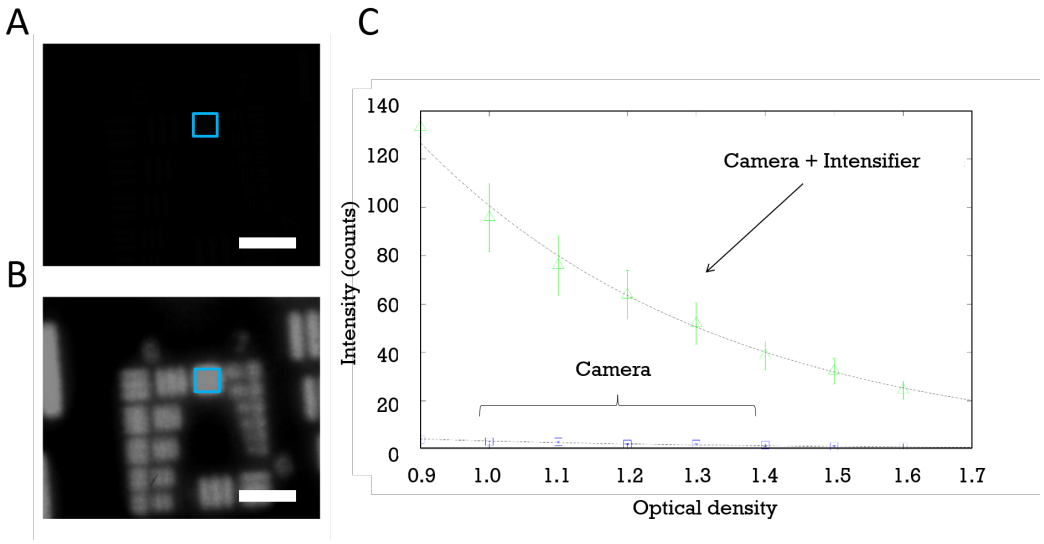

Figure 1.11: Wide-field images of a microscope calibration sample taken with (A) a CMOS camera and (B) a CMOS camera and an intensifier. The blue squares indicate the area in which the average intensity was calculated. A ND filter with an Optical Density (OD) of 0.9 was used. (C) Plot of the signal measured per OD ND filter and setup configuration. Image scale bar: 500 μm.

sity [60]. FLIM is a rapid and straightforward technique to map the lifetime in every pixel, which can be sensitive to refractive index [29, 61–63], viscosity [64], pH [65], quenching agents [66], ions [67] and interaction with other fluorophores via Förster Resonance Energy Transfer (FRET) [68–72]. This approach has been widely used for instance in membranes to study the conformation and distribution of the lipid domains [73]. The resulting FLIM images present contrast according to the fluorescence lifetime and depending on its sensitivity, the FLIM maps can be viewed as viscosity, pH or ion concentration maps, among others. An example of a FLIM map is presented in Figure 1.12.

1.3.3 Time-resolved fluorescence anisotropy imaging (tr-FAIM)

FLIM provides information about the fluorescence lifetime τ of the probe and time-resolved fluorescence anisotropy measurements provide information about its depolarisation. Tr-FAIM permits obtaining information about the rotational diffusion, the structure or function [74] of the targeted fluorophore by measuring

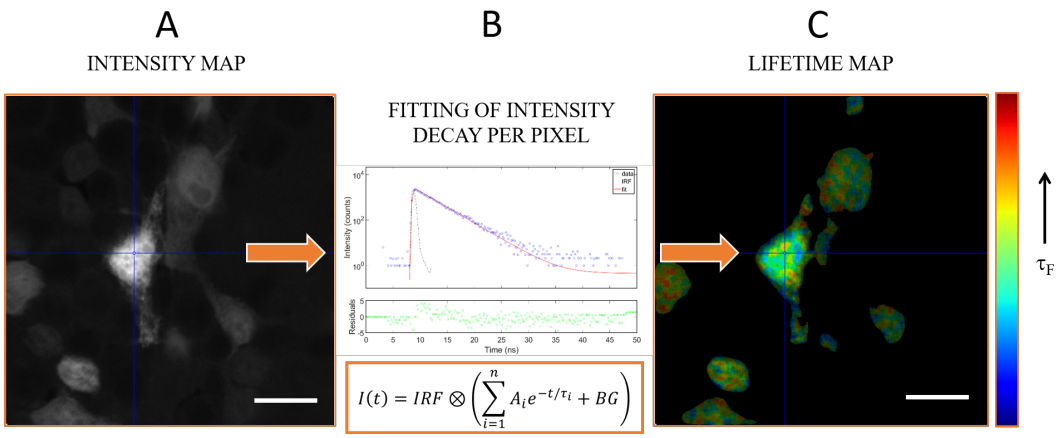

Figure 1.12: Example of some data acquired with the confocal-based TCSPC FLIM setup and the basic steps to obtain the FLIM map. (A) Intensity image. Each pixel has one intensity decay. (B) Decay fit per pixel with the convolution of the Instrument Response Function (IRF) with a multi-exponential model. (C) FLIM image. Image scale bar: 10 μm.

its anisotropy, given by the dipole transition moment orientation. Another phenomenon that can be studied with FAIM is FRET [68–72]. FRET can happen in between two different fluorophores (hetero-FRET) or identical ones (homo-FRET or emFRET). Lifetime studies are undertaken in order to identify hetero-FRET [75–77], while time-resolved-anisotropy studies are very powerful to detect homo-FRET [78–82], as generally no change in lifetime is observed.

1.4 Fluorescence recovery after photobleaching (FRAP)

FRAP was developed in the 1970s [83] and originally intended for use as a means to characterise the mobility of individual lipid molecules within a cell membrane [84]. It consists of briefly bleaching the sample in a defined area and, afterwards, observing its intensity evolution over time. This technique is straightforward to perform. The study of this evolution permits gaining information about the translational intracellular protein mobility [85–89]. From the acquired data the translational diffusion coefficient and the mobility fraction can be calculated. Figure 1.13 presents a diagram of a FRAP experiment.

FRAP outcome may vary among setups, which makes difficult to reproduce

exact results from other laboratories. The final outcome depends on the methodology, such as the intensity of the scanning and the bleach lasers, the bleach spot size, the speed rate during the data acquisition, etc [90–92]. Another additional parameter to the equation is the data analysis method, which depends strongly on the methodology of the data acquisition and the nature of the sample under investigation [84, 93–97]. Different models for calculating these parameters have been reported. This is based for instance on the configuration of the setup, the dimensions of the sample and the shape of the bleach spot area [84,93,95,96,98–103]. Although the classical approach [84, 93] for analysing the FRAP data is widely used, more advanced methods have recently been developed by different groups, where a more complex treatment of the FRAP data is undertaken [94, 97, 104, 105]. However, these methods are restricted by different constraints such as the bleach depth or the bleach spot geometry, which must be considered when performing the experiment. Overall, it is very important that when some FRAP results are reported in literature, the setup, the methodology and the data analysis approach are described in great detail.

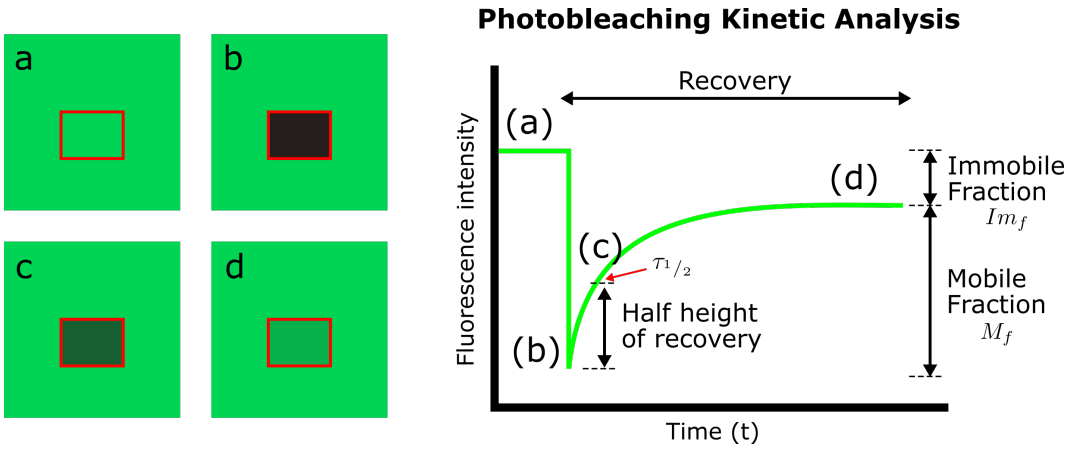

Figure 1.13: Confocal images of a fluorescence sample before bleaching (a), while bleaching (b) and after bleach (c-d). The graph on the right shows the recovery curve due to the bleach of the sample over time, with the different FRAP parameters.

Most of the equations for the FRAP data analysis imply a 2-dimensional trans-

lation of the probe across the sample [96, 102], which simplifies the problem. The formulae depend on the setup conditions and the sample itself. The application of these 2-dimensional equations are valid in the following cases: either the system has three dimensions but the bleaching happens in a cylindrical volume (this implies low Numerical Aperture (NA) objectives) through the sample plane, or if the sample is a 2-dimensional system. Single lipid bilayers constitute a 2-dimensional system, therefore the shape of the bleaching volume does not matter and a high NA objective such as ours can be used, which at the same time has a high light collection efficiency in comparison to low NA microscope objectives.

Another technique that is used for getting the dynamic behaviour of a biological sample is Fluorescence Correlation Spectroscopy (FCS), where very low concentrations of the fluorescent probes are required. It is based on measuring the fluctuations in fluorescence intensity in a small volume. For getting a proper statistical power, FCS requires taking many measurements. This is basically why FCS is more commonly used to study extremely fast processes such as diffusion [106]. At present FRAP is used much more widely that FCS, mainly because it can be accomplished on any standard confocal microscope, whereas FCS requires special instrumentation. They are complementary techniques. FRAP is suited to slower processes and FCS to fast ones [107].

1.5 Overview of the experimental setup

The objective of this section is to give an overview of the experimental setup we have in the laboratory, to introduce which fluorescence microscopy modalities were explored with this setup and which ones were used for the work in *Chapters 2, 3 and 4* of this thesis. Note that this section is mainly focused on describing in great detail the excitation optical path. More technical details about each fluorescence microscopy modality and the corresponding data acquisition procedure will be ex-

plained in the next chapters. Key factors to take into account in photon counting such as the instrument response function IRF and the $G-factor$ are also introduced and briefly discussed.

1.5.1 Experimental setup, fluorescence microscopy modalities and excitation optical paths

In our lab, we have a confocal(Leica TCS SP2)-based TCSPC FLIM setup with two TCSPC electronic cards from Becker & Hickl (SPC-150 Becker & Hickl) and two GaAsP hybrid detectors (Becker & Hickl HPM-100-400). A polarising beam splitter (BS) cube (Edmund optics) is located in front of the two hybrid detectors splitting the fluorescence into two orthogonal polarisations. This allows doing time-resolved fluorescence anisotropy imaging (tr-FAIM) recording the parallel and perpendicular intensity decays ($I_{\parallel}$ and $I_{\perp}$), with respect to the excitation, per pixel. FRAP experiments can also be performed with this setup due to the implementation of a high intensity laser.

The fluorescence microscopy modalities that are performed with this setup are: individual (*FLIM, tr-FAIM and confocal FRAP*) and simultaneous (F^3) fluorescence microscopy modalities. Each one will be explained by the description of Figure 1.14.

- **Individual fluorescence microscopy modalities**

  - **Fluorescence lifetime imaging FLIM and time-resolved fluorescence anisotropy imaging tr-FAIM**

    $FLIM$ and $tr-FAIM$ measurements are taken using the 467 nm pulsed laser. The beam path of the pulsed laser is schematically indicated in Figure 1.14 by a cyan line. The laser goes initially through a beam expander formed by the L_3 and L_4 lenses, where the beam diameter of the laser is reduced to a couple of mm. This means that $f_3 > f_4$, with f_3

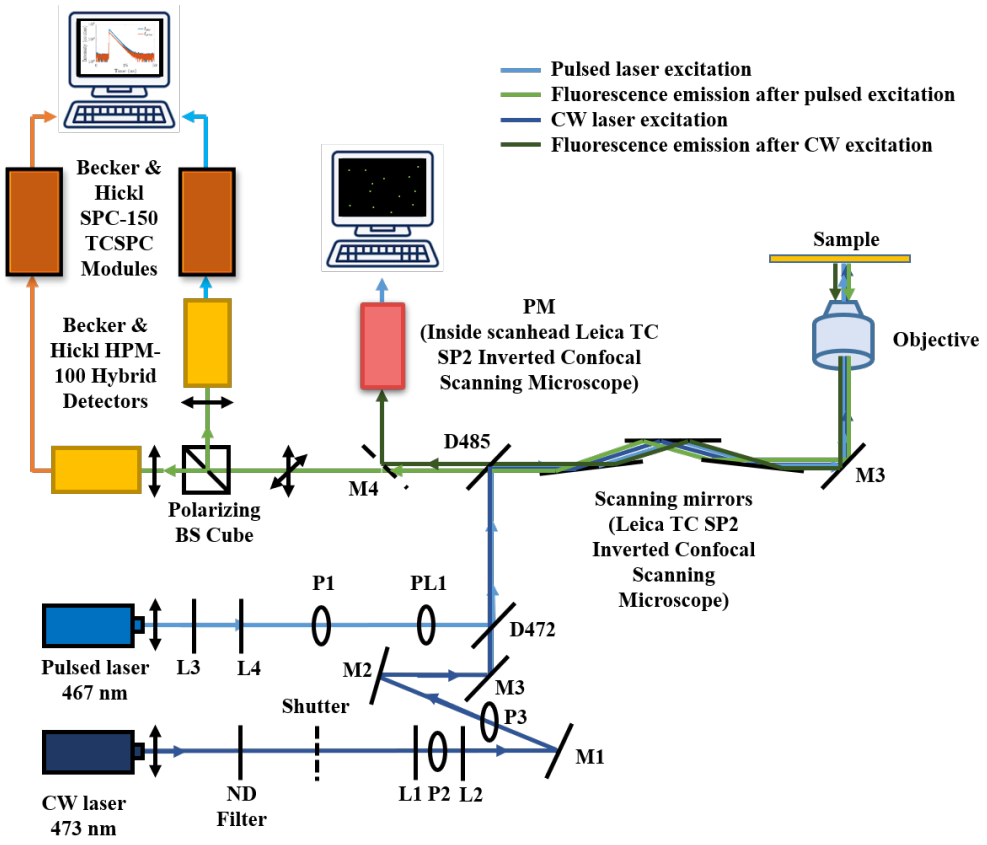

Figure 1.14: Schematic of the laboratory setup. L refers to lens, P to pinhole, PL to polariser, ND to neutral density, M to mirror, BS to beam splitter, D to dichroic, and PM to photomultiplier.

$= 100\ mm$ *and* $f_4 = 25\ mm$. The laser light strikes perpendicularly the first lens L_3 converging at its focal plane. The distance between lenses is such that the focal plane of L_3 coincides with the back focal plane of L_4. Thus, from the back focal plane of L_4, the light diverges back till reaching L_4 and goes through the lens parallel to the optical table. The reason for this initial beam reduction is related to a small input port located at the scanhead of the confocal microscope the light needs to go through before being spectrally filtered with the 485 dichroic filter ($D485$). Theoretically speaking, if $f_3/f_4 = 4$, the beam diameter at the end of the beam expander should be four times smaller than the initial one before going through the expander. Immediately after the

beam expander, the beam goes through a polariser, to make sure the excitation light is polarised, which is highly required when performing tr-anisotropy fluorescence measurements. After the polariser, the light is reflected by a 472 Dichroic Long Pass (DRLP) filter, which was customised for our lab (D472 in Figure 1.14). This filter placed at an angle of 45° respect to the pulsed and Continuous Wave (CW) lasers, allows a reflectance of $\sim 90\%$ at *467 nm* and a transmittance of $\sim 50\%$ at *473 nm*. See Figure 1.15 for more details. The beam reflects off the D485 filter and illuminates the sample (only light below *485 nm reflects off*) overfilling the back focal plane of the objective. Via reflection, the fluorescence emission is sent back to the D485 filter (only light above *485 nm goes through*), which is directed to the polarising Beam Splitter (BS) cube with the removal of the mirror M_4. The light is spectrally filtered before reaching the polarising BS cube and directed to the two GaAsP hybrid detectors. The signal from the detectors was fed into the two TCSPC cards in a PC running Windows 10. When FLIM measurements are performed, the polarising BS cube is removed and the fluorescence emission strikes the first GaAsP hybrid detector.

– **Confocal Fluorescence recovery after photobleaching FRAP**

Another fluorescence microscopy modality that can be explored with our lab setup is *confocal FRAP*. The pulsed laser (*467 nm*) is used to scan the sample before and after the intentional bleaching. The CW laser (*473 nm*) is used for this purpose and therefore is used just for a single scan of the sample. The optical path of the CW laser (dark blue line in Figure 1.14) is as follows: due to its high power (*153 mW*), a neutral density (ND) filter is immediately positioned in front of the CW laser to reduce its intensity down to around *15 mW*. After going

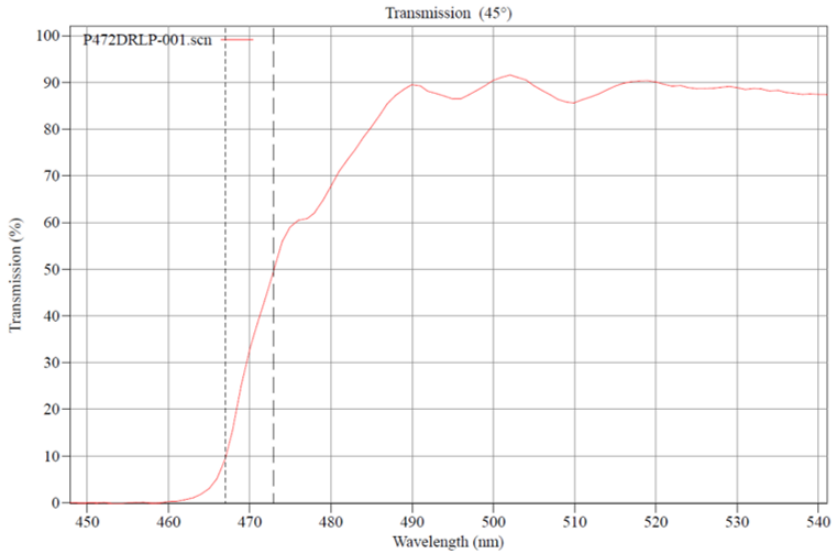

Figure 1.15: Diagram of the 472DRLP filter fabricated by Omega Optical, where transmission is plotted against wavelength.

through the ND filter, the beam must go through a shutter, which is enabled during the bleaching scan and disabled during the rest of the data acquisition. As the beam cross section of the laser does not follow a strict Gaussian function, the beam was reshaped. This was done locating a 150 micrometers pinhole (P_2) in between two lenses (L_1 and L_2) with identical focal lengths ($f_1 = f_2$) at the same distance. In this way, the beam diameter of the CW laser was spatially filtered and its dimensions preserved. Immediately after, the light is reflected by three mirrors (M_1, M_2 and M_3) and goes through the 472*DRLP* filter. From here onward, its excitation optical path is identical to the pulsed laser. The power of the CW laser is diminished during its optical path and it strikes the sample with around *5 mW*. The fluorescence emission coming out of the sample and caused by the excitation of both lasers, pulsed and CW, is directed to the photomultiplier (PM) located at the scan head of the confocal microscope, with the consequent creation of the confocal images. The mirror M_4 redirects the light to the PM and prevents any light reaching

the hybrid detectors. The illumination of the two lasers in the same focal plane was checked by imaging a convallaria sample at low intensities.

- **Simultaneous fluorescence microscopy modalities**

  - **F^3 microscopy**

    When the three microscopy techniques (FLIM, tr-FAIM and FRAP) are used simultaneously, the fluorescence emission caused by the pulsed laser excitation is sent to the GaAsP detectors and immediately after to the two TCSPC cards in a PC running Windows 10. In order to prevent any damage of the hybrid detectors, the fluorescence emission is blocked by mirror M_4 when the sample is excited and hence bleached with the CW laser. This fluorescence microscopy setup is termed F^3 and hence the presence of a filter (472*DRLP*) that allows both lasers to excite the sample simultaneously. A photographic image of the setup is shown in Figure 1.16.

1.5.2 Which setup modalities are used per chapter and what for?

In order to help the reader identify which fluorescence microscopy techniques were used per chapter, the following list is displayed herein:

- **Chapter 2 - Exploring the stretched exponential decay model as a FRET indicator for EGFP dimers**

  FLIM, tr-FAIM and confocal FRAP were applied individually to EGFP monomers and dimers in buffer/glycerol solutions at Room Temperature (RT). The objective was to distinguish between a non-FRET (EGFP monomer) and a FRET case (EGFP dimer) via time-resolved fluorescence anisotropy. The lateral mobility of both constructs was assessed via confocal

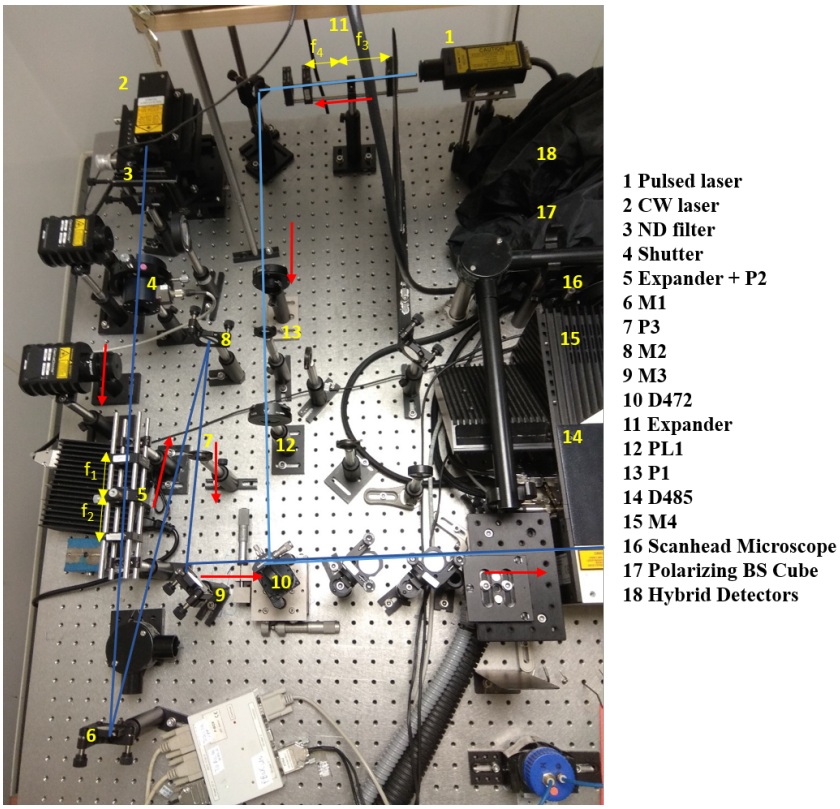

Figure 1.16: Photographic picture of the laboratory setup. Each one of the numbered elements refer to the nomenclature used in Figure 1.14.

FRAP and the fluorescence lifetime of EGFP monomer and dimer was investigated and correlated with the refractive index of the solution. Moreover, the dimerisation of the Coxsackievirus and Adenovirus Receptor (CAR) in live ($T = 37°$ *and 5%* CO_2) and fixed cells (*RT*) was investigated studying homo-FRET via time-resolved fluorescence anisotropy experiments.

- **Chapter 3 - Development of a Multi-Modal Confocal Fluorescence Microscopy Technique based on Time-Correlated Single Photon Counting**

  This multi-modal setup is named as F^3 and presented in *Chapter 3*, which implies using *FLIM, tr-FAIM and FRAP* simultaneously. For the calibration of the setup, solutions of the dye rhodamine 6G in water/glycerol were used and the setup was further tested with single lipid bilayers (SLBs), whose geometry is ideal to perform 2-dimensional FRAP experiments. Specifically,

the lateral mobility of the environmentally-sensitive dye di-4-ANEPPDHQ in di-oleyl-phosphatidycholine (DOPC) single lipid bilayers deposited onto a glass surface at RT was investigated.

- **Chapter 4 - Investigation of the Rotational Correlation Time Uncertainty and Distribution from Time-Resolved Fluorescence Anisotropy Data**

  The first half of *Chapter 4* consists of acquiring time-resolved fluorescence anisotropy images of the dye Fluorescein Isothiocyanate (FITC) in water and with different collection times. A theoretical expression for the rotational correlation time θ uncertainty was derived and the experimental equivalent was compared.

1.5.3 Instrument response function: definition and acquisition

In photon counting, the instrument response function (IRF) is the response of the instrument to a zero lifetime sample. If the pulse and the transit time of the detector signal was infinitely short, the IRF would be represented by a delta function. However, in practice, this is not the case and the IRF must be taken into account when the intensity decay is approximated by a multi-exponential model. The IRF temporal width is given by the optical pulse, detector and jitter timings, as follows:

$$\Delta t_{IRF}^2 = \Delta t_{optical\ pulse}^2 + \Delta t_{detector}^2 + \Delta t_{jitter}^2 \tag{1.97}$$

where Δ represents the temporal width and is squared to avoid sign errors.

Therefore, in order to obtain reliable fit parameters from the intensity decay, the fit approach must include the convolution of the IRF with the intensity decay model.

$$I(t) = \int_0^\infty IRF(t')I_{model}(t-t')dt' \tag{1.98}$$

where $I(t)$ is the measured intensity decay, t' is a temporal variable and $I_{model}(t-t')$

is the real shifted intensity decay defined by a multi-exponential model.

The IRF can be measured using a mirror or scattering sample, reflecting back the excitation light through the detection beampath. Another way of measuring the IRF and following previous protocols, is using a dilute fluorescence solution such as a solution of fluorescein quenched with iodide salt, whose width is very narrow (low fluorescence lifetime) in comparison to the experimental time window [108].

When time-resolved fluorescence decays are collected, the IRF is measured with similar number of counts on the peak and with identical settings. Otherwise, the collected IRF is not correlated with the actual time-resolved fluorescence data.

1.5.4 G-factor: definition and acquisition

The G-factor indicates the relative detection efficiencies of the parallel and perpendicular intensity channels. It needs to be measured and incorporated in the anisotropy measurements, it is denoted by G and present in the anisotropy equation:

$$r = \frac{I_{\parallel} - GI_{\perp}}{I_{\parallel} + 2GI_{\perp}} = \frac{I_{\parallel} - GI_{\perp}}{I_{tot}} \tag{1.99}$$

In microscopy, the G-factor can be measured with an isotropic solution of fluorophores with a very short rotational correlation time θ [20]. This ensures the total transition dipole randomisation of the excited dye population. The G-factor can be calculated from the ratio of the two channels, which is known as the $tail-matching$ method.

Equal detection efficiencies means $G = 1$. However, this is not strictly true if two detectors are used, since the transmittance and reflectance of the polarising beam splitter that decomposes the fluorescence emission in two orthogonal intensity signals may differ. The real efficiency of the two detectors will never be measured to be 1. One way to obtain the real detection efficiencies would firstly imply the alignment of the front detector with the polarising beam splitter by measuring the

maximum number of counts on the peak. Then, the second detector would be incorporated and the same method should be applied, while keeping the counts of the first detector as high as possible.

The calculated value for the G-factor is not that crucial, as long as the rest of the data is collected under the same conditions and with the same setup settings.

Note that equation 1.99 should be rewritten as follows:

$$r = \frac{I_{\parallel} - GI_{\perp}}{I_{\parallel} + x_{NA}GI_{\perp}} = \frac{I_{\parallel} - GI_{\perp}}{I_{tot}} \tag{1.100}$$

where x_{NA} refers to a factor due to depolarisation at high numerical aperture *NA* objectives. This depolarisation factor is equal to 1 at *NA* below 0.9. When the *NA* of the objective is above 0.9, the total x_{NA} is not 2 anymore and needs to be corrected to take into account the depolarisation induced by the objective [109, 110].

In this thesis, the time-resolved fluorescence anisotropy data presented is measured with a high NA objective (*63× 1.2 NA water-immersion lens*). However, this correction is not implemented in the data analysis since the depolarisation effect will be the same throughout all the experiments and hence it will not affect the data interpretation. Moreover, the choice of x_{NA} was found to have a small effect in the final result.

1.6 Data analysis procedures for FLIM, tr-FAIM and FRAP

The data analysis of the fluorescence data occupies a great part of this thesis. Therefore, a section introducing the most widely used methods for its analysis is compulsory. Specifically, several estimation procedures for the analysis of FLIM and tr-FAIM data will be introduced and briefly explained. Also, some strategies for the estimation of the anisotropy fit parameters will be presented, compared and dis-

cussed.

1.6.1 Estimation procedures for FLIM and tr-FAIM

In this section, several pixel-wise fitting approaches for the estimation of the fluorescence parameters are presented and briefly discussed. These are: Non-Linear Least Squares (NL-LS) and Maximum Likelihood (ML) methods. The Bayesian method is also mentioned for its excellent performance at low intensity levels. Although the author is aware of other fitting approaches that are also utilised to estimate the fluorescence parameters, such as the global analysis fitting method [111–113], phasor plot approach [114, 115], Principal Component Analysis (PCA) [116] and Maximum Entropy Method (MEM) [117, 118], they will not be discussed in this thesis.

1.6.1.1 Non-linear least squares method

In order to extract the different parameters from the intrinsic fluorescence decay, different methods can be applied and one of them is the non-linear least squares deconvolution method, which is possibly the most widely used approach for exponential analysis [119]. This method, as the method of moments, rely on a large amount of photons, so that the uncertainties in the data is given by a Gaussian distribution [20].

This method consists of the definition of a specific model and the goodness of the fit between the model and the experimental data is defined. The model parameters are determined by the iterative optimisation algorithm by minimising the χ^2, which gives the best fit. If y_i is the measured data and $F(t_i)$ the calculated one, dependent on time, the χ^2 is given by:

$$\chi^2 = \sum_{i=1}^{N} \frac{(y_i - F(t_i))^2}{\sigma_i^2} \tag{1.101}$$

The least square principle is based on the principle of maximum likelihood and the assumption that each y_i is a random variable from a Gaussian distribution of mean

$F(t_i)$ and standard deviation σ_i. This means the probability density function of the entire data set will be given by a Gaussian function P_g, whose mean value is given by μ_i:

$$P_g(n_i) = \prod_{i=1}^{N} \frac{1}{\sqrt{2\pi n_i}} e^{-\frac{(n_i-\mu_i)^2}{2n_i}} \tag{1.102}$$

where n_i is the number of photons per time bin.

The fit parameters appearing in μ_i would be determined by maximising $P_g(n_i)$, or equivalently, by minimising the χ^2:

$$\chi^2 = \sum_{i=1}^{N} \frac{(n_i-\mu_i)^2}{n_i} \tag{1.103}$$

As χ^2 depends on the number of data points, it is convenient to use the reduced χ^2 as a goodness of the fit indicator:

$$\chi_R^2 = \frac{1}{N-M} \sum_{i=1}^{N} \frac{(n_i-\mu_i)^2}{n_i} \tag{1.104}$$

where N is the number of data points, M is the number of fit parameters and $N-M$ accounts for the degrees of freedom [20].

As an example, if the fluorescence intensity decay $I(t)$ is described by a single exponential model $Ae^{-t/\tau}+B$, equations 1.103 and 1.104 are rewritten as follows:

$$\chi^2 = \sum_{i=1}^{N} \frac{(I(t_i) - IRF \otimes Ae^{-t_i/\tau} + B)^2}{I(t_i)} \tag{1.105}$$

$$\chi_R^2 = \frac{1}{N-M} \sum_{i=1}^{N} \frac{(I(t_i) - IRF \otimes Ae^{-t_i/\tau} + B)^2}{I(t_i)} \tag{1.106}$$

where A, τ and B are the fit parameters referring to the intensity amplitude, fluorescence lifetime and background, respectively. Therefore, *M=3*.

For a large photon count, the Poisson-distributed data converges towards nor-

mality and the non-linear least squares method is valid, delivering reliable estimation of the fit parameters [120, 121]. However, for a low number of counts, which mainly happens at the end of the intensity decay, the data is Poisson-distributed. This means, the non-linear least squares method is less accurate and deviates from the maximum-likelihood method performance when the number of counts is low [122, 123].

1.6.1.2 Maximum likelihood method

The likelihood function of a set of Poisson-distributed data is given by the combined probability of measuring a set of intensities I_i, where the model predicts μ_i [122]:

$$\mathscr{L}_i(I) = \prod_i \frac{\mu_i^{I_i}}{I_i!} e^{-\mu_i} \tag{1.107}$$

It is easier to use the logarithm of this expression:

$$-2\mathscr{L}_i(I) = 2\sum_i [\mu_i - I_i ln(\mu_i)] \tag{1.108}$$

Both methods, non-linear least squares (NL-LS) and maximum likelihood (ML), can be easily implemented in MATLAB routines to estimate the fit parameters of the collected intensity decays. Many softwares are available with the NL-LS method implemented, such as SPCImage [36], TRI2 [124] and FLIMfit [111]. The last two ones have also the possibility to apply a ML estimator. The Bayesian method is a robust estimator that has been shown to estimate with high accuracy lifetime parameters for low intensity levels [125, 126].

1.6.2 Time-resolved fluorescence anisotropy data fit approaches

A great part of this thesis is focused on the fit and interpretation of the time-resolved fluorescence anisotropy data, where some a priori assumptions need to be established. The number of assumptions and the weighting-factor may differ on the

applied method. For instance, when the parallel and perpendicular intensity decays ($I_{\parallel}$ and $I_{\perp}$) are fitted simultaneously, the fit method must estimate the number of fluorescence lifetimes τ of the total intensity signal I_{tot} and the anisotropy fit parameters. The total intensity decay is Poisson-distributed, which means the fit is weighted according to the Poisson statistics. On the other hand, the time-resolved fluorescence anisotropy data does not follow the Poisson statistics, which means a different weighting-factor must be introduced.

In the upcoming sections, the most popular methods for the time-resolved fluorescence anisotropy data analysis will be introduced, where the number of a priori assumptions that needs to be established and the weighting-factor choice are briefly discussed.

1.6.2.1 Fitting the parallel and perpendicular intensity decays ($I_{\parallel}$ and $I_{\perp}$) simultaneously

The parallel and perpendicular intensity decays ($I_{\parallel}$ and $I_{\perp}$), as a function of the total intensity decay I_{tot} and the anisotropy model r_{model}, are given by the following expressions [20, 127]:

$$I_{\parallel}(t) = \frac{1}{3} I_{tot}(t)[1 + 2r_{model}(t)] \tag{1.109}$$

$$I_{\perp}(t) = \frac{1}{3} I_{tot}(t)[1 - r_{model}(t)] \tag{1.110}$$

where the r_{model} expression depends on the shape of the probe and its extend of freedom to rotate and G is considered to be 1. In this example, we will focus on the case of a spherical probe going through a *hindered rotation* (*Section* 1.1.7.3), whose anisotropy expression is given by:

$$Hindered\ rotation \Rightarrow r_{model}(t) = (r_0 - r_\infty)e^{-t/\theta} + r_\infty \tag{1.111}$$

where r_0 is the initial anisotropy value, r_∞ is the limiting anisotropy and θ is the rotational correlation time.

The parallel and perpendicular intensity decay fits are performed simultaneously via expressing them as a convolution of the corresponding IRF component with expressions 1.109 and 1.110, respectively. If the non-linear least squares (NL-LS) method is applied to estimate the fit parameters and χ^2 is the goodness of fit, then:

$$\chi^2_A = \left(I_\parallel(t) - IRF_\parallel(t) \otimes \frac{1}{3} I_{tot,sim}[1 + 2r_{model}(t)]\right)^2 / I_\parallel(t) \tag{1.112}$$

$$\chi^2_B = \left(I_\perp(t) - IRF_\perp(t) \otimes \frac{1}{3} I_{tot,sim}[1 - r_{model}(t)]\right)^2 / I_\perp(t) \tag{1.113}$$

where $I_{tot,sim}$ is the simulated total intensity decay. $IRF_\parallel$ and $IRF_\perp$ are the parallel and perpendicular instrument response functions (IRFs) and IRF_{tot}=$IRF_\parallel$+2$IRF_\perp$.

If we assume the total intensity decay follows a single exponential model, then:

$$I_{tot,sim} = Ae^{-t/\tau} \tag{1.114}$$

where A is the intensity amplitude and τ the fluorescence lifetime.

Thus, the explicit equations (1.112 and 1.113) are as follows:

$$\chi^2_A = \left(I_\parallel(t) - IRF_\parallel(t) \otimes \frac{1}{3}(Ae^{-t/\tau})[1 + 2(r_0 - r_\infty)e^{-t/\theta})]\right)^2 / I_\parallel(t) \tag{1.115}$$

$$\chi^2_B = \left(I_\perp(t) - IRF_\perp(t) \otimes \frac{1}{3}(Ae^{-t/\tau})[1 - (r_0 - r_\infty)e^{-t/\theta})]\right)^2 / I_\perp(t) \tag{1.116}$$

From expressions 1.115 and 1.116, the fit parameters A, τ, r_0, r_∞ and θ are determined.

1.6.2.2 Fitting directly the time-resolved fluorescence anisotropy decay

When a sufficient capital of photons is available, it is very common to fit the time-resolved fluorescence anisotropy decay straightaway applying an anisotropy model, such as the ones for instance presented in *Section* 1.1.7.3. However, the problem arises in the weighting of the data during the performance of the estimator method. We know that the fluorescence intensity decays noise follows a Poisson distribution, however, no analytical solution defines the distribution of the time-resolved fluorescence anisotropy data. This means that the direct fitting of the anisotropy data can lead to unreliable fit parameters due to the lack of weighting.

In order to overcome this problem and to add a weighting to the anisotropy data, Lidke et al. derived an expression for the anisotropy variance applying propagation of errors for the two signals ($I_{\parallel}$ and $I_{\perp}$) [128]:

$$var(r) = \frac{(1-r)(1+2r)(1-r+G(1+2r))}{3I_{tot}} \tag{1.117}$$

where I_{tot} corresponds to the total emission intensity and r is the steady-state anisotropy (equation 1.12).

Equation 4.11 refers to the variance of the steady-state anisotropy values and it decreases with the total intensity signal I_{tot}. Hence, the importance of having a high number of photons to achieve reliable anisotropy values. This is why the tail of the time-resolved fluorescence anisotropy decay is hard to fit due to the high levels of noise. This weighting expression (equation 4.11) can be applied to each one of the anisotropy values of the time-resolved fluorescence anisotropy decay. If a NL-LS method is utilised to estimate the anisotropy fit parameters, the function that needs

to be minimised is given by χ^2:

$$\chi^2 = \big(r(t) - r_{model}(t)\big)^2 / var(r) \tag{1.118}$$

If we consider the case of a hindered rotation model for the anisotropy data and we explicitly write $var(r)$ within equation 1.118, then:

$$\chi^2 = \frac{\big(r(t) - [(r_0 - r_\infty)e^{-t/\theta} + r_\infty]\big)^2}{(1-r)(1+2r)(1-r+G(1+2r))/(3I_{tot})} \tag{1.119}$$

Note that to generate the time-resolved fluorescence anisotropy decay, the background level of each intensity signal must be equal. Otherwise, the polarised intensity decays need to be corrected for background signals. The counts measured for the nonexistent sample with each polariser position are subtracted from the measured data for the same polariser position. Different background levels for parallel and perpendicular intensity measurements are related to the gain of each one of the hybrid detectors, which does not necessarily have to coincide [20]. If the wrong background levels are considered, the time-resolved fluorescence anisotropy data may present an odd decay at the tail, which does not represent the real data.

1.6.3 FRAP data analysis methods

FRAP data analysis requires different steps to be taken into account in order to obtain reliable fit parameters. Normalisation methods are biased according to which FRAP parameter the user wants to determine. The classical method for the FRAP data analysis will be explained, along the three steps that must be applied prior to the any fit approach. The optimisation of the diffusion coefficient when using a confocal-based setup is also mentioned and briefly discussed, for a *circular* and *rectangular* bleached areas. Lastly, some more advanced FRAP data analysis methods are mentioned: the *ring-based* and *Hankel-transform* methods.

1.6.3.1 Classical method

The FRAP data analysis requires the application of three necessary corrections that must be done in order to get the optimal parameters:

1. **Background subtraction**

   First of all, the background must be subtracted. All our images have background, which can come from our Photomultiplier Tubes (PMTs) and the electronics. So it is more than advisable taking an image before performing our experiments with all the lasers off. Therefore, the postbleach intensity is given as follows:

   $$I_b(t) = I(t) - background \tag{1.120}$$

2. **Correct for fluorescence loss due to photobleaching**

   Another correction that must be performed is the one related to the fluorescence loss due to photobleaching. The sample is intentionally bleached in order to assess the lateral mobility, but at the same time it is also being bleached unintentionally during the post-bleach acquisition. This is the reason why the recovery curve never reaches the initial intensity, even if all the fluorophores were mobile. That's why every element of the data is multiplied by a factor ($I_{pre,ROI_{out}}/I_{post,ROI_{out}}$), where $I_{pre,ROI_{out}}$ is the prebleach intensity within a Region of Interest (ROI) far from the bleach spot, and $I_{post,ROI_{out}}$ the postbleach intensity within a ROI far from the bleach spot at any time. This gives rise to:

   $$I_{b,corr}(t) = I_b(t)\frac{I_{pre,ROI_{out}}}{I_{post,ROI_{out}}} \tag{1.121}$$

3. **Normalisation**

   Normalisation requires special attention [129]. A quite common strategy consists of dividing every frame by the first one, getting 100% of intensity for the

prebleach intensity images. This was introduced by Siggia et al. [130]:

$$I_{b,corr,Siggia}(t) = \frac{I_{b,corr,ROI_{in}(t)}}{I_{pre,ROI_{in}}} \tag{1.122}$$

where $I_{b,corr,ROI_{in}(t)}$ is the fluorescence intensity inside of the bleach spot at any time t and $I_{pre,ROI_{in}}$ is the prebleach intensity inside of the bleach spot.

With this normalisation, only the fraction of molecules M_f that contribute to the fluorescence recovery at the bleach spot can be determined. The rest of the molecules that are immobilised give rise to incomplete FRAP recovery curves and is equal to Im_f = *1* - M_f. Hence, M_f is defined as follows:

$$M_f = \frac{I_{b,corr,Siggia}(\infty) - I_{b,corr,Siggia}(0)}{I_{b,corr,Siggia}(t) - I_{b,corr,Siggia}(0)} \tag{1.123}$$

where $I_{b,corr,Siggia}(t)$, $I_{b,corr,Siggia}(0)$ and $I_{b,corr,Siggia}(\infty)$ are the fluorescence intensities inside the bleach ROI at any time t, at time $t = 0$ and at equilibrium, respectively.

The other normalisation method was introduced by Axelrod et al. [84]. This one permits only the determination of the half recovery time $\tau_{1/2}$, where the plateau value is set to 100%. This parameter ($\tau_{1/2}$) is defined as the time it takes for the fluorescence to recover to 50% of the asymptote (plateau) intensity. Using this normalisation method, the intensity in the bleach spot is given by the following expression:

$$I_{b,corr,Axelrod}(t) = \frac{I_{b,corr,ROI_{in}}(t) - I_{b,corr,ROI_{in}}(0)}{I_{b,corr,ROI_{in}}(\infty) - I_{b,corr,ROI_{in}}(0)} \tag{1.124}$$

where $I_{b,corr,ROI_{in}}(t)$, $I_{b,corr,ROI_{in}}(0)$ and $I_{b,corr,ROI_{in}}(\infty)$ are the fluorescence intensities inside the bleach ROI at any time t, at time $t = 0$ and at equilibrium, respectively.

If the FRAP data is fitted with a single exponential fit and a pure isotropic diffusion model is considered, the half-recovery time $\tau_{1/2}$ can be obtained from the following fit:

$$I_{b,corr,Axelrod}(t) = a(1 - e^{-t/\tau_D}) + c \tag{1.125}$$

where a and c are constants and the half-recovery time $\tau_{1/2}$ is related to the recovery time τ_D as follows:

$$\tau_{1/2} = \tau_D ln(2) \tag{1.126}$$

The half-recovery time $\tau_{1/2}$ may be also calculated applying the following equation [131]:

$$I_{b,corr,Axelrod}(t) = 100 \times \frac{I_{b,corr,Axelrod}(0) + I_{b,corr,Axelrod}(\infty)(t/\tau_{1/2})}{(1 + t/\tau_{1/2})} \tag{1.127}$$

Equations 1.125 and 1.127 consist of empirical approaches to calculate the half-recovery time $\tau_{1/2}$. However, Axelrod et al. [84] derived a somewhat complicated closed form for the fluorescence recovery curve considering a Gaussian profile beam for the laser. Years later, Soumpasis et al. [93] did the same considering a uniform circular disk profile beam. They both derived equations for the translational diffusion coefficients, relating the half-recovery time $\tau_{1/2}$ and the radius of the bleach laser spot r_n. The diffusion coefficient expressions derived by Axelrod and Soumpasis are as follows [84, 93]:

$$Axelrod \rightarrow D_t = 0.88\frac{r_n^2}{4\tau_{1/2}} = 0.22\frac{r_n^2}{\tau_{1/2}} \tag{1.128}$$

$$Soumpasis \rightarrow D_t = 0.224\frac{r_n^2}{\tau_{1/2}} \tag{1.129}$$

where r_n is the nominal radius from a user-defined bleaching spot radius and $\tau_{1/2}$ is the half time of recovery, defined as the time required for a bleach spot to recover half way between initial and steady state fluorescence intensities. Assuming Stokes-Einstein-Debye (SED) behaviour and the lateral diffusion of spherical molecules, the previous equation can be expressed in the following way:

$$D_t = \frac{k_b T}{6\eta\pi R_h} \tag{1.130}$$

where k_b is the Boltzmann constant, T is the absolute temperature, η is the viscosity and R_h is the hydrodynamic radius of the dye.

Therefore, the radius of the dye can be extracted from the previous equation:

$$R_h = \frac{k_b T}{6\eta\pi D_t} \tag{1.131}$$

1.6.3.2 Classical method with Confocal correction

- **Circular bleached ROI**

  Note that the above derivations assume a circular shape for the bleach spot, the sample is a 2-dimensional system and the diffusion during photobleaching is considered to be negligible, which is not necessarily true for confocal FRAP [96]. This can lead to an underestimation of the diffusion coefficient. This has given rise to different papers where this obstacle is thought to be overcome with different approaches. For instance, in the paper published by Minchul Kang and his colleagues, from the computation shown by Axelrod et al. [84], they derived an expression for the diffusion FRAP curve for confocal FRAP [96]:

$$I(t) = I_i\left\{1 - \frac{K}{1+\gamma^2+2t/\tau_D}\right\}M_f + (1-M_f)I(0) \tag{1.132}$$

where I_i is the prebleach fluorescence intensity within the bleach ROI, $I(0)$ is the postbleach initial fluorescence intensity within the bleach ROI, K is the bleaching-depth parameter, γ is the ratio of r_n and half width at the approximately 14% of bleaching depth from the top (r_e), $\tau_D = r_e^2/(4D_t)$ and M_f is the mobile fraction.

After a few steps of maths, they presented the following expression for the translational diffusion coefficient using a confocal system:

$$D_{Confocal} = \frac{r_e^2 + r_n^2}{8\tau_{1/2}} \tag{1.133}$$

When $r_e = r_n$, equation 1.133 is converted to $D = 0.25\frac{r_n^2}{\tau_{1/2}}$. The small difference in the proportionality constants of equations 1.128, 1.129 and 1.133 is related to the different assumptions of either Gaussian or uniform laser profiles.

- **Rectangular bleached ROI**

An expression for the FRAP recovery curve intensity for rectangular regions of any size and aspect ratio (with x and y dimensions) was presented by Deschout et al [132]. The derivation of this expression was based on considering a pixel-based acquisition data, which means using a laser scanning microscope. This work has the peculiarity that the Point Spread Function (PSF) is taken into account, where temporal and spatial data are used in order to achieve a more accurate and fast FRAP. They showed an expression for the recovery curve valid for a 2-dimensional diffusion model and a single photon illumination profile, with a Gaussian photo bleaching intensity distribution.

The single photon 2-dimensional rectangular FRAP (rFRAP) model is given

by the following equation:

$$\frac{I(x,y,t)}{I(x,y,0)} = 1 - \frac{K_0}{4}\left[erf\left(\frac{x+l_x/2}{\sqrt{r^2+4D_t t}}\right) - erf\left(\frac{x-l_x/2}{\sqrt{r^2+4D_t t}}\right)\right] \times \left[erf\left(\frac{y+l_y/2}{\sqrt{r^2+4D_t t}}\right) - erf\left(\frac{y-l_y/2}{\sqrt{r^2+4D_t t}}\right)\right]$$

where $I(x,y,t)$ is the fluorescence intensity at a time t, K_0 is a parameter that is related to the Gaussian shape of the microscope's imaging point spread function (PSF), l_x is the lateral length of the rectangular area and l_y the height, D_t is the translational diffusion coefficient, r has to do with the lateral resolution for single photon imaging and erf is the error function, given by:

$$erf(z) = \frac{2}{\sqrt{\pi}}\int_0^z e^{-x^2}dx \tag{1.134}$$

The recovery time τ_D was given by the following expression:

$$\tau_D = \frac{(L/2)^2}{4D_t} \tag{1.135}$$

where L is the length of the shortest side of the rectangle.

In summary, this method was able to generalise conventional FRAP theory and incorporate diffusion during photobleaching for rectangular bleaching ROI and was demonstrated to be more accurate than the classical methods [132].

1.6.3.3 More advanced FRAP data analysis methods

- **Ring-based method**

  Xiong et al. [97] provide a MATLAB code in order to do the FRAP data analysis on a rectangular area. The method they follow ensures a continuous distribution of diffusion coefficients under the condition of maximum entropy.

The analytical model is fitted to every individual pixel of the recovery images. They apply something known as the *'ring-based method'*, where the ROI is divided into *n* equally spaced rectangular ring areas. The spatial information given by each ring is averaged and provide the user a fast calculation of the FRAP parameters. The fluctuations during the data acquisition are corrected taking a region of reference.

They report that from simulations they have been able to distinguish two subpopulations if their diffusion coefficient differs by a factor 3, meanwhile with the classic FRAP, they would only be distinguished if they differed by a factor 8. In addition, this method also has the advantage that the data analysis can be undertaken down to signal-to-noise SNR = 2.4.

- **Hankel-transform method**

  One of the problems of the traditional methods is that they characterise the bleaching area with a certain shape, following the function given by the fit curve throughout the recovery process [133]. Also, intensity fluctuations are not taken into account in the data analysis. This cannot be accurate enough and leads to errors in the determination of the diffusion coefficient. One way to overcome this issue was introduced by Tsay and Jacobson, applying the Fourier transform. However, it has been noted that this method involves several problems. Tsay and Jacobson realised that their method was more sensitive to noise than the traditional ones [134]. In addition, the Fourier transform analysis has the limitation that it can be only performed for short times or large fields of view [135].

  The present method relies on solving *Fick's second law* for an isotropic 2-dimensional system by using the Hankel transform. For doing so, the system

has to be much larger than the initial dimensions of the bleached spot. The initial concentration of the fluorophores are assumed to have a circular symmetry. The Hankel-transform method is based on the circular average of the radial profiles instead of the whole image. Temporal fluctuations in illumination during the data acquisition are compensated during the recovery. This method proved its high accuracy by comparing experimental and simulated data, and the suppression of noise in the data. It also tracks the centre of mass in case some drift during the acquisition is detected [94]. However, this method is limited if the bleaching-depth is not above 50%, delivering unreliable translational diffusion coefficients.

1.7 Förster Resonance Energy Transfer Applications

In this section, the importance of FRET in life science will be introduced and briefly discussed. Some examples of how FRET can be applied to address a specific biological question is also presented in this section, distinguishing between homo- and hetero-FRET and the techniques applied for the study of this phenomenon, focusing on FLIM and time-resolved FAIM.

1.7.1 What is special about Förster Resonance Energy Transfer?

The obstacle of determining the proximity between two fluorophores due to limitations in the spatial resolution of the existing fluorescence microscopy techniques can be overcome by Förster Resonance Energy Transfer. This photophysical phenomenon happens in a distance of few nanometres ($\sim$*10 nm*), which is below the spatial resolution offered by the diffraction-limited and super-resolution fluorescence microscopy techniques.

Over the past 10 years, the rise of applications requiring genetic targeting of specific proteins has yielded an increased popularity within the FRET approaches.

However, one of the major obstacles to the widespread implementation of FRET studies in living cells, has been the lack of suitable fluorescence labels of specific intracellular proteins. This has been overcome by a long list of recently developed fluorescent proteins with a wide array of spectral profiles, resulting in a number of potential fluorescent protein pairs that are useful in FRET experiments [136–138].

1.7.2 Detection of homo-FRET via (tr-)FAIM

Clustering of proteins is routinely investigated by methods such as chemical cross-linking and coimmunoprecipitation. However, both of these techniques are prone to artifacts since some clustering may be formed. Microscopy homo-FRET have been developed to study clustering processes, where non-radiative energy between identical fluorophores takes place [81,139,140]. The emission spectrum and the fluorescence lifetime of the probes does not get affected, but the fluorescence anisotropy of the probe does, which decreases in the presence of homo-FRET. Therefore, (tr-)FAIM-FRET microscopy affords the imaging of molecular-scale clustering of identical (bio)molecules in cells. Anisotropy measurements have an unique ability to elucidate the occurrence of homo-FRET and have been used in living cells to study the effect of protein dimerisation, aggregation, etc. on cell functioning [40, 78–80].

In the work published by Sharma et al. [81], the size of lipid-dependent organisation of Glycosyl-Phosphatidylinositol-Anchored Proteins (GPI-APs) in live cells is investigated using homo and hetero-FRET-based experiments and combining theoretical models. They observed that various GPI-AP species were organised forming nanometer-sized clusters on the cell surface and underwent significant homo-FRET by observing a fast decay component in the time-resolved fluorescence anisotropy data and a significant reduction in steady-state anisotropy. Cluster size images were obtained from the anisotropy data (equation 1.61), when the probe's rotation is neglected.

The development of novel fluorescence microscopy setups to efficiently de-

tect homo-FRET has been reported. For instance, Cossec et al. [141] presented an innovative tr-FAIM setup combined with Total Internal Reflection Fluorescence Lifetime IMaging (TIRFLIM), where the homodimerization of wild-type Amyloid Precursor Protein (APP)-eGFP or of a mutated APP-eGFP was shown by measuring a combination of energy transfer rates. Nguyen et al. presented the development of a new setup modality: Fluorescence Polarisation and Fluctuation Analysis (FPFA) [142]. The fluorescence microscopy setup was validated by measuring several Venus based control-constructs in cell homogenates using a GFP specific antibody. The brightness of the Venus-constructs was shown to be correlated with the number of Venus units and the time-resolved fluorescence anisotropy decays were shown to decrease faster with an increase in the number of Venus units. The utility of FPFA was demonstrated by the measurement in living cells of the number of subunits in the α-isoform of Venus-tagged calcium-calmodulin dependent protein kinase-II (CaMKIIα) holoenzyme. The automatisation of this setup (FPFA) has been recently published and tested with Venus-constructs [143].

1.7.3 Detection of hetero-FRET via FLIM

In a collaborative work with **Dr. Zahra Timsah**, fluorescence lifetime imaging (FLIM) was performed in human embryonic kidney (HEK) 293T cells in order to investigate the binding between the ion channel TRPA1 and the membrane receptor FGFR2, related to the lung adenocarcinoma. The ion channel TRPA1 was tagged with GFP, acting as the donor, and FGFR2 was tagged with Red Fluorescence Protein (RFP), acceptor of the FRET pair. In order to map the binding site on TRPA1 and investigate the possibility of its N-terminal ankyrin repeat domain binding to FGFR2 proline-rich motif, the last 5 or 10 ankyrin repeats of TRPA1-GFP were truncated to generate Δ5 and Δ10. Lifetime studies revealed that truncating the last 10 ankyrin repeats abrogates the binding event, as its fluorescence lifetime increased with respect to Δ5, due to FRET [144]. Figure 1.17 shows the discussed

FLIM results.

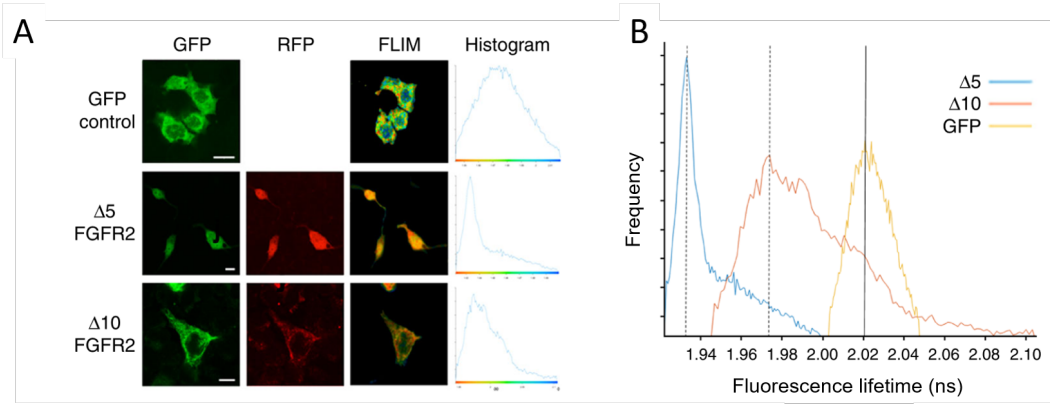

Figure 1.17: A,B FLIM experiment in HEK 293T cells co-transfected with FGFR2-RFP and Δ5-GFP or Δ10-GFP. Y-axis depicts the fluorescence lifetime frequency. Scale bar is 10 μm. HEK 293T cells that were transfected with an empty GFP vector (upper panel) were utilised as a control to establish the lifetime of GFP. Histograms (shown on the same scale) in (A) indicate lifetime changes in nanoseconds (ns), where a decrease in GFP lifetime (peak shift to the left of the yellow curve) correlates with a potential direct binding event between the two proteins [144].

The chromatic compaction was also investigated in living cells using FLIM-FRET by Lleres et al. [145]. The complex multiscale nature and composition of chromatic structure has represented a formidable challenge for structural biologists [146, 147]. Lifetime studies were performed on histone H2B tagged to either GFP or mCherry in order to study the chromatin compaction in living cells. FRET occured predonminantly from interactions between GFP and mCherry-tagged histones in separate nucleosomes, as the distance between them within the same nucleosome was above 10 nm. They showed that specific FRET interactions between the two tagged forms of histone H2B took place, by the spatial distinction of three populations of chromatic with three different FRET efficiency levels. These distinct FRET efficiency populations were related to different degrees of compaction. The highest FRET efficiency regions were consistent with the prediction to include regions of highest chromatin condensation such as heterochromatin clusters around the nucleoli and at the nuclear periphery. Also, the investigation of the compaction of all chromosomes when cells going through different stages of mitosis, was ad-

dressed by using FLIM-FRET. The FRET efficiency presented an increase in the compaction of the chromosomes from prometaphase to late anaphase, affecting chromatic organisation at the nucleosome array level. After this FRET increase, a subsequent decrease in chromatin compaction took place during telophase. Overall, FLIM-FRET was demonstrated to provide useful information about chromatin density levels at different cell stages.

Another example is given by Caron et al. [148], where, using FLIM-FRET, they studied the comformational changes of Transglutaminase type 2 (TG2) in live cells. The fluorescence biosensor formed by mCerulean fluorescent protein as a donor and the Yellow Fluorescence Protein (YFP) as an acceptor was the responsible of tracking the TG2 behaviour. Authors demonstrated that this FRET biosensor could measure effects of cell stress, changes in calcium levels and chemical inhibitors on the comformation and localisation of TG2 in living cells. FLIM-FRET was also applied to trace the catalytic activity of fluorescently tagged protein kinase Cα ($PKC\alpha$) in live and fixed cultured cells [149]. Very recently, FLIM-FRET was utilised to reveal the dynamic conformational transitions of the Epidermal Growth Factor Receptor (EGFR) in living Chinese Hamster Ovary (CHO) mammalian cells upon binding to the respective ligand. For this purpose, EGFR was covalently attached to the dye Atto390 [150].

These are just few examples of how FLIM-FRET can give insight to address a specific biological question. The combination of lifetime and FRET (FLIM-FRET) provides high spatial (nanometer) and temporal (nanosecond) resolution [151, 152]. Measuring the donor lifetime in the presence and absence (control) of the acceptor, one can accurately calculate the distance between donor and acceptor. One also needs to bear in mind that when 1-photon excitation FLIM-FRET experiments are performed, the apparent $E\%$ is produced, which is the FRET efficiency calculated on the basis of all donors (FRET and non-FRET). However, 2-photon excitation

FLIM, due to its higher sensitivity, is able to distinguish between the two populations, FRET and non-FRET, and therefore, two peaks of donor lifetimes show up. This allows a higher precision in the estimation of the distance between fluorophores. The 1-photon excitation FLIM setup could be sufficient for many situations, and the latter crucial for establishing comparative distances between proteins of interest, so it is important to distinguish the case scenario we are in [153].

1.8 Summary and Conclusion

This chapter has introduced the concepts of fluorescence, fluorescence lifetime and anisotropy and Förster Resonance Energy Transfer (FRET). Time-resolved fluorescence microscopy techniques based on time-correlated single photon counting (TCSPC) were introduced and briefly explained: Fluorescence lifetime imaging (FLIM) and time-resolved fluorescence anisotropy imaging (tr-FAIM). The steady-state fluorescence recovery after photobleaching technique was also briefly described. An overview of the laboratory setup was given, where the elements present in the optical path of the excitation beam were described, so as the different fluorescence microscopy modalities the setup affords, specifying which ones will be used in the upcoming chapters. An overview of the data analysis procedures for FLIM, tr-FAIM and FRAP was presented. In particular, different approaches for the time-resolved fluorescence anisotropy and FRAP data were explored and compared. Finally, some Förster Resonance Energy Transfer (FRET) applications were presented, where FLIM and tr-FAIM are utilised to investigate homo- and hetero-FRET, respectively. Some additional literature review will be introduced in the upcoming chapters, where specific information related and required by the chapter will get disclosed.

Chapter 2

Exploring the stretched exponential decay model as a FRET indicator for EGFP dimers

2.1 Motivation

Protein dimerisation in cells is of great importance within the field of biology. This phenomenon triggers many biological processes such as cell signalling. Fluorescence anisotropy is a powerful tool for the detection of homo-FRET. However, its interpretation and extraction of quantitative information is not that straightforward and requires prior assumptions. In this chapter, I describe a new data analysis approach to study protein dimerisation by fluorescence anisotropy. The novelty is in the use of stretched exponential decay model and it is demonstrated on the example of dimerisation of Enhanced Green Fluorescence Protein (EGFP). The application of this model to the time-resolved fluorescence anisotropy data provides additional information that other methods are not able to provide, such as the concentration of the donor molecules or the dimensions of the problem (2-dimensional or 3-dimensional). Thus, the main message of this chapter is to encourage all the time-resolved fluorescence anisotropy users to explore the stretched exponential model

possibilities as a way to interpret their results, which looks specially promising for the investigation of homo-FRET between proteins in living cells, as rotation is practically suppressed. In an additional note, fluorescence lifetime, FRAP and Molecular Dynamic (MD) simulations studies are highlighted as complementary tools, which may provide a broader picture of the problem under investigation.

2.2 Introduction

2.2.1 Green Fluorescent Protein

Green fluorescent protein (GFP) was the first protein extracted and purified from jellyfish Aequorea victoria [154] . It converts UV and blue light into green light, at an emission peak wavelength of 508 nm [155, 156]. GFP refers also to the first genetically encoded fluorophore, which demonstrates that a gene can be expressed in cells or organisms of interest. Before GFP, dyes had to be injected into cells, which is invasive. GFP is great for all forms of fluorescence microscopy and has been expressed in many species, including bacteria, yeasts, fungi, fish and mammals, including in human cells. The discovery and development of GFP led to a Nobel Prize in 2008 [154]. Several models have been proposed to explain the complex photophysics of this protein and its variants. Initially, two different stable and interconvertible forms of the chromophore, protonated and deprotonated, were proposed to explain the complex photophysics of wild-type GFP [157]. Later on, other models that implied three different configurations for the chromophore and a excited-state proton transfer mechanism were proposed in order to explain the excited-state dynamics of GFP [32–35]. These absorption bands are located within the UV-visible range at 400 nm, for the protonated A form, and around 475 nm, for the deprotonated B and I forms. More recently, Time-Correlated Single Photon Counting (TCSPC) experiments on a GFP-variant, Enhanced GFP (EGFP), allowed the distinction of the two deprotonated states B and I, where two different

fluorescence lifetimes were identified (3.4 ns and 2.7 ns). Therefore, further models were proposed to explain and understand the photophysical behaviour of these fluorophores [158]. X-ray crystallographic studies [159] have revealed that GFP is a barrel-shaped protein (27 kDa, made of 238 aminoacids), with a length of 4.2 nm and diameter of 2.4 nm. The chromophore of the protein lies at the centre of the structure, where 4 aminoacids are responsible for the fluorescence emission. Nowadays, this protein and its genetically encoded variants are extensively used in many biological applications, such as cell imaging, to monitor gene expression, to locate proteins, study their interactions and describe their dynamics [160, 161].

Also, the large size of GFP (27 kDa), converts it into an excellent candidate to reproduce the mobility of the proteins it is attached to or encoded in. Its quantum yield under UV-visible excitation light is $\Phi = 0.60$ [161] and due to the way its chromophore is formed, its rotational mobility and fluorescence lifetime are sensitive to environmental changes, such as viscosity [162] or refractive index [29], respectively. This postulates the GFP or any of its variants, as perfect candidates of living nano-probes [163].

2.2.2 Investigating homo-FRET via the application of the stretched exponential model to the time-resolved fluorescence anisotropy data

We have seen in *Section* 1.2.4.1 that the stretched exponential model can be applied to describe the donor's anisotropy depolarisation when the donor molecule transfers energy via FRET to acceptor molecules located at different distances from the excited molecule, where depolarisation due to rotation does not take place. The transfer of energy occurs among different molecules (hetero-FRET). However, a similar approach can be used to describe the depolarisation of the excited molecule within an isotropic solution of identical molecules due to homo-FRET. The deriva-

tion of the anisotropy expression of the initially excited molecule that is given in this section is based on the work of Bodunov et al. [164].

The initial excited molecules contribute predominantly to the emission anisotropy $\bar{r}$, as the luminescence of molecules excited by FRET is depolarised nearly completely [165]. Due to this reason, emission anisotropy $\bar{r}$ may be expressed in terms of the quantum yield Φ_1 of the initially excited molecules:

$$\frac{\bar{r}}{\overline{r_0}} = \frac{\Phi_1}{\Phi} \tag{2.1}$$

where $\overline{r_0}$ is the luminescence emission anisotropy $r(t)$ in the absence of FRET and Φ is the total quantum yield.

The emission anisotropy $r(t)$ of the initially excited molecules is determined by the probability $G(t)$ that the initially excited molecule is in the excited state at time t:

$$r(t) = r_0 G(t) \tag{2.2}$$

where r_0 is the emission anisotropy at $t = 0$. $G(t)$ takes into account the first event of the energy transfer from the initially excited molecule to secondary excited molecule and re-excitation of the initially excited molecule via different pathways.

The probability $G(t)$ presented in this chapter is calculated using the Huber-Hamilton-Barnett method [166]. This model assumes the system is formed of an isotropic distribution of molecules in a 3-dimensional medium. $G(t)$ is defined as follows:

$$G_H(t) = exp\Big(-\frac{N}{2}\int d^3R(1-e^{-2k_F})\Big) \tag{2.3}$$

where N is the concentration of molecules within the whole volume and k_F is the FRET constant rate.

Equation 2.3 takes the following form:

$$G_H(t) = exp\Big(-\sqrt{\frac{\pi}{2}}c\Big(\frac{t}{\tau}\Big)^{1/2}\Big) \tag{2.4}$$

where c is the dimensionless concentration of molecules:

$$c = \frac{4\pi}{3}NR_0^3 \tag{2.5}$$

where R_0 is the Förster distance at which the energy efficiency due to FRET is half.

Combining equations 2.2 and 2.4, the emission anisotropy $r(t)$ of the initially excited molecule is given by the following expression:

$$r(t) = r_0 e^{-\sqrt{\frac{\pi}{2}}c\left(\frac{t}{\tau}\right)^{1/2}} = r_0 e^{-\gamma t^{\delta}} \tag{2.6}$$

This is the so-called *stretched exponential model*, where $\delta = 1/2$ refers to a 3-dimensional system and

$$\gamma = \sqrt{\frac{\pi}{2\tau}}c \tag{2.7}$$

Equation 2.6 implies the Brownian translational motion of the molecules is slow enough that the distance in between chromophores can be considered constant.

Taking into account the probability $G(t)$, the excitation probability of the initially excited molecules can be expressed as follows:

$$I_1(t) = I_0 e^{-t/\tau} G(t) \tag{2.8}$$

where I_0 is the luminescence intensity at $t = 0$ and τ is the fluorescence lifetime.

Knowing the relation between the excitation probability and the quantum yield and considering a single-exponent decay of the total intensity $I(t)$ (an average flu-

orescence lifetime may be also introduced as an approximation), equation 2.1 is given by:

$$\frac{\bar{r}}{\overline{r_0}} = \frac{\Phi_1}{\Phi} = \frac{\int_0^\infty dt I_1(t)}{\int_0^\infty dt I(t)} = \frac{1}{\tau I_0}\int_0^\infty dt I_1(t) = \frac{1}{\tau}\int_0^\infty dt e^{-t/\tau} G(t) \tag{2.9}$$

Introducing the explicit expression of the probability $G(t)$ (equation 2.4) within equation 2.9, the result is:

$$\frac{\bar{r}}{\overline{r_0}} = \frac{1}{\tau}\int_0^\infty dt e^{-t/\tau} G(t) = 1 - f(y) \tag{2.10}$$

where

$$f(y) = \sqrt{\pi} y e^{y^2}[1 - erf(y)] \tag{2.11}$$

$$erf(y) = \frac{2}{\sqrt{pi}}\int_0^y dt e^{-t^2} \tag{2.12}$$

$$y = \frac{\sqrt{\pi}}{2\sqrt{2}} c \tag{2.13}$$

The FRET energy efficiency of the initially excited molecule will be given by $f(y)$:

$$E_{FRET} = f(y) = \sqrt{\pi} y e^{y^2}[1 - erf(y)] \tag{2.14}$$

This expression (equation 2.14) is equivalent to $E_{FRET} = 1 - \Phi_1$, where the total quantum yield $\Phi = 1$.

2.2.3 Coxsackievirus and Adenovirus Receptor (CAR)

CAR is a transmembrane protein (40 kDa and composed of 365 aminoacids) located within the cell-cell junctions and known for playing an important role in cell-cell adhesion [167, 168] and may play a role in lung cancer cell adhesion and invasion [169]. Recently, it has been reported that the CAR depletion in human lung cancer cells reduces the tumour growth [170].

It is also known that the CAR proteins organise themselves forming homo-dimers across the cell-cell junctions [171, 172] and when an adenovirus is detected by the protein CAR, a disruption in the dimerisation takes place, which affects the cell signalling deactivating the protein. Although some effects have been observed when the CAR natural cycle is modified, the mechanism is still not clear.

2.2.4 What is studied in this chapter?

The dynamics of two EGFP constructs, monomer and dimer, is investigated using fluorescence lifetime and anisotropy measurements in different glycerol/Phosphate-Buffered Saline (PBS)(X1) solutions. For the time-resolved fluorescence anisotropy interpretation of the EGFP dimer, two models are proposed (stretched and bi-exponential). The lateral mobility of the two EGFP constructs is also studied via FRAP, and steady-state anisotropy measurements at different excitation wavelengths present a comparison between EGFP constructs at the red-edge. Via MD simulations, the separation between EGFP monomers and their relative dipole orientation is calculated, where the E_{FRET} is obtained from. This permits a direct comparison with experiment. Also, the investigation of the anisotropy decays over time allows the assessment of the rotation for both constructs, not able to be extracted from the experimental data due to the presence of homo-FRET. MD simulations are presented as a useful and complementary tool to the experimental measurements, giving insight in regards to the actual dipole orientation between EGFPs.

The study of the disruption of coxsackievirus and adenovirus receptor (CAR) dimers tagged with GFP, when treated with the Adenovirus Ad5 Fibre-knob (Ad5FK), is investigated via homo-FRET in live and fixed human bronchial epithelial cells (HBEC). Two models are proposed for the interpretation of the time-resolved fluorescence anisotropy data, where steady-state anisotropy results are also presented.

2.3 Materials & Methods

2.3.1 Sample preparation

2.3.1.1 EGFP monomer and dimer in solution

Different mixtures of PBS(X1)/glycerol were made for both monomer and dimer EGFP constructs (Protein Production Facility, King's College London). The flexible linker holding the two EGFP monomers together was formed by 15 aminoacids, GGGGSGGGGSGGGGS, with an approximate length of 6 nm, where *G* and *S* stand for glycine and serine, respectively (Figure 2.1). Each solution contained a total volume of 2 ml, which was divided by two, for each one of the EGFP constructs. The percentage of glycerol per solution was calculated by volume and was as follows: 0, 5, 10, 15, 20, 25, 30, 35, 45 and 50. The initial stock solutions of monomer and dimer in buffer had a molarity of 89 μM, for the monomer, and 33.6 μM, for the dimer. A total of 10 μL per construct solution were mixed with 1 ml of buffer/glycerol, yielding a final concentration of 0.89 μM and 0.336 μM, for monomer and dimer samples, respectively. All the samples were made at room temperature and measured in a 8-well coverslip-bottom plate (ibidi).

2.3.1.2 Cell culture and transfection preparation

The cells used for the experiment were made by **Dr Elena Ortiz-Zapater**. The type of cells are the 16HBE cell line, that is an immortalised human bronchial epithelial (HBE) cell line. It's an easy cell line to grow, so the only recommendations are to use the appropriate growth medium and follow standard cell culture techniques.

16HBE cells were grown in MEM (Sigma M4655) culture medium containing 10% FBS (Fetal Bovine Serum Heat Inactivated – Gibco 10500-064) and 1% antibiotics (penicillin/streptomycin) maintained at 5% CO_2 and 37°C.

16HBE CAR-GFP expressing stable cell lines were produced using lentiviral

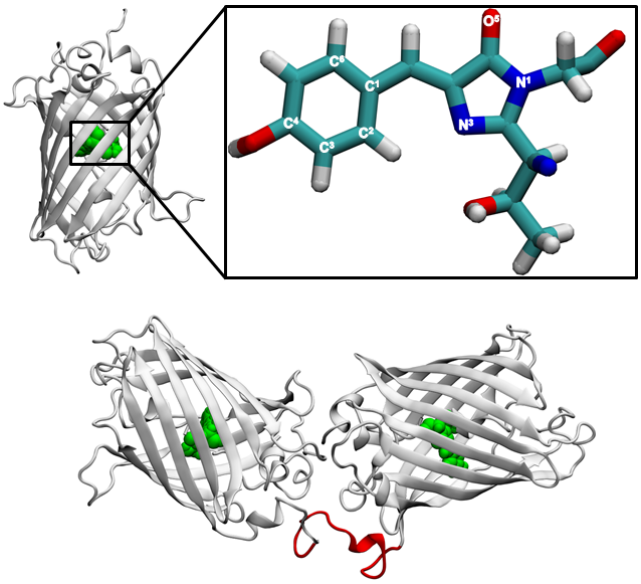

Figure 2.1: Illustration of the dimer configuration plus linker. The chromophore responsible for the fluorescence emission is shown in the enlarged view. The linker joins both proteins and is presented in red.

expression, where CAR stands for coxsackievirus and adenovirus receptor. CAR-GFP lentivirus particles were generated in 293T packaging cells (as in ref [168]) and these cells were maintained in Dulbecco's Modified Eagle Medium (DMEM) containing 10% FBS, supplemented with glutamine. Plasmids encoding full-length CAR have been described previously [173]. Full length CAR-GFP was cloned in frame into pHR9SIN-SEW lentiviral expression vector, which was a gift from Dr Adrian Thrasher (Institute of Child Health, UCL, London [174] and into pGEX-2T.

Cells were plated at high density onto 8-well coverslip-bottom plates (ibidi). 24 hours later, cells were treated with Bovine Serum Albumin (BSA) (control) or with Ad5 Fibre-knob (Ad5FK). Ad5FK was produced and purified as previously described [175] and was used at a final concentration of 100 μg/mL. The fixation of control and Ad5FK cells was undertaken as previously described elsewhere [176]. The CAR-GFP cells were fixed after 3 and 20 min of the adenovirus infection.

2.3.2 Fluorescence Polarisation Equipment

Single fluorescence decays for both intensity transients ($I_{\parallel}$ and $I_{\perp}$) were measured for EGF (monomer and dimer) solutions (from entire field of view) and GFP-CAR samples. The data acquisition for the GFP-CAR samples was focused on the cell-cell junctions with regular straight shapes and no over-expression of the fluorescence protein. A zoom in of the entire Field of View (FOV) of the sample was done and the data was acquired from a region of interest (ROI). Time-resolved fluorescence anisotropy measurements were taken with two TCSPC (Time-Correlated Single Photon Counting) cards (SPC-150 Becker & Hickl) in combination with an inverted confocal microscope (Leica TCS SP2). A schematic of the setup is presented in Figure 2.2. A RSP 500 excitation beam splitter and a 63X 1.2 NA water-immersion objective were used to acquire the data. A 467 nm diode laser (Hamamatsu PLP-10 470) was used for exciting the intensity decays. The laser repetition rate was set to 20 MHz, while the acquisition window on the TCSPC cards was accordingly adjusted to 50 ns. With 4096 time bins and an average laser power in the range of μW, the sample was scanned during 5 minutes in order to collect the integrated parallel and perpendicular intensity decays. The fluorescence emission was sent to the two GaAsP hybrid detectors (Becker & Hickl HPM-100-40). Before getting to the two detectors, the entire emission fluorescence light had to pass through a 514/30 band pass filter and immediately after the orthogonal polarisation components were separated using a polarising beam splitter cube (Edmund Optics). The signal from the detectors was fed into the two TCSPC cards in a PC running Windows 10. Lifetime measurements were performed in the same way but just using a single detector and a single TCSPC card.

All the monomer and dimer EGFP measurements in solution were taken at room temperature. During the acquisition of the GFP-CAR data, a mini-incubator (Digital Pixel) was placed on top of the microscope stage, which was able to keep

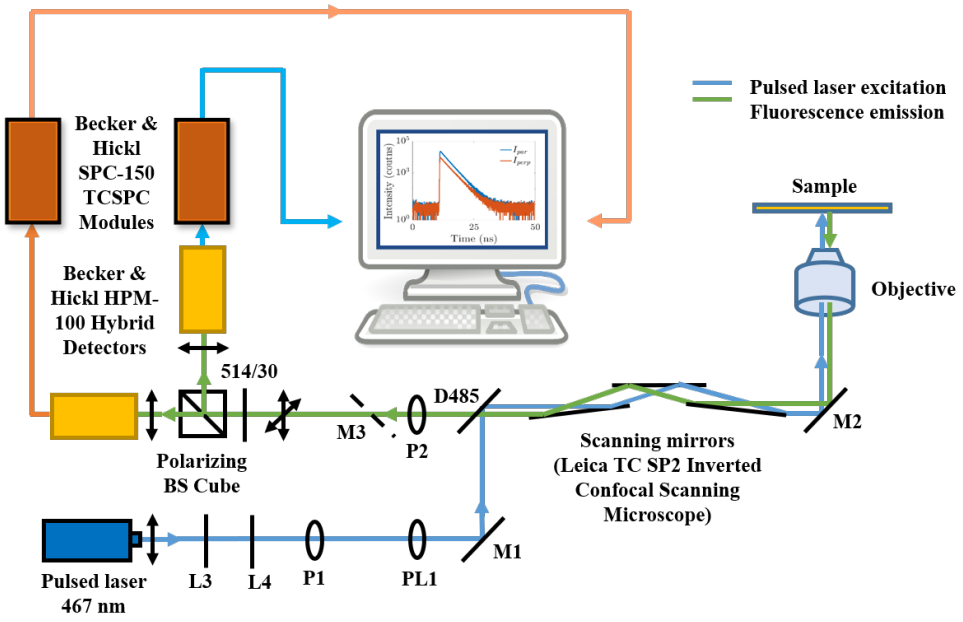

Figure 2.2: Schematic of the time-resolved fluorescence polarisation setup. M stands for mirror, P for pinhole, D for dichroic and PL for polariser.

the temperature and CO_2 levels constant (37°C and 5%, respectively).

The G-factor was measured using a μM solution of fluorescein (FITC) in 90% water and 10% glycerol. The instrument response function (IRF) was also collected by means of a quenched FITC solution in the same water/glycerol proportion. The quencher was sodium iodide (NaI) [108].

2.3.3 Fluorescence Polarisation Data Analysis

The anisotropy data was analysed with a home-built MATLAB script, as was the lifetime data. In order to analyse the anisotropy data, the pair of polarised decays were combined in such way that the time-resolved anisotropy decay was produced by using the following equation [20]:

$$r(t) = \frac{I_{\parallel}(t) - GI_{\perp}(t)}{I_{\parallel}(t) + 2GI_{\perp}(t)} \tag{2.15}$$

where $I_{\parallel}$(t) and $I_{\perp}$(t) are the parallel and perpendicular polarised emission signals, respectively. G is the G-factor. The anisotropy is normalised by the total intensity

detected. If parallel and perpendicular intensity decays are integrated, the steady-state anisotropy r is calculated via equation 1.37.

2.3.3.1 EGFP monomer in solution

For the case of the EGFP monomer, the model used for fitting the time-resolved fluorescence anisotropy decay was as follows:

$$r(t) = r_0 e^{-\frac{t}{\theta}} \tag{2.16}$$

where r_0 is the initial anisotropy determined by the relative orientation between the excitation and emission dipole transition moments, and the distribution of the orientation of the fluorophores. If the distribution is random and the dipole transition moments are parallel to each other, r_0 is equal to 0.4 when using single-photon excitation [20] and no additional depolarisation takes place. The rotational correlation time is given by θ, which corresponds to the time it takes the fluorophore to rotate 1 radian [20]. This model assumes that the protein rotates freely and depolarises totally throughout rotation after excitation within a time window of its fluorescence lifetime.

2.3.3.2 EGFP dimer in solution

For the EGFP dimer, two models for the fit of the anisotropy data were proposed:

1. **Bi-exponential**

   The bi-exponential model assumes that the depolarisation within the first excited state occurs via rotation and homo-FRET (as the two proteins are identical). Thus, this model allows the distinction of two different depolarisation pathways, rotation and FRET, via two exponential components:

$$r(t) = r_{01} e^{-\frac{t}{\theta}} + r_{02} e^{-\frac{t}{\phi}} \tag{2.17}$$

where r_{01} and r_{02} are the initial anisotropy values for each component. The rotational correlation time is given by θ (related to the tumbling of the protein) and ϕ=$\frac{1}{2k_T}$, where k_T is the FRET rate constant [79, 165, 177].

The FRET energy efficiency was calculated combining the FRET rate constant k_T with equations 1.42 and 1.45.

2. **Stretched exponential**

Equations 2.6 and 2.14 were applied to fit the time-resolved fluorescence anisotropy data and calculate the FRET energy efficiency, respectively.

The GFP-CAR time-resolved fluorescence anisotropy data was fitted with a **hindered rotation** (equation 1.36) and **stretched exponential** models. When the hindered rotation model was applied, the anisotropy depolarisation due to the exponential term was assumed to be purely related to FRET. No rotation was considered to take place.

All the time-resolved fluorescence anisotropy data fits were weighted using the variance expression for the steady-state anisotropy derived by Lidke et al. [128]:

$$v(r) = \frac{(1-r)(1+2r)(1-r+G(1+2r))}{3I_{tot}(t)} \tag{2.18}$$

where $I_{tot}(t)$ corresponds to the total emission intensity being equal to $I_{\parallel}(t)$ + $2GI_{\perp}(t)$.

Now, if the polarised intensity components are arranged such as the denominator of equation 2.15, the total intensity decay is generated. The total intensity decays were IRF deconvoluted and fitted with a double exponential model, such as:

$$I_{tot}(t) = I_{01}e^{-\frac{t}{\tau_1}} + I_{02}e^{-\frac{t}{\tau_2}} \tag{2.19}$$

where I_{01} and I_{02} are the intensity amplitudes related to τ_1 and τ_2, which are the

fluorescence lifetimes associated with two different excited states.

The intensity-weighted average lifetime was calculated as follows:

$$\tau_{avg} = \frac{\sum_{j=1}^{N} a_j \tau_j^2}{\sum_{j=1}^{N} a_j \tau_j} \tag{2.20}$$

where a_j corresponds to the intensity amplitude and τ_j to the lifetime associated with a different excitation state. N accounts for the number of components, which is N = 2 for our case.

2.3.4 Refractive Index Measurements

The refractive index of each buffer/glycerol solution was measured using an Abbe refractometer. A lamp (visible range) was used and the system was calibrated with water, whose value is very well known [178]. The readings were modified according to the reference given by the water refractive index and were all taken at room temperature. For each solution, five readings were taken (up to 4 decimals), yielding a final average with a low standard deviation.

2.3.5 Fluorescence Recovery After Photobleaching (FRAP) Equipment

For performing confocal FRAP, the same confocal microscope and objective were used. A simplified diagram of the setup is shown in Figure 2.3. The 467 nm diode laser (Hamamatsu PLP-10 470) was used for taking the pre- and post-bleach images. A solid-state CW laser at 473 nm with a power of $\sim$ 5 mW, was used for bleaching the sample by digitally zooming 8 times the initial field of view. The first laser was set to a repetition rate of 20 MHz and an average power of a few μWs to lower the unintentional bleaching as much as possible. After excitation, the fluorescence emission reached the photomultiplier inside the scanhead of the microscope by passing through a pinhole which was completely open. The advanced time-lapse wizard from the confocal microscope software allowed the acquisition of 3 pre-

bleach images, a single bleach image and a series of post-bleach images showing the full recovery of the bleached area. The total number of images taken was approximately 100, taking around 3-4 minutes to acquire. All the measurements were taken at room temperature.

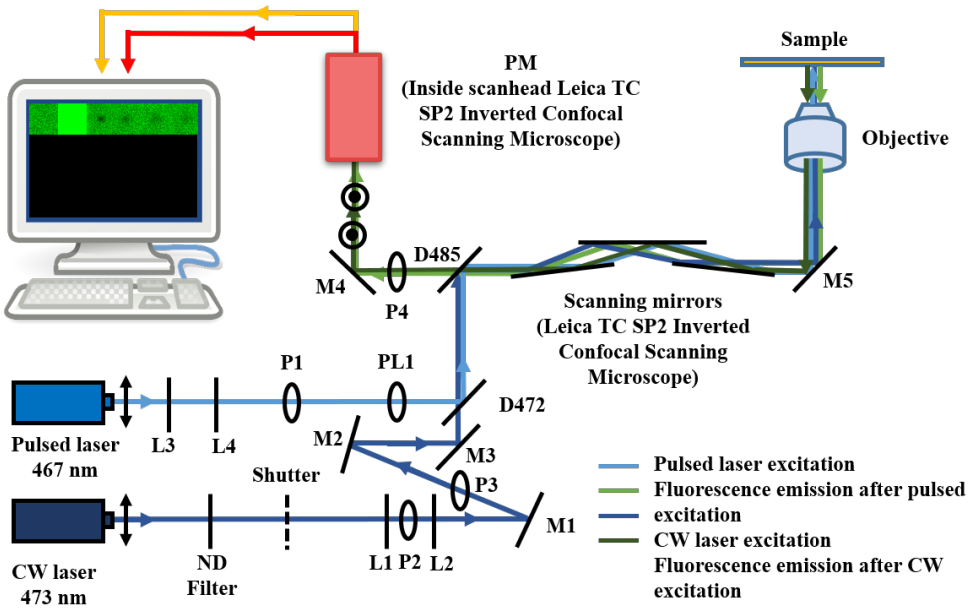

Figure 2.3: Schematic of the confocal FRAP setup. M stands for mirror, P for pinhole, D for dichroic, L for lens, PM for photomultiplier, ND for neutral density (filter) and PL for polariser.

2.3.6 FRAP Data Analysis

For the FRAP data analysis, the bleach area of every post bleach image was masked automatically by introducing the zoom factor as an input ($\times 8$) and its intensity was averaged in order to get the FRAP recovery curve over time. Unintentional bleaching was considered by normalising the ROI intensity by masking another ROI far enough from the the bleached area. The FRAP recovery curve was fitted (non-linear least squares) with a double exponential model and the half-recovery time $\tau_{1/2}$ was extracted by extrapolating the timing at half height.

$$I(t) = a - be^{-ct} - de^{-ft} \tag{2.21}$$

where *a, b, c, d* and f are constants, $I(t)$ is the normalised intensity and t the time after bleaching.

The mobile fraction was calculated applying the Soumpasis normalisation method [93]. In order to obtain the translational diffusion coefficient, the Stokes-Einstein-Debye behaviour was assumed:

$$D_t = \frac{(L/2)^2}{4\tau_{1/2}} = \frac{k_B T}{6\eta\pi R_h} \tag{2.22}$$

where L represents the minimum distance from the centre of the bleach rectangle to the edge of the bleach area [132] and R_h is the hydrodynamic radius of the probe.

As the data was obtained by scanning the sample, the bleaching step cannot be considered instantaneous and therefore there is some diffusion occurring during the bleaching. This is taken into consideration by introducing an additional parameter r_e, which stands for the effective radius of a postbleach profile. It accounts for the half width at the approximately 14% of bleaching depth from the top. Thus, equation 2.22 is converted into [96]:

$$D_t = \frac{(L/2)^2 + r_e^2}{8\tau_{1/2}} = \frac{k_B T}{6\eta\pi R_h} \tag{2.23}$$

In order to extract r_e, the initial postbleach image was normalised by the last prebleach image. Several profiles of the normalised bleach area were performed and an average or the cleanest profile is extracted. This depends on how efficient the bleaching is. A fit was performed on this average and r_e along the bleach depth K is extracted. The fit has the following shape [96]:

$$I(l) = 1 - Ke^{(-l^2/r_e^2)} \tag{2.24}$$

where $I(l)$ is the normalised intensity, K is the bleaching-depth parameter and l

refers to the dimensions of the bleach spot profile in μm.

Once r_e is calculated and thus the translational diffusion coefficient D_t, equation 2.23 can be rewritten as follows:

$$R_h = \frac{k_b T}{6\eta\pi D_t} \tag{2.25}$$

Therefore, the hydrodynamic radius of the probe can be calculated from its lateral mobility information.

2.3.7 Polarisation-Resolved Excitation and Emission Spectra

In order to investigate the anisotropy response of both EGFP constructs at the red-edge, steady-state anisotropy measurements of monomer and dimer in buffer/glycerol mixtures were carried out using a luminescence spectrometer (Perkin-Elemer LS-5) with cuvette (quartz) supported samples. Two polarisers were located in two different positions: between the excitation source and the sample and between the sample and the emission detector. The different configuration of the two polarisers allowed the acquisition of four different measurements: $I_{VV}(\lambda)$,$I_{VH}(\lambda)$,$I_{HH}(\lambda)$ and $I_{HV}(\lambda)$, where V refers to the vertical and H to the horizontal polarisation subscripts for excitation and emission polarisations. The steady state anisotropy measurements were taken from λ_{exc} = 350 nm to λ_{exc} = 520 nm, in 2 nm steps. The emission detection was set to 530 nm. The data analysis was carried out as described by others [179].

2.3.8 Molecular Dynamic Simulations

As part of a collaboration with **Professor Molteni**, **PhD student Alessandro Crnjar** carried out MD simulations of EGFP, monomer and dimer, in water. The objective was to find theoretical justification/evidence for either the bi-exponential or stretched-exponential model of EGFP dimer time-resolved fluorescence anisotropy. The analysis and interpretation of the data was done by myself and Professor Suh-

ling.

MD simulations were carried out for the EGFP monomer and dimer in water at T = 300 K and P = 1 bar. The EGFP construct was created from the X-ray structure at 1.9 Å resolution. For the dimer, a linker of 15 aminoacids (SGGGGSGGGGSGGGGS) was generated, which allowed keeping both monomers attached. The letters S and G refer to glycine and serine aminoacids, respectively. The total number of atoms for the monomer was 29922. The AMBER ff14sb force-field was used to study the dynamics of both constructs in 10 ps time steps. The FRET efficiency was obtained by extracting the relative dipole orientation between constructs, κ^2, and their separation, R. Equation 1.44 is introduced in equation 1.45, which yields the following E_{FRET} expression:

$$E_{FRET} = \frac{1}{\left(\frac{R}{R_0}\right)^6 + 1} = \frac{1}{\left(\frac{R}{0.02108}\right)^6 \frac{1}{\kappa^2 n^{-4} Q_D J(\lambda)} + 1} \tag{2.26}$$

κ^2 is defined as follows:

$$\kappa^2 = ((\vec{D} \cdot \vec{A}) - 3(\vec{D} \cdot \vec{R})(\vec{A} \cdot \vec{R}))^2 \tag{2.27}$$

where $\vec{D}$ and $\vec{A}$ are the transition dipole moments of the donor and acceptor chromophores, respectively, and $\vec{R}$ is the distance between the two chromophores, calculated as the average of four vectors linking the coordinates of the donor and acceptor surrogate GFP benzylidene C^1 and C^2 and imidazolone N^3 and C^4 atoms within the fluorophores [180] (Chapter2/Figure 2.1).

For the EGFP, the transition dipole moment has been defined as the normalised average of the vector that connects atoms C^6 and O^5, and the one that connects atoms C^3 and N^1 [180] (Figure 2.1).

The simulated time-resolved anisotropy decays for monomer and dimer where

also extracted by calculating their transition dipole moments and relative orientations. The simulated time-resolved anisotropy decay associated with the dimer was given by an average of the two monomers. The anisotropy finds geometrical interpretation in the Auto-Correlation Function (ACF) of the transition dipole moment [38, 181–184], which is defined as a single unit vector for each chromophore:

$$r(t) = \frac{2}{5}\left\langle \frac{3(\vec{\mu}(t_0)\cdot\vec{\mu}(t_0+t))^2}{2} - \frac{1}{2}\right\rangle_{t_0} \tag{2.28}$$

where $\vec{\mu}(t)$ is a given transition dipole moment as a function of time, and the brackets mean an average over every possible starting time t_0. A discreet version of equation 2.28, that can be implemented for the post-production of a simulation trajectory, is given by:

$$r(t) \approx \frac{2}{5}\frac{1}{T-t}\sum_{t'=0}^{T-1-t}\frac{3(\vec{\mu}(t')\cdot\vec{\mu}(t'+t))^2-1}{2} \tag{2.29}$$

where T is equal to the number of time steps in the trajectory. For the given chromophore, $\vec{\mu}$ is given as the normalised average of the the vector that connects atoms C^6 and O^5, and the one that connects atoms C^3 and N^1 (Figure 2.1) [180].

The MD simulations were run for 500 ns, which were truncated into 10 trajectories of 50 ns each. This allowed better statistics. The ACF can be then computed on the last 9 trajectories and averaged. The first trajectory is discarded as it is effected by the initial system equilibration.

The water molecules in this simulation were behaving according to model TIP3P [185]. The TIP3P model was chosen because it yields accurate values for the rotational correlation time θ, although it is inaccurate in the modelling of water viscosity [186, 187]. Nevertheless, useful results can be obtained for the rotational correlation time θ. Using θ, the rotational diffusion coefficient can be calculated if

a Stokes-Einstein-Debye behaviour is considered:

$$D_{r,sphere} = \frac{1}{6\theta} = \frac{k_B T}{8\eta\pi R_h^3} \tag{2.30}$$

where k_B is the Boltzmann constant, T the absolute temperature, η the viscosity and R_h the hydrodynamic radius of the fluorophore.

2.4 Results and discussion

2.4.1 The EGFP Fluorescence Lifetime Versus Environmental Refractive Index

Here I describe how I verified that the fluorescence lifetime is almost the same for both EGFP monomer and dimer in identical environmental conditions.

For the data analysis of the fluorescence lifetime, each intensity decay has been fitted with two components, as a mono-exponential model did not fit well, in terms of residuals and χ_R^2 (χ_R^2 >1.75). This lies in the fact that EGFP involves complex photophysics related to proton transfer kinetics [158], and therefore multi-exponential models have been proposed for the fitting of its intensity decay [158, 188]. In our case, when illuminating the sample with blue light (467 nm), two components are identified, which are associated to two different excited states identified in the absorption spectrum [158, 189]. In Figure 2.4A and B two representative intensity decays for monomer and dimer in solution in 25% glycerol are presented, collecting around 10,000 counts at the peak. Two fluorescence lifetimes are assigned for each one of the constructs: 2.04 ns (39.26%) and 2.77 ns (60.74%) for the monomer; 2.07 ns (43.61%) and 2.74 ns (56.39%) for the dimer. The χ_R^2 resultant from the fits are 1.17 and 1.07, respectively.

The Strickler-Berg formula (equation 1.7) was validated by plotting the inverse fluorescence lifetime of each of the construct against the square of the environmen-

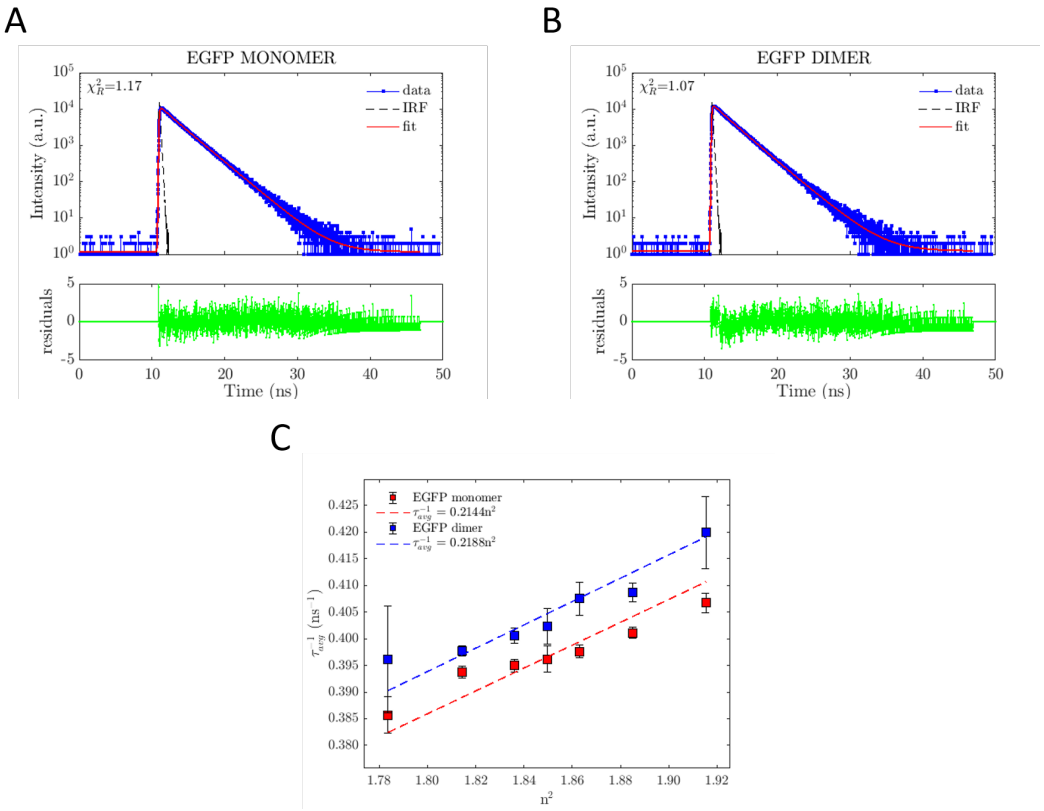

Figure 2.4: Representative total intensity decays for (A) monomer and (B) dimer, in a solution of 25% glycerol. For each plot, the data is presented along the IRF, fit and residuals. (C) Inverse of the average fluorescence lifetime against the square of the refractive index, per solution and EGFP construct. The data for both constructs is fitted showing a linear relationship as established by the Strickler-Berg law.

tal refractive index n^2 (Figure 2.4C). It has been reported that the relative quantum yield of EGFP in different solvents has almost no effect on the fluorescence lifetime [29]. Therefore, the relationship between the fluorescence lifetime and the refractive index of the environment can be considered to follow the same expression (equation 1.7). The EGFP dimer fluorescence lifetime is consistently lower than the monomer fluorescence lifetime in all solutions with different refractive index (Table 2.1). This decrease in the lifetime may be assigned to an effective greater environmental refractive index due to the presence of the other EGFP monomer and the flexible linker that maintains both EGFP monomers connected.

It is important to mention that although we can observe a difference in lifetime

between monomer and dimer, the percentage difference is around 1%, which makes this effect almost negligible and allows the assignment of identical fluorescence lifetimes for both constructs as a good approximation.

Table 2.1: Average fluorescence lifetime and inverse, for EGFP monomer and dimer, per refractive index and viscosity composition sample.

			EGFP monomer			**EGFP dimer**		
% glycerol	**n ± 0.0005**	$n^2 \pm$ **0.0008***	τ_{av} (ns)	χ^2_R	τ_{av}^{-1} (ns^{-1})	τ_{av} (ns)	χ^2_R	τ_{av}^{-1} (ns^{-1})
0	1.3355	1.7836	2.593 ± 0.023	1.34	0.3857 ± 0.0034	2.524 ± 0.064	1.42	0.3961 ± 0.0100
5	1.3470	1.8144	2.540 ± 0.007	1.34	0.3938 ± 0.0011	2.515 ± 0.006	1.26	0.3977 ± 0.0010
10	1.3550	1.8360	2.531 ± 0.007	1.30	0.3950 ± 0.0012	2.496 ± 0.009	1.42	0.4006 ± 0.0014
15	1.3600	1.8496	2.524 ± 0.015	1.29	0.3962 ± 0.0024	2.486 ± 0.020	1.08	0.4023 ± 0.0033
20	1.3650	1.8632	2.515 ± 0.008	1.25	0.3976 ± 0.0012	2.454 ± 0.019	1.28	0.4075 ± 0.0031
25	1.3730	1.8851	2.493 ± 0.006	1.26	0.4011 ± 0.0010	2.447 ± 0.010	1.17	0.4087 ± 0.0017
30	1.3840	1.9155	2.459 ± 0.011	1.17	0.4067 ± 0.0019	2.382 ± 0.038	1.19	0.4199 ± 0.0067

$^{*}\Delta n^2 = \sqrt{2n}\,\Delta n$

Presented errors are associated to standard deviations of average values

2.4.2 Time-Resolved Fluorescence Anisotropy Measurements

The anisotropy behaviour of monomer and dimer EGFP constructs in solution was investigated and compared. For each solution in buffer/glycerol and EGFP construct, a total of 10 anisotropy decays was acquired.

2.4.2.1 EGFP monomer and dimer time-resolved fluorescence anisotropy decays

Figure 2.5 presents the time-resolved fluorescence anisotropy decays per EGFP construct and solution viscosity. It demonstrates how the time-resolved fluorescence anisotropy decays for the monomer follow a single exponential model. In the case of the dimer, a mono-exponential decay model is inappropriate and more components are needed to fit the anisotropy decay. This is in agreement with work done on similar constructs [142]. The reason lies in the fact that during the excited state the EGFP dimer experiences FRET, meanwhile the only way the EGFP monomer depolarises is via rotation. The FRET effect can be clearly seen at the beginning of the EGFP dimer time-resolved fluorescence anisotropy decay as a very fast and short component. Therefore, the EGFP dimer time-resolved fluorescence

anisotropy decay do not follow a single exponential behaviour. In order to interpret the EGFP dimer anisotropy decays, two models have been proposed for their fits: *bi-exponential and stretched exponential*. Both models assume that the depolarisation of each one of the proteins is total and that the protein configuration is totally isotropic and randomised, without any preferential direction within the solution.

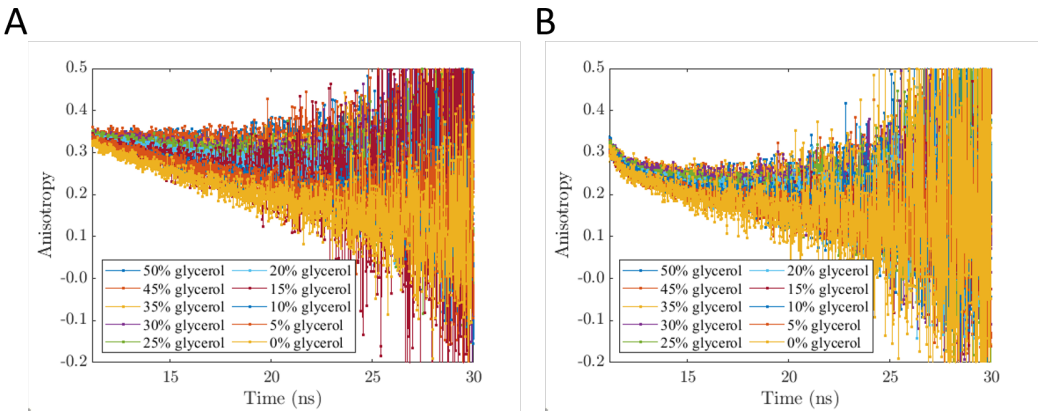

Figure 2.5: Time-resolved anisotropy decays in different PBS(X1)/glycerol mixtures for (A) EGFP monomer and (B) EGFP dimer.

2.4.2.2 Comparison of EGFP monomer and dimer rotational correlation times

In Figure 2.6A and B, two representative intensity decays for the parallel and perpendicular components, per EGFP construct and for the same PBS(X1)/glycerol solution, are shown. Representative time-resolved fluorescence anisotropy decays for monomer and dimer in 10% glycerol and 90% buffer along with their fits are presented in Figure 2.6. The fit for the anisotropy data of the monomer can be observed in the middle graph (Figure 2.6C). It follows a single exponential model with no baseline. This model assumes that the protein undergoes total depolarisation after a certain time. On the other hand, the dimer anisotropy data is fitted with the aforementioned models (Figure 2.6D and E). The residuals of both fits are almost identical, leading to very similar χ_R^2 values. Therefore, both models give the same answer in terms of goodness of fit, while the bi-exponential model implies an

additional parameter in comparison to the stretched exponential model. The EGFP dimer tr-anisotropy decay was also fitted with the hindered rotation model, however the fit was poor, implying it did not represent the data well.

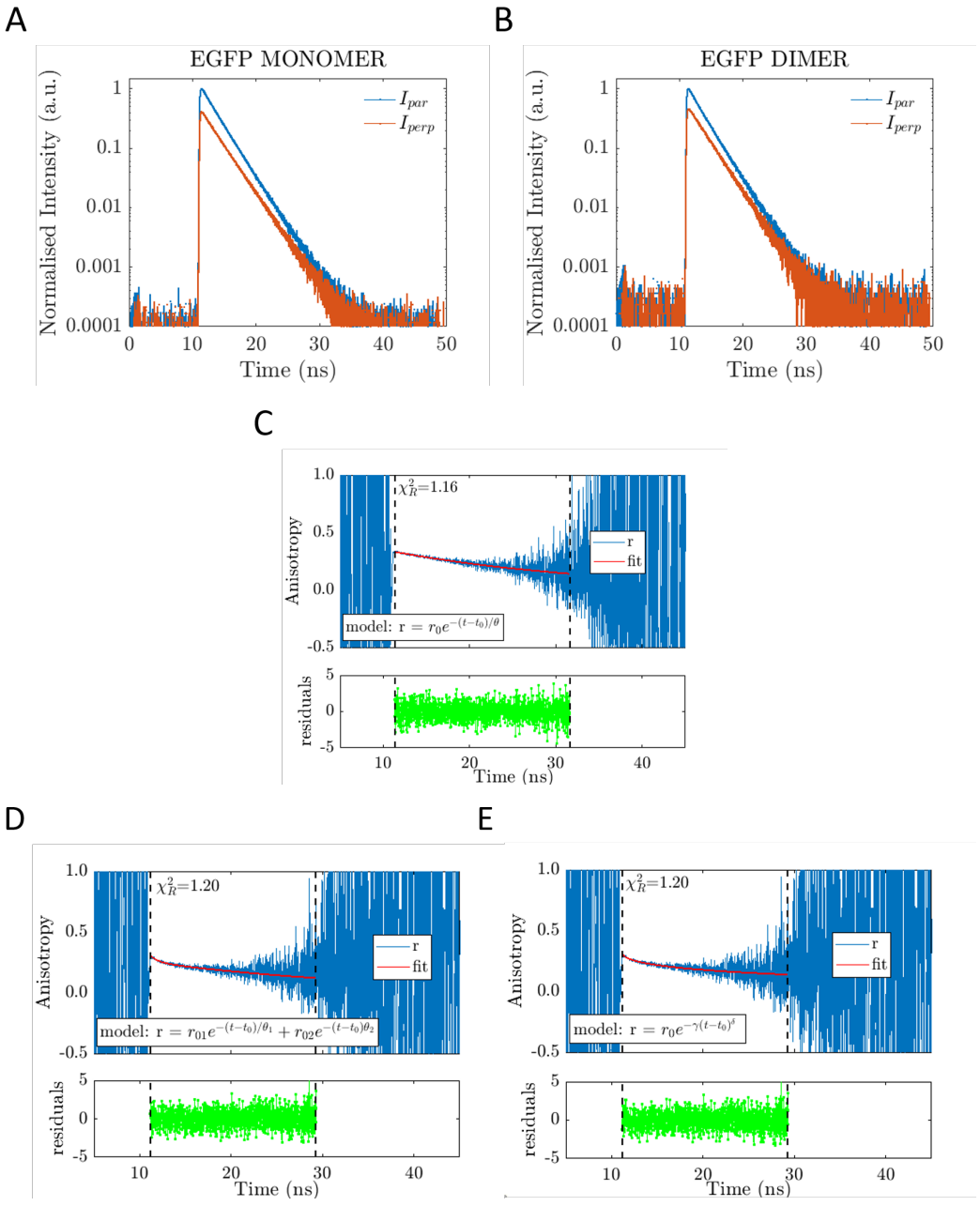

Figure 2.6: (A,B) Representative $I_{\parallel}$ and $I_{\perp}$ for monomer and dimer. (C) Representative time-resolved fluorescence anisotropy decay and fit for the EGFP monomer with a mono-exponential model. Time-resolved fluorescence anisotropy decay for EGFP dimer and fitted with a (D) double and (E) stretched exponential models. The solvent is 10% glycerol and 90% buffer.

The viscosity of each of the solutions was calculated by a method developed by Nian-Sheng Cheng [190], which takes into account the water/glycerol ratio of the solution and its temperature. We assumed the buffer viscosity was identical to water. The rotational correlation times obtained from the single and bi-exponential models, for monomer and dimer, are plotted against the solution viscosity (Figure 2.7A). Also, a decrease in the initial anisotropy value due to FRET depolarisation is noticeable in the dimer data only (Figure 2.7B).

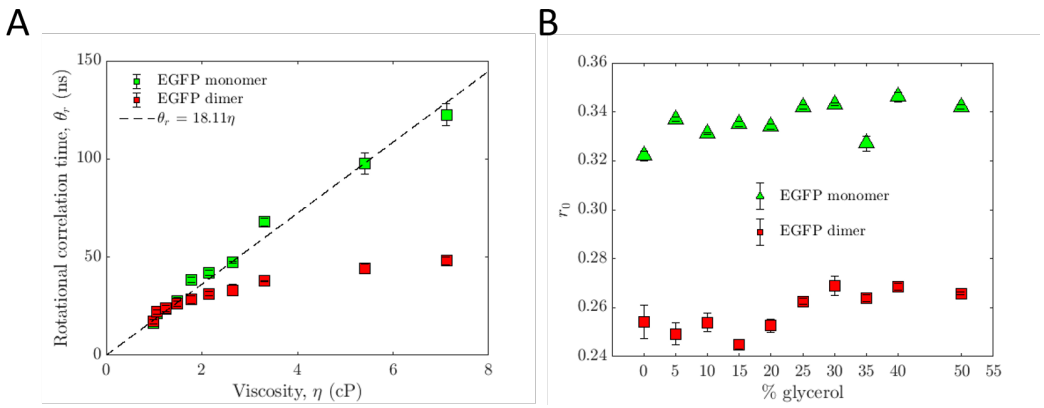

Figure 2.7: (A) Rotational correlation time against viscosity for monomer and dimer. The monomer data is fitted with a linear equation, which gives rise to a radius for the monomer of 2.607 $\pm$ 0.005 nm. (B) Initial anisotropy values for monomer and dimer extracted from the single exponential and bi-exponential fits.

The monomer data shows that the higher the viscosity is, the slower it rotates on average, which is in agreement with equation 2.30. Its data can be fitted with a linear expression, related to equation 2.30, from which the hydrodynamic radius of the protein can be extracted. The result we obtained is R_h = 2.457 $\pm$ 0.005 nm, where the uncertainty associated with this magnitude was obtained by error propagation from the uncertainty of the fit gradient ($\pm$ 0.91 ns/cP). The fit passes through the origin as expected from equation 2.30. This is in good agreement with other values previously reported [191, 192]. All the fit parameters are presented in Table 2.2.

The rotational correlation time of the dimer EGFP construct follows a similar

Table 2.2: Fit parameters from anisotropy decay per EGFP monomer sample composition.

% **glycerol**	η **(cP)**	r_0	θ **(ns)**	χ_R^2
0	0.981	0.322 ± 0.002	16.46 ± 0.20	1.15
5	1.064	0.337 ± 0.001	21.42 ± 0.42	1.18
10	1.249	0.331 ± 0.000	23.36 ± 0.26	1.20
15	1.482	0.335 ± 0.010	27.60 ± 2.00	1.17
20	1.776	0.334 ± 0.001	38.60 ± 1.34	1.11
25	2.154	0.342 ± 0.001	41.90 ± 1.46	1.13
30	2.648	0.343 ± 0.000	47.39 ± 0.55	1.17
35	3.302	0.327 ± 0.003	67.89 ± 2.00	1.12
45	5.410	0.346 ± 0.002	97.62 ± 5.55	1.13
50	7.128	0.342 ± 0.001	122.56 ± 5.52	1.19

trend. However, it shows a lower rotational correlation time in comparison to the monomer and maintains a lower slope compared to the monomer. The rotational correlation time θ becomes nearly constant for viscosities above 5 cP, approximately. In the simple model accounting only for Brownian rotational motion, this would imply that the dimer has faster rotation and thus smaller gyration radius compared to the monomer. This is obviously incorrect and therefore a model accounting only for FRET is applied via the stretched exponential function. Note that the FRET parameter ϕ presents no correlation with viscosity. The initial anisotropy values r_0 associated with the FRET component are approximately constant throughout the varying viscosity samples (Figure 2.8A).

2.4.2.3 Stretched exponential fit parameters

From the fitting of the EGFP dimer time-resolved fluorescence anisotropy decays with a stretched exponential function (last term of equation 2.6), the fit parameters r_0 and γ were extracted. The behaviour of these parameters for varying viscosity solutions can be observed in Figure 2.8B. The initial anisotropy r_0 presents no correlation with the solution viscosity. However, the parameter γ decreases with an increase in the viscosity of the solution. In Table 2.3 all the fit parameters extracted from the bi-exponential and stretched exponential functions are presented.

Table 2.3: Fit parameters from anisotropy decay per EGFP dimer sample composition and anisotropy model.

	Bi-exponential					Stretched exponential		
% glycerol	r_{01}	θ (ns)	r_{02}	ϕ (ns)	χ^2_R	r_0	γ	χ^2_R
0	0.254 ± 0.007	17.16 ± 1.06	0.047 ± 0.003	0.51 ± 0.05	1.15	0.311 ± 0.002	0.229 ± 0.012	1.17
5	0.249 ± 0.004	22.12 ± 1.20	0.054 ± 0.000	0.77 ± 0.11	1.20	0.315 ± 0.005	0.211 ± 0.005	1.21
10	0.254 ± 0.004	23.94 ± 1.63	0.054 ± 0.006	0.78 ± 0.23	1.20	0.316 ± 0.004	0.198 ± 0.008	1.22
15	0.245 ± 0.002	26.35 ± 1.29	0.050 ± 0.006	0.74 ± 0.11	1.20	0.302 ± 0.003	0.185 ± 0.006	1.21
20	0.253 ± 0.003	28.40 ± 2.08	0.053 ± 0.005	0.70 ± 0.13	1.15	0.310 ± 0.003	0.177 ± 0.007	1.17
25	0.263 ± 0.001	31.30 ± 1.16	0.055 ± 0.004	0.76 ± 0.09	1.16	0.321 ± 0.002	0.168 ± 0.003	1.17
30	0.269 ± 0.004	33.10 ± 2.99	0.045 ± 0.003	0.68 ± 0.17	1.12	0.317 ± 0.002	0.147 ± 0.003	1.14
35	0.264 ± 0.001	37.86 ± 0.23	0.045 ± 0.002	0.78 ± 0.04	1.16	0.313 ± 0.004	0.140 ± 0.004	1.16
45	0.267 ± 0.001	44.01 ± 2.37	0.044 ± 0.004	0.72 ± 0.04	1.14	0.313 ± 0.002	0.125 ± 0.004	1.18
50	0.266 ± 0.000	48.15 ± 1.96	0.042 ± 0.003	0.75 ± 0.15	1.13	0.310 ± 0.002	0.120 ± 0.004	1.18

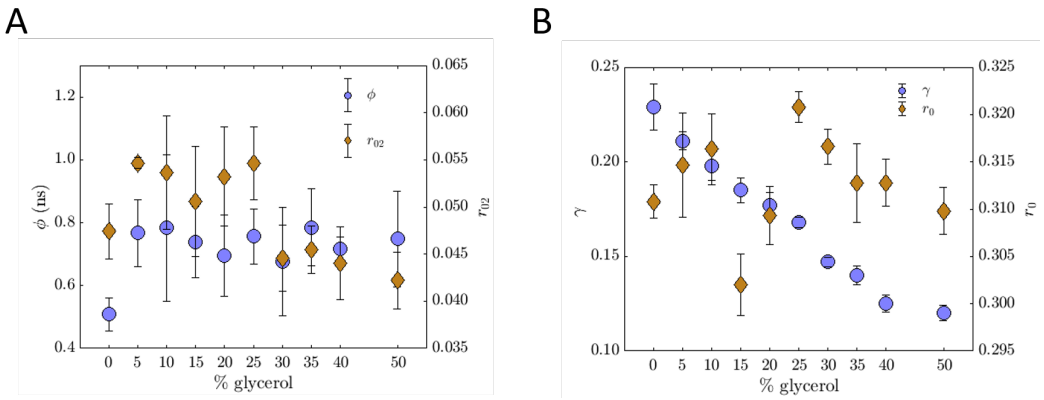

Figure 2.8: Anisotropy decay parameters against sample composition (% glycerol) calculated from two different models: (A) bi-exponential and (B) stretched exponential model.

Note that the parameter δ is fixed to 0.5, accounting for a 3-dimensional system. However, δ can be set and calculated as an additional fit parameter. This was investigated and presented in Figure 2.9A, where the fit parameter δ is plotted against the solution viscosity and fitted with a linear expression. From this expression, the gradient and intercept were obtained, 0.02094 (1/cP) and 0.5594, respectively. The low gradient and close intercept to the theoretical value 0.5 (blue line in Figure 2.9A) indicate that the assumption of a 3-dimensional system is in agreement with the experimental results.

According to equation 2.7, the fit parameter γ depends on the molecule concentration c and the fluorescence lifetime τ. Introducing the EGFP monomer fluorescence lifetime τ within the expression 2.7 and knowing γ (both determined exper-

imentally), the dimensionless molecule concentration c was calculated and plotted against the solution viscosity in Figure 2.9B. Very similar molecule concentrations c were obtained for free and fixed δ values, showing a decrease with the solution viscosity. The same trend is followed by the FRET energy efficiency, when equation 2.14 is applied (Figure 2.9C). Table 2.4 presents all the parameters involved in the elaboration of Figure 2.9. We previously demonstrated that the experimental fit parameter δ was very close to the theoretical one (0.5). Thus, only the fit parameters calculated with $\delta = 0.5$ will be subject of any further data analysis in the current and upcoming sections.

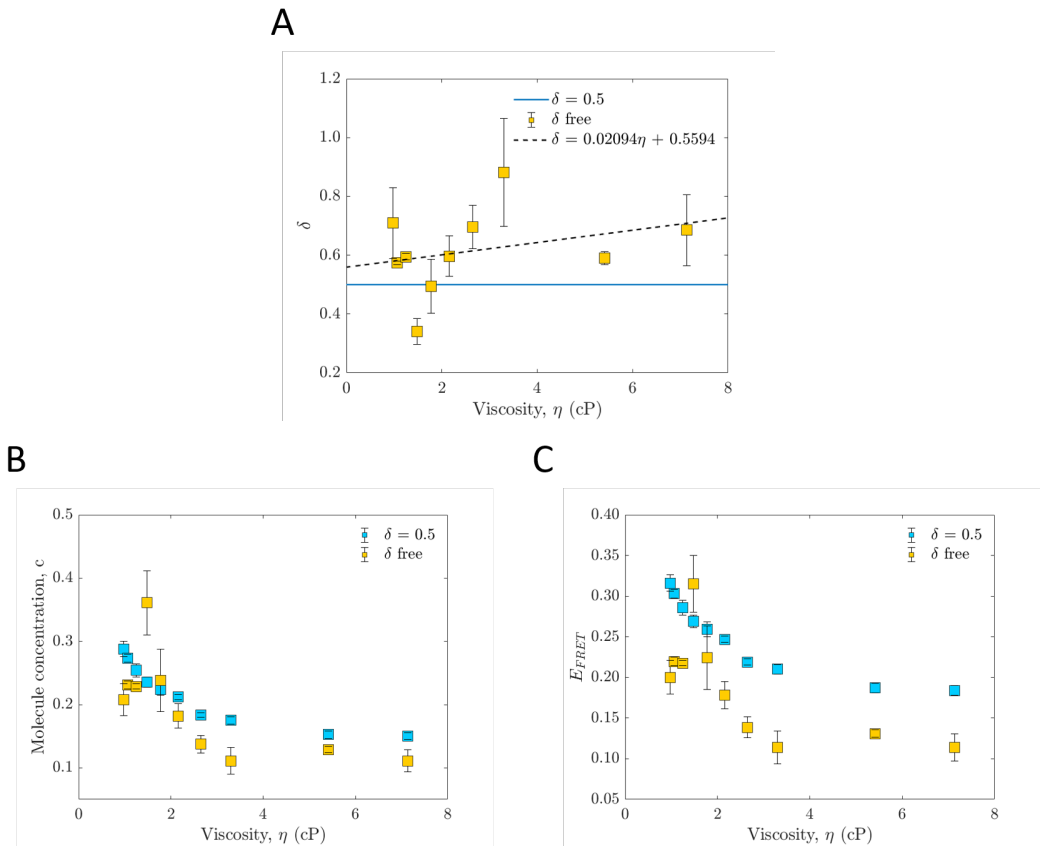

Figure 2.9: Stretched exponential model fit parameters and extracted values. (A) δ, (B) molecule concentration c and (C) E_{FRET} against viscosity's solution.

Theoretically, we expect the molecule concentrations c and thus the E_{FRET} to remain constant across the varying solution viscosities. However, we have seen that

Table 2.4: Fit parameters from stretched exponential anisotropy decay fit per EGFP dimer solution viscosity, with $\delta = 0.5$ and free. The EGFP fluorescence lifetime is given by the third column.

			δ=1/2			δ free			
% glycerol	η (cP)	τ_D (ns)	γ (ns$^{-1/2}$)	c	E_{FRET}	δ	γ (ns$^{-\delta}$)	c	E_{FRET}
0	0.981	2.647 ± 0.008	0.229 ± 0.012	0.297 ± 0.012	0.316 ± 0.010	0.710 ± 0.120	0.121 ± 0.030	0.208 ± 0.025	0.200 ± 0.021
5	1.064	2.625 ± 0.004	0.211 ± 0.005	0.273 ± 0.006	0.303 ± 0.005	0.575 ± 0.006	0.166 ± 0.006	0.231 ± 0.007	0.219 ± 0.005
10	1.249	2.598 ± 0.003	0.198 ± 0.008	0.254 ± 0.010	0.286 ± 0.009	0.595 ± 0.012	0.162 ± 0.005	0.229 ± 0.004	0.217 ± 0.003
15	1.482	2.560 ± 0.035	0.185 ± 0.006	0.236 ± 0.008	0.269 ± 0.008	0.340 ± 0.043	0.330 ± 0.058	0.361 ± 0.051	0.315 ± 0.035
20	1.776	2.520 ± 0.020	0.177 ± 0.007	0.224 ± 0.009	0.259 ± 0.009	0.495 ± 0.091	0.192 ± 0.056	0.238 ± 0.050	0.217 ± 0.003
25	2.154	2.513 ± 0.030	0.168 ± 0.003	0.212 ± 0.004	0.247 ± 0.004	0.596 ± 0.069	0.132 ± 0.022	0.182 ± 0.019	0.315 ± 0.035
30	2.648	2.459 ± 0.021	0.147 ± 0.003	0.184 ± 0.004	0.219 ± 0.004	0.696 ± 0.074	0.093 ± 0.016	0.137 ± 0.014	0.224 ± 0.039
35	3.302	2.472 ± 0.010	0.140 ± 0.004	0.175 ± 0.006	0.210 ± 0.006	0.881 ± 0.184	0.064 ± 0.020	0.111 ± 0.021	0.178 ± 0.017
45	5.410	2.386 ± 0.010	0.125 ± 0.004	0.153 ± 0.006	0.187 ± 0.006	0.590 ± 0.022	0.095 ± 0.005	0.129 ± 0.005	0.138 ± 0.013
50	7.128	2.411 ± 0.020	0.120 ± 0.004	0.153 ± 0.005	0.184 ± 0.006	0.685 ± 0.120	0.076 ± 0.016	0.111 ± 0.002	0.114 ± 0.020

this is not the case (Figure 2.9B and C). We investigated the effect of the refractive index n on the molecule concentration c via the quantum yield Φ. The quantum yield Φ_i of the PBS(X1)/glycerol solution mixtures was calculated setting Φ_1 = 0.60 for 0% glycerol as a reference. We have seen in *Section* 1.1.6 that the quantum yield is given by the product of the fluorescence lifetime τ and the radiative lifetime k_r:

$$\Phi = \tau k_r \tag{2.31}$$

According to the Strickler-Berg formula (equation 1.7), the radiative lifetime k_r is proportional to the square of the solution refractive index n^2. If we define the proportionality constant as k_r^0, for each solution viscosity, equation 2.31 can be rewritten as follows:

$$k_r = n^2 k_r^0 \longrightarrow \Phi_i = \frac{n_i^2 k_r^0}{n_i^2 k_r^0 + k_{nr}} \tag{2.32}$$

where k_{nr} is the the non-radiative rate constant.

We consider k_{nr} and k_r^0 to remain constant across the varying solution viscosities and we determine their values for the 0% glycerol solution (Φ_1 = 0.60 and τ = 2.647 ns). The result is as follows:

$$k_r^0 = 0.1272 \pm 0.0004\ ns^{-1}\ and\ k_{nr} = 0.151 \pm 0.001\ ns^{-1} \tag{2.33}$$

Now, starting from the experimental molecule concentration c_1 for 0% glyc-

erol, the rest of the molecule concentrations c_i are determined via their ratio. Combining equations 1.44 and 2.5, the molecule concentration c_i per PBS(X1)/glycerol solution mixture is given by:

$$c_i = c_1 \left(\frac{n_1}{n_i}\right)^2 \left(\frac{\Phi_i}{\Phi_1}\right)^{1/2} \tag{2.34}$$

The corrected Φ and c are presented in Table 2.5, with the experimental c for comparison. We can see that the correction of the molecule concentration c_{corr} is constant throughout the varying solution viscosities. These results state that some additional corrections should be applied to explain the experimental results (c_{exp}). This may be related to a change in the extinction coefficient of the molecule and the integral overlap between excitation and emission spectra with the environmental refractive index. When calculating the individual molecule concentrations c_i, the relative orientation between proteins κ^2 was assumed to be constant. A slight variation on this parameter could also alter the final result and explain the experimental findings. Another explanation for the decrease of the experimental molecule concentration c could be related with rotation. If the proteins experience any rotation, a greater depolarisation due to Brownian motion may explain why the molecule concentration decreases with the solution viscosity.

Table 2.5: Experimental molecule concentration c_{exp} and corrected molecule concentration c_{corr} and quantum yield Φ_{corr}, per EGFP varying solution viscosity.

% **glycerol**	c_{exp}	$\Phi_{corr} \pm$ **0.002**	$c_{corr} \pm$ **0.012**
0	0.297 ± 0.012	0.600	0.297
5	0.273 ± 0.006	0.606	0.291
10	0.254 ± 0.010	0.608	0.289
15	0.236 ± 0.008	0.611	0.287
20	0.224 ± 0.009	0.613	0.285
25	0.212 ± 0.004	0.615	0.283
30	0.184 ± 0.004	0.616	0.281
35	0.175 ± 0.006	0.619	0.279
45	0.153 ± 0.006	0.623	0.274
50	0.153 ± 0.005	0.625	0.273

Moreover, we noticed that k_r^0 (0.1272 ns^{-1}) differs significantly from the value found in *Section* 2.4.1 ($\sim$ 0.215 ns^{-1}). It has been previously demonstrated that the experimental Strickler-Berg formula may not determine accurately the fluorescence lifetime rate constants, where the non-radiative rate constant may vary across solutions [193]. Also, Figure 2.4 plots the inverse of the fluorescence lifetime $1/\tau$, instead of the radiative rate constant k_r. Although, this has been argued to be a good approximation, a minimum difference between them may yield a change on the molecule concentration c. On top of that, following Hirayama's approach [194,195] ($1/\tau = k_r + k_{nr} = k_r^0 n^2 + k_{nr}$), if the inverse of the fluorescence lifetime $1/\tau$ is plotted against the square of the refractive index n^2 and fitted with a linear expression with intercept, the non-radiative rate constant k_{nr} was found to be much lower than the calculated experimentally in this section (not shown). Thus, we consider the results presented in *Section* 2.4.1 as qualitative.

2.4.2.4 Calculation of the separation R between EGFP monomers for the stretched and bi-exponential models

In this subsection, the distance between EGFP monomers was calculated, per refractive index solution and anisotropy data model.

From the experimental fit parameters of the EGFP dimer time-resolved fluorescence anisotropy data, the FRET energy efficiency was calculated, where the stretched and bi-exponential models were applied. In the previous subsection it was shown that for the stretched exponential model, E_{FRET} was calculated applying equation 2.14. For the bi-exponential model, the combination of equations 1.42 and 1.45 gave rise to the FRET energy efficiency. While the FRET energy efficiencies obtained from the stretched exponential model were found between 0.184 and 0.316, the calculated ones from the bi-exponential model were given by much higher values within a narrower range (between 0.612 and 0.723) (Table 2.6).

Via equation 1.45 and assuming κ^2 = 2/3 as a first approximation, E_{FRET} simulated curves and R_0 were generated for each refractive index solution n. The integral overlap of the absorption and emission spectra for EGFP is $J(\lambda) = 8.691 \times 10^{14} \frac{nm^4}{Mcm}$, with an extinction coefficient ε = 55,900 $M^{-1}cm^{-1}$ and a quantum yield Φ = 0.60 [161]. Φ was not corrected for each sample as we previously demonstrated and presented in Table 2.5 that it barely varied across the varying refractive index solutions (less than 5%). Then, making use of the same equation (1.45), the fluorophore separation R was calculated for each E_{FRET} value per time-resolved fluorescence anisotropy model. This is presented in Figure 2.10 and Table 2.6. As expected, lower values for R were calculated for the bi-exponential model (centred at 4 nm, approximately) in comparison to the stretched exponential model (centred at $\sim$ 5.5 nm), as according to equation 1.45, the FRET energy efficiency E_{FRET} is inversely proportional to the fluorophore separation R.

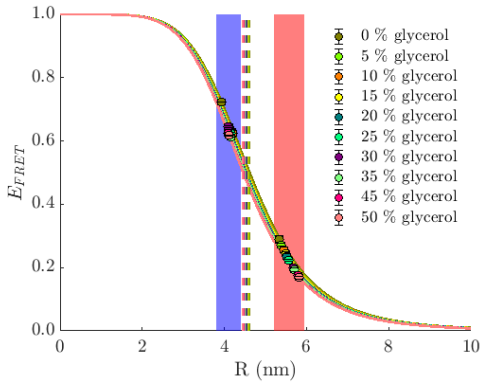

Figure 2.10: The FRET energy efficiency plotted versus the donor-acceptor separation for the bi-exponential (blue shade plot) and the stretched exponential model (red shade plot). R_0 is plotted with dashed vertical lines for each solution. κ^2=2/3.

Thus, different models yield a different outcome in terms of E_{FRET} and R. Results state that the stretched exponential model may explain the experimental time-resolved fluorescence anisotropy data more accurately, as there is no logic in considering that the EGFP dimer rotates faster than the EGFP monomer. To confirm this, MD simulations will be presented in the upcoming section, where the

Table 2.6: FRET energy efficiencies, donor-acceptor distances and relevant parameters, for bi- and stretched exponential models, per refractive index and viscosity composition sample.

					Bi-exponential		**Stretched exponential**	
% glycerol	**η (cP)**	**n $\pm$ 0.0005**	**R_0 (nm)**	**τ_D (ns)**	E_{FRET}	**R_{DA} (nm)**	E_{FRET}	**R_{DA} (nm)**
0	0.981	1.3355	4.614	2.647 $\pm$ 0.008	0.723 $\pm$ 0.001	3.933 $\pm$ 0.002	0.316 $\pm$ 0.010	5.355 $\pm$ 0.054
5	1.064	1.3525	4.575	2.625 $\pm$ 0.004	0.631 $\pm$ 0.000	4.183 $\pm$ 0.001	0.303 $\pm$ 0.005	5.391 $\pm$ 0.023
10	1.249	1.3575	4.564	2.598 $\pm$ 0.003	0.624 $\pm$ 0.000	4.195 $\pm$ 0.001	0.286 $\pm$ 0.009	5.445 $\pm$ 0.041
15	1.482	1.3655	4.546	2.560 $\pm$ 0.035	0.634 $\pm$ 0.003	4.147 $\pm$ 0.010	0.269 $\pm$ 0.008	5.492 $\pm$ 0.035
20	1.776	1.3715	4.532	2.520 $\pm$ 0.020	0.644 $\pm$ 0.002	4.106 $\pm$ 0.006	0.259 $\pm$ 0.009	5.519 $\pm$ 0.040
25	2.154	1.3775	4.520	2.513 $\pm$ 0.030	0.624 $\pm$ 0.003	4.153 $\pm$ 0.008	0.247 $\pm$ 0.004	5.557 $\pm$ 0.016
30	2.648	1.3825	4.508	2.459 $\pm$ 0.021	0.645 $\pm$ 0.002	4.081 $\pm$ 0.006	0.219 $\pm$ 0.004	5.679 $\pm$ 0.018
35	3.302	1.3890	4.494	2.472 $\pm$ 0.010	0.612 $\pm$ 0.001	4.167 $\pm$ 0.003	0.210 $\pm$ 0.006	5.714 $\pm$ 0.036
45	5.410	1.4030	4.464	2.386 $\pm$ 0.010	0.625 $\pm$ 0.001	4.100 $\pm$ 0.003	0.187 $\pm$ 0.006	5.790 $\pm$ 0.037
50	7.128	1.4070	4.456	2.411 $\pm$ 0.020	0.617 $\pm$ 0.002	4.115 $\pm$ 0.006	0.184 $\pm$ 0.006	5.816 $\pm$ 0.034

No error associated to viscosity η

Not presented error for R_0 due to its fixed and low value per solution

Presented errors are associated to standard deviations of average values

τ_D corresponds to the fluorescence lifetime of the EGFP monomer

fluorophore separation R and the FRET energy efficiencies will be extracted and compared with the experimental data.

2.4.3 Molecular Dynamic (MD) simulations

MD simulations were performed with the main objective of assessing which of the aforementioned models (bi-exponential or stretched exponential) describes the EGFP dimer dynamics best. For every time step, the fluorophore distance R, and the relative dipole orientation κ^2 between proteins were calculated as previously described (*Section* 2.3.8). With the help of these parameters, the absolute FRET energy efficiency was calculated using equation 2.26.

2.4.3.1 Separation R between EGFP monomers

Figure 2.11A corresponds to the temporal evolution of the fluorophore separation R. Its histogram is calculated and presented in Figure 2.11B, where it can be observed that the fluorophore separation R distribution follows a Gaussian function and therefore, mean and standard deviation values can be extracted from the fit. Thus, this yields $\overline{R}$ = 4.56 $\pm$ 0.07 nm. This means that the distance between the two EGFPs remains very constant over time.

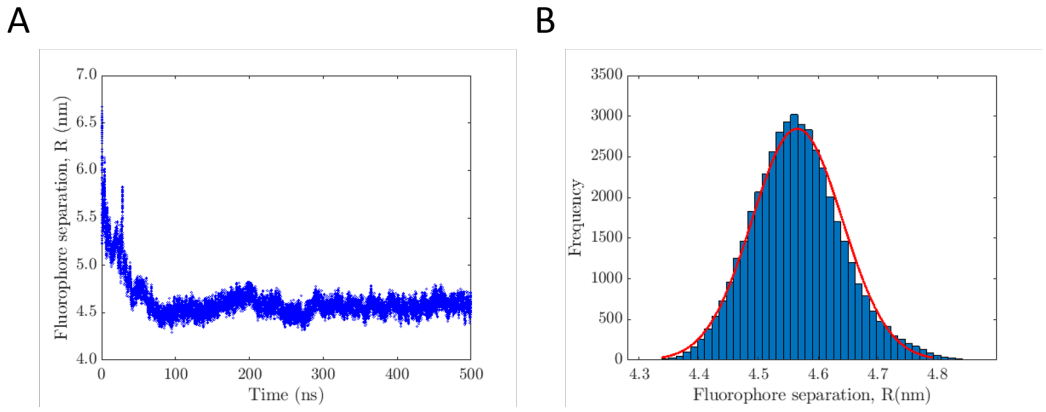

Figure 2.11: (A) Temporal evolution and (B) histogram of the fluorophore separation R. From the histogram fit, the mean value and standard deviation are 4.56 nm and 0.07 nm, respectively.

If the experimentally calculated distance between EGFP monomers R (Figure 2.10 and Table 2.6), via time-resolved fluorescence anisotropy measurements, is compared to the simulations (Figure 2.11), it can be observed that the simulation results are located in between the bi-exponential and stretched exponential fluorophore separations R.

Notice that for the calculation of the experimental separation R between EGFP monomers, the dipole orientation κ^2 was assumed to be 2/3, as a first approximation. If we rearrange equation 1.45, the expression used for the calculation of R was:

$$R = R_0 \left(\frac{1 - E_{FRET}}{E_{FRET}} \right)^{1/6} \tag{2.35}$$

As R_0 is proportional to κ^2 (equation 1.44), κ^2 values below 2/3 would imply lower R_0 and thus R. This may justify why the experimental separations R between EGFP monomers, when the stretched exponential model is applied, lie above the simulated fluorophore separation R. The opposite case scenario (κ^2 above 2/3) would support the use of the bi-exponential model to interpret the experimental time-resolved fluorescence anisotropy results. The next subsection will elucidate about the nature of κ^2 to try to verify any of the aforementioned experimental assumptions.

2.4.3.2 Relative dipole orientation κ^2 between EGFP monomers

The dipole orientation between proteins was also investigated and presented in Figure 2.12. The temporal evolution of κ^2 is given by Figure 2.12A, from where a histogram of events is created (Figure 2.12B).

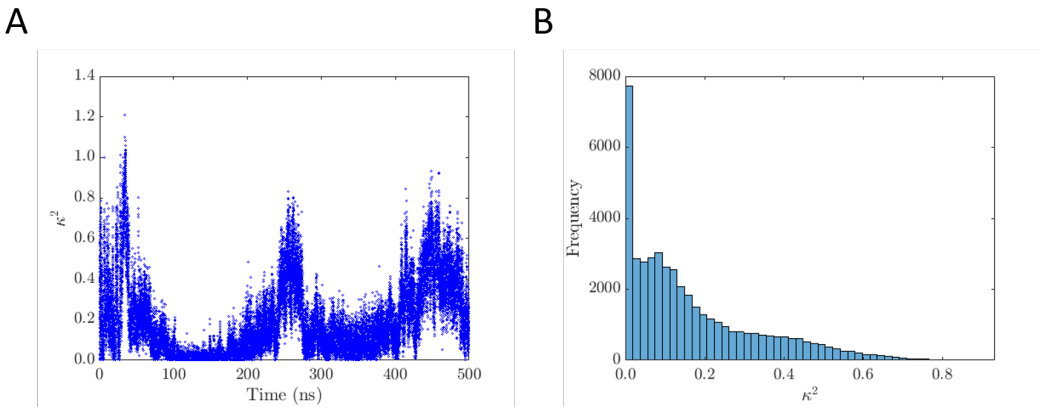

Figure 2.12: (A) Temporal evolution and (B) histogram of the relative dipole orientation κ^2 between EGFP monomers.

According to Figure 2.12B, the κ^2 range goes from 0 to 0.9180, below the parallel configuration between fluorophores given by $\kappa^2 = 1$. The κ^2 histogram shows three distinctive populations representing the three dominant relative orientation of the fluorophores in the dimer. The first one corresponds to $\kappa^2 = 0$, which accounts for the most predominant trend. This means that the two proteins are located perpendicular to each other most of the time. The second population centres around $\kappa^2 = 0.1$, where a peak of events is located. This corresponds to the second most populated area, indicating a smooth tumbling of one fluorophore with respect to the other around a T-shaped configuration. And finally, the third and least populated area corresponds to a peak located around 0.4. From here onward κ^2 decays progressively till reaching zero events before getting to $\kappa^2 = 1$. The increase of κ^2 indicates a similar situation to the previous one (smooth tumbling of one fluorophore respect to the other around a T-shaped configuration) but with more space exploration. This makes sense as the more space is explored, the longer the tumbling takes and there-

fore less events are registered.

A histogram of κ^2 is effectively a probability density function (pdf) of the number of events between κ^2 and $\kappa^2 + \Delta\kappa^2$. The experimental anisotropy data presented above was fitted with two different models using the average $\kappa^2 = 2/3$. We can see now thanks to the MD simulations that this is not a very good approximation. So in order to prove this, a fit of the κ^2 histogram was attempted with its pdf [196] (not presented), without any success:

$$p(\kappa^2) = \left[\frac{2}{\sqrt{3\kappa^2}}\right]\left[ln(2+\sqrt{3}) - g\left(\kappa^2\right)\right] \tag{2.36}$$

where $g(\kappa^2) = 0$ for $0 < \kappa^2 < 1$ and $g(\kappa^2) = \ln(\sqrt{\kappa^2 - 1} + \sqrt{\kappa^2})$ for $1 < \kappa^2 < 4$.

The outcome is not surprising considering the underlying assumptions. First of all, the dynamic average for the orientation factor is assumed [197]. This would be the case if the rotational Brownian motion was much faster than the time it takes for the transfer energy to happen between fluorophores [196, 198]. From the MD simulations, we can see that this criteria is not met if we have a look at the κ^2 histogram (Figure 2.12B), where a mean value for this quantity is clearly located below the dynamic average $\kappa^2 = 2/3$. Also, an additional assumption for the pdf(κ^2) construction is considering donor and acceptor totally independent from each other, which means all angular orientations for both constructs are permitted to be explored. The linker attached to the two proteins does not allow this criteria to be met. As argued in the previous subsection, the location of the simulated mean κ^2 below 2/3 reinforces the use of the stretched exponential model to interpret the experimental time-resolved fluorescence anisotropy results.

Since the dynamic regime is not able to explain our results, we also tried to fit them within a static regime, which means the FRET rate constant is much faster than the rotational Brownian motion the fluorophores experience. In the static av-

eraging regime, the average κ^2 depends on the ratio between R and $\overline{R_0}$, where the last one accounts for the Förster distance with $\kappa^2 = 2/3$. Steinberg et al. related this quantity with R/$\overline{R_0}$, assuming total isolation of each donor-acceptor pair and randomly orientated single dipoles (isotropic system and dipole-dipole interaction approximation) [197]:

$$\langle\kappa^2\rangle = \begin{cases} 0 & R \leq \frac{2}{5}\overline{R_0} \\ \frac{2}{3}\frac{\left(R-\frac{2}{5}\overline{R_0}\right)}{\overline{R_0}} & \frac{2}{5}\overline{R_0} \leq R \leq \frac{7}{5}\overline{R_0} \\ \frac{2}{3} & R \leq \frac{7}{5}\overline{R_0} \end{cases} \tag{2.37}$$

The set of fluorophore separations given by the MD simulations is found between $\frac{2}{5}\overline{R_0}$ and $\frac{7}{5}\overline{R_0}$, which corresponds to 1.85 and 6.47 nm (Figure 2.11B). Knowing that the mean fluorophore separation is $\langle R\rangle = 4.56 \pm 0.07\ nm$ and applying the middle expression of equation 2.37, the average κ^2 will be $\langle\kappa^2\rangle = 0.3906$. This is a very high value in comparison with the κ^2 data obtained from the MD simulations (Figure 2.12B). Calculating an average κ^2 for our data would not be reasonable as, as previously pointed [199,200], a system like ours, would most likely be described by a much narrower range of geometries, giving rise to an also narrower κ^2 distribution (Figure 2.12B), different from the theoretical predictions [196]. This is the main reason why our system cannot be described by any of the aforementioned equations 2.36 and 2.37.

2.4.3.3 Calculation of FRET energy efficiency from the separation R and the relative dipole orientation κ^2 between EGFP monomers

Figure 2.13 contains the temporal evolution of the calculated FRET energy efficiency E_{FRET} and its histogram.

A direct comparison between Figure 2.10 and Figure 2.13B tells us that the stretched exponential model fits the MD simulations better than the bi-exponential model. However, it must be noticed that the calculations for the experimental E_{FRET} were done for a dynamic regime ($\kappa^2 = 2/3$), while the ones calculated from the MD simulations are based on the extracted κ^2 values.

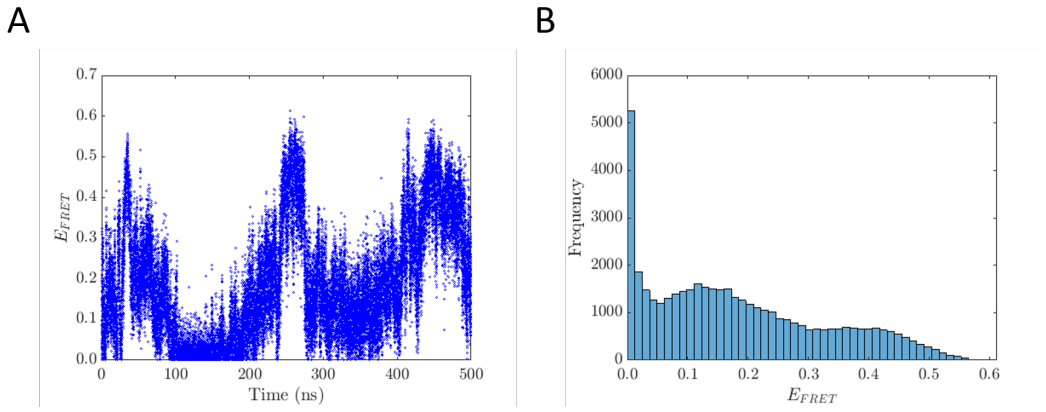

Figure 2.13: (A) Temporal evolution and (B) histogram of the FRET energy efficiency E_{FRET}.

The E_{FRET} extracted from the MD simulations is encountered within a range of 0 and 0.6 (Figure 2.13B), showing a very similar trend to the κ^2 distribution, where the majority of the events happen also at $E_{FRET} = 0$. The fact that the FRET energy efficiencies lie below 0.5 tells us that the FRET rate constant is not very rapid, in comparison to the rotational Brownian motion, which further supports that the system cannot be treated either as frozen, within a static configuration. This reinforces the use of the stretched exponential model for the experimental anisotropy data interpretation (Figure 2.10). Following the same argument of the non calculation of an average κ^2, it can also be applied for the one corresponding to E_{FRET}, albeit some work has been done on this regards for the description of the E_{FRET} distribution in a static isotropic regime [200]. In Figure 2.14 the fluorophore separation R is plotted against κ^2 along its FRET energy efficiency.

The MD simulations present a repetitive pattern for R and κ^2 over time. This

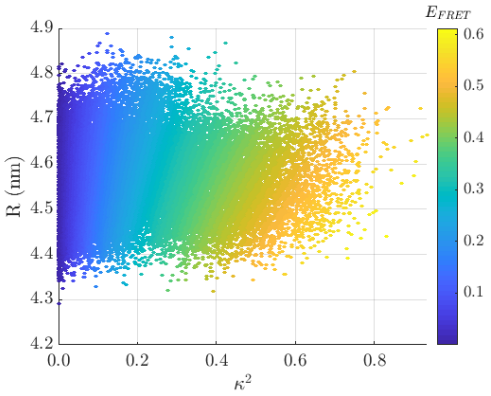

Figure 2.14: E_{FRET} per fluorophore separation and κ^2, extracted from the MD simulations. The FRET energy efficiency was calculated using equation 2.26.

means that E_{FRET} should also present the same pattern independently on the solution viscosity, as this factor just slows down the process but should yield the same outcome (Figure 2.13). Figure 2.14 presents how E_{FRET} is distributed across a combination of fluorophore distances R and relative dipole orientations κ^2 between proteins. Experimentally, we have seen that E_{FRET} (through γ) varies for each solution viscosity, which yields different fluorophore separations R. So, although the acceptor concentration is not supposed to change, we speculate that the effect of the refractive index makes γ vary and as a consequence E_{FRET}.

2.4.3.4 Simulation of time-resolved anisotropy decays for monomer and dimer EGFPs

Using the MD simulation data, we made an attempt to understand the molecular dynamics of the EGFP monomer and dimer. We simulated the time-resolved anisotropy decays for both EGFP constructs and fitted them similarly to real experimental data.

Simulated EGFP monomer time-resolved anisotropy decays

For the monomer, the anisotropy decay was fitted with a single exponential model without baseline. The rotational correlation time extracted from the fit was 4.60 $\pm$

0.04 ns. The goodness of fit was $R^2 = 0.9792$. This low value for the rotational correlation time in comparison with the experimental rotational correlation time (16.46 $\pm$ 0.20 ns) was due to the model (TIP3P) used for water in the MD simulations. In this model, the water viscosity of TIP3P (0.321 cP) [185–187] at RT is considerably lower than actual water viscosity (1 cP).

The single exponential model used for the fit of the simulated time-resolved anisotropy decays, assumes the protein is freely rotating and its shape can be modelled as a sphere. In order to assess how good this spherical approximation is, the anisotropy decay was also fitted with a bi-exponential model, giving rise to two identical rotational correlation times (not shown). This means the spherical model is a good approximation to be applied to our system. The individual anisotropy decays for the EGFP monomer and per time window (every 50 ns) are presented in Figure 2.15A, while its average anisotropy decay and fit are given by Figure 2.15B.

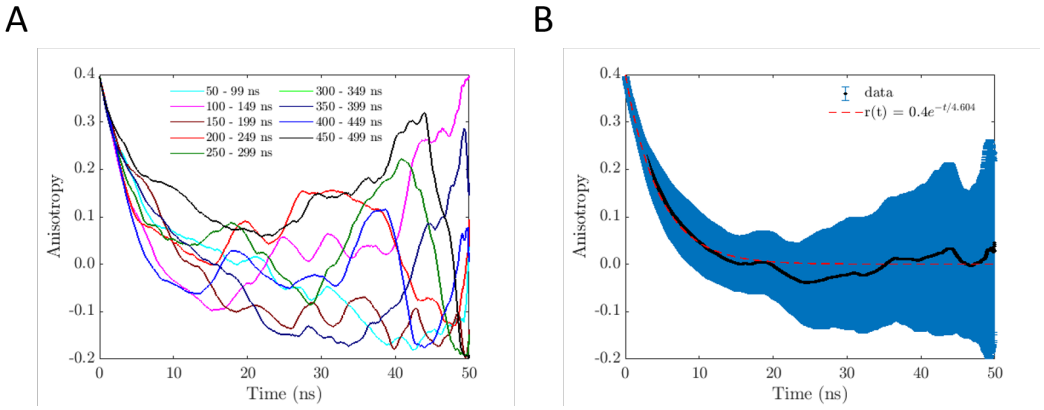

Figure 2.15: (A) Individual time-resolved anisotropy decays for the EGFP monomer and (B) average with fit.

Simulated EGFP dimer time-resolved anisotropy decays

Similarly, the average tr-anisotropy decay was simulated for both chromophores of the dimer (Figure 2.16A and B). Finally, the two anisotropy decays were aver-

aged and fitted (Figure 2.16C). The data was initially fitted with a bi-exponential model, where one component presented a long rotational correlation time. Therefore, the contribution of this component was reduced to r_∞ yielding a hindered rotation model. The fit parameters and goodness of fit were found to be as follows: r_0 = 0.3975 ± 0.0008, r_∞ = 0.0604 ± 0.0003, θ = 9.62 ± 0.05 ns ($\approx 2 \times \theta_{monomer}$) and $R^2 = 0.9794$.

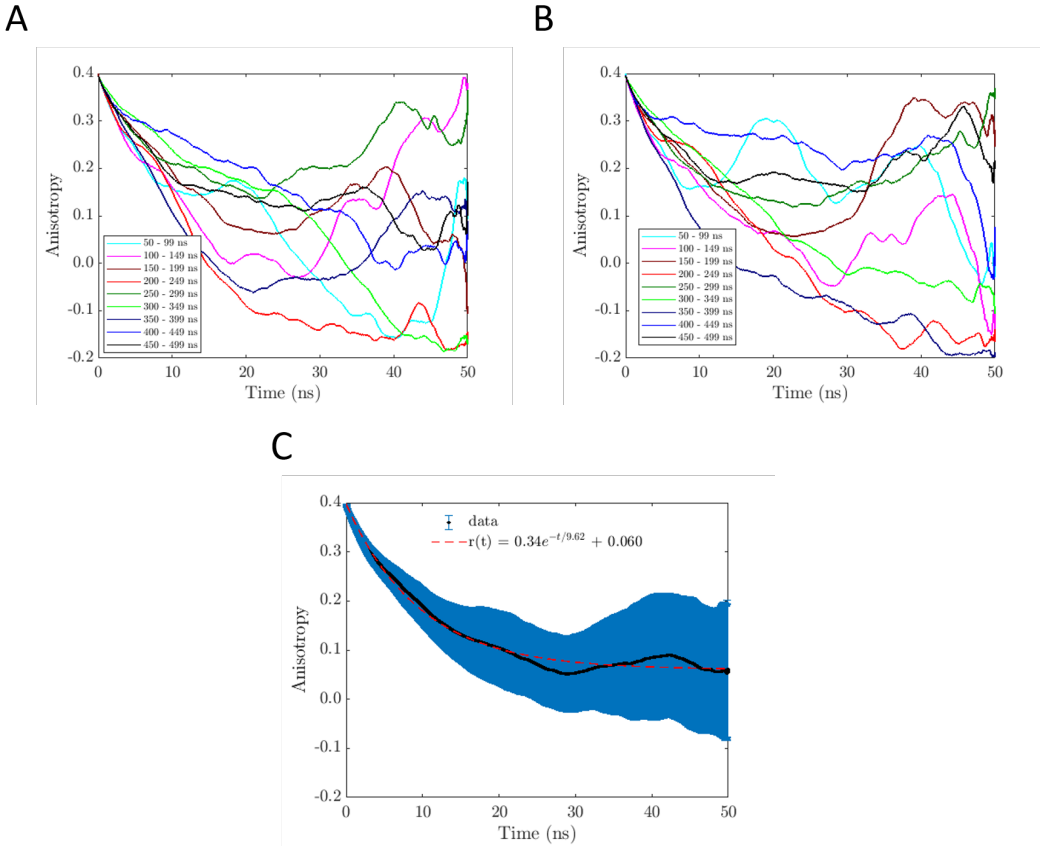

Figure 2.16: Individual tr-anisotropy decays for the EGFP dimer, where (A) corresponds to the first monomer and (B) to the second monomer. (C) Final average tr-anisotropy decay for the EGFP dimer with fit.

According to the modified Kinosita's expression (equation 1.34), we considered the entire dimer (2 EGFP monomers and flexible linker) as a rotating entity and each protein to experience some wobbling motion [37]. Therefore, the rotational motion is associated to the first term of equation 1.34 (τ_M) and the individual wobbling to τ_{eff}. Coming back to our results, we can observe that τ_M is the com-

ponent that goes towards infinity, yielding r_∞ and as a consequence to the hindered rotation model for r(t). This means the whole EGFP construct barely experiences any rotation. However, from the second component, τ_{eff}, we can see there is some wobbling associated to each EGFP protein, which yields a distribution of κ^2. This wobbling takes longer than the rotational motion experienced by the EGFP construct as a single and isolated monomer, 9.62 ns vs 4.60 ns, which definitely rules out the bi-exponential model for the interpretation of the experimental anisotropy data.

The rotational correlation time of a molecule, considered to be spherical, can be expressed by the Stokes-Einstein-Debye equation [20]:

$$\theta = \frac{\eta V}{k_B T} \tag{2.38}$$

where η is the viscosity of the solvent, V is the molecular volume of the fluorescence emitter, k_B is the Boltzmann constant and T is the temperature in K.

Therefore, the rotational correlation time of a certain molecule is directly proportional to its environmental viscosity. So this basically means that by knowing that the EGFP monomer rotates 1 radian during 4.60 ns on average when the solution viscosity is 0.321 cP, we can infer the rotational correlation time of the EGFP monomer when η = 1 cP, which yields 14.33 $\pm$ 0.12 ns. This value is in good agreement with the experimentally found rotational correlation time, θ = 16.46 $\pm$ 0.20 ns. Because the actual solvent is PBS(X1), whose viscosity we ignore but we certainly know that is above and close to 1 cP (water viscosity at RT), the difference between the simulated and experimental rotational correlation times should get lower, showing an improved agreement between themselves.

2.4.4 FRAP: lateral diffusion of the two EGFP constructs

FRAP should distinguish molecules by their size. The fluorescence recovery is expected to be slower for larger molecules in the same environment. To verify this hypothesis, we conducted FRAP experiments with EGFP monomer and dimer in two different solutions (35% and 50% glycerol). An average of 10 measurements per solution and construct were acquired.

Some representative data is shown in Figure 2.17. The fit of the selected profile for the confocal correction is presented in Figure 2.18, from where the half width at approximately 14% of bleaching depth from the top r_e and the bleaching-depth parameter K were extracted. In Table 2.7 the fit parameters of the FRAP recovery curve fits for EGFP monomer and dimer in 50% and 35% glycerol are presented. These fits corresponds to the ones displayed in Figure 2.19. For each EGFP construct and solution, the half-recovery time, mobile fraction, bleach depth and translational diffusion coefficient were calculated and displayed in Table 2.8.

Table 2.7: Fit parameters and goodness of fit for monomer and dimer FRAP recovery curves in 50% and 35% glycerol solutions.

		Fit parameters					Goodness of fit
% glycerol	EGFP	a	b	c	d	f	R^2
505050pt¡ -**50**pt¿	**Monomer**	1.002 ± 0.005	0.447 ± 0.098	0.028 ± 0.004	0.543 ± 0.096	0.112 ± 0.023	0.992
	Dimer	1.103 ± 0.084	0.477 ± 0.056	0.010 ± 0.006	0.611 ± 0.223	0.071 ± 0.017	0.989
353535pt¡ -**35**pt¿	**Monomer**	1.005 ± 0.006	0.476 ± 0.100	0.222 ± 0.063	0.534 ± 0.100	0.044 ± 0.007	0.990
	Dimer	1.007 ± 0.023	0.150 ± 0.199	0.267 ± 0.440	0.862 ± 0.188	0.052 ± 0.012	0.989

For both solutions (35% and 50% glycerol), the monomer presents a lower half-recovery time in comparison to the dimer, which means its FRAP curve recovers faster (Table 2.8 and Figure 2.19). This indicates its volume is smaller and therefore it diffuses quicker than the dimer. Interestingly, the recovery was nearly complete for the monomer, indicating total fraction mobility M_f, but not for the dimer. If the volume of the dimer is double the volume of the monomer and both are modelled as spheres, the hydrodynamic radius of the dimer should be $2^{\frac{1}{3}}$ times the hydrodynamic radius of the monomer. From the translational diffusion coeffi-

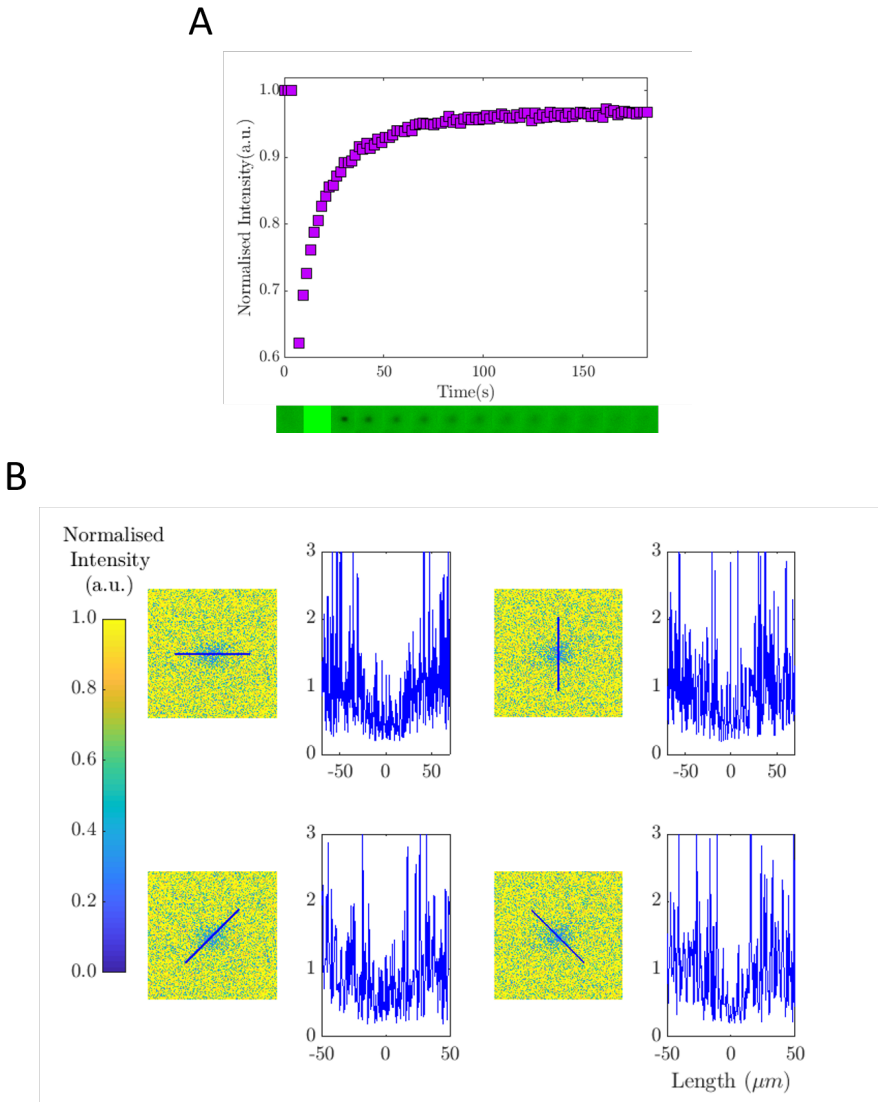

Figure 2.17: Representative FRAP data for EGFP monomer in 35% glycerol. (A) corresponds to the FRAP recovery curve and (B) to the different angular-oriented bleach spot profiles of the normalised first postbleach image. Each image has 512x512 pixels with a pixel size of 0.465030 μm. The confocal FRAP images in (A) are just some frames taken from the actual data to give an idea of how it looks like. The scale colours for (A) and (B) images are false. The dimensions of each frame is 238×238 μm^2.

cients it can be inferred that the dimer has on average a Stokes radius approximately 1.5 times the monomer. The discrepancy between the experimental and the theoretical result could be explained by the fact there is an additional element in the equation, the linker, which could effectively contribute to the total volume of the dimer construct. Therefore, the ratio between the hydrodynamic radii of monomer

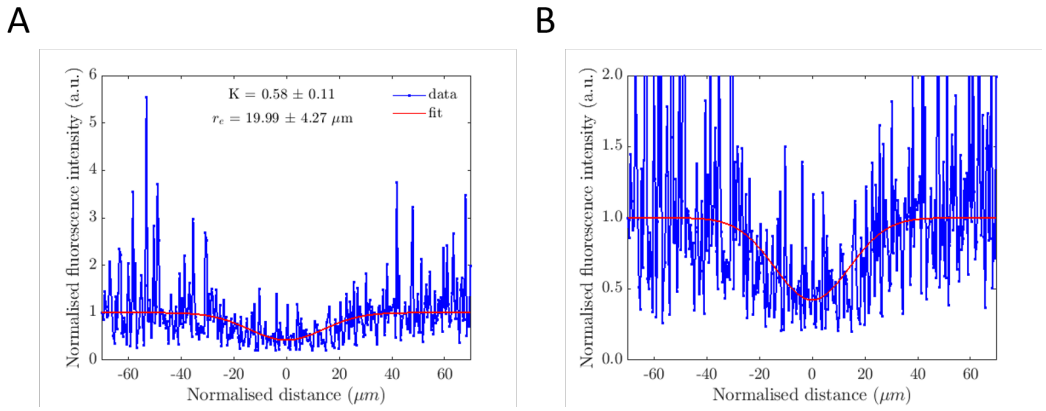

Figure 2.18: Profile data of the normalised first postbleach image with fit. (A) corresponds to the entire data and (B) it is just a zoomed version of the first one.

and dimer should be above $2^{\frac{1}{3}}$.

Table 2.8: EGFP monomer and dimer half-recovery times, mobility fractions, bleach depth percentages and translational diffusion coefficients for two varying viscosity solutions.

% **glycerol**	**EGFP**	$\tau_{1/2}$ **(ns)**	M_f (%)	**K**	D_t (μm^2/**s**)
505050pt¡ -**50**pt¿	**Monomer**	11.3 ± 0.5	98.4 ± 1.3	0.49 ± 0.04	5.4 ± 1.0
	Dimer	13.0 ± 1.0	95.0 ± 4.3	0.45 ± 0.08	3.8 ± 0.6
353535pt¡ -**35**pt¿	**Monomer**	6.6 ± 0.3	98.5 ± 1.9	0.42 ± 0.06	10.1 ± 1.7
	Dimer	9.2 ± 0.6	93.1 ± 2.3	0.22 ± 0.11	5.7 ± 1.0

Note that when applying equation 2.22, the hydrodynamic radii for monomer and dimer were calculated, which gave high values (above 3.5 nm) compared to the theoretical hydrodynamic radius of EGFP ($\sim$ 2.5 nm [191, 192]). Assuming the other parameters – room temperature T and viscosity η - are correct, this indicates that the translational diffusion coefficient should be higher in order to deliver the right EGFP hydrodynamic radius. The low translational diffusion coefficients can be most likely due to the non-negligible diffusion during the bleaching. Therefore, the confocal correction approach to overcome this issue through r_e is not appropriate to this specific case. Nonetheless, we may still extract some information regarding how different the translational diffusion coefficients are in terms of their ratio.

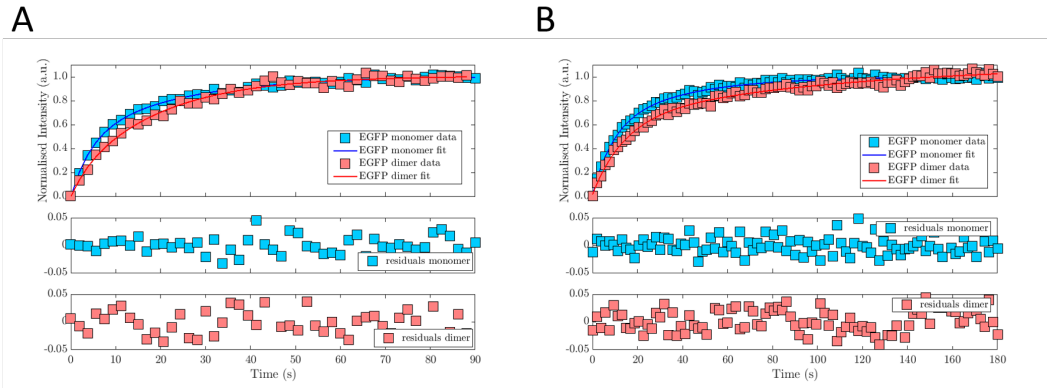

Figure 2.19: Representative FRAP recovery curves for EGFP monomer and dimer in (A) 35% and (B) 50% glycerol. For each curve, a fit is applied and the parameters presented in Table 2.7.

2.4.5 Red-edge failure of homo-FRET between EGFPs in varying viscosity solutions

The red-edge effect for both EGFP constructs, monomer and dimer, in buffer, 10/90% and 30/70% glycerol/PBS(X1) was investigated via steady state anisotropy measurements (Figure 2.20), as previously explained. As a general trend, the steady state anisotropy for monomer and dimer increases with the excitation wavelength and gets higher with viscosity. This is the case due to an increase in the restriction of movement, which leads to higher rotational correlation times, according to equations 2.30 and 2.38. Therefore, this also yields higher steady state anisotropy values, according to the Perrin equation.

$$r = \frac{r_0}{1 + \tau/\theta} \tag{2.39}$$

where r is the steady state anisotropy, r_0 is the initial anisotropy value, τ is the fluorescence lifetime and θ is the rotational correlation time.

Both EGFP constructs register their lowest r values at lower excitation wavelengths most likely due to the promotion of the electrons to higher excited states, above S_1. These excited states are short-lived but allow for partial depolarisation.

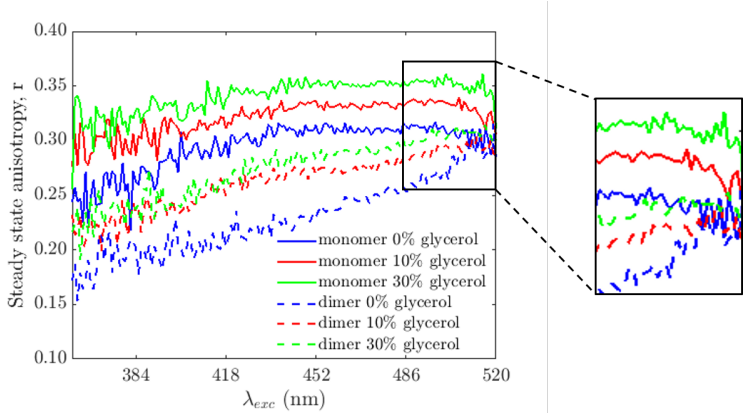

Figure 2.20: Steady state anisotropy measurements at different excitation wavelengths for EGFP monomer and dimer in PBS(X1).

The monomer features higher steady-state anisotropy values compared to the dimer. This has to do with the presence of homo-FRET for the dimer configuration, which provides an additional pathway for depolarisation after excitation and therefore as an outcome lower anisotropy values are acquired. The anisotropy response seems to flatten for the monomer from 440 to 490 nm. It finally decays at the red-edge, registered around 505-510 nm, as no electrons are able to reach the first excited electronic state S_1. On the other hand, at the red-edge, the dimer response undergoes a sudden rise, indication of progressive suppression of homo-FRET. We would expect the dimer steady state anisotropy to be located above the monomer one if homo-FRET ceases, as rotation would be the only possible depolarisation pathway for both constructs and the dimer's volume is larger than the monomer's one.

2.4.6 Preliminary results of Fluorescence lifetime studies of GFP-CAR in live and fixed cells

The main point of these experiments is the investigation of the protein dimerisation process, focusing on the transmembrane protein CAR. Fluorescence lifetime measurements were carried out in live and fixed cells to provide information about the environmental refractive index n via the Strickler-Berg relationship (equation 1.7).

The fluorescence lifetime of each GFP-CAR sample condition was calculated

from the combination of the parallel and perpendicular intensity decays. 10 repeats were performed for each sample condition and the total intensity decay was fitted with a double exponential model. The average fluorescence lifetime was calculated and plotted according to equation 2.20. Representative intensity decays ($I_{\parallel}$, $I_{\perp}$ and I_{tot}) and the average fluorescence lifetime per cell condition are presented in Figure 2.22. The calculated total intensity decay per cell condition was fitted by using a non-linear least squares regression routine. As an example, one measurement performed on the fixed cells after 3 min of the adenovirus infection, gave rise to the following fit parameters: τ_1 = 1.54 ns (25.97 %) and τ_2 = 2.49 ns (74.03 %), with χ^2_R = 1.28. These two fluorescence lifetimes have been previously associated with two different excited states of GFP [158, 189]. Table 2.9 summarises the results presented in Figure 2.22.

Table 2.9: Fit parameters and goodness of fit for GFP-CAR total intensity decay per cell condition.

Cell Condition		τ_i **(ns)**	χ^2_R
Live	**Control**	2.33 ± 0.03	2.47
Fixed	**Control**	2.29 ± 0.03	2.09
	3 min	2.36 ± 0.02	1.39
	20 min	2.27 ± 0.03	2.24

In fixed cells, the fluorescence lifetime of the untreated control cells (2.29 ns) was lower than of the cells treated with Ad5FK for three minutes (2.36 ns). However, after 20 minute treatment with Ad5FK, the fluorescence lifetime returned close to the control lifetime (2.27 ns). This suggests that the refractive index in the membrane surrounding the CAR-GFP is similar in the untreated control cells and the 20-minute treated cells. It appears lower in the cells treated with Ad5FK for only three minutes. Moreover, the fluorescence lifetime for the live cells is in general higher in comparison to the fixed cells. This means that in live cells, the proteins may be located in a lower refractive index environment, surrounded for instance by more water in comparison to the fixed cells (Strickler-Berg formula).

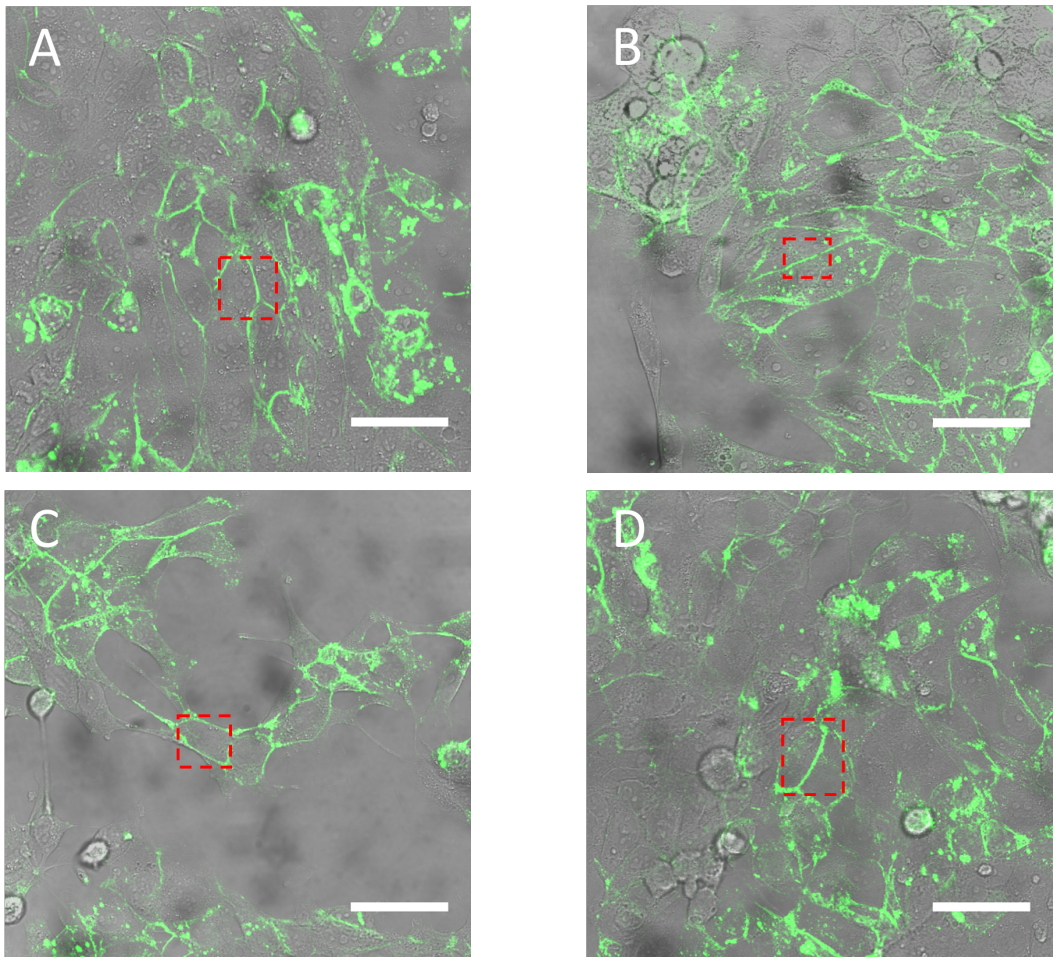

Figure 2.21: Confocal images and ROI of representative areas for the (A) control live cells, (B) fixed untreated cells, (C) fixed three-minute treated cells and (D) fixed 20-minute treated cells. The time-resolved fluorescence anisotropy decays were extracted from the ROI highlighted in red dash line. The scale bar corresponds to 50 μm.

These fluorescence lifetime studies find biological interpretation in the relocation of the proteins after cells uptake of the adenovirus Ad5FK. The CAR proteins arrangement is such within the cell membrane and across the cell-cell junctions that dimers tend to be formed [171, 172]. The presence of Ad5FK disrupts the CAR dimers and leads to protein relocation. This would be the step that takes place between the control and the three-minute treated cells. After a while, CAR proteins may come back to their initial position, which is given by a similar response in fluorescence lifetime in comparison to the fixed control cells.

The conclusions stated in this subsection may be true. However, one needs to

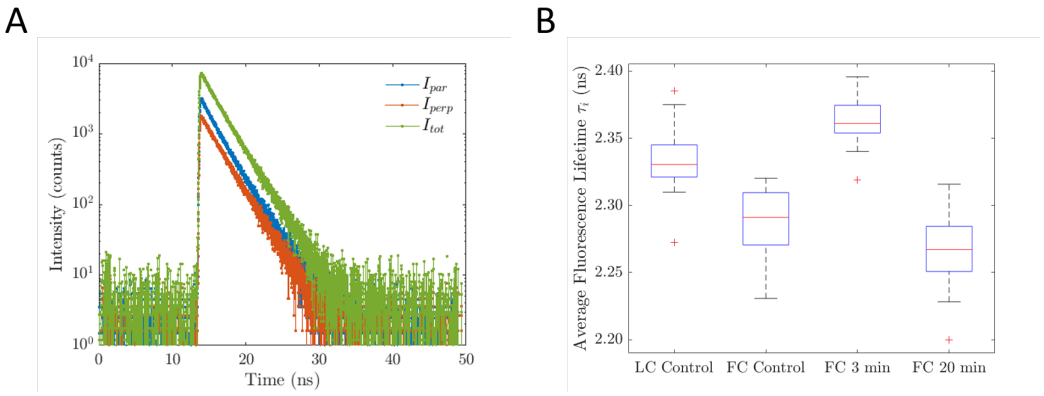

Figure 2.22: (A) Representative parallel, perpendicular and total intensity decays, per measurement. Specifically, this corresponds to a measurement taken from the fixed cells batch after 3 min of Ad5FK uptake. (B) Intensity weighted average fluorescence lifetime per cell condition. LC stands for live cell and FC for fixed cell. On each box, the central mark indicates the median, and the bottom and top edges of the box indicate the 25^{th} and 75^{th} percentiles, respectively. The whiskers extend to the most extreme data points not considered outliers, and the outliers are plotted individually using the '+' symbol.

take into account that changes in the environmental refractive index may be also due to the presence or absence of proteins, which may contribute to the local environmental refractive index. Therefore, fluorescence lifetime studies give insight about the relocation of proteins but also about their presence or absence. In order to uniquely determine the relocation of CAR consequence of its dimer interruption, homo-FRET studies were carried out via time-resolved and steady-state fluorescence anisotropy measurements.

2.4.7 Preliminary results of Time-resolved and Steady-State Fluorescence Anisotropy studies of GFP-CAR in live and fixed cells

Here we study homo-FRET applying two different models to the time-resolved fluorescence anisotropy data:

1. **Hindered rotation**

2. **Stretched exponential**

An example of the acquired intensity decays and the calculated anisotropy decay, per ROI and cell condition, can be observed in Figure 2.23.

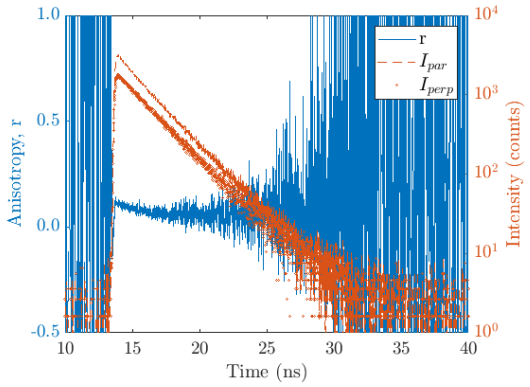

Figure 2.23: Representative parallel, perpendicular and anisotropy decays for the batch of fixed cells 3 min after Ad5FK cell uptake.

1. **Hindered rotation model**

   The hindered rotation model assumes equal FRET rate constants between two proteins at fixed positions. Figure 2.24 presents a summary of the fit parameters r_0, ϕ and r_∞ per cell condition.

   For this model, r_0 and ϕ present their highest values for live cells (Figure 2.24B and C). The limiting anisotropy r_∞ associated with the untreated live cells is very similar to the one given by the fixed untreated cells. For the fixed cells, r_0 and r_∞ present a very similar behaviour, where the highest values are registered at fixed three-minute treated cells. For these two parameters, the results given by the control and fixed 20-minute treated cells are almost identical. However, the FRET parameter ϕ presents a slightly different trend, where the values given by the fixed untreated and 3-minute treated cells are almost identical and larger than the FRET parameter ϕ associated with the fixed 20-minute treated cells. Note that only useful information can be extracted from the r_∞ fit parameter associated with the untreated live cells. When the cells are fixed, anisotropy depolarisation occurs only via FRET, where no ro-

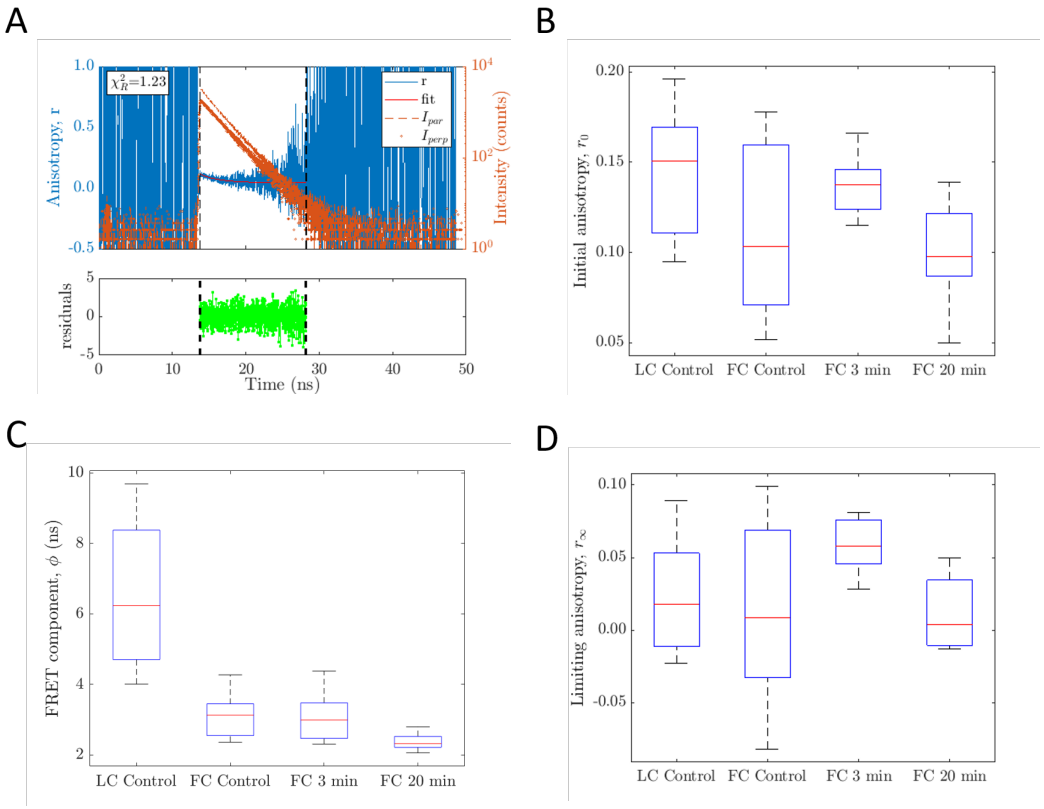

Figure 2.24: (A) Representative parallel, perpendicular and anisotropy decays with fit - hindered rotation model. This data corresponds to the batch of fixed three-minute treated cells. The fit parameters are: $r_0 = 0.115 \pm 0.002$, $\phi = 2.60 \pm 0.31$ ns and $r_\infty = 0.043 \pm 0.003$. (B) Initial steady state anisotropy r_0, (C) parameter associated to FRET and (D) limiting anisotropy r_∞ for each cell condition.

tation takes place. This explains why its average value is that close to zero and consistent across the cell conditions. Therefore, this parameter cannot determine cluster size or environmental viscosity. The hindered rotation model fit parameters are displayed in Table 2.10.

The FRET energy efficiency was calculated from the FRET parameter ϕ. The results are presented in Figure 2.25. E_{FRET} presents a very large span per cell condition, creating an overlap among distinctive results. The highest E_{FRET} values are encountered in the live untreated and fixed three-minute treated cells. Lower values are found in the fixed untreated and 20-minute treated cells. These results suggest that the maximum FRET energy efficiency

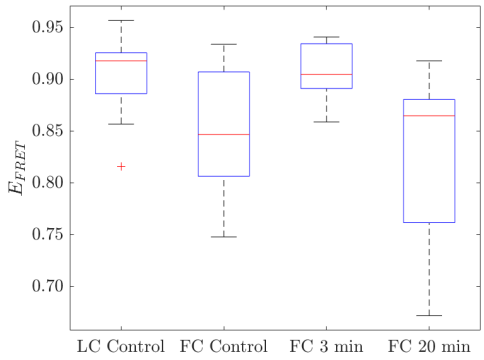

Figure 2.25: FRET energy efficiency calculated from the FRET parameter ϕ extracted from the hindered rotational model, per cell condition.

occurs after three minutes of having treated the cells with Ad5FK, where the the greatest number of proteins may be located. This contradicts the initial dimerisation of the CAR protein (fixed untreated cells), where the greatest transfer of energy via FRET is expected.

We conclude that these results are not reliable and additional measurements must be taken.

2. **Stretched exponential model**

The stretched exponential model assumes a combination of different FRET rate constants due to the transfer of FRET energy between donor and acceptors located at different positions. Figure 2.27 presents a summary of the fit parameters r_0 and γ. In Table 2.10 the stretched exponential fit parameters are also presented.

The fit parameter r_0, behaves identically to the initial anisotropy extracted from the hindered rotation model, presenting consistency across the fixed treated and untreated cells. The γ parameter behaves in an opposite way in comparison to r_0. Its lowest value is registered for the living cells control. For the fixed cells, the control presents the highest value. It decreases for the fixed three-minute treated cells and finally rises again for the fixed 20-minute

treated cells.

Using γ, the FRET energy efficiency was calculated applying equation 2.14 (Figure 2.27A). This gave some insight about the interaction between units via FRET. The higher γ is, the higher the depolarisation via FRET takes place, which may imply more oligomeric CAR units are encountered within that time position after the adenovirus Ad5FK uptake. This supports the disruption of the CAR oligomers once the adenovirus Ad5FH is intercepted by the cell membrane followed by the reorganisation of the proteins to their initial position at longer times.

Table 2.10: Average fit parameters and goodness of fit of hindered rotation and stretched exponential models per cell condition.

Cell Condition		Hindered rotation				Stretched exponential		
		r_0	ϕ (ns)	r_∞	χ^2_R	r_0	γ	χ^2_R
Live	Control	0.14 ± 0.04	6.54 ± 2.03	0.02 ± 0.04	1.19	0.17 ± 0.03	0.34 ± 0.13	1.22
Fixed	Control	0.11 ± 0.04	3.07 ± 0.63	0.02 ± 0.05	1.19	0.15 ± 0.03	0.54 ± 0.25	1.20
	3 min	0.13 ± 0.02	3.09 ± 0.70	0.05 ± 0.02	1.16	0.15 ± 0.02	0.33 ± 0.08	1.16
	20 min	0.11 ± 0.03	2.38 ± 0.26	0.02 ± 0.03	1.18	0.14 ± 0.02	0.56 ± 0.25	1.20

Steady-state anisotropy results were also presented (Figure 2.27B), showing an excellent agreement with the results extracted from the application of the stretched exponential model to fit the time-resolved fluorescence anisotropy data. However, the large standard deviations associated to the stretched exponential fit parameters indicates that additional measurements must be taken in order to confirm the results.

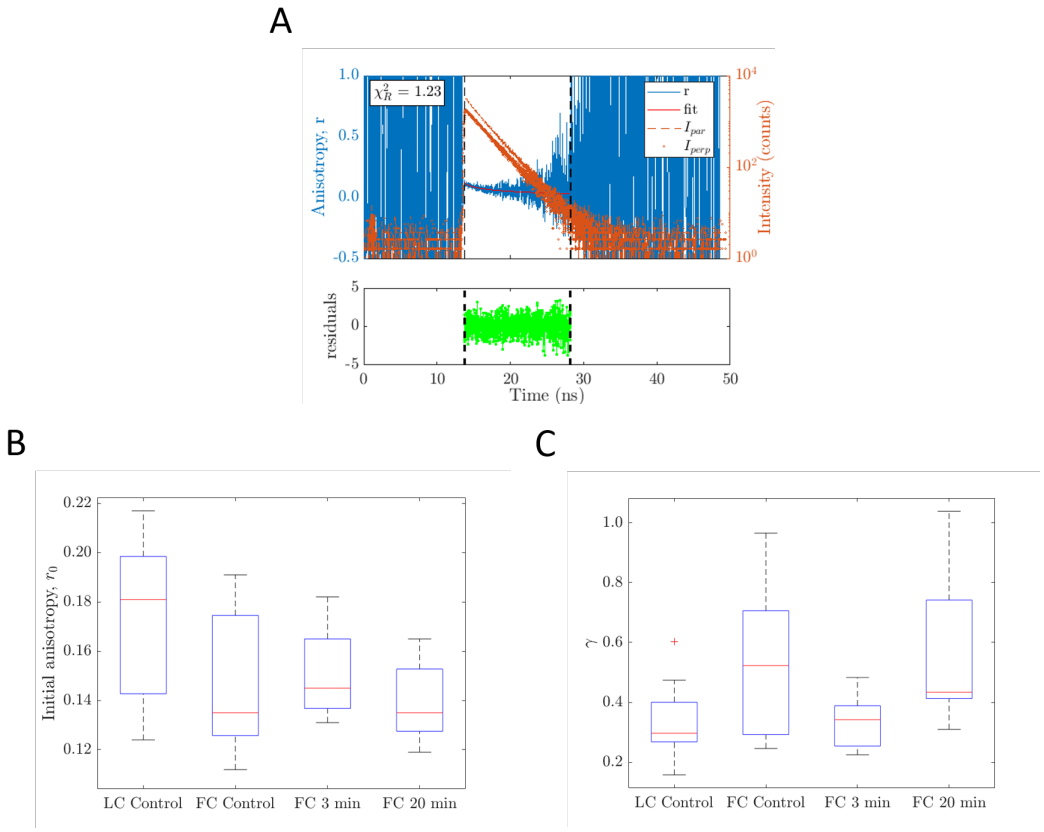

Figure 2.26: (A) Representative parallel, perpendicular and anisotropy decays with fit - stretched exponential model. This data corresponds to the batch of cells fixed 3 minutes after the Ad5FK uptake. The fit parameters are: $r_0 = 0.131 \pm 0.003$, $\gamma = 0.381 \pm 0.016$ with $\delta = 0.5$. (B) Initial steady-state anisotropy and (C) γ parameters.

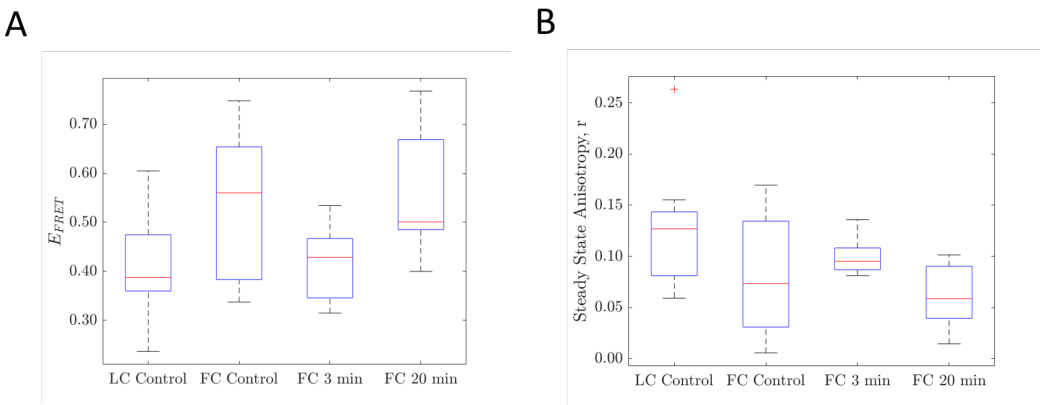

Figure 2.27: (A) E_{FRET} extracted from the stretched exponential model per cell condition. (B) Experimental steady-state fluorescence anisotropy per cell condition.

2.5 Summary & Conclusion

The work presented in this chapter was split in two main sections that may be named as follows:

1. **Investigating the dynamics of EGFP monomers and dimers in varying viscosity/refractive index solutions**

2. **Investigating the dynamics of GFP-CAR in live and fixed cells**

1. The relationship between the EGFP monomer and dimer fluorescence lifetime and the environmental refractive index was proven to follow the Strickler-Berg law. A small difference in fluorescence lifetime between monomer and dimer constructs per refractive index solution was observed and is probably related to the presence of the linker and the other EGFP monomer. Experimental anisotropy studies demonstrated the ability to distinguish the EGFP monomers and dimers via the observation of the beginning of the time-resolved fluorescence anisotropy decays. The EGFP monomer time-resolved fluorescence anisotropy decays were successfully fitted with a single exponential model. From the anisotropy data and knowing the solution viscosity, the hydrodynamic radius of the EGFP monomer was calculated, showing an excellent agreement with the literature. The EGFP dimer time-resolved fluorescence anisotropy data was best fitted with a stretched exponential model. FRAP studies revealed a slower translational diffusion coefficient associated with the EGFP dimer construct, which is consistent as its gyration radius is larger than the EGFP monomer's. Spectrally resolved steady-state fluorescence anisotropy measurements were conducted on the EGFP construct. An increase of anisotropy was observed in the EGFP dimer near the red-edge of the excitation range. This verifies the decrease in homo-FRET near the red-edge of the excitation spectrum. The additional data provided by the MD simulations gave insight into the protein's dynamics, not able to be observed experimentally, and supported the use

of the stretched exponential model for the interpretation of the dimer experimental data. Also, the experimental rotational correlation time of the monomer construct in water was shown to be in good agreement with the one extracted from the MD simulations.

2. CAR proteins tagged with GFP were expressed in live human bronchial epithelial cells and investigated through fluorescence lifetime and time-resolved fluorescence anisotropy. A batch of these samples were kept alive, as a control. The other batch of cells was fixed and divided in three different groups: control, three-minute treated and 20-minute treated cells. The cells were treated with the adenovirus Ad5FK. Via lifetime measurements, environmental refractive index information was extracted. The results suggest that the proteins may experience some relocation, in terms of environmental refractive index, from Ad5FK uptake as different lifetimes were measured per cell condition. The fluorescence lifetime outcome associated with the fixed untreated and 20-minute treated cells were found to be almost identical, where the three-minute treated cells presented a higher fluorescence lifetime (lower environmental refractive index). This may mean that the CAR proteins relocate themselves to their original position after the uptake of the adenovirus Ad5FK. Time-resolved fluorescence anisotropy data was acquired and the hindered rotation and stretched exponential models were applied and compared for the interpretation of the anisotropy data. The stretched exponential model was shown to present a better agreement with the steady-state fluorescence anisotropy results, consistent with the dimer disruption. Note that these results are preliminary results. Therefore, identical measurements must be taken in order to built up more robust statistics and reconfirm the findings presented in this chapter.

Overall, two different techniques, polarisation measurements (with the application of the stretched exponential model) and MD dynamic simulations, were combined and presented to derive in a single outcome by adding complementary

information in the study of the dynamics of two different EGFP standards in solution. Lastly, the interpretation of the dimer disruption (CAR-GFP) given by the stretched exponential model was shown to be consistent and in good agreement with the steady-state fluorescence anisotropy results.

Chapter 3

Development of a Multi-Modal Confocal Fluorescence Microscopy Technique based on Time-Correlated Single Photon Counting

3.1 Motivation

The work presented in this chapter arises from the idea of installing a multi-modal fluorescence setup in the laboratory, previously developed in our group [201]. The original idea was to explore the potential of the setup further in detail with the ultimate goal of applying it to live cells. The setup is named F^3 as three fluorescence techniques are part of it: Fluorescence lifetime imaging (FLIM), time-resolved fluorescence anisotropy imaging (tr-FAIM) and fluorescence recovery after photobleaching (FRAP). The main advantage of F^3 is the broad number of parameters closely related with each other that the user is provided with, from a limited photon budget and in a single measurement, which is especially interesting for characterising live cells. In short, having access to so much information just pressing one button and the challenge of dealing with so much disparate data was one of the

main driving forces that made this work happen.

3.2 Introduction

Fluorescence microscopy is a very attractive and popular tool for the imaging and study of living cells. It allows obtaining information on the macromolecular dynamics, interactions, location and structure. The emission properties - fluorescence spectrum, intensity, lifetime, polarisation and evolution in time of these parameters - are environmentally sensitive and therefore provide a great deal of information about the dynamics and intracellular environments surrounding the fluorescence probe [74, 202, 203]. The dynamics of living cells happen on different timescales: from picoseconds to up to hours, depending on the particular phenomenon taking place. Therefore, for each timescale, different information can be extracted. For the shortest timescale processes related to conformational changes can be observed, meanwhile on the largest timescale some chemical reactions occur [204]. This permits the use of different fluorescent microscopy techniques, each of them predominant and/or relevant at some point of this wide timescale range. Some examples of this are the following techniques: FRAP [83, 84, 98–100], which allows observing processes happening on a timescale of seconds. On the other hand, FLIM [60,202,203,205–209] and tr-FAIM [78,128,210,211] can go down to a time resolution of picoseconds.

3.2.1 Combining FRAP, FLIM and tr-FAIM - F^3 microscopy

The combination of the aforementioned techniques minimises potential damage to a biological sample, which is especially relevant when studying living cells. Too much light exposure of the sample can cause a modification of its morphology and can lead to phototoxicity and photobleaching. Therefore, when dealing with living cells we want to avoid their exposure to light as much as possible, so a simultaneous rather than a consecutive or sequential collection of data is preferred,

maximising the information available from a limited photon budget [212]. Several groups have reported results by using two of these techniques, either independently or combined [213–216]. What we present here is a continuation of work [217] previously undertaken in our group, where these three techniques - F^3 - were simultaneously applied for the first time [201]. The experimental setup is based on an inverted confocal microscope combined with Time-Correlated Single Photon Counting (TCSPC) detection with two hybrid GaAsP photomultipliers detectors. This setup allows these three techniques to be performed simultaneously and different information be extracted with no need of exposing the sample to the high intensity light of the laser more than once. On top of that, one of the main advantages of the setup is that the size of the targeted fluorophore can be inferred, in the case when the system is isotropic and uniform, without having any previous knowledge about the viscosity of the environment.

3.2.2 Structure and Biological Importance of Cell Membranes

Cell membranes (also known as plasma membrane) surround the cytoplasm of living cells, creating a physical separation between the intracellular components and the extracellular environment. This selective barrier regulates the substances getting inside and outside of cells and organelles, thus facilitating the transport of materials needed for survival. Therefore, it is selectively permeable to ions and organic molecules [218]. It also helps maintain the shape of the cell by anchoring the cytoskeleton. Cell membrane consists mainly of lipids, proteins, and carbohydrates. Its composition is not set but constantly changing and can vary during the different cell stages of its development [219]. The membrane is held together by various intermolecular forces, such as vaan der Waals and hydrogen bonds.

1. Lipids

   Lipids can be of three different classes: phospholipids, glycolipids and sterols, where in most cells, depending on the type, the most abundant lipids

are the phospholipids, where they can constitute up to 50% of the total lipid composition in plasma membranes [218, 220].

- Phospholipids

  Phospholipids can form lipid bilayers due to their amphiphilic nature. They generally consist of two hydrophobic carbon fatty acid tails and a hydrophilic head consisting of a phosphate group. The latter ones face the water within both the cytoplasm and extracellular space. The fatty acid tails constitute the great majority of the lipid structure. Depending on the degree of unsaturation of the tails, the fluidity of the membrane is compromised. Therefore, if a kink is present along the chain, which indicates lipids unsaturation (presence of a double bond), the lipids packing decreases, which has a direct impact on the melting temperature of the membrane [221].

- Glycolipids

  Glycolipids are carbohydrate-attached lipids by a glycosidic (covalent) bond. The presence of a monosaccharide or oligosaccharide bound to a lipid moiety is the essential feature of a glycolipid. The saccharides that are attached to the polar head groups on the outside of the cell are the ligand components of glycolipids. The role of the these lipids consists of facilitating cellular recognition and maintaining the stability of the cell membrane [221].

- Sterols

  Sterols are important organic molecules and subgroup of the steroids, where in animals can be present as cholesterol. These molecules play an important role in the fluidity of the cell membrane, determined by the degree of its dispersion. The presence of large quantities of cholesterol

in between the hydrophobic fatty tails confers stiffness on the membrane.

2. Proteins

   The proteins encountered within the cell membrane, approximately accounts for half its mass. This is due to their relevance in several biological activities such as cell-cell interaction, signalling, transportation of substances across the membrane, etc [218]. There are three main types of membrane proteins: integral (transmembrane), peripheral and lipid-anchored proteins [218]. This classification accounts for differences in regards to their function, location, structure and interacting elements.

3. Carbohydrates

   Carbohydrates or saccharides perform numerous roles in living organism. For example, in eukaryote cells, they play an important role in the cell-cell recognition. They are located on the surface of the cell and are able to recognise host cells and share information. Also, saccharides and derivatives include other important roles in fertilization, blood clotting and development, for instance [219].

3.2.3 Artificial Cell Membranes - Single Lipid Bilayers (SLBs)

In an attempt to describe and understand the cell membrane itself, many models have been proposed throughout history. However, the only one that prevails over time and that has been modernised in the current times with its basics remaining constant, is the fluid mosaic model of S. J. Singer and G. L. Nicolson (1972) [222]. This model establishes that the biological membrane can be described as a 2-dimensional liquid in which lipid and protein molecules diffuse more or less easily. According to this model, different microdomains formed by a specific composition (elements mentioned in the previous section) are identified within the cell

membrane, which are the so-called 'lipid rafts'. These domains confer the cell membrane different properties such as fluidity and protein trafficking [223, 224].

In order to understand the physical behaviour of cell membranes and further apply and validate F^3, artificial lipid bilayers have been made, which resemble the biological cell membrane. Single Lipid Bilayers (SLBs) were created by the deposition of Small Unilamellar Vesicles (SUVs) on a hydrophilic substrate [225]. These samples are ideal for performing FRAP experiments as the system can be considered as 2-dimensional, which means the translational diffusion occurs across a plane, being also 2-dimensional. This implies straightforward equations for its data analysis and no incompatibility with the high NA of the microscope objective [84, 93, 96]. Low NA objectives are mainly used for this technique in order to avoid diffusion through the SLB plane. However, a 2-dimensional system like a SLB implies no translational diffusion in z, which means a high NA objective may be used. F^3 has never been applied to study SLBs. Thus, this work presents for the first time a new multi-modal microscopy technique F^3 applied to these specific systems.

3.2.4 F^3 microscopy on SLBs

3.2.4.1 Lipid and Dye

The lipid is a phospholipid derivative that belongs to the subgroup of the phosphatidylcholines. More specifically, the lipid used in the laboratory is di-oleyl-phosphatidycholine (DOPC). This unsaturated lipid is purchased from Avanti Polar Lipids and needs to be stored in the freezer at - 20°C for preservation. Its phase transition temperature is - 16.5°C [226], and therefore exists in the fluid like liquid crystalline state at room temperature. Lipids containing the choline group moiety are the most abundant in eukaryotic cells and therefore, DOPC is one of the most common lipids used to model the biological cell membrane.

The dye 2-di-butylaminonaphthylethylpyridinium propyl-2-hydroxy-3-dimethyl-hydroxyethyl quaternary ammonium cation (di-4-ANEPPDHQ) was used to probe the SLB microenvironments, sitting in between the lipids conforming the system. It was purchased from Thermo Fisher Scientific and diluted in Dimethyl Sulfoxide (DMSO). This dye is a fast-response probe that operates by change in its electronic structure and was originally developed as a probe of membrane voltage [227]. Also, this dye is useful for visualising cholesterol-enriched lipid domains in model membranes, sensing directly the membrane fluidity. It is also known that this environmentally-sensitive membrane dye is able to distinguish between phases in model membranes through a blueshift in the spectrum [228]. Among other properties, this dye shows high sensitivity to membrane lipid packing, a narrow emission spectrum to avoid cross-talk with other dyes and high photostability [229, 230]. Moreover, di-4-ANEPPDHQ has unique properties due to the two positive charges of its headgroup. The first one is a decrease on the rate of internalisation of the dye within the bilayer. This is due to a delay triggered by the double positive charge on the rate of flipping from the outer to the inner leaflet of the bilayer. The second unique property is its water-solubility, which needs no detergents among others [229]. All these properties together make this dye an ideal candidate for advanced imaging of lateral plasma membrane heterogeneity [231].

Laurdan is another environmentally-sensitive membrane dye that has been more widely studied in regards to its physical and chemical properties [232]. Unfortunately, Laurdan suffers from low phototostability, high internalisation and requires phototoxic UV excitation [230]. The advantage of Laurdan is its ability to distinguish between the plasma membrane and the nuclear membrane, that has lower rigidity [233]. This dye is geometrically and biophysically similar to di-4-ANEPPDHQ. Its radius is around 5 Å. The chemical structures of laurdan and di-4-ANEPPDHQ are shown in Figure 3.1.

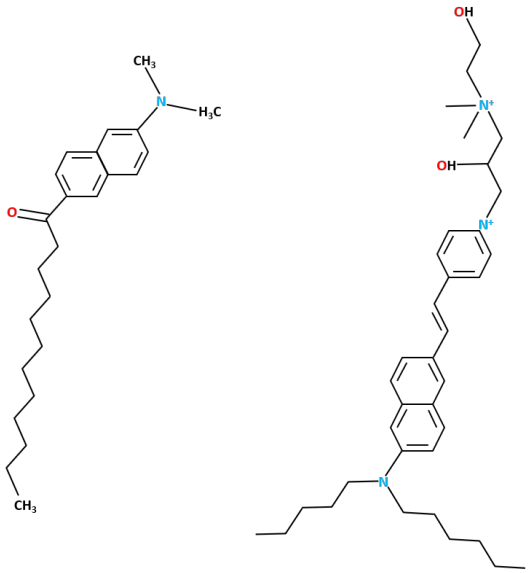

Figure 3.1: Structures of the polarity-sensitive membrane dye (left) laurdan and (right) di-4-ANEPPDHQ (adapted from reference [231, 234]).

The polarity these dyes are able to probe in their environment is related to the performance of the push-pull mechanism they have in their structure. This push-pull mechanism ensures that after light absorption, the charge is transferred from the donor (nitrogen) to the acceptor (oxygen) group, creating a highly dipolar excited state. Thus, the polarity these dyes sense will be determined by the extend of this charge exchange [235].

3.2.5 Literature Review on the Study of Supported Lipid Bilayers SLBs and other Similar Lipid Systems with Fluorescence Techniques & Environmentally-Sensitive Dyes

3.2.5.1 Fluorescence Lifetime and Spectral Measurements

Many studies on cell membranes have been undertaken in order to reveal information about their packing, phase-order, hydration and polarity among others. The main goal is understanding the cell membrane conformation and behaviour, fundamental entity of the entire organism. For this purpose, different environmentally-sensitive dyes have been synthesised throughout all these years looking for the per-

fect candidate that fulfils different aspects such as high photostability, optimal internalisation through live cells, narrow emission spectra that allows clear distinction between different bands, etc. Some of these dyes that present advantages and disadvantages are for instance laurdan, derivative of prodan and di-4-ANEPPDHQ [230].

Fluorescence lifetime and spectral imaging/point measurements have been performed with these dyes within artificial and/or biological cell membranes. Fluorescence lifetime measurements are not dependent on the dye concentration, which implies no need of any initial calibration. Also, hydration information can be extracted from lifetime parameters, as some fluorescence quenching may occur with the presence of water molecules, which yields a decrease on the probe's fluorescence lifetime. On the contrary, spectral imaging requires prior calibration as it depends on intensity parameters. Specifically, lifetime studies have been reported to offer higher contrast between liquid-ordered and liquid-disordered phases when using the dye di-4-ANEPPDHQ, whose spectral shift is just 60 nm [236].

Application examples of fluorescence lifetime or spectral imaging techniques on different model and/or cell membrane types and with different environmentally-sensitive dyes are presented below. One example is the work undertaken by Ulrich et al. [226], where a phase diagram of the lipid DOPC is investigated by using differential scanning calorimetry ranging from -40°C to 10°C. As previously mentioned in *Section* 3.2.4.1, Jin et al. [229] showed for the first time how di-4-ANEPPDHQ was able to distinguish between phases by using ordered and disordered-phase Large Unilamellar Vesicles (LUVs) with and without cholesterol depletion. Later on in 2013, Kwiatek et al. [237] presented a new range of environmentally-sensitive dyes (PY3304, PY3174 and PY3184) where a lipid order quantification was performed by using both fluorescence lifetime studies and spectral measurements in artificial bilayers and live cells. Generalised polarisation results are derived from the emission spectra and reveals information in regards to the lipid packing. A year

later, Segzin et al. [230] reported on different properties of a list of environmentally-sensitive dyes, including di-4-ANEPPDHQ and laurdan, by performing emission spectra measurements. The potency of the time-resolved fluorescence parameters was investigated by Kilin et al. [238] using the dye F2N12S in cell and model (LUVs) membranes. Also, the ordered and disordered phases were highly discriminated by using fluorescence lifetime imaging on Giant Unilamellar Vesicles (GUVs) with this same dye. Two years later in 2017, Segzin et al. [231] assessed the potential of the dye di-4-ANEPPDHQ and other environmentally-sensitive dyes in stimulated emission depletion (STED) microscopy to study membrane nano-domains. This was carried out by doing some spectral measurements in cell-derived GUVs, live Chinese hamster ovary (CHO) cells and Human Immunodeficiency Virus (HIV) particles.

To the best of my knowledge, only three publications describe a dye/lipid system investigated using FLIM at room temperature [236, 239, 240]. The first one is the work undertaken by Owen et al. [236], where the lifetime maps of DOPC LUVs and live cells are acquired with the di-4-ANEPPDHQ dye. A single exponential model is applied for fitting the DOPC LUV lifetime data, where a peak of 1.850 ns is detected. Another similar system is the one described by Le Marois et al. [239], where an investigation of the lifetime parameters of di-4-ANEPPDHQ in model ordered and disordered-phase membranes (GUVs) was carried out. She reported an average lifetime of 1.80 ns for the disordered-phase model. More recently, a paper from Steele and coworkers [240] came out where a fluorescence lifetime of 2.22 $\pm$ 0.03 ns was reported for the dye di-4-ANEPPDHQ in DOPC liposomes at RT.

3.2.5.2 Time-Resolved Fluorescence Anisotropy Measurements

Anisotropy measurements are sensitive to the dipole orientation of the fluorophore, reporting on its local environment, such as viscosity. It has been proven that some dyes, such as the one used in this work, are sensitive to the environment, such

as lipid phase (ordered or disordered) [231, 240, 241]. A wobble-in-a-cone model (equation 3.7) is extensively used in order to reveal some information about its packing and therefore membrane fluidity, when for instance the levels of cholesterol are modified or the phase changes [241]. The packing parameter is given by [240]:

$$S^2 = \frac{r_\infty}{r_0} = \left[\frac{1}{2}cos(\phi)(1+cos(\phi))\right]^2 \tag{3.1}$$

where ϕ is the semi-angle of a cone where the probe is free to wobble. At 0° the probe is considered to be frozen and $S^2 = 1$. $S^2 = 0$ in the limit of unrestricted motion.

Others before have studied similar systems to ours but not identical. For instance, in 2010, Honigmann and coworkers [241] undertook different experiments in SLBs at RT. with different membrane reporters - di-4-ANEPPDHQ was not one of them. With time-resolved measurements, they applied the wobble-in-a-cone model and found a rotational diffusion coefficient for pure DOPC membranes of around 2.4×10^7 $\mu m^2 s^{-1}$. Also, the ordered and disordered phases of these model membranes were distinguished via steady-state measurements. In 2012, Aguilar et al. [242] performed some time-resolved measurements with the dye laurdan (alike in structure to ours) and reported the following anisotropy parameters for DOPC GUVs at 22°C: $\theta = 2.05 \pm 0.02$ ns, $r_0 = 0.33$ and $r_\infty = 0.07$. Time-resolved measurements were also performed by Le Marois et al. [239] with di-4-ANEPPDHQ, where a hindered rotational model was applied for the fit of the time-resolved anisotropy measurements. She reported a rotational correlation time of 4.48 ns for DOPC GUVs. And finally, a very recent work, reported on the time-resolved anisotropy parameters when using the same dye as ours on DOPC liposomes at RT: $\theta = 3.32$ ns, $r_0 = 0.276$ and $r_\infty = 0.120$. The lipid packing was also presented by calculating the S^2 parameter via equation 3.1 and found to be 0.44 ± 0.13 [240].

3.2.5.3 Fluorescence Correlation Spectroscopy and Fluorescence Recovery After Photobleaching

Fluorescence Correlation Spectroscopy (FCS) and FRAP have become two of the most commonly used types of techniques to measure the rate of lipids and protein lateral diffusion within biological membranes [85, 243], such as those of red blood cells [244]. This is mainly due to its easy integration within a wide-field or confocal microscope.

Previous FCS and FRAP work revealed a rather broad distribution of experimental translational diffusion coefficients for DOPC lipids, due most likely to variations in experimental conditions between individual studies. For instance, Pincet et al. reported a translational diffusion coefficient for 1,2-dioleoyl-sn-glycero-3-phosphoethanolamine-N-(7-nitro-2-1,3-benzoxadiazol-4-yl) (ammonium salt) (DOPE-NBD) and 1,2-dioleoyl-sn-glycero-3-phosphoethanolamine-N-(lissamine rhodamine B sulfonyl) (ammonium salt) (DOPE-Rho) lipids in the outer monoloyer of DOPC SLBs onto a glass support of $1.9 \pm 0.3\ \mu m^2/s$ [88]. Other studies, reported and compared FCS and FRAP results of DOPC SLBs with the headgroup-labeled RhoPE (1,2-dimyristoyl-sn-glycero-3-phosphoethanolamine-N-(lissamine rhodamine B sulfonyl) (ammonium salt)), supported on a glass surface. The found values are as follows: $D_{t,FCS} = 2.6 \pm 0.2\ \mu m^2/s$ and $D_{t,FRAP} = 4.0 \pm 0.3\ \mu m^2/s$. An overstimation on the FRAP results is discussed and pointed out to be related with the choice of the FRAP curve fit and the introduced uncertainty in the bleach correction. It may also be due to the different time scales of the two techniques, where there is a higher prominence of barriers hindering diffusion on longer scales in those specific membranes. FRAP has low requirements on SNR, which is an advantage over FCS, where high SNR data is needed. Also, additional unique information from FRAP is able to be extracted, such as the immobile fraction of fluorophores diffusing across the lipid structure [89]. Another example is given by

Ladha et. al, where DOPC estable virtually solvent-free SLBs labelled with the fluorophore NBD-PE (N-(7-Nitrobenz-2-Oxa-1,3-Diazol-4-yl)-1,2-Dihexadecanoyl-sn-Glycero-3-Phosphoethanolamine, Triethylammonium Salt) were investigated with an optical and electrical chamber where FRAP measurements were performed. The resultant translational diffusion coefficient was 13.4 ± 0.7 μm^2/s [245].

Many studies have highlighted the influence of the nature of the substrate, on where the lipid structure rests, on its lateral mobility [246, 247]. Its interaction seems to have a direct impact on this experimental value. When the SLBs are made and supported on glass or quartz, a thin film of water (10-20 Å) is created between the lipids and the solid support [248, 249], fundamental for a reliable measure of the lateral diffusion. However, if any interaction between the hydrophilic substrate and large integral membrane proteins within the lipid structure takes place, these proteins get pinned to the substrate with their consequent immobilisation [250, 251]. On the other hand, another popular substrate used for the deposition of the SLBs is mica, due to its flatness. However, it seems to facilitate the interaction between the membrane and the support. Glass surfaces create a thicker water layer between both elements, although its roughness can cause a decrease in the lateral diffusion [252, 253]. The overestimation of the lateral mobility of the bilayer has been attributed to the contribution of friction forces between the inner and outer leaflets of the bilayer when closely located to the solid substrate [88]. Therefore, different tricks have been proposed and applied in order to solve these problems by increasing the distance between the SLB and the solid. Some of them are the polymer-cushioned bilayers. Renner et al. reported a 70-fold higher lateral diffusion coefficient for the same SLBs on mica in comparison to on a polymer cushion. They attributed this difference to a lower hydrophilicity of the polymer cushion, which has an impact on the properties of the aqueous layer [254]. In other studies, an identical translational diffusion coefficient in DOPC SLBs was encountered for

different supporting solids [255]. A problem with the polymer cushion is that its structure depends strongly on the method of preparation [246]. Another approach was proposed and successfully tested by Wagner et al. introducing a newly designed polyethylene glycol cushion, Polyethylene Glycol (PEG) between membrane and substrate. This tethered polymer-supported lipid bilayer system was proven to increase the mobile fraction of some membrane proteins. Its length provides a soft support, the covalent linkage of the membrane to the supporting glass or quartz substrates provides an increased stability and minimum interaction with the solid support [246].

Another factor that contributes to the variation in the reported diffusion coefficients is the dye being traced [88, 89, 247]. The fluorescence tracers used in lipid membranes are usually photostable and bright, with similar physico-chemical and structural properties to the membrane lipids. Different results were found by Chiantia et al., where different dyes were traced in SLBs/mica. This difference was specially pronounced in the disordered-phase of the lipids and correlated with the different electrostatic charge of the dye, creating a different electrostatic interaction with the negatively charged mica surface [256]. Also, it has been demonstrated via correlated FCS and molecular dynamic (MD) simulations the non-neutral role of the dye-labeled lipids to report on the lateral mobility of the lipid bilayer, decreasing its diffusion rate up to 20% with respect to the unlabeled species [257–259]. Besides, the dye concentration and lipid bilayer composition have been shown to impact directly on the diffusion measurements based on dye-label lipids. The diffusion coefficient of laurdan in DOPC GUVs was shown to increase with the concentration of RHB (Rhodamine B linked to 1,2-dioleoyl-sn-3-phosphatidylehanolamine) [259].

Higher diffusion coefficients are reported for non-planar structures, such as GUVs, giant liposomes and sponge phases. This is due to the lack of interaction with the solid substrate, previously argued. Therefore, they can be considered free-

standing membranes and mimic the biological membrane in a more accurate manner. Also, when the dimensions of the lipid structure is big enough, the curvature can be neglected and considered to be planar [88,247,259]. Still, the SLBs are very attractive systems to study the lateral mobility of the lipids under different conditions, where a high stability can be achieved by applying previously mentioned approaches and its well-defined geometry facilitates its characterisation [247]. Figure 3.2 shows some graphical and experimental data of GUVs and SLBs with the di-4-ANEPPDHQ dye.

Some studies where the lateral mobility of SLBs was measured via FCS, reported that when the lipids system is created by the fusion of vesicles, such as in our case, a single diffusion coefficient cannot describe the system satisfactory [247, 260]. Previous work suggested this could be associated to some immobilisation of lipid molecules on the surface [261]. Others proposed this phenomenon to be related to some interaction of the lipids with pore-like defects on the substrate surface [262]. Chiantia et al. associated this slow diffusion with fluorophore aggregates or vesicles onto the SLB surface [263, 264].

3.3 Materials & Methods

3.3.1 Samples preparation

3.3.1.1 Rhodamine 6G samples

Several solutions of Rhodamine 6G (R6G) in different viscosity mixtures of water/glycerol were made, ranging from 90% to 100% glycerol, approximately. The final concentration of R6G for each solution was 5 μM. The percentage of glycerol was calculated via a comparison with the solution's refractive index [265].

3.3.1.2 Supported Lipid Bilayers

The materials and detailed protocol are specified in Appendix A. The SLBs protocol is based on the one created by Yuji Zhu in August 2015 from the Moral-Mirabal Research Group based in the Department of Chemistry and Chemical Biology at McMaster University, Canada. This protocol was optimised and adapted to our experiments by **Augoustina Maria Economou**.

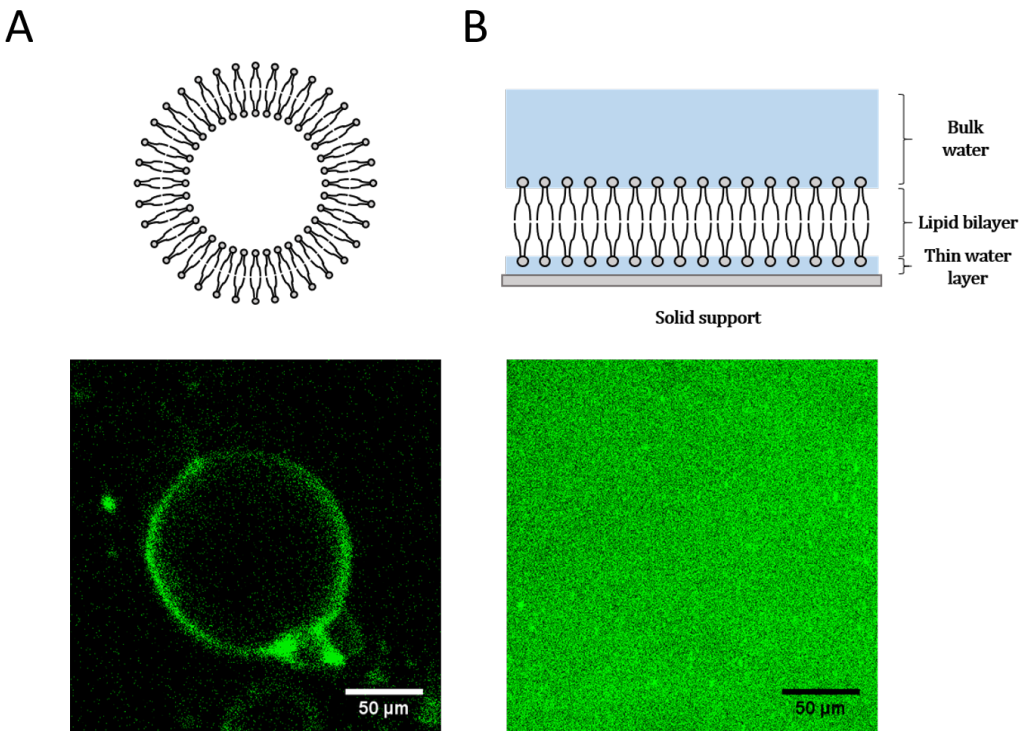

Figure 3.2: Cartoon and fluorescence confocal image of (A) GUV and (B) SLB. The cell membrane composition is DOPC and the used probe for visualisation purposes is di-4-ANEPPDHQ.

3.3.2 F^3 Setup & Acquisition Procedure

For performing F^3, a pair of synchronised TCSPC cards (SPC-150 Becker & Hickl) in combination with an inverted confocal microscope (Leica TCS SP2) was used. A schematic of the setup is presented in Figure 3.3. For the pre-bleach and post-bleach images, a picosecond diode laser (Hamamatsu PLP-10 470) at 467 nm was used at a repetition rate of 20 MHz and low power (μW) in order to narrow down

the Instrumental Response Function (IRF). For bleaching the sample, a solid-state Continuous Wave (CW) laser at 473 nm was used, with an average power of around 5 mW. Using the time-lapse acquisition series wizard, we set 3 pre-bleach images which were measured at a low excitation intensity. The next one corresponded to the bleach scan, where the CW laser was used and the sample bleached using typically a zoom factor of 16 for the R6G samples, and of 8 for the SLBs. Finally, a series of post-bleach images were recorded using the low intensity laser in order to get the FRAP recovery curve. The fluorescence emission was spectrally filtered by a 500 nm long-pass filter (Thorlabs 500LP) and separated into orthogonal polarisations by a beam splitter cube (Edmund Optics). The two orthogonally polarised beams were sent onto two GaAsP hybrid detectors (Becker & Hickl HPM-100-400). The detectors were protected from damage by excessive illumination by a shutter automatically closing during the bleaching step involving higher laser power (5 mW). The signal from the detectors was fed into the TCSPC cards in a PC running Windows 10. Time and polarisation-resolved images (128×128 pixels) were recorded with 256 time channels in a time window of 50 ns. A 63× 1.2 NA water-immersion objective was used to acquire the pair of polarised images. Around 250-300 images (cycles) were recorded in order to get the whole FRAP recovery curve, which required a total acquisition time of $\sim$ 5-10 min (for the R6G samples) and $\sim$ 35-40 min (for the SLBs).

For comparison and to validate the F^3 FRAP results, confocal FRAP was also performed. The setup used for this purpose was the same as mentioned in *Chapter* 2 (*Section* 3.1.3). Also, the data analysis follows similar guidelines as the ones described for the F^3 FRAP data. The only difference is that the data acquisition does not involve photon counting, as the signal is collected by the photomultiplier located in the scanhead of the confocal microscope. Also, the spatial resolution of the images is 512×512 pixels with a pixel size of 465.03 nm and a temporal spacing

between images of half the encountered for the F^3 FRAP data.

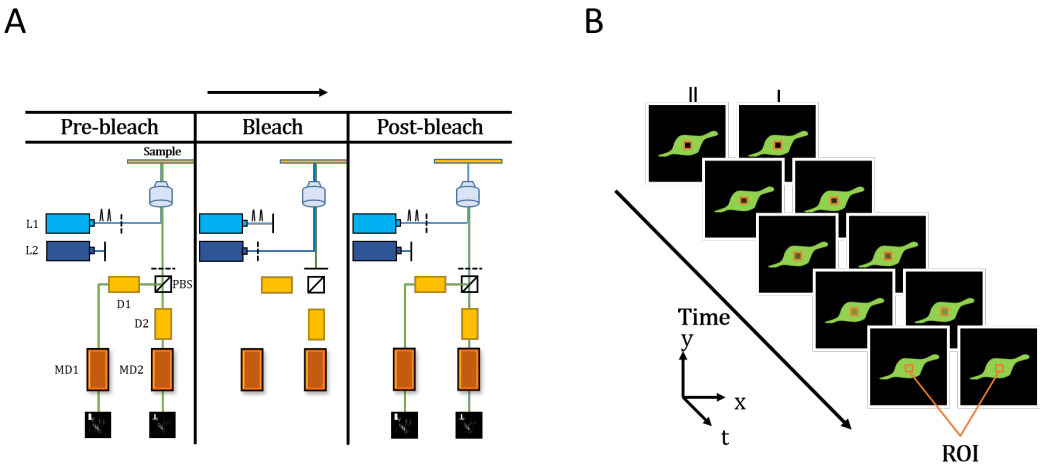

Figure 3.3: (A) F^3 input and (B) output diagrams. The first diagram presents the involved elements during the data acquisition. The second diagram displays the series of images (parallel and perpendicular) acquired during the experiment. L1 and L2 refer to the pulsed and CW lasers, respectively. D refers to detector, MD to module (electronic) and PBS to polarising beam splitter. Figures adapted from reference [201].

3.3.3 F^3 data analysis

The F^3 data was analysed with a home-built MATLAB script. In order to analyse the FLIM and FAIM data, the pair of polarised images were all summed, by component. This gave rise to two images: a parallel and a perpendicular intensity image. Adding the former ones according to $I_{tot} = I_{\parallel} + 2GI_{\perp}$, the total intensity map can be obtained. G accounts for the efficiency ratio between detection paths, including detectors. If G is equal to 1 it means that both detection paths are equally efficient. $I_{\parallel}$(t) and $I_{\perp}$(t) are the parallel and perpendicular polarised emission signals, respectively. The total intensity decay per pixel was deconvoluted by the IRF and the resultant was fitted with a single-exponential model:

$$I_{tot}(t) = IRF \otimes (I_0 e^{-t/\tau_F} + B) \tag{3.2}$$

where I_0 is the intensity amplitude, τ_F the fluorescence lifetime and B the background.

Also, by the recombination of both images, a fluorescence anisotropy map was reconstructed according to equation 3.3. Similarly, the steady-state fluorescence anisotropy image can be produced by adding up all the photons per pixel and polarisation transient and applying the same equation.

$$r(t) = \frac{I_{\parallel}(t) - GI_{\perp}(t)}{I_{\parallel}(t) + 2GI_{\perp}(t)} \tag{3.3}$$

where the anisotropy is normalised by the total intensity detected.

For the dye R6G in water/glycerol solutions, the dye is assumed to rotate freely and have a random distribution within the solution. This reconstruction has been achieved by fitting pixel by pixel the generated time-resolved anisotropy decays with the following expression:

$$r(t) = r_0 e^{-t/\theta} \tag{3.4}$$

where r_0 is the initial anisotropy determined by the relative orientation between the excitation and emission dipole transition moments, and the distribution of the orientation of the fluorophores. If the distribution is random and the dipole transition moments are parallel to each other, r_0 is equal to 0.4 when using single-photon excitation [20]. The rotational correlation time is given by θ, which corresponds to the time it takes the fluorophore to rotate 1 radian [20].

For the dye di-4-ANEPPDHQ in a DOPC SLB the fluorophore is considered to have restricted mobility due to the presence of the bilayer lipids that act as barriers. Therefore, a hindered rotation model is applied to its anisotropy data. This means the probe is free to wobble within the semi-angle of a cone [20, 37, 38]. For the extraction of the anisotropy parameters per pixel, parallel and perpendicular

intensities per pixel were fitted according to the following equations [266]:

$$I_{\parallel}(t) = \frac{1}{3} I_{tot}(t)[1 + 2r(t)] \tag{3.5}$$

$$I_{\perp}(t) = \frac{1}{3} I_{tot}(t)[1 - r(t)] \tag{3.6}$$

where I_{tot}(t) corresponds to the total emission intensity being equal to $I_{\parallel}$(t) + 2$I_{\perp}$(t) and r(t) is given by the following expression:

$$r(t) = (r_0 - r_\infty)e^{-t/\theta} + r_\infty \tag{3.7}$$

The limiting anisotropy value is given by r_∞ and is the value to which the anisotropy decays in time scales longer than the fluorophores lifetime and θ is the apparent rotational correlation time [20].

To generate the rotational correlation time map, the $I_{\parallel}$ and $I_{\perp}$ decays per pixel are recombined, according to equation 3.3, to generate the time-resolved anisotropy decay. An initial binning of the two intensity images must be performed in order to increase the number of counts per decay. If a binning of 5×5 is required to extract the fluorescence lifetime parameters, at least a binning of m = n + 1 must be applied for the reconstruction of the anisotropy decay per pixel. This is mainly due to the fact that each polarised intensity decay obeys a double-exponential model, which implies more degrees of freedom and therefore larger number of photons are needed to obtain acceptable uncertainties.

A weighted fit was performed for the extraction of the anisotropy parameters by applying the variance expression introduced by Lidke et al. [128]. A map for the steady state anisotropy standard deviation was produced. The variance of the

anisotropy is therefore given by the following equation [128]:

$$v(r) = \frac{(1-r)(1+2r)(1-r+G(1+2r))}{3I_{tot}(t)} \tag{3.8}$$

The standard deviation of r is given by sd(r)=$\sqrt{v(r)}$.

If the polarised intensity components are arranged such as the denominator of equation 3.3, the total intensity image is generated. According to equation 3.8, the total intensity is inversely proportional to the steady-state anisotropy standard deviation, which permits the clear visualisation of the bleach spot.

For R6G in water/glycerol solution, a single G-factor was measured. However, for the dye di-4-ANEPPDHQ in a DOPC SLB, the G-factor matrix was calculated. For this case, the ratio between parallel and perpendicular intensity decays of a stock solution of FITC ($\sim 5\,\mu$M) diluted in water was measured. Before dividing both transients, the background per intensity decay must be corrected/subtracted to account for the each of the detector's background. Figure 3.4 shows the steps needed to be taken in order to generate a G-factor matrix for the entire image on a pixel-basis. This method is more accurate than the previous one (calibration with R6G in water/glycerol solutions). However, its histogram presents a very homogeneous distribution, which seems to indicate that this approach is a good estimation.

Intensity images per component were binned in order to obtain a reasonable amount of counts at the peak for successful fits. For FLIM and FAIM, a binning of 3×3 pixels was used. Histograms of the FLIM and steady-state anisotropy maps were also generated for every reconstructed image.

If all the pixels information is summed, the result is a total single decay per polarisation. This is analogous to acquire a single decay per component by scan-

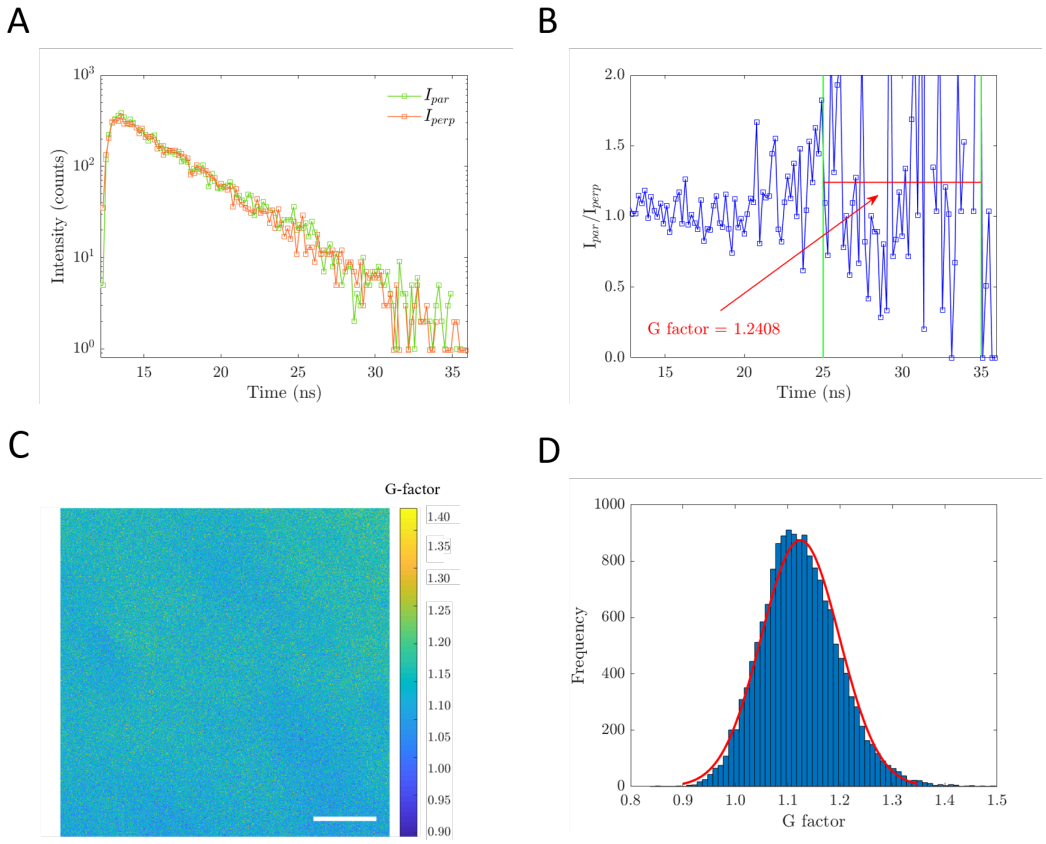

Figure 3.4: Representative G-factor data correspondent to the pixel position (75,75). (A) Parallel and perpendicular intensity decays after background subtraction. (B) G-factor decay given by the ratio of the two polarisation intensity decays. A mean value for that pixel position of 1.2408 in the selected range (within the magenta lines) is obtained. (C) G-factor map. (D) G-factor histogram and fit with μ = 1.124 and σ = 0.075. Scale bar: 50 μm.

ning the entire field of view. By using this approach and the previously mentioned equations, individual parameters for the fluorescence lifetime, rotational correlation time and steady-state fluorescence anisotropy, for instance, are extracted. The integrated time-resolved fluorescence anisotropy decay for the labelled-lipid system was fitted with equation 3.7 straightaway.

3.3.4 Translational and Rotational Diffusion

In solution, assuming Stokes-Einstein-Debye behaviour, the rotational diffusion coefficient (D_r) can be calculated from the rotational correlation time θ:

$$D_r = \frac{1}{6\theta} = \frac{k_B T}{8\eta\pi R_h^3} \tag{3.9}$$

where k_B is the Boltzmann constant, T the absolute temperature, η the viscosity and R_h the hydrodynamic radius of the fluorophore.

The FRAP data was also analysed with a MATLAB script. Every pair of polarised images per frame were summed, obtaining a total intensity image per frame. The bleach region of interest (ROI) was automatically masked by introducing the zoom factor as an input ($\times$16 for R6G and $\times$8 for the SLBs experiments). For every single image, the total amount of counts per ROI was added, giving rise to the intensity recovery curve. The rest of the F^3 *FRAP* data analysis is described in *Section* 3.1.5 of *Chapter* 2. When *confocal FRAP* was performed, the entire FRAP data analysis of *Section* 3.1.5 of *Chapter* 2 can be applied here.

For FRAP, a binning of 5$\times$5 was applied and the final recovery curve smoothed with a Gaussian Kernel filter, with σ = 2.

If both techniques, tr-FAIM and FRAP, are combined, the hydrodynamic radius of the fluorophore can be inferred without having any previous knowledge about the viscosity of the environment. This is possible by the rearrangement of the SDE equations for rotational and translational diffusion mobilities. Let's recall the SDE equation that describes the translational diffusion coefficient of the probe:

$$D_t = \frac{k_B T}{6\eta\pi R_h} \tag{3.10}$$

Combining equations 3.9 and 3.10, the hydrodynamic radius of the probe is given

by:

$$R_h = \sqrt{\frac{3}{4}\frac{D_t}{D_r}} = \sqrt{\frac{9}{2}m} \tag{3.11}$$

where m corresponds to the gradient of plotting D_t against $\frac{1}{\theta}(6D_r)$ and is equal to $\frac{4}{18}R_h^2$.

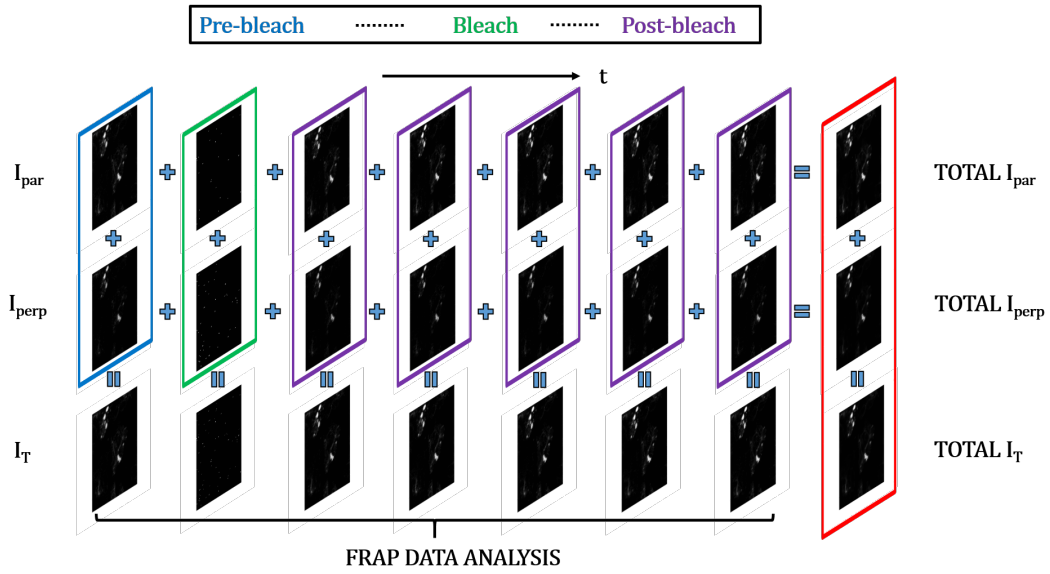

Figure 3.5: F^3 data acquisition and analysis. The three steps performed during the data acquisition and presented in Figure 3.3A are indicated by colours: pre-bleach in blue, bleach in green and post-bleach in purple. The first raw corresponds to the parallel intensity images per time data point, the second one to the perpendicular intensity images and the last one to the total intensity images. From the former raw, the FRAP data analysis is undertaken. An integration of all the parallel intensity images yields the total parallel intensity one. The same happens with the perpendicular transient. The combination of these two images gives rise to the anisotropy (steady-state and time-resolved) maps. The last element of the last column is the total intensity image, which is the combination and integration of the two previous ones. From this image, the fluorescence lifetime map is calculated.

The Stokes-Einstein-Debye equations are applied to R6G in water/glycerol solutions, where the dye rotates freely and is modelled as a sphere. However, this approach considers the spherical molecule to be surrounded by a viscous liquid medium, meanwhile the labelled-lipids are surrounded by the internal membrane and also by the external one. The Stokes Paradox states that the effect of the external medium surrounding the membrane may imply a certain limitation in the

translational diffusion coefficient of the probe. In order to overcome this limitation, Saffman and Delbruck developed a model named after them to describe Brownian motion (diffusion) in biological membranes [39]. The updated equations used to characterise the rotational and translational diffusion consider the labelled-lipid to have a cylindrical shape:

$$D_r = \frac{k_B T}{4\eta\pi R_h^2 h} \tag{3.12}$$

$$D_t = \frac{k_B T}{4\eta\pi h}\left(ln\frac{\eta h}{\eta^{'} a} - \gamma\right) \tag{3.13}$$

where η is the lipid viscosity, $\eta^{'}$ is the viscosity of the surrounding medium (water), h is the thickness of the membrane, a stands for the radius of the dye and γ is the Euler-Mascheroni constant, which is ~ 0.577.

The hydrodynamic radius of the probe can be used by combining these two models, as performed with the Einstein-Stokes-Debye equations. However, several assumptions about the system must be made. We will assume the lipid bilayer is free-standing, which means it is surrounded by aqueous phases on both sides, although this is not exactly true as our SLBs are deposited onto a glass substrate, where only a thin water layer exists between membrane and substrate. The size of the system is considered as infinite. Saffman-Delbruck model applies to a thin layer of viscous fluid surrounded by a less viscous fluid, which is water. Therefore, the approximations done for a biological membrane are as follows: $R_h \sim$ h and $\frac{\eta}{\eta^{'}} \sim 10^2$. The hydrodynamic radius is therefore given by the combination of equations 3.12 and 3.13:

$$R_h = \sqrt{4.0280\frac{D_t}{D_r}} = 4.9161\sqrt{\theta D_t} \tag{3.14}$$

For the SLB work, both models, Stokes-Einstein-Debye and Saffman-Delbruck, are applied and compared.

3.3.4.1 Refractive Index Measurements

The refractive index of each water/glycerol R6G solution was measured with the help of an Abbe refractometer. A lamp (visible range) was used and the system was calibrated with water, whose value is very well known (0.3 cP) [178]. The readings were modified according to the reference given by the water refractive index and were all taken at room temperature. For each solution, five readings were taken (up to 4 decimals), yielding a final average along with a very low standard deviation. The refractive index readings were converted into viscosity [265].

3.3.4.2 Excitation and Emission Spectra

As a reference, the emission spectra of the probe di-4-ANEPPDHQ in lipid solution is measured by using a luminescence spectrometer (Perkin-Elemer LS-5) with a quartz cuvette. The sample is excited at 485 nm and the emission i0

00

s recorded from 500 to 800 nm, in 2 nm steps.

The absorption spectrum is obtained by using an absorption spectrometer (Hitachi U-4100 dual beam spectrometer), with a square-based quartz cuvette. The absorption spectra are recorded from 350 to 600 nm in 2 nm steps and the solvent response that accompany the dye is subtracted. Therefore, another identical measurement is taken for the solvent itself, which in this case is the SLB buffer. In the visible range, the absorption and excitation spectra are alike, so we can refer to it as 'excitation spectrum'.

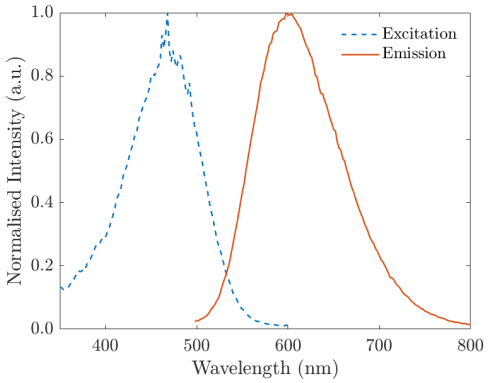

Figure 3.6: Emission and Excitation spectra of di-4-ANEPPDHQ in DOPC Lipid Solution.

3.4 Results & Discussion

3.4.1 Setup Calibration with Rhodamine 6G

3.4.1.1 Fluorescence Lifetime Studies

We start the F^3 setup calibration by assessing the R6G fluorescence lifetime response in different refractive index (and viscosity) solutions. A total amount of 5 measurements per sample were taken. The main objective consists of validating the Strickler-Berg relationship [25], which establishes that the fluorophore's fluorescence lifetime is inversely proportional to the square of its environmental refractive index [267]. A single exponential model was applied for the description of the total intensity decay per pixel. The fit was performed with additional deconvolution of the IRF as presented in equation 3.2, ensuring $1 < \chi^2_R < 1.5$. In the case χ^2_R was out of this range, the outcome was not taken into account for the overall distribution, which was found to be uniform, as expected for a dye in an homogeneous solution. The IRF was measured by using a solution of FITC in water quenched by NaI. An example of the intensity decays (parallel, perpendicular and total) encountered in every image per pixel and after binning can be observed in Figure 3.7A. A representative fit of each total intensity decay per pixel is given by Figure 3.7B. Finally,

the last row of Figure 3.7 shows a representative fluorescence lifetime map and histogram. The histogram is fitted with a Gaussian distribution and from it the mean fluorescence lifetime is extracted.

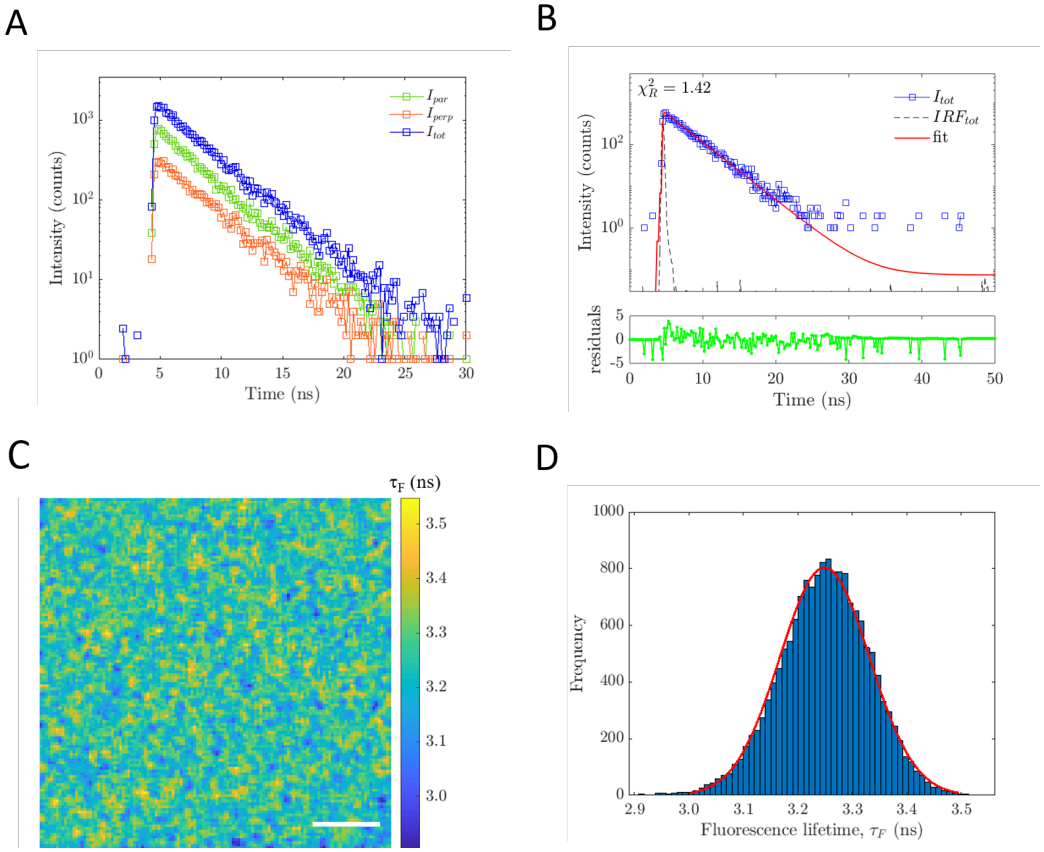

Figure 3.7: Representative fluorescence lifetime data of the R6G solution with 98.48 % glycerol and 1.52 % water for 1 pixel. (A) Parallel, perpendicular and total intensity decays. (B) Total intensity fit with parameters I_0 = 245.9331, τ_F = 3.1507 and BG = 0.0347. (C) Fluorescence lifetime map with a pixel size of 1.8601 μm. (D) Fluorescence lifetime map histogram and fit with μ = 3.25 and σ = 0.08 ns. Scale bar: 50 μm.

Figure 3.8 presents no correlation between τ_F^{-1} and n^2, which means the Strickler-Berg relationship is not followed by these two variables. The reason could lie in the fact that the refractive indices of all the solutions with a certain glycerol/water composition span a small range. This does not allow a clear distinction between fluorescence lifetime responses, giving rise to almost identical answers. All the fluorescence lifetime values are extracted from a Gaussian fit of the correspondent fluorescence lifetime map histogram and finally averaged. A summary can

be observed in Table 3.1, whose fluorescence lifetime values are in good agreement with previously reported ones for rhodamine 6G in glycerol, with a similar molar concentration and at room temperature [268].

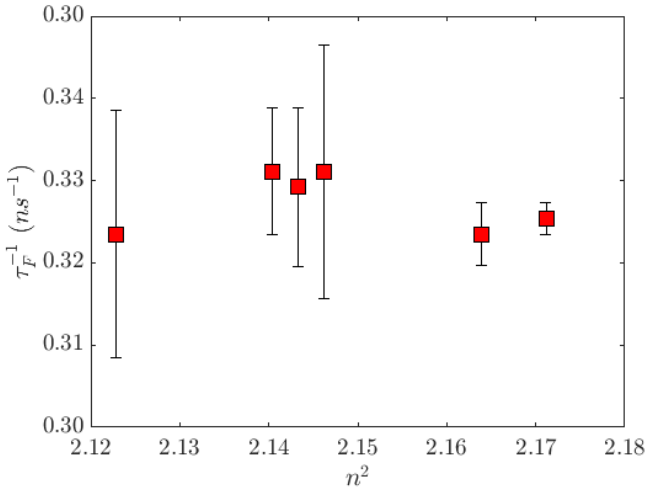

Figure 3.8: Inverse of fluorescence lifetime per R6G solution against its quadratic environmental refractive index.

Table 3.1: Refractive index and fluorescence lifetime per R6G glycerol-water solution.

% **glycerol**	**n** $\pm$ **0.0005**	n^2 $\pm$ **0.0008**	τ_F **(ns)**	**1/**τ_F **(ns**$^{-1}$**)**
100.00	1.4735	2.1712	3.25 $\pm$ 0.01	0.308 $\pm$ 0.001
98.48	1.4710	2.1638	3.26 $\pm$ 0.02	0.306 $\pm$ 0.002
94.67	1.4650	2.1462	3.22 $\pm$ 0.08	0.311 $\pm$ 0.008
94.34	1.4640	2.1433	3.23 $\pm$ 0.05	0.310 $\pm$ 0.004
93.36	1.4630	2.1404	3.22 $\pm$ 0.04	0.311 $\pm$ 0.003
89.37	1.4570	2.1228	3.26 $\pm$ 0.08	0.307 $\pm$ 0.007

3.4.1.2 Steady-State Anisotropy

Representative data for a solution of rhodamine 6G in 98.48% glycerol and 1.52% water is presented in this section. From the F^3 data, the steady state anisotropy and its standard deviation maps were generated as explained in *Section* 3.3.3. The steady-state anisotropy map (Figure 3.9A) presents a slightly skewed distribution, instead of a uniform one (Figure 3.9B). The steady-state anisotropy histogram was fitted with a Gaussian function (μ = 0.27 and σ = 0.045). This skewed distribution

is not expected as the solution is homogeneous (water/glycerol) and, apart from molecular rotation, there are no additional depolarisation effects/pathways happening in any specific locations. The skewed distribution of the steady-state anisotropy map may be related to a laser misalignment. A minimum misalignment in the excitation laser may alter the ratio between the parallel and perpendicular intensity decays per pixel. The calculated G-factor was obtained as a ratio between the parallel and perpendicular intensity decays of the entire field of view instead of a pixel by pixel-based acquisition data. The generation of a G-factor map would assign a pixel by pixel G-factor value, which may amend the non-uniform steady-state anisotropy map (Figure 3.9A).

The steady-state anisotropy standard deviation map (Figure 3.9C) presents a consistent distribution such as the steady-state anisotropy map (Figure 3.9A), apart from the central region where the intentional bleaching has taken place. A Gaussian fit of Figure 3.9C gives rise to a mean value of 0.030 and a standard deviation of 0.001. Figure 3.10 shows similar representative data for the total intensity quantity. The uniformity in the steady-state anisotropy standard deviation, apart from the central area, means that the variance of each anisotropy data point is in the same order of magnitude due to its strong dependence on the integrated total intensity, whose values are of a much larger order of magnitude in comparison to the steady state anisotropy ones (equation 3.8). In Table 3.2 all the mean results for each quantity (steady state anisotropy, its standard deviation and total intensity) at different R6G solution viscosities are recorded. The viscosity of each R6G solution is calculated by using the method developed by Nian-Sheng Cheng [190], which takes into account the water/glycerol ratio of the solution and its temperature (T = 22°). The difference in viscosity among R6G solutions is big enough to observe a different response in terms of steady state anisotropy, which increases with viscosity (Figure 3.11A). If the inverse of the steady-state anisotropy is plotted against the inverse of

the solution's viscosity, the inverse of the initial anisotropy r_0 can be inferred from the fit intercept, applying equations 3.9 and 3.15 (Figure 3.11A). The data is fitted with a linear relationship, from where the gradient and intercepts are inferred: 262 $\pm$ 67 cP and 3.3 $\pm$ 0.1. If the inverse of the intercept is calculated, the following r_0 is obtained: 0.30 $\pm$ 0.01. The steady-state anisotropy r increases with the solution's viscosity due to the higher restriction in mobility the dye experiences, which slows down its rotational correlation time. According to the Perrin equation (equation 3.15), if the fluorescence lifetime and the initial anisotropy remain constant, the steady-state anisotropy increases with the viscosity [20].

$$r = \frac{r_0}{1 + \tau/\theta} \tag{3.15}$$

The fluorescence lifetime has been previously shown to remain constant (Figure 3.8 and Table 3.1) and further studies will show that this can also be translated to the initial anisotropy value, as expected, as the only additional depolarisation pathway is related to the NA of the objective, which is identical to all measurements.

The dependence of the standard deviation of the steady-state anisotropy on the viscosity of the solution is also assessed. We have already mentioned that $sd(r)$ does depend very strongly on the total amount of photons I_{tot}. According to equation 3.8, $sd(r)$ drops with the square root of I_{tot}, for a fixed steady-state anisotropy r value. In our case, r does vary within a limited range. However, this variation is that small in comparison to the total amount of photons that the relationship between variables seems to be followed anyways (Figure 3.11B and C).

3.4.1.3 Time-Resolved Fluorescence Anisotropy Studies

The dependence of the dye's rotational correlation time θ on the viscosity of the solvent is calculated by integrating all the counts by time bin and intensity decay across the entire FOV (Table 3.3). The initial anisotropy values r_0 per solution's vis-

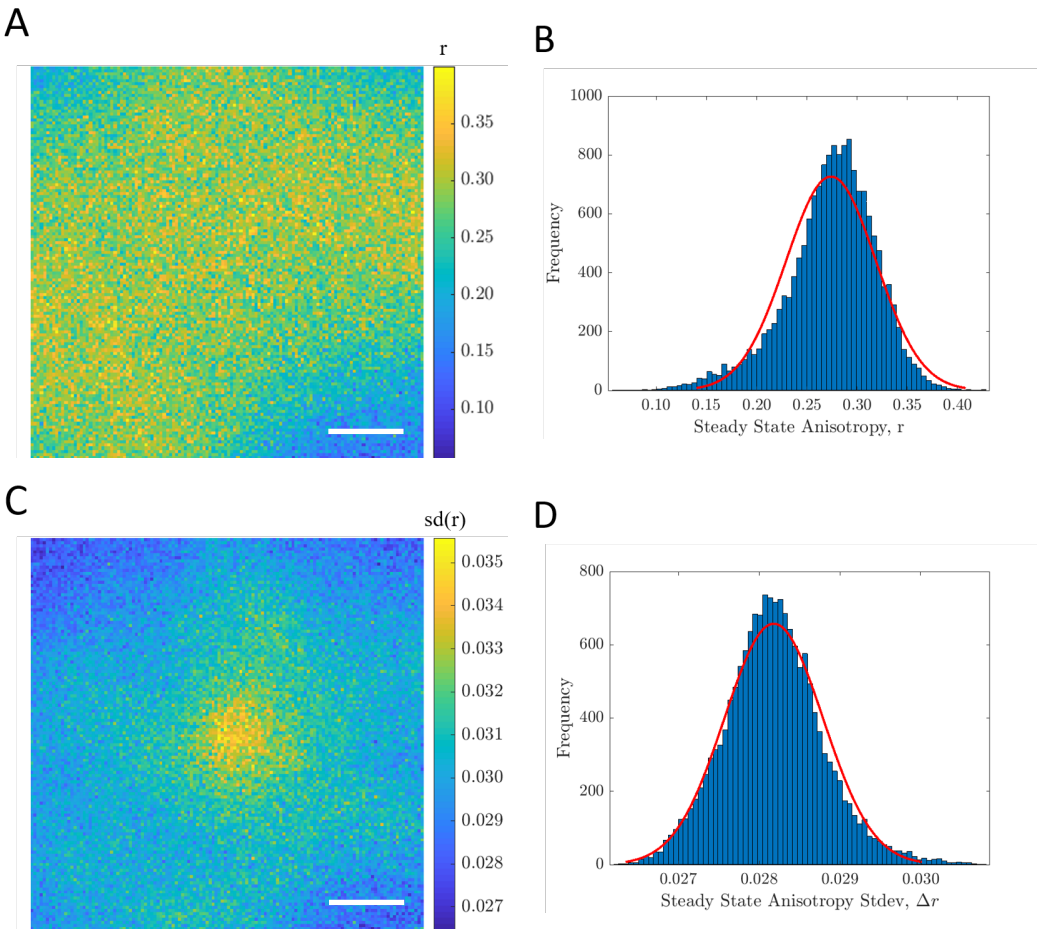

Figure 3.9: Representative steady-state anisotropy and steady-state anisotropy standard deviation data of the R6G solution with 98.48 % glycerol and 1.52 % water. (A,B) Steady-state anisotropy map and histogram. The fit of the histogram gives arise to $\mu = 0.27$ and $\sigma = 0.045$. (C,D) Steady-state anisotropy standard deviation map and histogram. The fit of the histogram yields to the following parameters: $\mu = 0.03$ and $\sigma = 0.001$. Scale bar: 50 μm.

cosity are also displayed in Table 3.3. These values are in good agreement with the r_0 extracted from the relationship of r^{-1} and η^{-1}, for each solution's viscosity (r_0 = 0.30 $\pm$ 0.01). Representative intensity decays (parallel and perpendicular) along its anisotropy decay of a R6G solution with 98.48% glycerol, is displayed in Figure 3.12. If the rotational correlation time is plotted against the solution viscosity, the hydrodynamic radius of the dye can be calculated by using equation 3.9, where the dye's shape is modelled as a sphere. The result yields a hydrodynamic radius for R6G of $R_{h,rot}$ = 0.411 $\pm$ 0.001 nm.

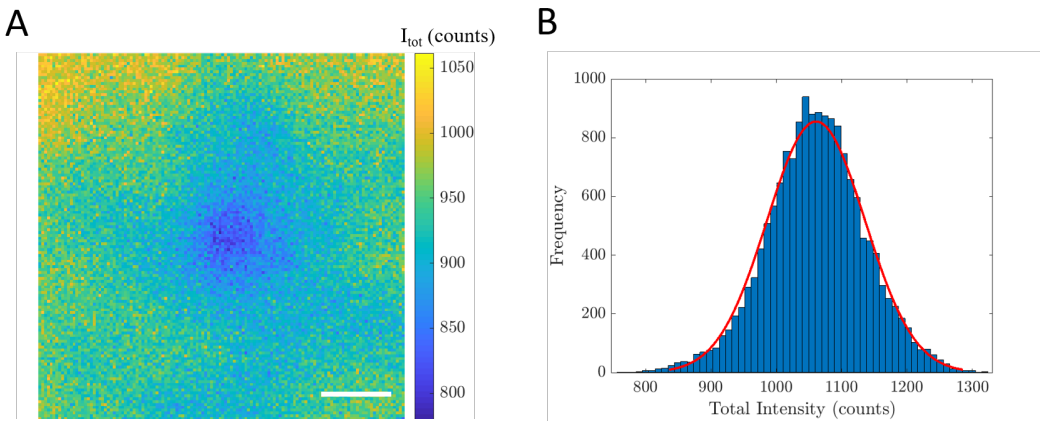

Figure 3.10: Representative intensity data for R6G solution with 98.48 % glycerol and 1.52 % water. (A) Intensity map. (B) Intensity histogram. The fit parameters are: μ = 1060 and σ = 75. Scale bar: 50 μm.

Table 3.2: Steady-state anisotropy, steady-state anisotropy standard deviation and intensity per R6G water-glycerol solution.

% **glycerol**	**Viscosity (cP)**	**r**	**sd(r)**	**I (counts)**
100.00	1178.60	0.287 ± 0.009	0.0540 ± 0.0022	720 ± 26
98.48	911.02	0.276 ± 0.002	0.0451 ± 0.0006	1090 ± 41
94.67	500.34	0.266 ± 0.003	0.0427 ± 0.0004	1059 ± 17
94.34	476.41	0.263 ± 0.004	0.0425 ± 0.0009	1082 ± 70
93.36	473.81	0.254 ± 0.005	0.0492 ± 0.0031	770 ± 84
89.37	239.13	0.228 ± 0.008	0.0557 ± 0.0140	730 ± 180

A map of the rotational correlation time dependence on solvent viscosity is calculated in order to visualise how consistent this quantity (θ) is across the FOV.

Some representative data for R6G in a solution of 94.67% glycerol and rest of water is presented in Figure 3.13. Figure 3.13A corresponds to the calculated time-resolved fluorescence anisotropy decay of a single pixel along its fit. Figure 3.13B accounts for the rotational correlation time map and on its right hand side its histogram is displayed (Figure 3.13C). It is worth to mention that the histogram of the rotational correlation time is always encountered to present an unsymmetrical distribution, with one side of the former slightly skewed. While the other quantities (fluorescence lifetime, steady-state anisotropy and total intensity), exhibit a normal distribution (or should exhibit a normal distribution if no laser misalignment issues

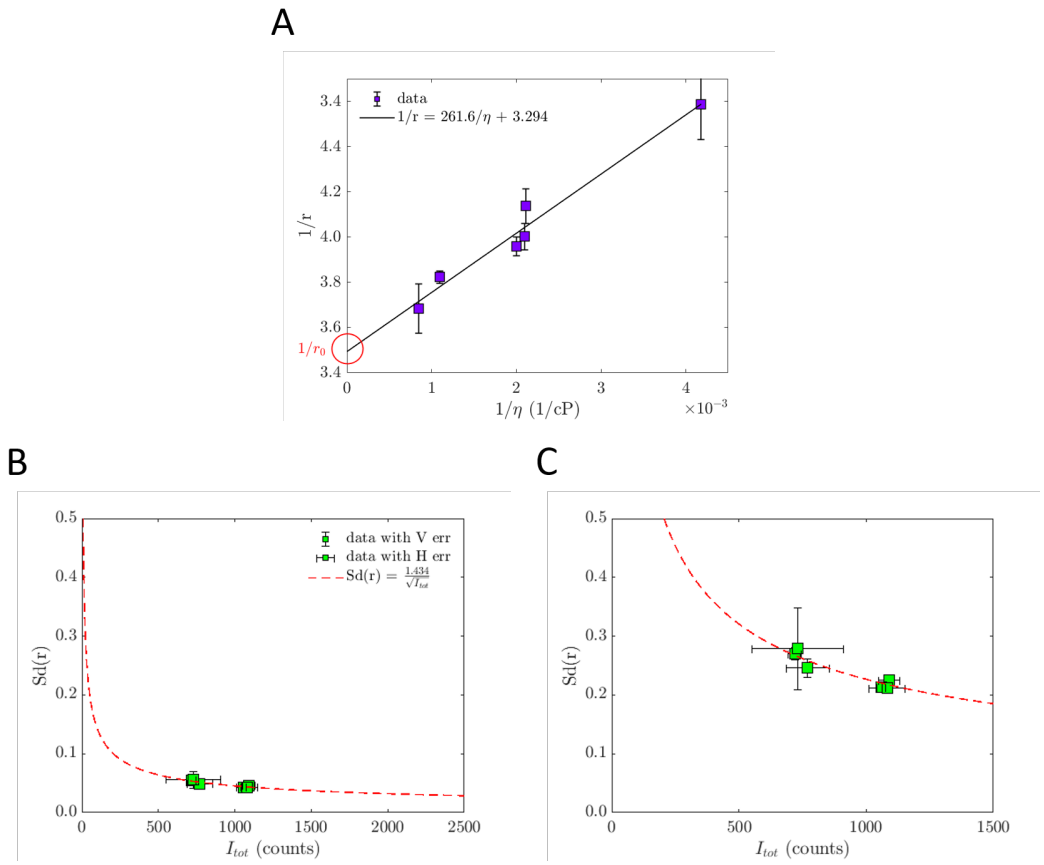

Figure 3.11: (A) Inverse of steady-state anisotropy against inverse of R6G solution viscosity. The data is fitted with a linear relationship, whose fit parameters are: gradient (261.6 ± 66.9 cP) and intercept (3.294 ± 0.155). (B) Steady-state anisotropy standard deviation against total number of counts per R6G solution. The values are extracted from the fit parameters of the produced map histograms. (C) Enlarged view of (B).

were encountered), this parameter θ presents a different distribution. Question that one might come up with are: Is it real? Does the theory predict this same behaviour or is there any experimental uncertainty associated with the final result that may justify the shape of its distribution? Does the distribution present this shape due to the inefficiency and/or failure of the fits? Some inefficient fits may overestimate the rotational correlation time and explain its uneven shape. The explanation of this phenomenon is the subject of the following chapter.

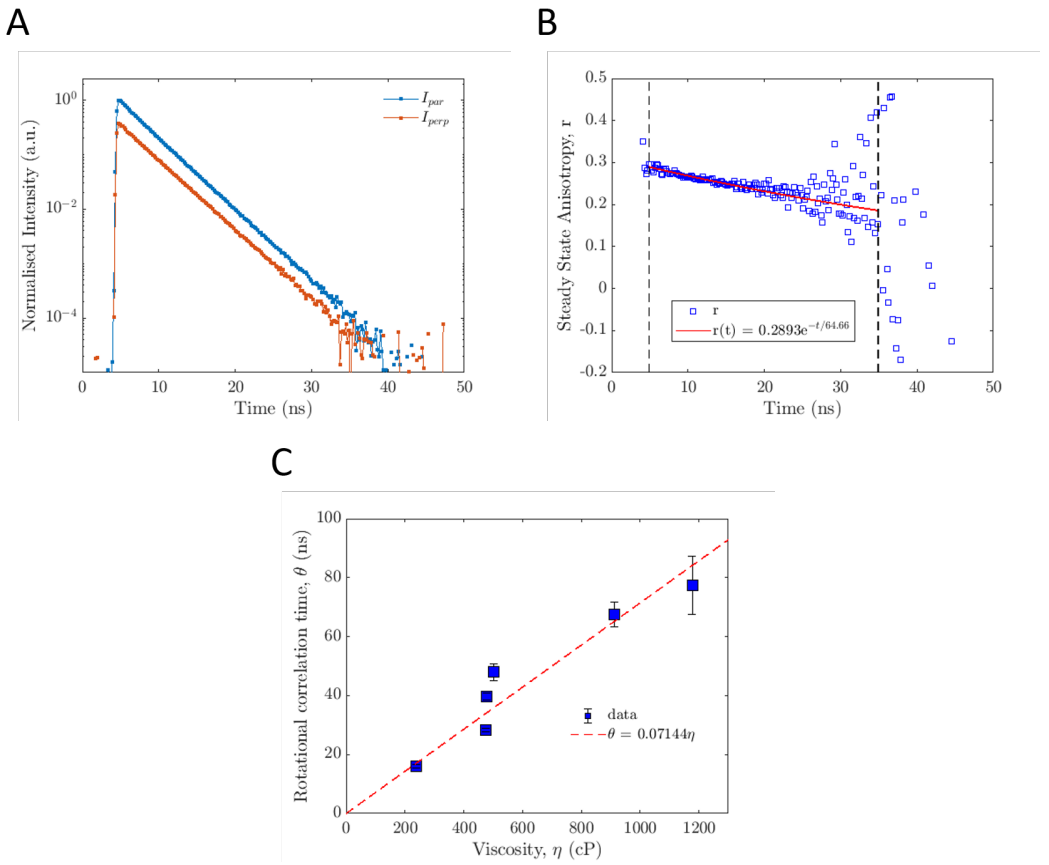

Figure 3.12: Representative time-resolved anisotropy data from the integration of all the image pixels signal and for R6G solution in 98.48 % glycerol and 1.52 % water (η = 911.02 cP). (A) Parallel and perpendicular normalised intensity decays. (B) Time-resolved anisotropy decay and fit. (C) Rotational correlation time against viscosity R6G solution, with a gradient of 0.07 $\pm$ 0.01 ns/cP.

Table 3.3: Fit parameters of the integrated time-resolved anisotropy decay per R6G water-glycerol solution.

% **glycerol**	**Viscosity (cP)**	r_0	θ **(ns)**
100.00	1178.60	0.300 $\pm$ 0.008	77.3 $\pm$ 9.9
98.48	911.02	0.290 $\pm$ 0.001	67.5 $\pm$ 4.1
94.67	500.34	0.287 $\pm$ 0.003	48.0 $\pm$ 2.8
94.34	476.41	0.288 $\pm$ 0.003	39.7 $\pm$ 1.1
93.36	473.81	0.281 $\pm$ 0.006	28.3 $\pm$ 0.6
89.37	239.13	0.272 $\pm$ 0.009	15.9 $\pm$ 0.6

3.4.1.4 F^3 and Confocal Translational Diffusion

The translational diffusion coefficient of the R6G dye in glycerol/water solutions of varying viscosities was calculated. A total amount of five measurements for each

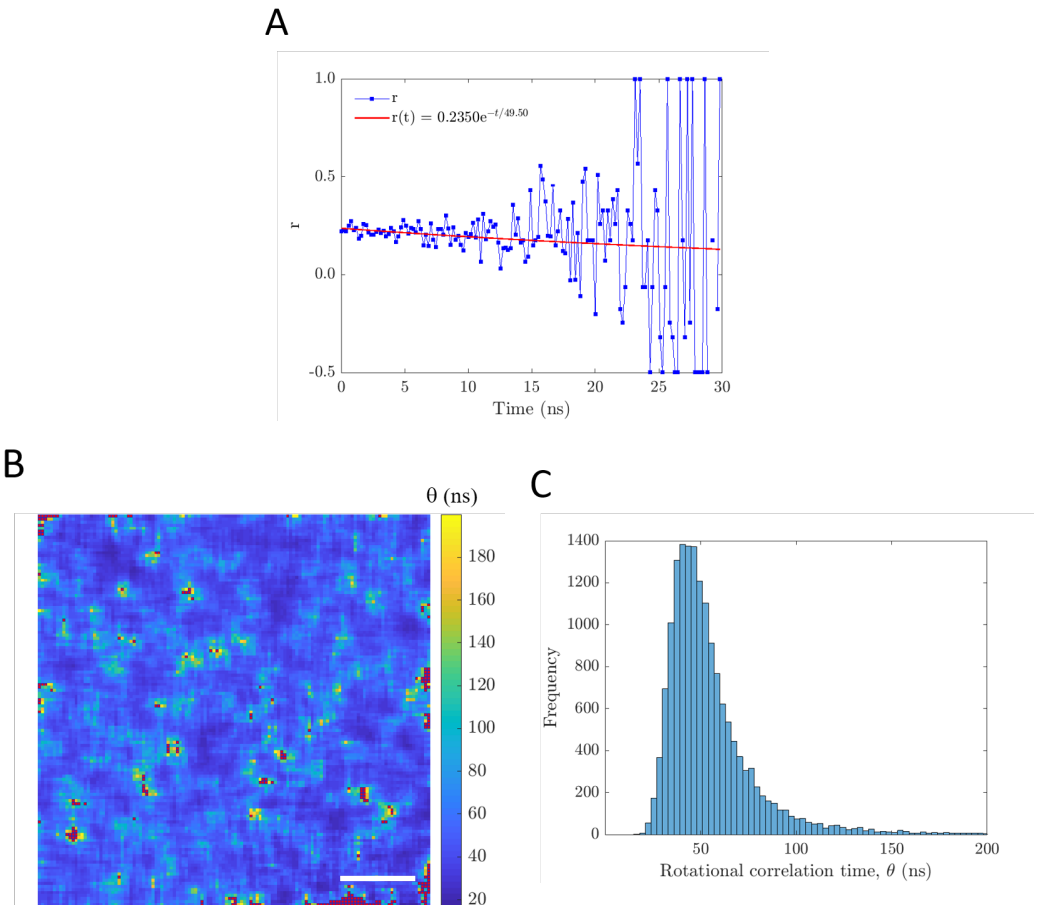

Figure 3.13: (A) Time-resolved fluorescence anisotropy decay and fit, (B) rotational correlation time map and (C) histogram for some representative R6G data (94.67% glycerol). A binning of n = 3 (7×7 pixels) has been applied. The red dots displayed on the map correspond to that rotational correlation time values beyond 200 ns, which was set as a threshold. Scale bar: 50 μm.

sample.

Examples of some representative FRAP data for both techniques, F^3 and confocal, are presented in Figures 3.14 and 3.16. In both figures, the upper graph (Figures 3.14A and 3.16A) correspond to a representative FRAP recovery curve fitted with a double exponential model (equation 2.21). Figures 3.15 and 3.17 present the bleach spot profile fit per technique, respectively. All the translational parameters are displayed in Tables 3.4 and 3.5, for F^3 and confocal FRAP, respectively. It is not surprising that the F^3 FRAP data (Figure 3.14) presents a lower signal-to-noise ratio (SNR) in comparison to the confocal FRAP data (Figure 3.16), as its acquisition

is based on time-resolved single photon detection, which makes the data analysis more laborious. This is reflected in the large standard deviations associated with the half-recovery time mean parameters (Table 3.4). Therefore, F^3 data requires additional spatial smoothing methods that allows the enhancement of the signal.

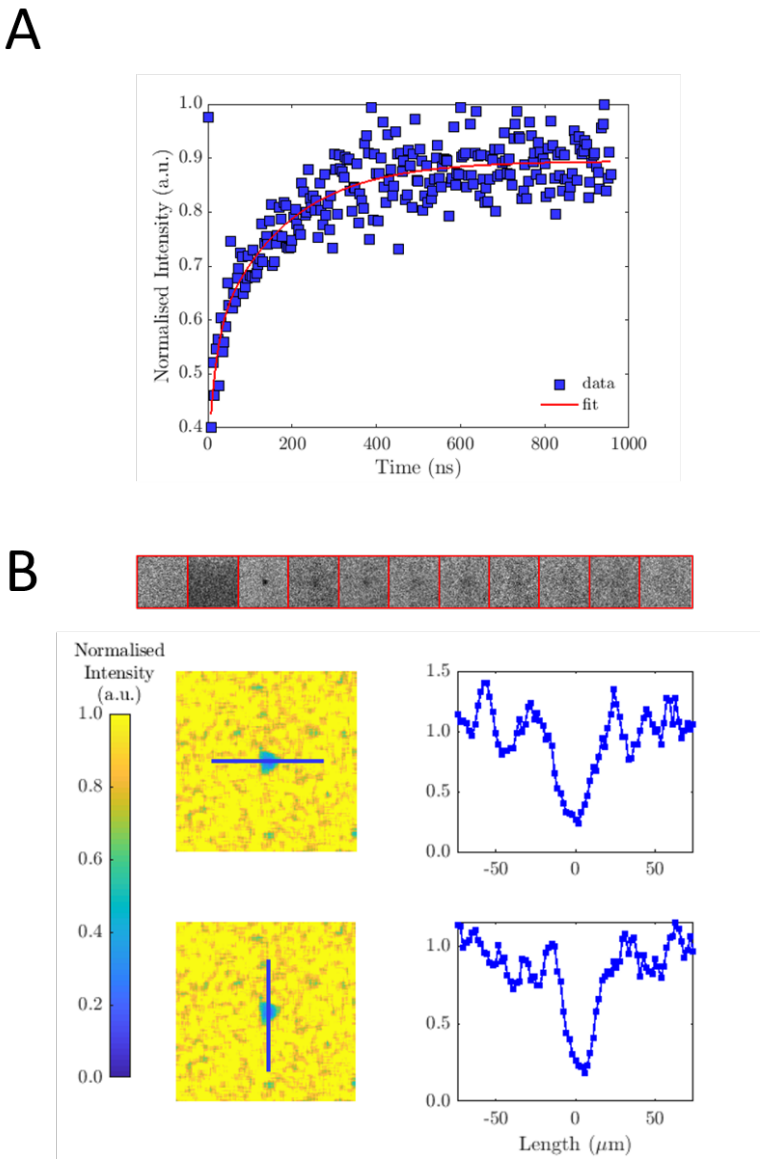

Figure 3.14: Representative data for R6G in 98.48% glycerol and 1.52% water. (A) Corresponds to the FRAP recovery curve and (B) to the different angular-oriented bleach spot profiles of the normalised first postbleach image. Each image has 128×128 pixels with a pixel size of 1.9 μm. The scale colours for (A) and (B) images are false. The dimensions of each frame is 238×238 μm^2.

The hydrodynamic radius of R6G can be inferred from the slope of the plot of

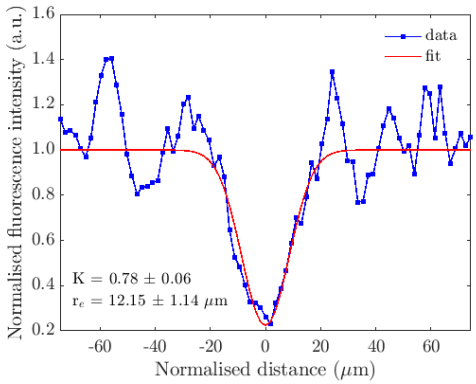

Figure 3.15: Profile data of the normalised first postbleach image with fit.

Table 3.4: Parameters extracted from the F^3 FRAP data per R6G glycerol/water solution.

% glycerol	Viscosity (cP)	r_e (μm)	$\tau_{1/2}$ (s)	F^3 D_T (μm^2/s)
100.00	1178.60	10.1 ± 0.2	67 ± 14	0.51 ± 0.23
98.48	911.02	14.4 ± 2.1	99 ± 28	0.50 ± 0.14
94.67	500.34	14.1 ± 0.4	44 ± 6	0.82 ± 0.15
94.34	476.41	15.3 ± 2.7	39 ± 7	0.99 ± 0.20
93.36	473.81	12.9 ± 2.0	26 ± 8	1.27 ± 0.19
89.37	239.13	13.0 ± 1.4	17 ± 3	2.09 ± 0.25

the translational diffusion coefficient D_t against the inverse viscosity of the solvent for both F^3 and confocal FRAP via equation 2.23 (Stokes-Einstein-Debye). The viscosity and temperature must be known. The results are plotted in Figure 3.18 and the data is fitted with a polynomial equation of first order. The calculated hydrodynamic radii per technique are as follows: R_{h,F^3} = 0.43 ± 0.10 nm and $R_{h,Conf}$ = 0.36 ± 0.06 nm. Therefore, we demonstrated F^3 FRAP against confocal FRAP.

3.4.1.5 F^3 and Confocal Translational Diffusion against Rotational Diffusion

If the translational and rotational information is combined, the hydrodynamic radius of the dye can be obtained straightaway, without any prior knowledge about viscosity. This has been done by plotting the average translational diffusion coefficient per R6G glycerol/water solution against the inverse of its corresponding rotational correlation time (Figure 3.19). Thus, for both FRAP techniques, the hy-

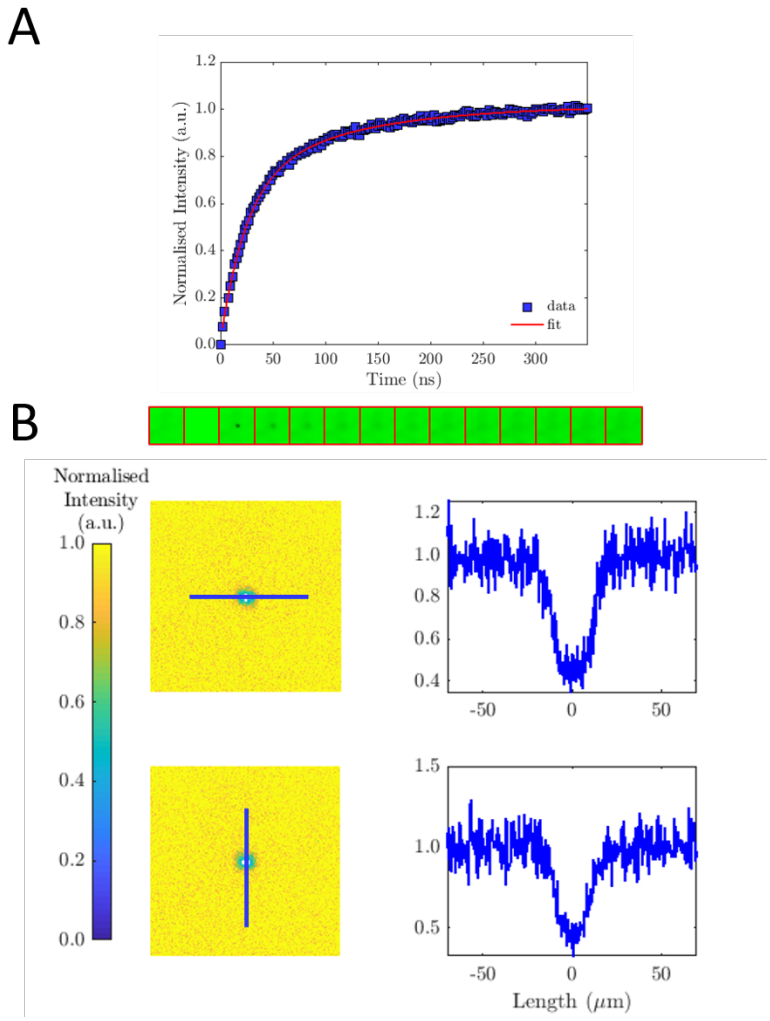

Figure 3.16: Representative data for R6G in 94.67 % glycerol and 5.33 % water. (A) Corresponds to the FRAP recovery curve and (B) to the different angular-oriented bleach spot profiles of the normalised first postbleach image. Each image has 512×512 pixels with a pixel size of 0.46 μm. The scale colours for (A) and (B) images are false. The dimensions of each frame is 238×238 μm^2.

drodynamic radius of R6G is calculated applying equation 3.11. The results for each technique are presented in Table 3.6. The hydrodynamic radii are very similar when the anisotropy and FRAP techniques are performed individually. Overall, the hydrodynamic radius of the dye is in good agreement with the work presented by A. J. Bain et al. [269], Müller et al. [270] and Gendron et al. [271] (R_h = 0.46, 0.53 and 0.51 nm, respectively). J. Bain and coworkers calculated the volume of the dye by performing picosecond anisotropy studies in anisotropy media, while Müller and

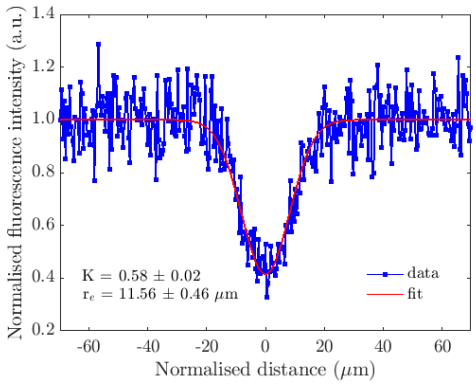

Figure 3.17: Profile data of the normalised first postbleach image with fit.

Table 3.5: Parameters extracted from the confocal FRAP data per R6G glycerol/water solution.

% glycerol	Viscosity (cP)	r_e (μm)	$\tau_{1/2}$ (s)	Confocal D_T (μm^2/s)
100.00	1178.60	11.3 ± 0.6	75.6 ± 0.4	0.37 ± 0.03
98.48	911.02	11.9 ± 0.8	52.4 ± 5.0	0.61 ± 0.06
94.67	500.34	11.6 ± 0.1	35.0 ± 1.6	0.86 ± 0.07
93.36	473.81	11.3 ± 0.5	22.9 ± 0.7	1.27 ± 0.09
89.37	239.13	13.2 ± 0.8	17.2 ± 1.4	2.61 ± 0.33

Gendron calculated the translational diffusion coefficient of rhodamine 6G using multi-colour dual-focus FCS and Pulsed Field Gradient–Nuclear Magnetic Resonance in combination with FCS, respectively. Although our results are of the same order or magnitude as the results presented in literature, they are smaller, which may be most likely due to artefacts introduced by FRAP.

Table 3.6: Hydrodynamic radius of R6G extracted from the combination of the rotational correlation time information and the confocal and F^3 FRAP data.

FRAP Type	$R_{h,FRAP\&rot}$ (nm)
Confocal	0.42 ± 0.04
F^3	0.39 ± 0.08

3.4.2 F^3 applied to Di-4-ANEPPDHQ in DOPC SLBs at RT

3.4.2.1 Fluorescence Lifetime Studies

In this work, we first investigated the fluorescence lifetime response of the dye di-4-ANEPPDHQ in DOPC SLBs at room temperature (RT). Representative intensity

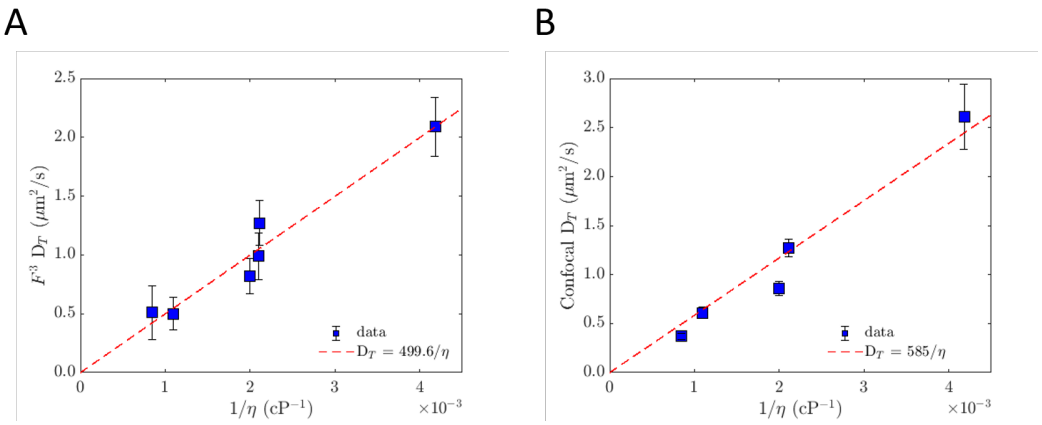

Figure 3.18: (A) F^3 and (B) confocal trasnlational diffusion coefficients against inverse of R6G solution's viscosity.

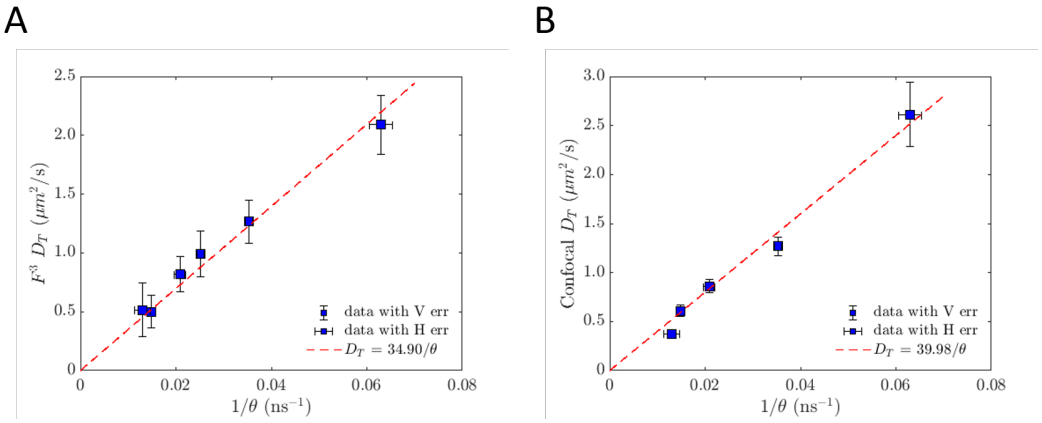

Figure 3.19: (A) F^3 and (B) confocal translational diffusion coefficient against inverse of rotational correlation time for R6G in varying water/glycerol viscosity solutions.

decays ($I_{\parallel}$, $I_{\perp}$ and I_{tot}) per pixel and total intensity fit are displayed in Figure 3.20A and B. Fluorescence lifetime maps per measurement were created and their corresponding histograms generated - Figure 3.20C and D. The average fluorescence lifetime parameter per measurement was obtained by fitting each histogram distribution with a Gaussian function. The overall average fluorescence lifetime is given by $\tau_F = 2.10 \pm 0.06$ ns. Our results are in good agreement with the values reported by Owen et al., Le Marois et al. and Steele et al. [236, 239, 240], although, as previously pointed out, they studied systems that are not identical to ours, as their membranes are not planar but in vesicle form. The investigation of the fluorescence

lifetime τ of a lipid system provides information about its hydration and polarity. Therefore, if the system is highly hydrated, a decrease on its fluorescence lifetime via quenching is expected [272].

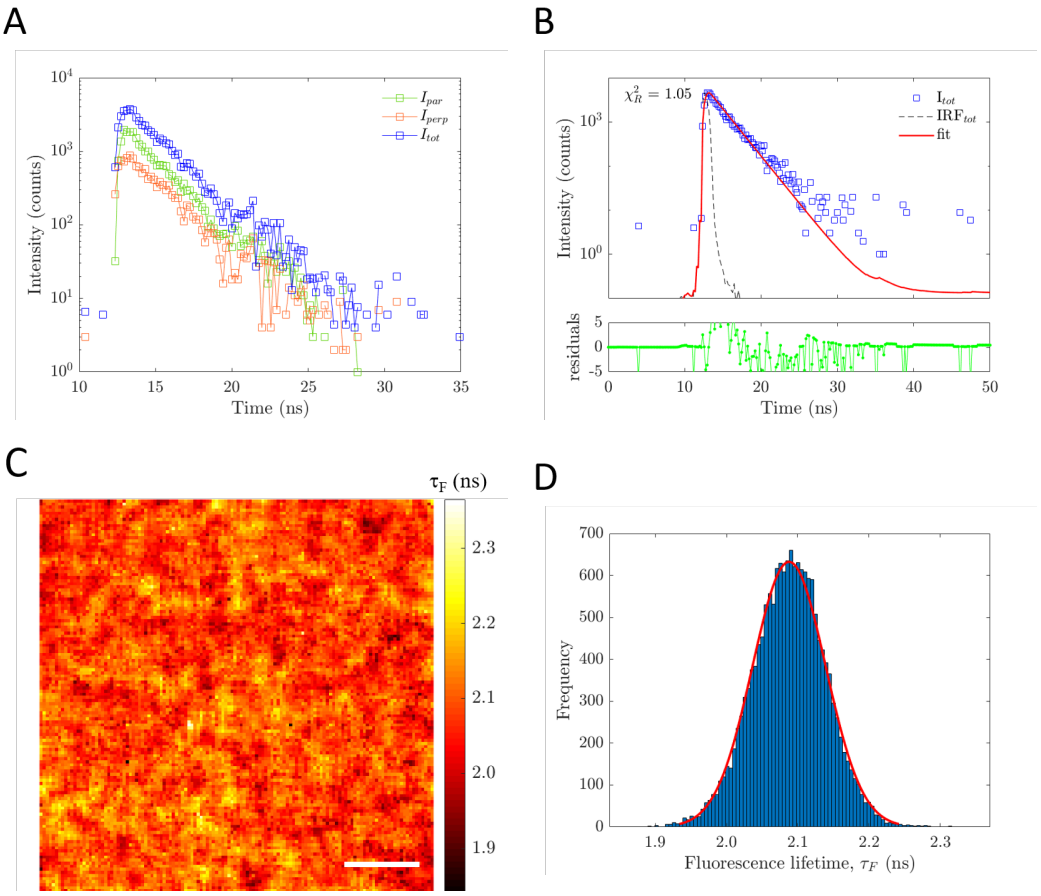

Figure 3.20: Representative fluorescence lifetime data of di-4-ANEPPDHQ in DOPC SLB at RT. (A) Parallel, perpendicular and total intensity decays. (B) Total intensity fit with $\tau_F = 2.0285 \pm 0.0219$ ns. (C) Fluorescence lifetime map. (D) Fluorescence lifetime map histogram and fit with $\mu = 2.09$ and $\sigma = 0.05$ ns. Scale bar: 50 μm.

3.4.2.2 Steady-State Anisotropy Studies

As a continuation of the FLIM data analysis, the FAIM results were also analysed. The steady-state anisotropy images were built up as explained in *Section* 3.3.3. The same G-factor used for the generation of the total intensity decays per pixel was also applied here. A representative map along with its histogram is presented in Figure 3.21A and B. Its standard deviation is also presented along its corresponding total

intensity image, where the bleach spot is clearly displayed in the middle of the field of view (FOV) (Figure 3.21C and D). The steady-state anisotropy r is consistent across the entire FOV (Figure 3.21A), so are the steady-state anisotropy r standard deviation and the total intensity I_{tot}, apart from the central region where the intentional bleaching took place (Figure 3.21C and D). The reason for the consistency of these parameters (r, $sd(r)$ and I_{tot}) across the FOV is related to the predisposition of the fluorescence probe's dipole to organise tangentially to the plane of the membrane, between the lipids [239]. This probe's arrangement across the sample yields similar steady-state anisotropy information across the entire image. The same argument can be used to explain the uniform distribution of $sd(r)$ and I_{tot} across the FOV (Figure 3.21C and D). A disagreement in uniformity of r, $sd(r)$ and I_{tot} across the FOV can be attributed to excitation laser misalignment issues, as previously suggested (*Section* 3.4.1.2).

3.4.2.3 Time-Resolved Fluorescence Anisotropy Studies

Time-resolved anisotropy results are also presented. An example of the integrated time-resolved fluorescence anisotropy decay of one measurement is shown in Figure 3.23. The time-resolved fluorescence anisotropy decay is fitted with a hindered rotational model, which yields the following anisotropy parameters: $r_0 = 0.09$, $\theta = 2.17$ ns and $r_\infty = 0.02$. The low rotational correlation time θ and the presence of a limiting anisotropy value r_∞ indicate that the lipid bilayer constitutes an anisotropic system, whose lipids restrict the rotational mobility of the fluorescence probe. Interestingly, a consensus on low values for the initial anisotropy r_0 of the total time-resolved fluorescence anisotropy decays across all the measurements, was found ($r_0 = 0.11 \pm 0.03$). The reason for this low r_0 may be due to the anisotropic nature of the excitation laser. The excitation laser is polarised, which means its electric field orientation is defined and fixed. When the excitation light illuminates the sample (bilayer system), the polarisation of the electric field of the excitation

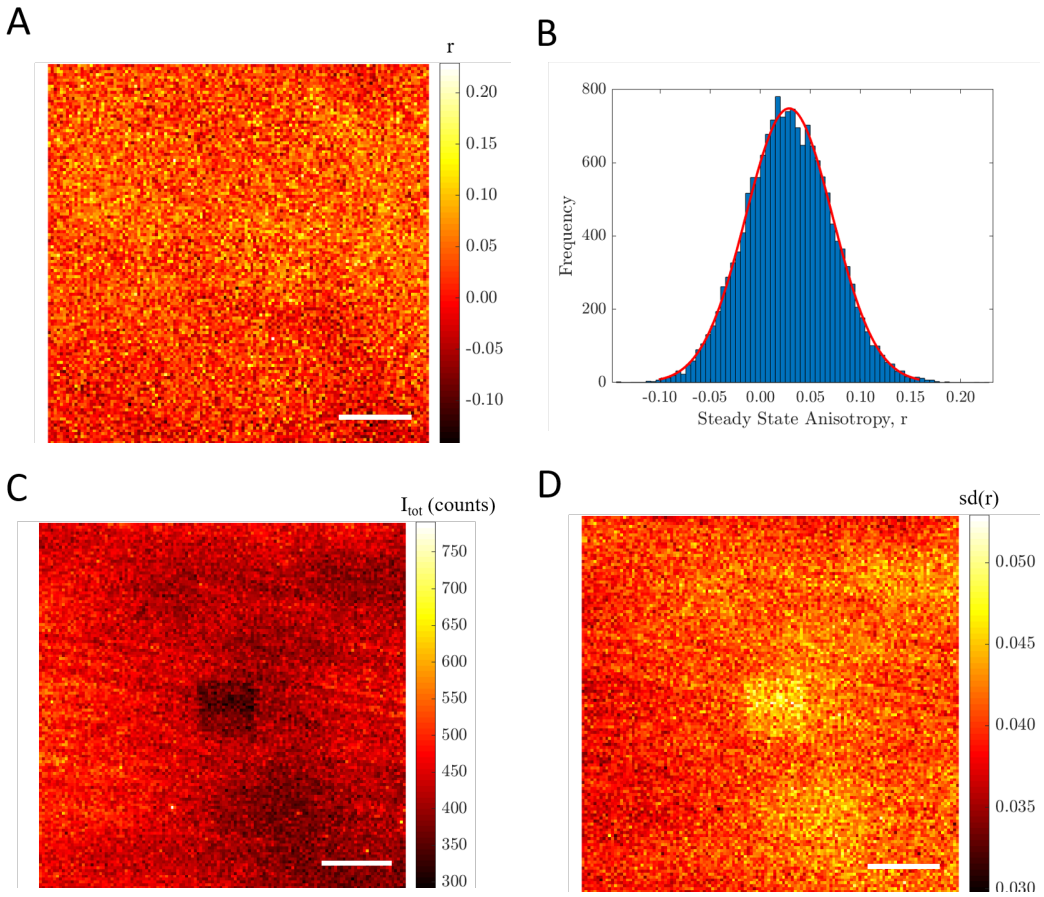

Figure 3.21: Representative steady state anisotropy data, its standard deviation and the total amount of counts per pixel of di-4-ANEPPDHQ in DOPC SLB at RT. (A) Steady state anisotropy map (binning with n = 1). (B) Fitted steady state anisotropy distribution with $\mu = 0.029$ and $\sigma = 0.004$. (C) total intensity and (D) δr maps. Scale bar: 50 μm.

laser is arranged orthogonally to the lipids' orientation. As the fluorescence probe di-4-ANEPPDHQ organises tangentially to the plane of the membrane [239], its orientation is expected to be very similar to the lipid one. This may reduce the photoselection efficiency and therefore r_0 (Figure 3.22). This depolarisation effect along with that caused by the high numerical aperture NA of the objective, could yield a low value for the initial anisotropy value r_0 and explain the presented findings. This argument assumes no Förster Resonance Energy Transfer (FRET) takes places between fluorescence probes and the absorption and emission dipoles of the fluorescence probes are identical. All the FLIM and FAIM parameters are presented in Table 3.7.

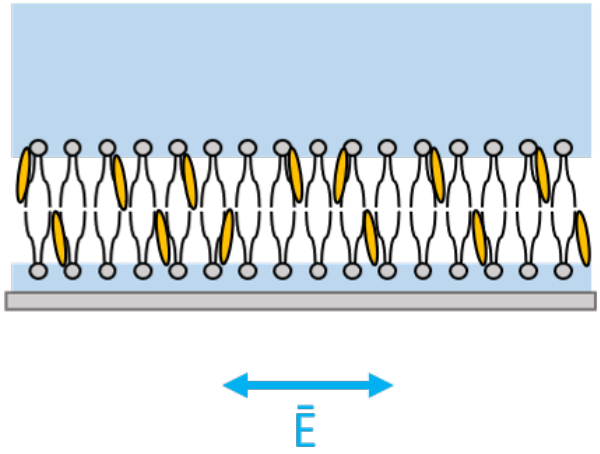

Figure 3.22: Representation of the supported lipid bilayer system onto the glass surface. The oval shape in orange represents the fluorescence probe, whose dipole orientation goes along its largest axis. The electric field of the excitation laser is shown below in blue.

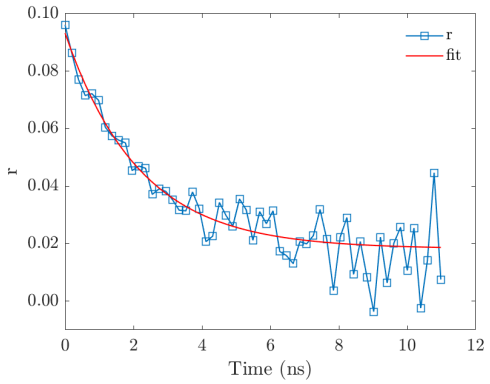

Figure 3.23: Representative time-resolved anisotropy decay of di-4-ANEPPDHQ in DOPC SLB at R.T extracted from the entire field of view. The decay is fitted with the hindered rotation model. The fit parameters are: $r_0 = 0.09$, $\theta = 2.17$ ns and $r_\infty = 0.02$.

As done for the R6G in water/glycerol solutions, the individual rotational correlation times per pixel are presented in this work. In this case, the parallel and perpendicular intensity decays were fitted and the anisotropy parameters were extracted (equations 3.5, 3.6 and 3.7). The construction of this map is more challenging due to the presence of an additional parameter, r_∞. Some representative data is presented in Figure 3.24, where the fit of the individual intensity decays and of the resultant time-resolved fluorescence anisotropy decay is presented in Figure 3.24A and B. In

Figure 3.24C and D, the rotational correlation time map along its histogram is displayed. Once more, a skewed distribution for this parameter is encountered when plotting its histogram.

As previously mentioned, a direct comparison between our results and others' work is not possible as, to the best of our knowledge, no characterisation of an identical system to ours has been reported yet. However, we can find some similarities with the results presented by Le Marois et al. and Steele et al. [239,240], where very similar rotational correlation times are reported. Meanwhile Marois et al. reports a rotational correlation time of θ = 4.48 ns in DOPC GUVs, Steele et al. reports a bit lower one (θ = 3.32 ns) in DOPC liposomes. All these measurements were also taken at RT. In our case, a good agreement with these results was found by reporting an average rotational correlation time of 2.36 ± 0.26 ns. Interestingly, the rotational correlation time of a related dye (laurdan) in DOPC GUVs at RT was found to be very similar to ours (θ = 2.05 $\pm$ 0.02 ns) [242]. Also, a similar lipid packing to ours, given by S^2, was also reported in the work published by Steele et al. [240]. The trend of this dye to locate in the outer leaflet of the lipid membrane, may confer it high mobility, which derives in a low rotational correlation time [238, 273].

Table 3.7: FLIM and FAIM parameters for di-4-ANEPPDHQ in DOPC SLB at RT.

$\bar{\tau_F}$ (ns)	$\bar{r}$	$\bar{r_0}$	$\bar{r_\infty}$	$\bar{\theta}$ (ns)	$\bar{D_r}$ (ns^{-1})	$\bar{S^2}$
2.10 ± 0.06	0.048 ± 0.007	0.11 ± 0.03	0.06 ± 0.01	2.36 ± 0.26	0.07 ± 0.01	0.44 ± 0.13

As laurdan and di-4-ANEPPDHQ are structurally and biophysically similar, the viscosity of the lipid bilayer may be calculated by defining a hydrodynamic radius for the dye of 5 $\AA$ and applying the Stokes-Einstein-Debye model (equation 3.9), which assumes an spherical shape for the dye, or the Saffman-Delbruck model (equation 3.12), which applies for a free standing membrane. The assumption of the thickness of the membrane $h \sim R_h$ (laurdan dye) is introduced in the equation. The average local/micro-viscosity of the artificial membrane in the dye's

vicinity obtained with the Saffman-Delbruck and Stokes-Einstein-Debye models is summarised in Table 3.8.

Table 3.8: Average viscosity values of DOPC SLB given by the di-4-ANEPPDHQ rotational diffusion parameters (Table 3.7) and applying the Saffman-Delbruck and Stokes-Einstein-Debye models (equations 3.12 and 3.9, respectively).

$\eta_{r,Saffman-Delbruck}$ **(cP)**	37 ± 4
$\eta_{r,Stokes-Einstein-Debye}$ **(cP)**	18 ± 2

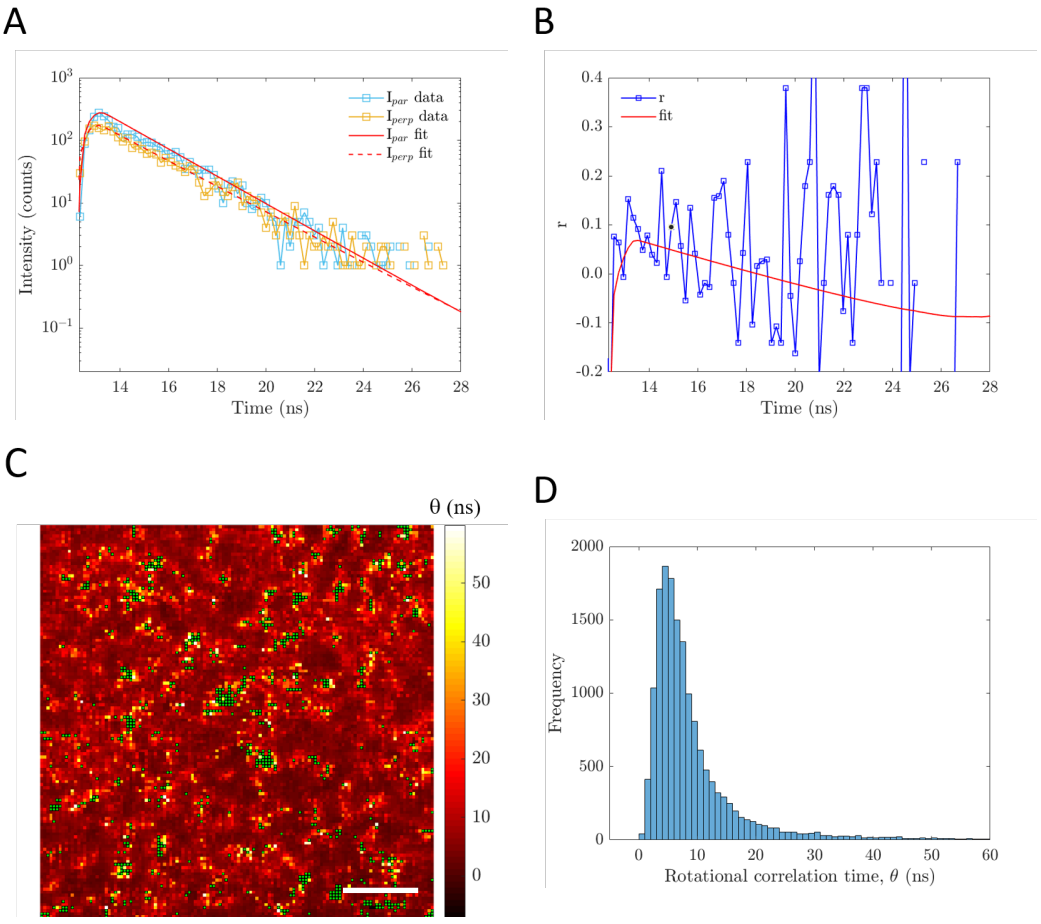

Figure 3.24: Representative time-resolved anisotropy data of di-4-ANEPPDHQ in DOPC SLB at RT for the pixel position (10,10). (A) Parallel and perpendicular intensity decays with fit. The fit parameters are: $\tau_{F,1}$ = 1.99 ns and $\tau_{F,2}$ = 3.80 ns for the parallel intensity component, and $\tau_{F,1}$ = 2.14 ns and $\tau_{F,2}$ = 3.96 ns for the perpendicular one. (B) Time-resolved anisotropy decay with fit. The fit parameters are: r_0 = 0.10 and θ = 17.47 ns. (C) Rotational correlation time map. The green dots correspond to NaN values. (D) Rotational correlation time histogram. Scale bar: 50 μm.

3.4.2.4 Translational Diffusion via F^3 FRAP

The FRAP data from the F^3-microscopy setup was extracted and analysed in a similar manner as the R6G data in water/glycerol. Therefore, the data was normalised and from the two normalisation methods (Siggia & Axelrod [84, 130]), the mobile fraction M_f and half-recovery time $\tau_{1/2}$ were extracted. From the normalised first post-bleach image, the bleach spot profile was obtained and fitted with a Gaussian function - results not presented. This yielded the effective bleach radius r_e and the bleach depth. With all this information, the translational diffusion coefficient was determined using the confocal equation (first term of equation 2.23). An example of the FRAP recovery curve of one of the seven analysed FRAP data sets is presented in Figure 3.25 along with a tile of representative total intensity images where the three FRAP stages (pre-bleach, bleach and post-bleach) can be observed. On the bottom, the summary of different FRAP parameters is shown. These are: mobile fraction M_f, half-recovery time $\tau_{1/2}$ and translational/lateral diffusion coefficient D_t.

We found a translational diffusion coefficient of approximately one order of magnitude below previously reported values in literature ($D_{t,exp}$ = 0.15 $\pm$ 0.06 $\mu m^2/s$). This suggests that the lateral mobility is clearly restricted. As in the case of the calculation of the SLB micro-viscosity from anisotropy measurements, we applied Saffman-Delbruck and Stokes-Einstein-Debye models to describe the translational diffusion with the objective of obtaining the macro-viscosity of the system under investigation. For the Saffman-Delbruck model, several assumptions must be done. The height of the lipid-fluorophore is assumed to be the same as its hydrodynamic radius ($h \sim R_h$), laurdan's (5 Å). Also, the ratio between the inside and outside viscosities is reduced to 10^2 ($\eta/\eta' = 10^2$).

High values for the macro-viscosity may confirm an underestimation of the translational diffusion coefficient due to a strong interaction between the solid sup-

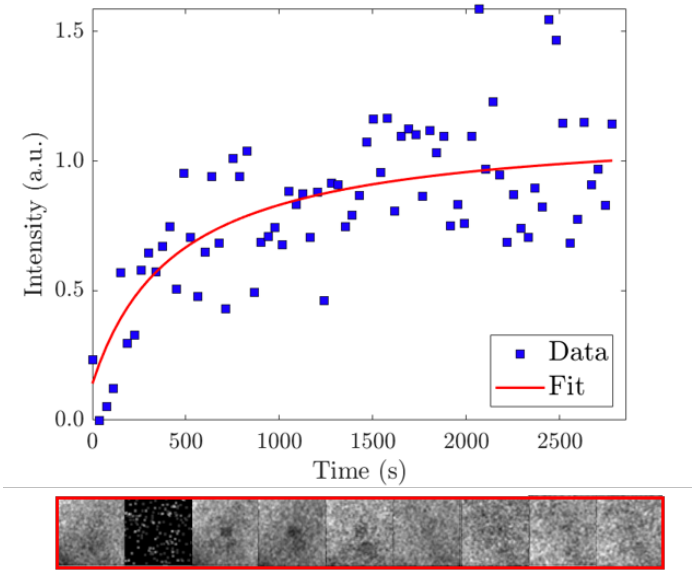

Parameters	Mean value
Mobile fraction, M_f (%)	98 ± 4
Half-recovery time, $\tau_{1/2}$ (s)	677 ± 75
Diffusion coefficient, D_t ($\mu m^2/s$)	0.15 ± 0.06

Figure 3.25: Representative FRAP recovery curve with fit of di-4-ANEPPDHQ in DOPC SLB at RT along some representative F^3 FRAP images (pixel size = 1.8601 μm). On the bottom the extracted FRAP parameters are displayed.

Table 3.9: Average viscosity values of DOPC SLB given by the di-4-ANEPPDHQ translational diffusion parameters (Table in Figure 3.25) and applying the Saffman-Delbruck and Stokes-Einstein-Debye models (equation 3.13 and second term of equation 2.23, respectively).

$\eta_{t,Saffman-Delbruck}$ **(cP)**	15902 ± 5042
$\eta_{t,Stokes-Einstein-Debye}$ **(cP)**	2640 ± 837

port and the outer leaflets of the model membrane. Due to the anisotropic nature of the model membrane, given by the limiting anisotropy value r_∞ extracted from the time-resolved fluorescence anisotropy data, we may expect the lipid-probe feels lower restriction in mobility during rotation than during its translation. This explains that the micro-viscosity given by the rotational diffusion coefficient models are of several orders of magnitude lower than the ones reported via translation. The more than apparent mismatch between viscosities, micro and macro (Tables 3.8 and 3.9, respectively), does not allow calculating the hydrodynamic radius by com-

bining the rotational and translational diffusion coefficients, as done for the setup calibration with the dye R6G in water/glycerol solutions.

The D_t extracted from the SLBs experiment is much lower than the one obtained from the R6G data in water/glycerol solutions, which indicates that if their hydrodynamic radii may be considered of comparable dimensions (5 Å), the diffusion of the dye across the lipid bilayers is much slower than the one experienced by the R6G dye in an homogeneous solution. This is apparent by assessing the half-recovery times, where the calibration experiment ran for a maximum of 10 minutes, meanwhile the SLBs needed a total acquisition time of 45 minutes to complete de FRAP curve. The addition of a confocal correction via the calculation of r_e did not change the initial diffusion coefficient in a great manner, which means that the diffusion of the dye across the SLB during bleaching can be considered negligible.

Before acquiring the F^3 data, some confocal imaging of the SLBs was performed in order to assess the smoothness of its morphology. It has been reported that addition of vesicles onto the SLB bilayer surface implies some restriction in the lateral mobility of the model membrane. Via Atomic Force Microscopy (AFM) the contribution of these vesicles was observed when removed, with a consequent increase in the translational diffusion coefficient of the membrane [263, 264]. During the preparation of our samples, a thorough washing process was carried out, which aided the acquisition of clean SLB confocal images, where very few vesicles were observed. To make sure about the lipid bilayer structure, thickness, flatness, etc. some AFM is more than advised to be performed, which has been extensively used before by others to investigate similar samples [274, 275]. This technique allows a high resolution that permits the observation of membrane structures and even individual molecules.

Encountering high mobile fractions (98%) suggests that the SLBs tend towards complete recovery in spite of its slow motion. This is indicative of free diffusion

and has been already reported by others [245]. However, it is difficult to assess the end of the FRAP curve, where a plateau in the data must be reached. This implies a direct dependence between unintentional bleaching and acquisition time.

As previously mentioned and to the best of our knowledge, identical experiments to ours have not been reported in literature so far. GUVs with laurdan have been reported to present higher lateral mobility values than those encountered in SLBs, so this technique could be applied on them and compared with the response given by di-4-ANEPPDHQ, for instance. Another interesting and widely used approach, is the use of MD simulations [257–259] to calculate translational diffusion coefficients. The interaction between membrane and glass surface could be assessed by determining the lateral mobility of di-4-ANEPPDHQ within a DOPC SLB and varying the distance between the solid support and the lipid bilayer. This could give some insight in regards to the strength of these interactions and the role of the dye within the model membrane.

3.5 Summary & Conclusion

The content of this chapter was split in two main sections:

1. *Section* 3.4.1: 'Setup Calibration with Rhodamine 6G'
2. *Section* 3.4.2: 'F^3 applied to Di-4-ANEPPDHQ in DOPC SLBs at RT'

1. The F^3 setup was calibrated with R6G in solutions of glycerol/water at different weight percents and at RT. Firstly, the fluorescence lifetime of R6G in each solution was calculated. Fluorescence lifetime maps per sample were generated and from the histogram its mean value was extracted. Strickler-Berg relationship [25] that links the probe's fluorescence lifetime and the solution's refractive index n was investigated. No correlation was found, concluding that the observation of this trend was challenging due to the range of n investigated. Our results were in good agreement with previously reported values for R6G in glycerol at RT. [268].

Via FAIM, steady-state anisotropy and its standard deviation maps were also created. Average parameters per solution were extracted from their histograms. As expected, the steady-state anisotropy of the fluorophore increased with the solution's viscosity and the bleach spot was represented in the $sd(r)$ by its highest values, according to the expression introduced by Lidke et al. [128]. The standard deviation $sd(r)$ is high if the number of counts is low. This is the case in the bleach spot. From the steady-state anisotropy and solution's viscosity information, the initial anisotropy r_0 was calculated ($r_0 = 0.304 \pm 0.014$). This is in good agreement with the r_0 values that were a posteriori extracted from the time-resolved fluorescence anisotropy decay fits. The overall rotational correlation time map per solution was also calculated by applying a free rotation model (equation 3.4). The grainy mess of the rotational correlation time map is possibly due to the presence of noise. Differences in counts per pixel and the binning of the image may contribute to the appearance of a patchy pattern across the FOV. The hydrodynamic radius of the dye was obtained by plotting the probe's rotational correlation time against the solution's viscosity. A value of $R_h = 0.411 \pm 0.001$ nm was found. Confocal and F^3 FRAP were also performed and compared. This was the case in order to validate the FRAP results given by F^3. The lateral mobility of the dye across the aqueous solution was assessed by calculating its translational diffusion coefficient. For both approaches, these coefficients were plotted against the viscosity of the solution and the hydrodynamic radius was again calculated, being: $R_{h,Confocal} = 0.37 \pm 0.06$ nm and $R_{h,F^3} = 0.4 \pm 0.1$ nm, respectively.

Finally, the main purpose of the setup was addressed, which was gaining information about the hydrodynamic radius of the fluorophore by combining rotational and translational information and without any priori knowledge about the viscosity. This was carried out and the results were as follows: $R_{h,Confocal,rot} = 0.42 \pm 0.04$ nm and $R_{h,F^3,rot} = 0.40 \pm 0.08$ nm. Results were in the expected order of magnitude,

as most of these type of fluorophores have alike hydrodynamic radii and in good agreement with previously reported values by others [269]. Table 3.10 summarises all the calculated R6G hydrodynamic radii per technique/approach.

Table 3.10: Summary of the found R6G hydrodynamic radii R_h per technique and approach.

Technique/Approach	**R6G R_h (nm)**
Anisotropy/θ & η	0.411 ± 0.001
FRAP/Confocal D_t & η	0.37 ± 0.06
FRAP/F^3 D_t & η	0.4 ± 0.1
FRAP & Anisotropy/Confocal D_t & η	0.42 ± 0.04
FRAP & Anisotropy/F^3 D_t & η	0.40 ± 0.08

2. After a successful calibration with R6G, the setup was further tested and applied to model membranes. Specifically, the fluorescence response of the environmentally-sensitive dye di-4-ANEPPDHQ was studied within some planar model membranes (DOPC SLBs). We investigated via FLIM the fluorescence lifetime response of the probe, which gave an average value of 2.10 ± 0.06 ns. This was also obtained from the fitted fluorescence lifetime distributions per τ image. The fluorescence lifetime of this dye in different model membranes was found in literature and in good agreement with our results, where 1.85, 1.80 and 2.22 ns were reported [236,239,240]. For high levels of water molecules inserted in the membrane, a decrease in the fluorescence lifetime τ via water quenching of the probe sensing the lipid bilayer micro-environment is expected. This was found by Ma et al. when measuring the fluorescence lifetime of the environmentally-sensitive dye laurdan in small and large vesicles. The laurdan lifetime was reported to be shorter in the smaller vesicles and suggested to be a consequence of a higher interaction with water molecules due to the increase in membrane bending [272]. Therefore, changes in this parameter can be employed to report on the membrane hydration, which may be altered by variations in a dye's local lipid environment, such as changes in membrane curvature and enrichment in saturated lipids or cholesterol [276–278].

Following the same previous guidelines, the steady-state anisotropy map was calculated along its standard deviation, where a consistency across the FOV was found and related to the fluorescence probe's dipole predisposition to organise tangentially to the plane of the membrane. A lower steady-state anisotropy standard deviation response is found within the central bleached region, where the number of counts is significantly reduced (equation 3.8). Discrepancies in homogeneous maps, and therefore normal distributions, (apart from $sd(r)$ and I_{tot} at the bleach spot) for these parameters were related to a minor laser misalignment.

The overall rotational correlation time of the probe was calculated by integrating all the polarisation intensity decays per pixel. The hindered rotation model (equation 3.7) was applied and the anisotropy parameters extracted. The mean rotational correlation time was $\theta = 2.36 \pm 0.26$ ns. Le Marois et al. and Steele et al. found similar responses of this same dye but in other lipid structures (4.48 and 3.32 ns, respectively) [239, 240]. A similar lipid packing ($S^2 = 0.44 \pm 0.13$) as the reported by Steele et al. ($S^2 = 0.44 \pm 0.03$) was found, which may indicate the trend of this dye to locate in the outer leaflet of the membrane, which provides the dye high rotational mobility [240]. The rotational mobility of laurdan in DOPC GUVs was also investigated by Aguilar et al. and found to be also very similar to our result (2.05 ns) [242].

In the rhodamine 6G work, the solution's viscosities were calculated. However, in the SLBs case, the micro-viscosity of the lipid bilayer is unknown. For this reason, the hydrodynamic radius is assumed to be laurdan's, for common features with di-4-ANEPPDHQ, and the local viscosity was obtained by applying the Stokes-Einstein-Debye and Saffman-Delbruck equations for the rotational Brownian motion (eqs. 3.9 and 3.12). The results are presented in Table 3.8, where different outcomes are given by different approaches. This suggests that the spherical approximation of the di-4-ANEPPDHQ probe's volume is not a good estimation.

Rotational correlation time maps were also produced, where the hindered rotation model was applied for the assessment of the probe's wobbling across the sample but by fitting the parallel and perpendicular intensity decays per pixel (eqs. 3.5 and 3.6). As encountered in the construction of the rotational correlation time map for R6G in water/glycerol solutions, a grainy mess was found across the FOV and related to the presence of noise and the effect of the binning on its distribution across the map.

FRAP information of the dye was also obtained and the FRAP curve was found to recover very slowly. This gave rise to a lateral mobility ($D_{t,exp}$ = 0.15 $\pm$ 0.06 μm^2/s) of the dye across the SLB of at least one order of magnitude below previously reported values [88, 89, 245]. We argued that the underestimation of the diffusion coefficient may be related to the interaction among the substrate and the membrane, slowing down the lateral mobility of the dye. Very high values for the membrane macro-viscosity were obtained in comparison to the micro-viscosity extracted from the rotational Brownian motion (Tables 3.9 and 3.8), which may confirm the strong interaction between substrate and membrane. Another reason that may explain this disagreement lies in the anisotropic nature of the membrane. When the probe moves laterally, such as it happens when FRAP is applied, it comes across a bunch of lipids, which constitutes a great opposition to its lateral movement to happen. However, the fluorescence probe spins very quickly, as we have shown in this work, as it sits in between the lipids. Therefore, we can conclude that the nature of the drag forces related to these two Brownian motions (rotational and translation) is different and micro and macro- viscosities cannot be compared. This did not allow the combination of the rotational and translational information in order to infer the hydrodynamic radius of the environmentally-sensitive dye. In order to assess the methodology and the data analysis approach, other model membranes with other dyes can be measured in order to obtain a direct comparison, such as

laurdan in DOPC GUVs [242], for instance.

The low Signal-to-Noise Ratio (SNR) of the data was another impediment to assure a reliable result of the translational diffusion coefficient. We spatially binned the FRAP data with the consequent loss in spatial resolution. More advanced approaches that reduce the noise may be considered in the future, with the application of alternative algorithms to filter the present noise [279]. MD simulations were also proposed to assess the degree of interaction between membrane and substrate by measuring the lateral mobility of the dye across the lipid bilayer with varying the distance between solid support and model membrane [257–259]. Finally, AFM studies could broaden the knowledge of the sample by assessing its distribution, thickness, uniformity, etc. in a nano-scale [263, 264, 274, 275]. The main parameters provided by F^3 are displayed in Table 3.11.

Table 3.11: Mean F^3 parameters for the dye di-4-ANEPPDHQ in DOPC SLBs.

Parameter	*Result*
τ_F **(ns)**	2.10 ± 0.06
r	0.048 ± 0.007
r_0	0.11 ± 0.03
r_∞	0.06 ± 0.01
θ **(ns)**	2.36 ± 0.26
$D_{r,exp}$ **(ns^{-1})**	0.07 ± 0.01
S^2	0.44 ± 0.13
$\eta_{r,Saffman-Delbruck}$ **(cP)**	37 ± 4
$\eta_{r,Stokes-Einstein-Debye}$ **(cP)**	18 ± 2
$\eta_{t,Saffman-Delbruck}$ **(cP)**	15902 ± 5042
$\eta_{t,Stokes-Einstein-Debye}$ **(cP)**	2640 ± 837
$D_{t,exp}$ **(μm^2/s)**	0.15 ± 0.06

In summary, the calibration of the F^3 setup with R6G in solutions of water/glycerol at different weight percents has revealed that by combining FLIM, FAIM and FRAP, the hydrodynamic radius of a dye in an isotropic media can be inferred without any prior knowledge about the solution's viscosity and with excellent agreement with the results obtained by using FRAP and FAIM individually.

On top of that, the same setup was applied to the enviromentally-sensitive dye di-4-ANEPPDHQ in DOPC SLBs. Albeit this work is based on some preliminary results, its outcome found to be promising but the results given by FRAP not fully understood yet. The potential of F^3 could be explored and applied to other heterogeneous systems, such as sol gels or other polymer network structures, in order to obtain information about their micro and macro- viscosity, and its fluorescence lifetime response.

Chapter 4

Investigation of the Rotational Correlation Time Uncertainty and Distribution from Time-Resolved Fluorescence Anisotropy Data

4.1 Motivation

This theoretical and experimental work was mainly driven to give an answer to two scientific questions:

1. *How many photons are necessary for time-resolved fluorescence anisotropy measurements?*

2. *What is the shape of the rotational correlation time distribution of an homogeneous solution?*

4.2 Introduction

Time-correlated-Single Photon Counting (TCSPC) data obeys Poisson statistics [280]. Poisson statistics in photon counting describe the probability of a photon

to fall into a time channel bin. If N is the number of photons at one time bin position of the measured intensity decay histogram, the Poisson noise associated to this quantity N is given by $\sqrt{N}$ [280, 281]. Therefore, the longer the measurement time, the more counts are accumulated and the smaller the uncertainty is. This means that the Poisson noise scales up with the signal strength as $\sqrt{N}$, where the signal-to-noise (SNR) also increases with $\sqrt{N}$.

The main goal of TCSPC is the estimation of the fluorescence lifetime parameter τ. Köllner et al. [282] presented and described for the first time an analytical solution for determining its uncertainty with high accuracy as a function of the signal strength. This was based on a multinomial approach, equivalent to the Poisson-based method, when the number of counts N is relatively large [280,281,283]. It has also been shown that both approaches give the same parameter estimates when the maximum likelihood fitting is used [284]. The multinomial approach was applied in this work due to its mathematical rigour and because it leads to a straightforward estimation of the lifetime variance for a certain signal strength. In this work, Köller et al. estimated that 185 photons are needed to measure a fluorescence lifetime of 2.5 ns with an accuracy of 10% [282].

Time-resolved fluorescence polarisation (anisotropy) also relies on the TCSPC principle, where two orthogonal-polarised intensity decays ($I_{\parallel}$ and $I_{\perp}$) are recorded photon by photon. The time-resolved fluorescence anisotropy decay is derived from these two transients, whose photon counts are distributed according to Poisson statistics. When the fluorescence lifetime is estimated from the total intensity decay, approaches such as the least-squares and maximum likelihood are applied and the data is weighted according to the Poisson statistics, showing efficiency in the delivery of accurate parameter estimates. However, to the best of my knowledge, there is no analytical expression that describes the counts distribution of the time-resolved fluorescence anisotropy decay.

The uncertainty associated to each anisotropy data point was derived and introduced by Lidke et al. [128], by applying a standard propagation of errors for uncorrelated signals. This approach assumes no variance for the G-factor. Although the statistics followed by the counts distribution of the time-resolved fluorescence anisotropy decay are unknown, this expression can be applied to weight the time-resolved fluorescence anisotropy data for the estimation of the rotational correlation time θ.

In this chapter, in line with the work presented by Lidke et al. [128], the rotational correlation time uncertainty is calculated making use of the Perrin equation for a freely rotating probe (no r_∞). A propagation of errors for the fluorescence lifetime τ and the steady-state anisotropy r is applied, where the initial anisotropy r_0 is considered to be a constant. The found expression for the rotational correlation time uncertainty is compared with the θ uncertainty inferred from a weighted least-squares fitting and its magnitude is investigated under certain experimental boundary conditions. The outcome of this research is presented in *Section* 4.3.

The Fluorescence lifetime imaging (FLIM) map of a probe in an homogeneous and isotropic solution, presents a normal distribution as each pixel is expected to deliver an almost identical answer. The fluorescence lifetime τ probability density function pdf(τ) can be described mathematically by a Gaussian function and the mean μ and standard deviation σ are extracted. If fluorescence anisotropy imaging (FAIM) is applied to a sample with the same previously mentioned features, the steady-state anisotropy map also displays a normal (Gaussian) distribution, from which μ and σ are calculated. However, when the pdf(θ) of an isotropic and homogeneous solution is investigated via means of time-resolved FAIM (tr-FAIM), it differs significantly from a Gaussian distribution. The distribution of these parameters (τ, r and θ) was previously reported [179, 201, 285] and presented in *Chapter* 3 of this thesis. Since the sample is isotropic and homogeneous, it sounds reasonable

to expect a normal distribution for this parameter (θ). This problem becomes very interesting from a mathematical point of view and its investigation is conducted in section 4.4. The objective of section 4.4 is to conclude how real the distribution is, or if, on the contrary, it presents an erroneous shape related to the performance of the data analysis procedure, for instance. The problem is approached simulating normal distributions for τ and the steady-state anisotropy r, from where the θ distribution is generated applying the Perrin equation for a freely rotating probe.

Therefore, two different cases will be studied in this chapter:

- *Section* 4.3: 'Estimation of the Rotational Correlation Time Uncertainty from a Single Decay'.

- *Section* 4.4: 'Rotational Correlation Time Distribution from an Image'.

4.3 Estimation of the Rotational Correlation Time Uncertainty from a Single Decay

4.3.1 Description of Theoretical Uncertainty Equations

The derivation of the theoretical uncertainty equations applied in this work are presented in the next three subsections.

4.3.1.1 Fluorescence Lifetime

The derivation of the fluorescence lifetime variance $var(\tau)$ starts from considering a background-free mono-exponential decay with a fluorescence lifetime τ. The probability a photon will fall into channel i will be given by p_i, where $\Sigma p_i = 1$. The probability p_i is defined as follows [282]:

$$p_i = \int_{\Delta_t} d(t)dt \tag{4.1}$$

where Δ_t is the temporal interval corresponding to channel i and $d(t)$ is the probability density function of the mono-exponential decay. This is given by:

$$d(\tau,T,t) = \frac{1}{\tau} exp(-t/\tau) \frac{1}{1-exp(-T/\tau)} \tag{4.2}$$

where T is the time window and the second term of the equation corresponds to its normalisation to the finite time window T.

Integrating over t, the probabilities p_i are given by:

$$p_i(\tau,T,t) = \int_{(i-1)T/k}^{iT/k} d(\tau,T,t)dt = exp(-is/k) \frac{exp(s/k)-1}{1-exp(-s)} \tag{4.3}$$

where $s = T/\tau$ is the number of lifetimes in the measurement time window T and the channels are numbered from 1 to k.

The Fisher information matrix describes the amount of information data provides about an unknown parameter that an observable random variable carries. If y_i represents the average number of photons in channel i and its distribution is given by an exponential function, the random variable will be the vector t that describes the time domain and the unknown parameter will be the fluorescence lifetime τ. The number of counts y_i in (time) channel i is equal to Npi, where N is the total number of photons. The Fisher-information matrix in terms of y_i is given by [282]:

$$F_{hj} = \sum_i \frac{1}{y_i} \frac{\partial y_i}{\partial \alpha_h} \frac{\partial y_i}{\partial \alpha_j} \tag{4.4}$$

where α_h and α_j are the h^{th} and j^{th} unknown parameters α.

Knowing that $y_i = Npi$ and considering $\alpha_h = \alpha_j = \tau$, equation 4.4 can be rewritten as follows:

$$F_{\tau,\tau} = \sum_i \frac{1}{Np_i} \frac{\partial Np_i}{\partial \tau} \frac{\partial Np_i}{\partial \tau} = N \sum_i \frac{1}{p_i} \frac{\partial^2 p_i}{\partial \tau^2} \tag{4.5}$$

For this case the Fisher-information matrix is a number and the variance is given by its inverse [282]:

$$var_N(\tau) = (F_{\tau,\tau})^{-1} = \frac{1}{N}[F(N=1)]^{-1}_{\tau,\tau} \tag{4.6}$$

Combining equations 4.3, 4.5 and 4.6, the fluorescence lifetime variance is given by the following expression [282, 286, 287]:

$$v_N(\tau, T, k) = \frac{1}{N}\tau^2 var_1(s,k) \tag{4.7}$$

where $var_1(s,k)$ is:

$$var_1(s,k) = \frac{k^2}{s^2}[1-exp(-s)] \times \left(\frac{exp(s/k)[1-exp(-s)}{[exp(s/k)-1]^2} - \frac{k^2}{exp(s)-1}\right)^{-1} \tag{4.8}$$

The relationship between $var_1(r,k)/\tau^2$ and $s = T/\tau$ can be observed in Figure 4.1, where this dependence is presented for a different number of time channels k [282].

From Figure 4.1 it can be seen that for each time resolution k, the normalised lifetime variance is given by parabolas, where an optimal value exists and is given by its minimum. It can also be observed that this minimum shifts to the right with k, lowering its value till getting to a plateau case scenario, where a global minimum for the normalised lifetime variance is found. Under ideal conditions (infinite, continuous measurement window) $var_1(r,k)$ is equal to 1, which happens when k and T/τ are very large.

The fluorescence lifetime standard deviation will be given by the square root of its variance:

$$sd_N(\tau, T, k) = \frac{\tau}{\sqrt{N}}\sqrt{var_1(s,k)} \tag{4.9}$$

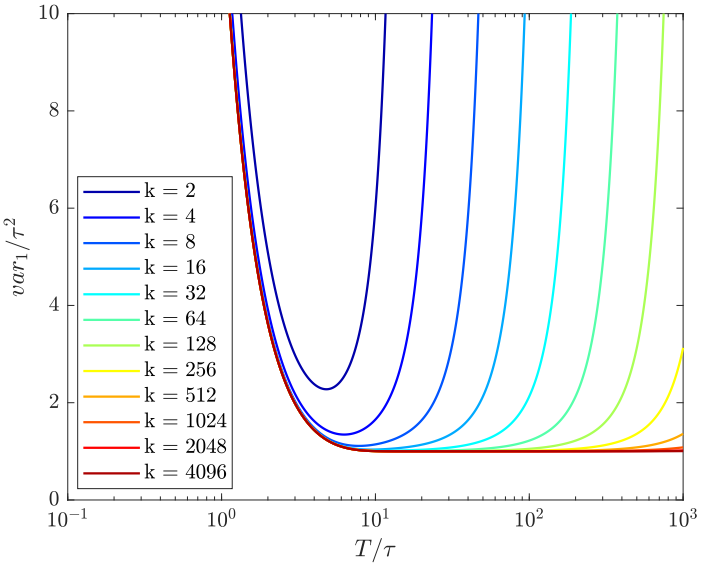

Figure 4.1: Normalised variance of τ against T/τ for different time resolutions. The normalised variance decreases with the number of photons N. Figure adapted from reference [282]

4.3.1.2 Steady-State Anisotropy

The steady-state anisotropy function is given by:

$$r = \frac{I_{\parallel} - GI_{\perp}}{I_{\parallel} + x_{NA}GI_{\perp}} \tag{4.10}$$

where $I_{\parallel}$ and $I_{\perp}$ are the parallel and perpendicular polarised emission signals, respectively. G corresponds to the efficiency ratio in between detectors and x_{NA} is an empirical correction factor that depends on the NA of the objective. If G is equal to 1 that means both detectors are equally efficient. The anisotropy is normalised by the total intensity detected.

The total intensity for low-NA detection is given by $I_{\parallel}$+2G$I_{\perp}$, where x_{NA} is therefore equal to 2. This corresponds to the parallel-beam detection case. If the NA of the objective is rather high, x_{NA} will be in between 1 and 2. It is very important to identify in which case the data is taken, thus the wrong r_0 is avoided, so as the wrong decay profile for r. While the experimentally observed r_0 can be corrected

through the adjustment of the G factor, the r shape cannot. In the work presented in this chapter we consider as a good approximation $x_{NA} = 2$.

By knowing that the photons collected follow a Poisson distribution, an expression for the anisotropy variance can be extracted by applying propagation of errors for the two signals [128]:

$$var(r) = \frac{(1-r)(1+2r)(1-r+G(1+2r))}{3N} \tag{4.11}$$

where N corresponds to the total emission intensity being equal to $I_{\parallel} + 2I_{\perp}$.

Therefore, the standard deviation of r will be given by the square root of its variance, such as:

$$sd(r) = \frac{1}{\sqrt{3N}}\sqrt{(1-r)(1+2r)(1-r+G(1+2r))} \tag{4.12}$$

While the Poisson statistics are applied to weight the intensity decays to extract the lifetime parameters; this distribution is applied to weight the steady-state anisotropy data.

4.3.1.3 Rotational Correlation Time

Depolarisation by rotational diffusion of spherical probes is described by the Perrin equation [20]:

$$r = \frac{r_0}{1+\frac{\tau}{\theta}} \tag{4.13}$$

where r is the observed anisotropy, r_0 is the intrinsic anisotropy of the molecule, τ is the fluorescence lifetime and θ is the rotational correlation time.

The degree of probe depolarisation depends on the relation between the rotational correlation time θ and the fluorescence lifetime τ. If the rotational correlation time is much shorter than the fluorescence lifetime ($\theta \ll \tau$), then the anisotropy is

zero. On the other hand, if the rotational correlation time is much larger than the fluorescence lifetime ($\theta \gg \tau$), then the measured anisotropy r is equal to the fundamental anisotropy r_0.

Rearranging equation 4.13:

$$\theta = \frac{\tau}{\frac{r_0}{r} - 1} \tag{4.14}$$

If we consider that τ and r are the only parameters statistically significant and independent from each other, then the rotational correlation time uncertainty will only depend on the fluorescence lifetime and steady-state anisotropy uncertainties. Using propagation of errors, the rotational correlation time uncertainty will be given by:

$$\Delta\theta = \sqrt{\left(\frac{\partial\theta}{\partial\tau}\right)^2 \Delta\tau^2 + \left(\frac{\partial\theta}{\partial r}\right)^2 \Delta r^2} \tag{4.15}$$

Therefore:

$$\Delta\theta = \sqrt{\left(\frac{1}{\frac{r_0}{r} - 1}\right)^2 \Delta\tau^2 + \left(\frac{r_0\tau}{(r_0 - r)^2}\right)^2 \Delta r^2} \tag{4.16}$$

If we consider $\Delta\tau = sd(\tau)$ (equation 4.9), $\Delta r = sd(r)$ (equation 4.12) and $G = 1$, then equation 4.16 can be rewritten and simplified as:

$$\Delta\theta = \frac{\theta}{\tau\sqrt{N}} \sqrt{\tau^2 var_1(s,k) + \frac{\theta^2 r_0^2}{r^4}\left[r(1-r) + \frac{2}{3}(1-r^3)\right]} \tag{4.17}$$

If we replace r by its equivalence, according to the Perrin equation (equation 4.13), $\Delta\theta$ is given by:

$$\Delta\theta = \frac{\theta}{\tau\sqrt{N}} \sqrt{\tau^2 var_1(s,k) + \frac{\theta^2}{r_0}\left(1 + \frac{\tau}{\theta}\right)^3 \left[\frac{2}{3}\frac{r_0^{-1}}{\left(1 + \frac{\tau}{\theta}\right)^{-1}} + 1 - \frac{r_0}{1 + \frac{\tau}{\theta}} - \frac{2}{3}\frac{r_0^2}{\left(1 + \frac{\tau}{\theta}\right)^2}\right]} \tag{4.18}$$

If the last term of the square root within the brackets is expressed as a sum, the

result is as follows:

$$\Delta\theta = \frac{\theta}{\tau\sqrt{N}} \sqrt{\tau^2 var_1(s,k) + \frac{\theta^2}{r_0}\left(1+\frac{\tau}{\theta}\right)^3 \sum_n \left[\begin{cases} +\frac{2}{3} & n=-1 \\ +1 & n=0 \\ -1 & n=+1 \\ -\frac{2}{3} & n=+2 \end{cases}\right] \left(\frac{r_0}{1+\frac{\tau}{\theta}}\right)^n} \tag{4.19}$$

When the number of time bins is considered infinite, $var_1(s,k) \to 1$ and equation 4.19 is modified as follows:

$$\Delta\theta = \frac{\theta}{\tau\sqrt{N}} \sqrt{\tau^2 + \frac{\theta^2}{r_0}\left(1+\frac{\tau}{\theta}\right)^3 \sum_n \left[\begin{cases} +\frac{2}{3} & n=-1 \\ +1 & n=0 \\ -1 & n=+1 \\ -\frac{2}{3} & n=+2 \end{cases}\right] \left(\frac{r_0}{1+\frac{\tau}{\theta}}\right)^n} \tag{4.20}$$

Equations 4.19 and 4.20 can be rewritten as follows:

$$\frac{\Delta\theta}{\theta} = \frac{1}{\tau\sqrt{N}} \sqrt{\tau^2 var_1(s,k) + \frac{\theta^2}{r_0}\left(1+\frac{\tau}{\theta}\right)^3 \sum_n \left[\begin{cases} +\frac{2}{3} & n=-1 \\ +1 & n=0 \\ -1 & n=+1 \\ -\frac{2}{3} & n=+2 \end{cases}\right] \left(\frac{r_0}{1+\frac{\tau}{\theta}}\right)^n} \tag{4.21}$$

$$\frac{\Delta\theta}{\theta} = \frac{1}{\tau\sqrt{N}} \sqrt{\tau^2 + \frac{\theta^2}{r_0}\left(1+\frac{\tau}{\theta}\right)^3 \sum_n \left[\begin{cases} +\frac{2}{3} & n=-1 \\ +1 & n=0 \\ -1 & n=+1 \\ -\frac{2}{3} & n=+2 \end{cases} \right] \left(\frac{r_0}{1+\frac{\tau}{\theta}}\right)^n} \tag{4.22}$$

The last two equations (4.21 and 4.22) will be applied in the upcoming sections for the investigation of the rotational correlation time uncertainty.

4.3.2 Materials & Methods

4.3.2.1 Simulation of Perrin Equation Parameters

In order to estimate the uncertainty associated with θ, an array of fluorescence lifetimes and rotational correlation times was generated in MATLAB, ranging both from 10^{-2} to 10^3 ns, and equation 4.21 was applied for $N = 1$. This means $\Delta\theta/\theta$ was normalised with the number of photons N and $\Delta\theta/\theta_{N=1}$ was plotted instead. This was done for several time resolutions k and time windows T. The initial anisotropy r_0 was set to 0.4.

4.3.2.2 Fluorescence anisotropy imaging of FITC in water

Sample and Equipment

A μM solution of fluorescein (FITC) in water was made and measured at room temperature in a 8-well coverslip-bottom plate (ibidi).

The setup used for measuring the sample is described in *Chapter* 2 (*Section* 3.2.1). The only difference is that instead of measuring single decays, images were acquired with 512×512 pixels and 1024 time bins per intensity transient decay ($I_{\parallel}$ and $I_{\perp}$). A 500LP filter was placed in front of the hybrid GaAsP detectors (Becker & Hickl HPM-100-40). Four FITC images were measured with different collection times each: 30, 90, 60 and 120 minutes. The instrument response function

(IRF) collection was done by measuring a FITC sample in water/glycerol (90/10%) quenched with sodium iodide (NaI) [108]. One IRF image was taken with an acquisition time of 30 minutes, 512×512 pixels and 1024 time bins per intensity decay.

Data Analysis

- **Fluorescence Lifetime**

  The total intensity decay I_{tot} per pixel was reconstructed by summing the parallel and perpendicular transient decays per pixel according to the denominator of equation 4.10 with $x_{NA} = 2$. The fluorescence lifetime was obtained by weighted non-linear least squares fitting (Levenberg-Marquardt algorithm) of the total intensity decay in each pixel. The data was weighted according to the Poisson statistics and approximated by a model by minimising the square of the difference between the model and the data, the so-called residuals (res^2 or χ^2). The model used for fitting the data was a single-exponential function:

$$I_{tot}(t) = IRF \otimes (I_0 e^{-t/\tau_F} + B) \tag{4.23}$$

  where I_0 is the intensity amplitude, τ_F the fluorescence lifetime and B the background.

  The standard deviation per fit parameter and pixel was obtained by calculating the Jacobian matrix, which is a matrix that contains the partial derivatives of the model function with respect to the fit parameters. If there are three fit parameters and the data has 1024 data points, the size of the Jacobian matrix will be n×m = 1024×3. Once the algorithm (Levenberg-Marquardt) converged minimising res^2, the fit parameters were found and the Jacobian matrix was given as a numeric matrix. The covariance matrix was obtained by calculating the inverse of the Jacobian matrix by its transpose and the

standard deviation per fit parameter was obtained by applying the square root on the diagonal of the covariance matrix. In this case, for three fit parameters, the covariance matrix will have a size of m×m = 3×3. This data analysis was undertaken for the four FITC data sets with varying total collection times.

- **Time-resolved Fluorescence Anisotropy and Steady-State Anisotropy**

  In order to compare the experimental with the theoretical rotational correlation time uncertainties, time-resolved anisotropy decays were reconstructed, according to equation 4.10 and fitted with a free rotational model:

$$r(t) = r_0 e^{-t/\theta} \tag{4.24}$$

  where r_0 is the initial anisotropy determined by the relative orientation between the excitation and emission dipole transition moments, and the distribution of the orientation of the fluorophores. If the distribution is random and the dipole transition moments are parallel to each other, r_0 is equal to 0.4 when using single-photon excitation [20]. The rotational correlation time is given by θ, which corresponds to the time it takes the fluorophore to rotate 1 radian [20].

  The 120 minutes FAIM data set was used for this purpose. Different regions of interest (ROI) with different number of pixels were selected and the parallel and perpendicular intensity decays integrated per time bin. From the total parallel and perpendicular intensity decays, the time-resolved fluorescence anisotropy decay was reconstructed and fitted as previously stated by equation 4.24. The fit parameter standard deviations were calculated using the same method applied to the FLIM data with a weighting given by equation 4.11. For each ROI, the steady-state anisotropy data was also calculated adding up all the photons per ROI pixel and polarisation transient and apply-

ing equation 4.10. The steady-state anisotropy standard deviation is given by equation 4.12. Finally, the fluorescence lifetime per ROI was calculated using the Perrin equation 4.13 and equation 4.9 was applied to calculate its standard deviation.

A G-factor map per FAIM data set was generated by dividing the parallel by the perpendicular intensity decays per pixel within a fixed and low-noisy region at the tail of the decays.

4.3.3 Results & Discussion

4.3.3.1 Simulated Data

Dependence of Rotational Correlation Time Uncertainty with Time Resolution: 3 and 2-dimensional Maps

According to equation 4.21, Figures 4.2 and 4.3 show the dependence of $\Delta\theta/\theta_{N=1}$ with τ and θ for different time channels k, with a constant time window T = 50 ns. The last plot of both figures corresponds to the ideal case where there is no dependence on T nor on k ($var_1(s,k) \rightarrow 1$) (equation 4.22). In Figure 4.3, a continuous line of black dots indicates for which θ and τ values the minimum $\Delta\theta/\theta_{N=1}$ takes place. The red dashed line stands for equal values of θ and τ, with a gradient of 1.

According to equation 4.21 the magnitude of $\Delta\theta/\theta$ decreases with the total amount of photons N. This means that a collection of more photons yields a decrease on $\Delta\theta/\theta$.

The highest values of $\Delta\theta/\theta_{N=1}$ are registered at low number of time channels k (colour bar of Figures 4.2 and 4.3). When the number of time channels k decreases, $\Delta\theta/\theta_{N=1}$ increases its magnitude as it triggers at short τ values. Meanwhile high values of $\Delta\theta/\theta_{N=1}$ take place for short lifetimes τ at low number of time channels k, this trend changes its location when the number of time channels increases, showing up at two extreme cases:

1. Large τ and short θ.

2. Short τ and large θ.

If the minimum for $\Delta\theta/\theta_{N=1}$ is calculated, it can be observed that for all the cases this is located at very close positions to $\tau/\theta = 1$ (dashed red line of Figure 4.3). However, while this is the behaviour found for the ideal case (no dependence on T and k) and large number of time channels k, this is not the case at low time resolutions when θ and τ are low. This is best observed in Figure 4.3, where a clear deviation of the location of this minimum is spotted when the amount of time channels k lowers. The more number of time channels are used, the lower this deviation is and the closer the minimum position for $\Delta\theta/\theta_{N=1}$ gets to the condition $\tau/\theta = 1$. The most extreme case can be observed in the first plot of Figure 4.3, where the number of time channels k consists of 8. The minimum $\Delta\theta/\theta_{N=1}$ is located at θ positions from $\theta \sim 10^{-2}$ ns to $\theta = 1$ ns and with $\tau \sim 1$ ns. It can also be inferred from these graphs that from a certain time resolution (number of time channels k), the position of this minimum shows no dependence with T and k and it can be defined by a perfect straight line where τ/θ goes to 1. When this happens, the approximation $var_1(s,k) \to 1$ can be used and equation 4.22 must be applied.

This subsection gives a general idea of how the location of the minimum uncertainty associated to θ varies with θ itself, τ, k and the time window T. However, the next subsection will employ a more detailed data analysis by the visualisation of multiple cross sections at fixed θ positions, where the magnitude of $\Delta\theta/\theta_{N=1}$ is investigated with k across the entire τ range, with $T = 50$ ns. This will allow us to understand better the big picture of the problem.

Note that all these examples are referred to a time window of $T = 50$ ns, but this could be expanded for different time windows.

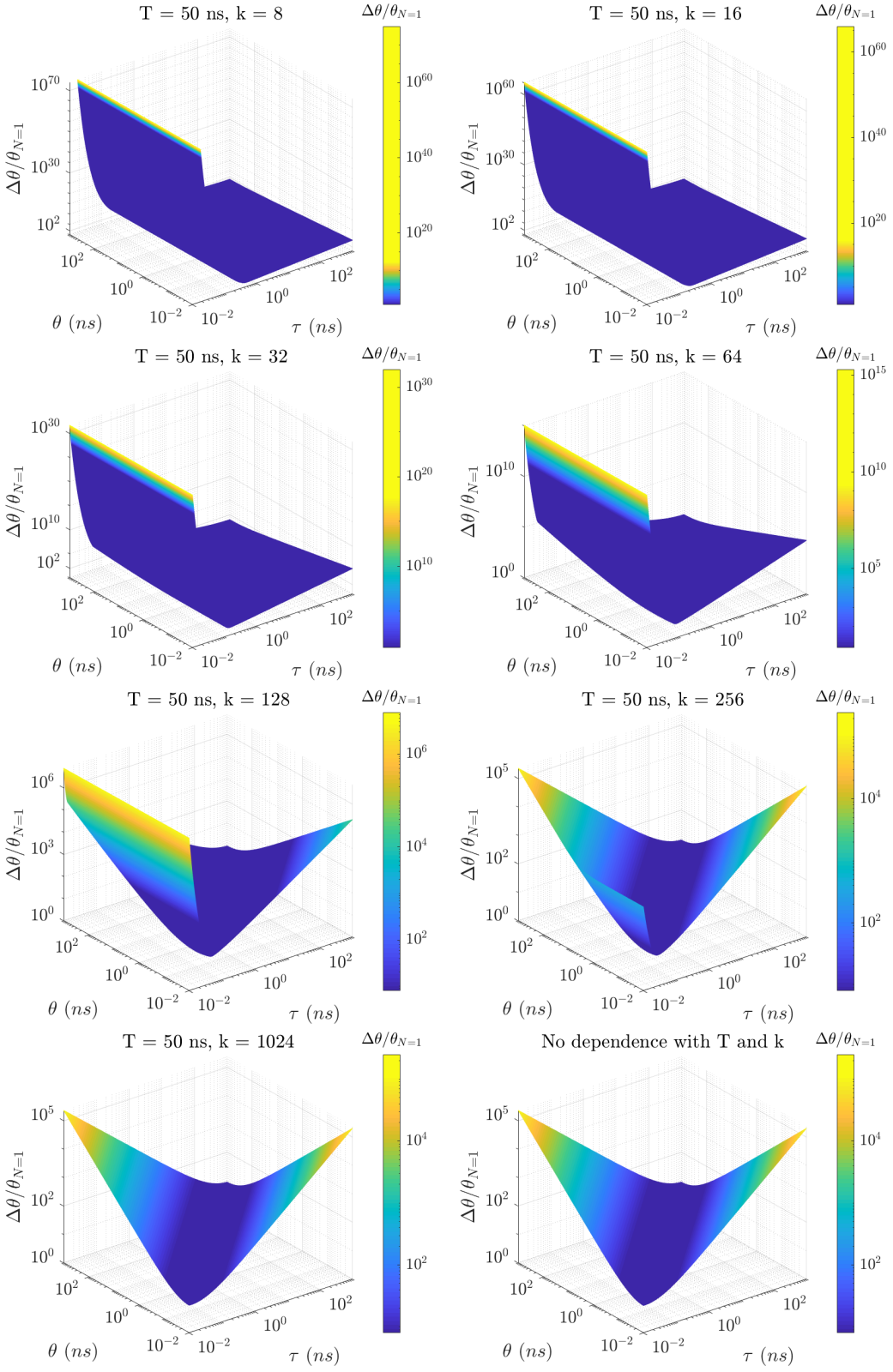

Figure 4.2: 3D plots showing the dependence of $\Delta\theta/\theta_{N=1}$ with τ and θ for different time resolutions k and constant time window T. The last case has no dependence with T and k.

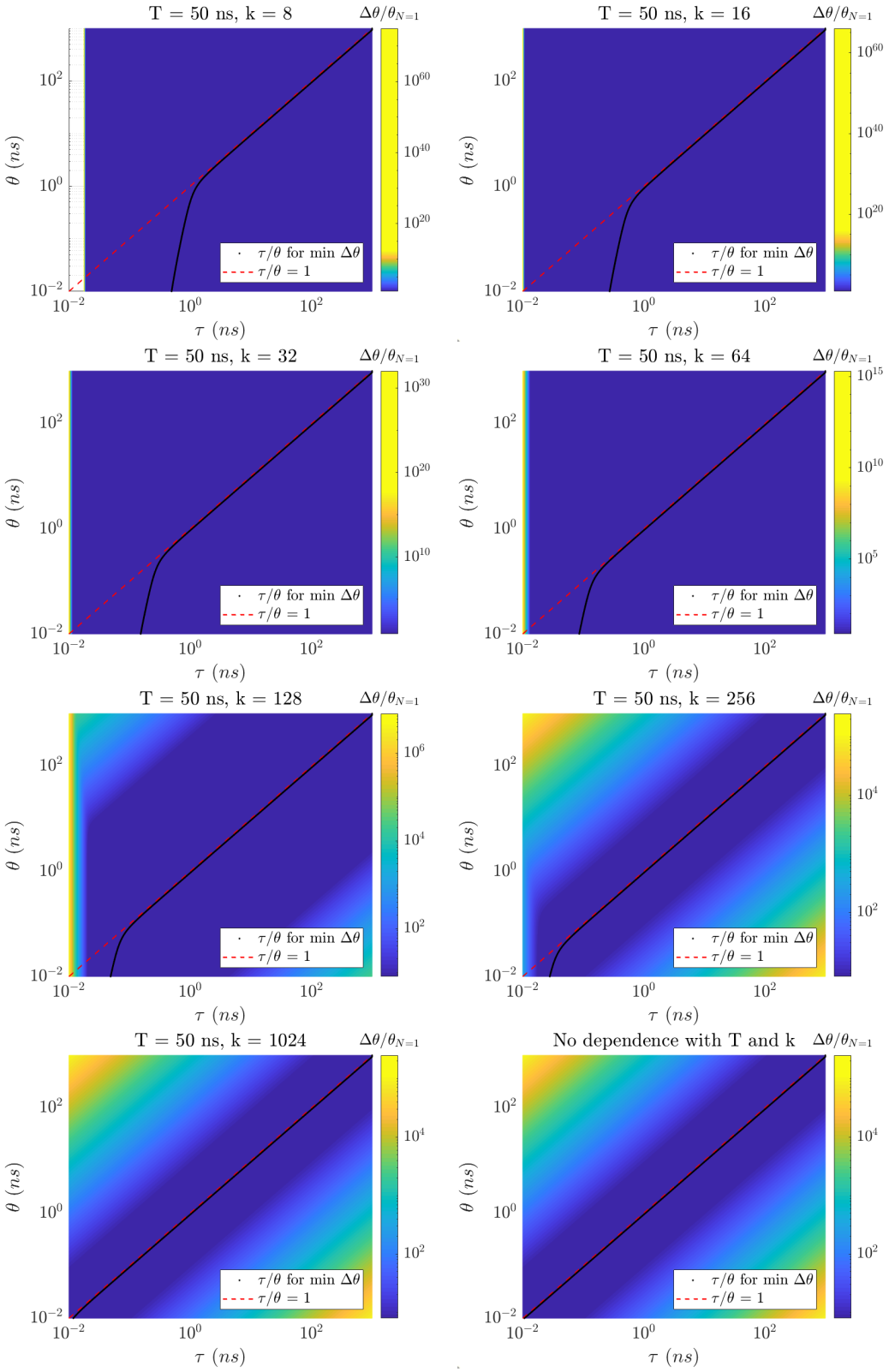

Figure 4.3: 2D representation of the dependence of $\Delta\theta/\theta_{N=1}$ with τ and θ for different time channels k and constant time window T. The last case has no dependence with T and k. The minimum $\Delta\theta/\theta$ is found for every single combination of τ and θ and plotted along the condition $\tau/\theta = 1$.

Dependence of Rotational Correlation Time Uncertainty with Time Resolution: Cross Sections

A combination of multiple cross sections of Figure 4.2 at certain θ positions is presented in Figure 4.4. The dependence of the minimum position of $\Delta\theta/\theta_{N=1}$ and its evolution with the number of time channels k is displayed at the following θ positions: 10^{-2}, 10^{-1}, 10^{0}, 10^{1}, 10^{2} and 10^{3} ns.

From Figure 4.4, it can be observed that when the number of time channels k is large enough, a common global minimum for $\Delta\theta/\theta_{N=1}$ is reached over the entire τ range at one specific θ position, where the ratio τ/θ is close to 1. If we focus on the specific case of k = 16, the common minimum is reached when θ approaches 1. This allows a better visualisation of the initial deviation of the position of the minimum $\Delta\theta/\theta_{N=1}$ for $\theta \leq 1$ ns and low time resolutions k. The deviation of the position of the minimum $\Delta\theta/\theta_{N=1}$ within 10^{-2} ns $\leq \theta \leq 1$ ns is reversed by increasing the number of time channels k. For instance, at $\theta = 10^{-1}$ ns this is done with a minimum number of 32 time channels, approximately. On the contrary, at certain θ cross sections, the position of the minimum $\Delta\theta/\theta_{N=1}$ does not vary with k. For this specific case scenario, it happens from θ = 10 ns, where all the time resolution curves fall onto the same global minimum. In Figures 4.2 and 4.3, this happens from $\theta \sim 1$ ns, as the lowest number of time channels displayed is k = 8.

All these results suggest that in order to achieve the lowest experimental uncertainty for θ when the time-resolved anisotropy decay is recorded, as a general trend, one must choose a probe whose τ is equal or very close to θ [288]. For low time resolutions, the lowest uncertainty associated with θ for a probe with a certain τ is found at $\theta \leq \tau$, approximately. While from Figures 4.2 and 4.3 it was not possible to infer and compare the magnitude of the uncertainty associated with θ for short τ and θ at low and high time resolutions (given by the number of time channels k),

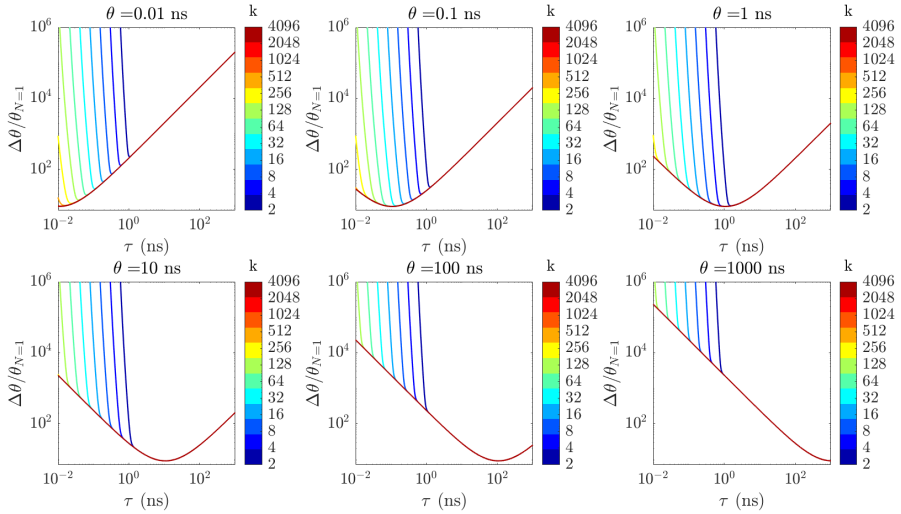

Figure 4.4: Dependence of minimum $\Delta\theta/\theta_{N=1}$ with τ and k for a fixed θ and time window T. This example is given for $T = 50$ ns.

Figure 4.4 is able to provide us with this information. The value of the optimal $\Delta\theta$ increases at these short ranges, where a higher time resolution k is necessary in order to decrease the θ uncertainty. This makes sense if we think the entire rotation of the probe is better visualised at the excited state when this happens faster than its τ ($\theta \leq \tau$). However, if θ is too short (very fast rotation) the recording of this rotation will be more difficult and a higher time resolution will be needed for more accurate results. The opposite case scenario would be difficult to explain, if the minimum uncertainty for θ was located at $\theta \geq \tau$ for short τ and θ values and low time resolution k. This would mean that an increase in the time resolution would be needed in order to decrease the uncertainty of θ when the rotation of the probe happens in a longer time scale in comparison to its excited state lifetime. This does not make sense as an increase in the time resolution would not lead to any improvement in the rotational correlation time uncertainty.

In this work, we have normalised $\Delta\theta/\theta$ to the number of photons N ($\Delta\theta/\theta_{N=1}$) and its minimum has been located for a range of τ and θ. However, the problem could be tackled the other way around. By knowing all the parameters, τ, θ, r_0, k,

T and the number of photons N, one can calculate what would be the uncertainty associated with θ. Moreover, if all these parameters were known but N, one could track the total number of photons needed to be collected during the time-resolved anisotropy measurement for the desirable θ accuracy. The total amount of photons N (signal strength) is given by:

$$N = \sum_{i=1}^{k} I_{tot,i} = \sum_{i=1}^{k} I_{\parallel,i} + 2G \sum_{i=1}^{k} I_{\perp,i} \tag{4.25}$$

where i goes from 1 to the total amount of time channels k.

Overall, the data analysis of this simulated data helps define optimal boundary conditions in order to collect accurate values for θ, where the role the time resolution k plays varies with T/τ.

This work refers to T = 50 ns but the dependence of $\Delta\theta/\theta_{N=1}$ with τ, θ and k for different time windows can also be investigated. Moreover, the same data analysis can be undertaken by defining cross sections of plots alike Figure 4.2 at certain fixed τ positions. This was done and presented in Appendix B.

4.3.3.2 Theoretical vs Experimental Fluorescence Lifetime Uncertainties

In this subsection, the uncertainty associated with experimental fluorescence lifetime recordings will be compared with its theoretical uncertainty given by equation 4.9.

Representative FLIM maps are presented in Figure 4.5A and B, for the FAIM data sets with acquisition times of 30 and 120 minutes, respectively. Inserted within the FLIM maps, representative parallel and perpendicular intensity decays for one pixel are displayed. From the FLIM maps per FAIM data set, the correspondent fluorescence lifetime histograms were generated (Figure 4.5C) and plotted together for comparison. The same procedure was followed for the assessment of the fluores-

cence lifetime standard deviation $sd(\tau)$ per pixel image. The results are presented in Figure 4.5D.

From the inserted plots of Figure 4.5A and B, it can be observed that the number of photons N per pixel differs from one data set to the other, as they are taken with different acquisition times. For the 30 minutes FAIM data set, the number of counts of the presented representative $I_{\parallel}$ and $I_{\perp}$ decays at the peak is approximately 20, meanwhile for the 120 minutes FAIM data set is around 70. The lower SNR present in the individual intensity decays for shorter acquisition times may lead to an underestimation of the fit parameters when the total intensity decay is approximated with a single-exponential model [289]. This τ shift is clearly observed in Figure 4.5C, where the FLIM map histograms per FAIM data set are plotted and fitted with a Gaussian distribution. The mean τ increases with the image time collection, which increases with the total amount of photons N per pixel. Moreover, the FLIM map distribution narrows down when the time collection increases, leading to the true fluorescence lifetime τ and a reduced standard deviation of its normal fit. The $sd(\tau)$ per pixel and FAIM data set is also investigated and presented in Figure 4.5C. As predicted by equation 4.9, this parameter decreases its magnitude with the number of counts N (analogous to longer collection times). Therefore, a shift of $sd(\tau)$ is observed among the FAIM data sets. The fluorescence lifetime standard deviation $sd(\tau)$ map distributions are also fitted with a Gaussian function, which narrow down with N and whose mean value decrease with the number of counts N. The total amount of photons N per pixel and FAIM data set are presented in Table 4.1, so as the mean experimental fluorescence lifetime, extracted from the FLIM map distribution fit, and its experimental and theoretical standard deviations. Although the fluorescence lifetime is underestimated when the number of counts N is low, the calculated fluorescence lifetime standard deviations are still valid as they have a much stronger dependence on N than on the fluorescence lifetime itself.

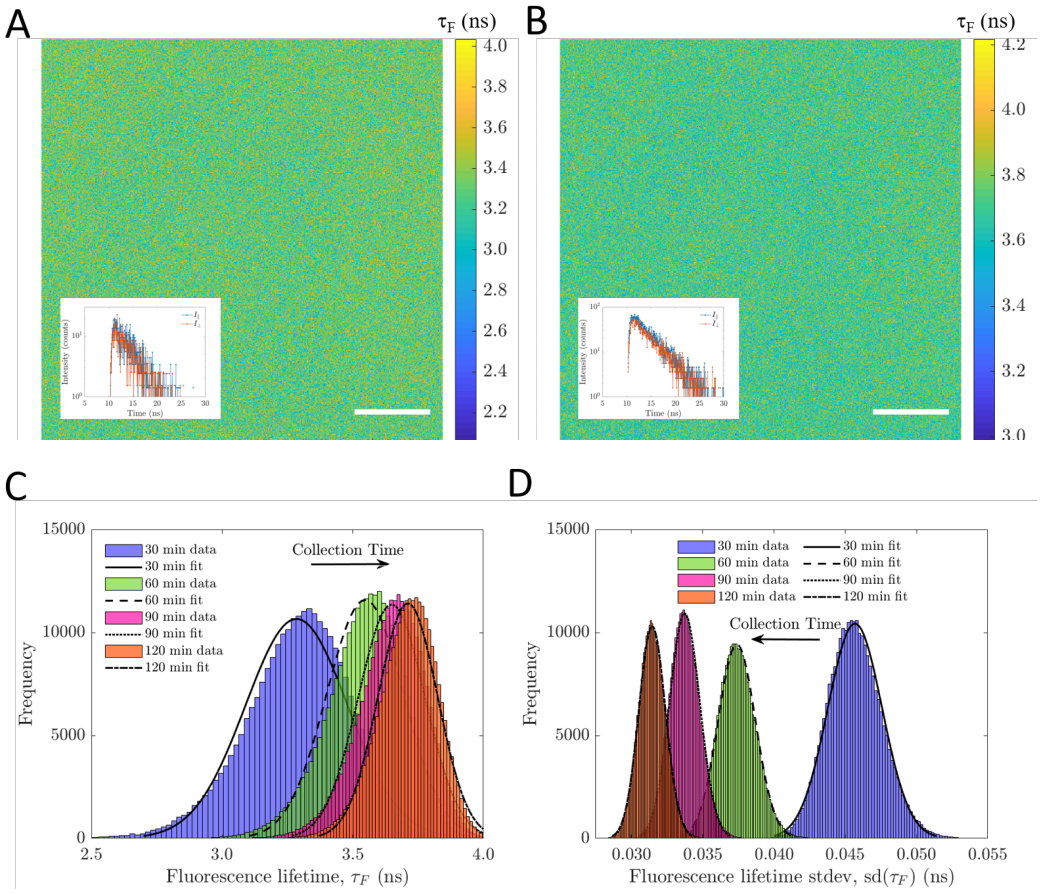

Figure 4.5: FLIM maps with representative parallel and perpendicular intensity decays for the (A) 30 minutes and (B) 120 minutes FAIM data sets. (C,D) Fitted FLIM map and sd(τ) histograms with a Gaussian distribution per FAIM data set. Map scale bars: 50 μm.

Table 4.1: Mean fluorescence lifetime parameters and standard deviations per FAIM data set.

Time (min)	**N (photons)**	τ_{exp} **(ns)**	**sd(τ)$_{exp}$ (ns)**	**sd(τ)$_{th}$ (ns)**
30	3900	3.29	0.05	0.05
60	8000	3.55	0.04	0.04
90	12000	3.65	0.03	0.03
120	16000	3.71	0.03	0.03

Figure 4.6 presents the relationship between these two magnitudes, $sd(\tau)_{exp}$ and $sd(\tau)_{th}$. The data is fitted with a linear model that goes almost through zero, with a gradient of 1.086 $\pm$ 0.377, an intercept of 0.002 $\pm$ 0.014 ns and a goodness of fit of R^2 = 0.9807. This fit model with a very close gradient to 1 validates equation 4.9 [282] and it is used with confidence in equations 4.21 and 4.22 for the

investigation of the rotational correlation time uncertainty.

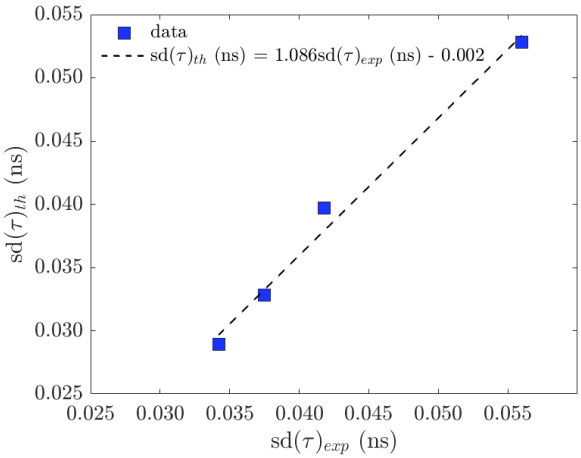

Figure 4.6: Theoretical fluorescence lifetime standard deviation sd(τ) plotted against the experimental sd(τ) per FAIM data set. The data is fitted with a polynomial function of first order: $sd(\tau)_{th}$ = *(1.08* $\pm$ *0.377)*$sd(\tau)_{exp}$ *- (0.002* $\pm$ *0.014).*

4.3.3.3 Theoretical vs Experimental Rotational Correlation Time Uncertainties

In this subsection the experimental and theoretical θ uncertainties are compared for several cases, where different amount of photons N are collected per case.

The time-resolved fluorescence anisotropy decay fit parameters per ROI with varying N from the 120 minutes FAIM data set are presented in Table 4.2. The χ^2_R of the time-resolved fluorescence anisotropy fit, the G-factor, the steady-state anisotropy and the fluorescence lifetime calculated from the Perrin equation (equation 4.13) and per ROI are also presented in Table 4.2. Representative intensity decays ($I_{\parallel}$ and $I_{\perp}$) and fitted time-resolved fluorescence anisotropy decay, for a ROI with $N = 1.39\times10^6$ counts of the 120 minutes FAIM data set, are presented in Figure 4.7A and B, respectively. Figure 4.8 indicates where the mean experimental data (τ = 3.91 ns and θ = 0.50 ns) is located within the plot given by Figure 4.3 (last row, first column), where $sd(\theta)/\theta_{N=1}$ is calculated for an array of fluorescence life-

times τ and rotational correlation times θ, with a time resolution k = 1024 and time window T = 50 ns.

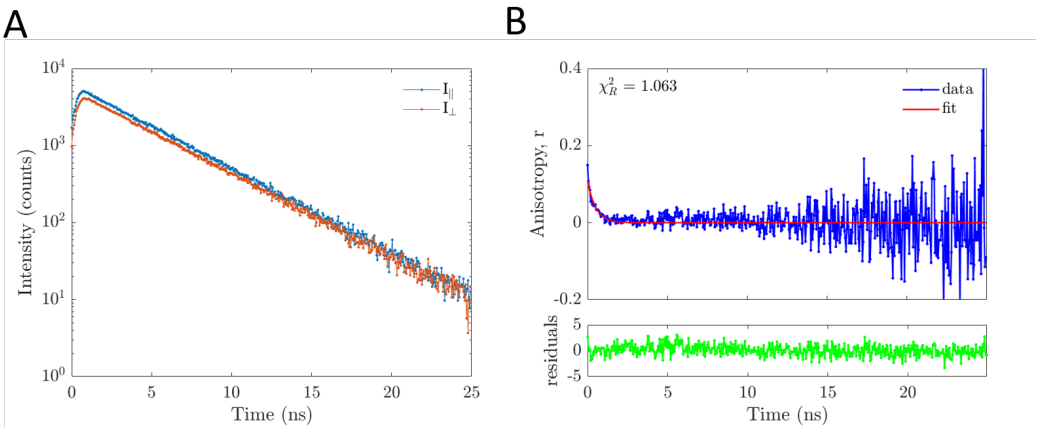

Figure 4.7: (A) Parallel and perpendicular decays for a ROI with N = 1.39×10^6 of the 120 minutes FAIM data set. (B) Time-resolved fluorescence anisotropy decay and fit of the same ROI.

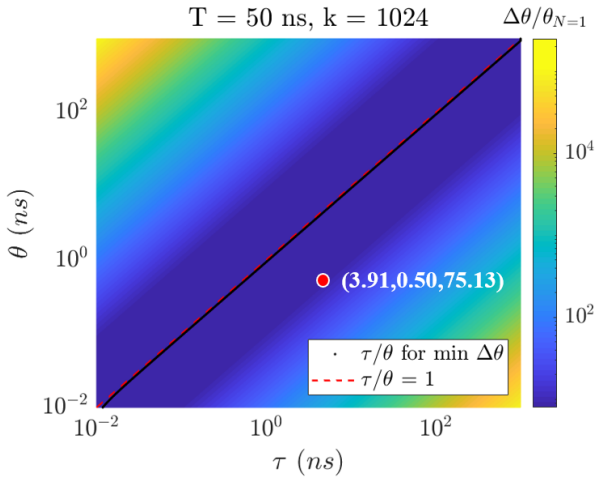

Figure 4.8: Location of experimental data within the simulated plots given by equation 4.21. The number of time channels k = 1024 and the time window is T = 50 ns.

Table 4.2: Experimental time-resolved fluorescence anisotropy, steady-state anisotropy and fluorescence lifetime parameters per ROI of the 120 minutes FAIM data set.

N (photons)	θ_{exp} (ns)	sd(θ)$_{exp}$ (ns)	$r_{0,exp}$	sd(r_0)$_{exp}$	χ^2_R	r	sd(r)	G-factor	τ_{Perrin} (ns)	sd(τ_{Perrin})$_{th}$ (ns)
1.1×10^6	0.51	0.04	0.104	0.007	1.076	0.0122	0.0008	1.149	3.876	0.003
1.4×10^6	0.50	0.03	0.109	0.007	1.063	0.0121	0.0007	1.151	3.985	0.003
1.7×10^6	0.50	0.03	0.112	0.006	1.107	0.0128	0.0006	1.149	3.830	0.003
2.1×10^6	0.50	0.03	0.111	0.006	1.152	0.0124	0.0006	1.152	3.939	0.003
3.4×10^6	0.54	0.03	0.109	0.005	1.450	0.0137	0.0005	1.148	3.726	0.002
3.9×10^6	0.53	0.03	0.109	0.005	1.527	0.0132	0.0004	1.149	3.847	0.002

From the time-resolved fluorescence anisotropy decay fits, the experimental fit parameters are obtained and from the rotational correlation time parameter and its standard deviation, $sd(\theta)/\theta$ can be calculated directly. This is presented in the third column of Table 4.3. Equation 4.22 is applied to calculate the theoretical values for $sd(\theta)/\theta_{N=1}$ and $sd(\theta)/\theta$, where G is considered to be 1. The results are displayed in the first two columns of the Theoretical block of Table 4.3. For a comparison with the real case, the experimental G-factor is introduced in the initial equation 4.16 and the approximation $var_1(s,k) \to 1$ is applied, as the time resolution is large enough to be able to consider this case (k = 1024). Overall, this yields the following expression for the rotational correlation time uncertainty:

$$\Delta\theta = \frac{1}{\sqrt{N}}\sqrt{\theta^2 + \left(\frac{r_0\tau}{(r_0-r)^2}\right)^2 \frac{(1+r)(1+2r)(1-r+G(1+2r))}{3}} \tag{4.26}$$

From this equation, the last two columns of Table 4.3 are generated, where the steady-state anisotropy r and the G-factor appear explicitly in the equation.

Table 4.3: Experimental and theoretical $sd(\theta)/\theta$ for N_{exp} and N = 1. The theoretical results are divided in two columns, indicating which G-factor was used for getting the final results.

Experimental			**Theoretical**			
			G = 1		**Experimental G**	
N (photons)	**θ (ns)**	**sd(θ)/θ**	**(sd(θ)/θ)$_{N=1}$**	**sd(θ)/θ**	**(sd(θ)/θ)$_{N=1}$**	**sd(θ)/θ**
1.1×10^6	0.51	0.08	76.44	0.07	79.29	0.08
1.4×10^6	0.50	0.07	76.59	0.06	79.48	0.07
1.7×10^6	0.49	0.06	72.68	0.05	75.39	0.06
2.1×10^6	0.50	0.06	74.82	0.05	77.65	0.05
3.4×10^6	0.54	0.05	68.87	0.04	71.42	0.04
3.9×10^6	0.53	0.05	71.07	0.04	73.72	0.04

Theoretical values of $sd(\theta)/\theta$ (for G = 1 and $G \neq 1$) are plotted against the experimental $sd(\theta)/\theta$ (Figure 4.9A). A linear relationship between variables is found, for both G-factor cases. When G = 1, the fit gradient is given by 1.244 $\pm$ 0.387 and the intercept is - 0.025 $\pm$ 0.025, with a goodness of fit of R^2 = 0.9808. When the

experimental G-factor is applied, the gradient of the fit is 1.290 ± 0.399 and the intercept is - 0.026 ± 0.025, with R^2 = 0.9804. The uncertainties of the intercepts are of the same order of magnitude as the intercepts themselves. This indicates a fit with intercept fixed to zero would be valid. The last two data points (Figure 4.9A), per G-factor case, that present the lowest sd(θ)/θ values are the correspondent to the highest number of photons ($N = 3.4\times10^6$ and 3.9×10^6 counts). When the number of photons N increases, the time-resolved fluorescence anisotropy decay fit gets worse, which is indicated by an increase on the χ^2_R. Non-linearities in the signal show up with more strength as the number of photons increases possibly due to differential and/or integral non-linearities on the time to amplitude converter (TAC) of the TCSPC electronic card. This effect is clearly observed on the last two data points, where the time-resolved fluorescence anisotropy decays present a wavy shape as they progressively decay to zero (Figure 4.7B). As a consequence, these two data points are off the general trend and will not be considered for the final fits (Figure 4.9B). The new fits have reduced gradients compared to the previous cases and closer to 1. For G = 1, the gradient of the fit is 0.9545 ± 0.4317, the intercept is - 0.0038 ± 0.0301 and the goodness of fit is given by R^2 = 0.9789. When the experimental G-factor is considered, the fit gradient and intercept are: 0.9892 ± 0.4102 and - 0.0039 ± 0.0282, respectively. The goodness of fit is R^2 = 0.9802. For the new fits, a better agreement between the theoretical and experimental results is presented, specially when the experimental G-factor is used.

These results state that the equation that has been derived in this work for estimating the uncertainty of the rotational correlation time (equation 4.21) is valid and that in order to obtain optimal results, the G-factor must be exactly 1, otherwise a different approach must be undertaken (equation 4.26).

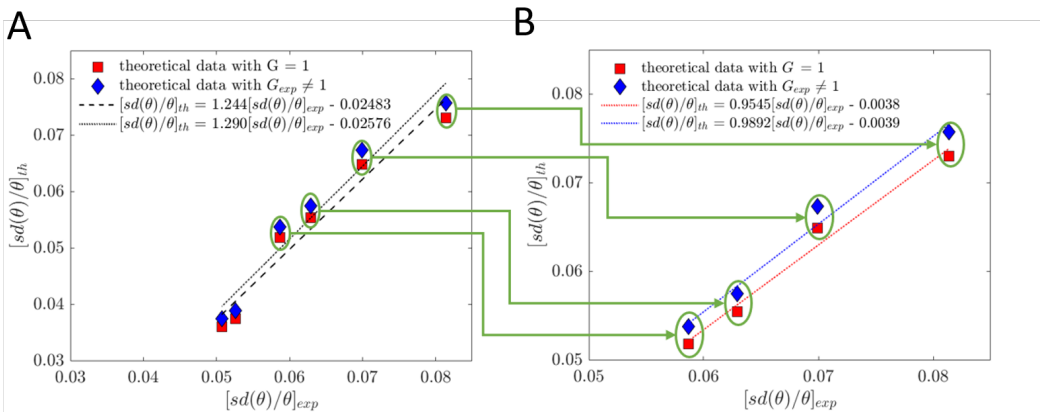

Figure 4.9: (A) Plot of the theoretical and experimental sd(θ)/θ values per 120 minutes FAIM data set ROI. The data per G-factor is fitted with a first degree polynomial model. (B) The second graph is an enlarged view of the first one.

4.4 Rotational Correlation Time Distribution from Image

4.4.1 Materials & Methods

4.4.1.1 Analytic/Symbolic Approach

The rotational correlation time probability density function $pdf(\theta)$ is calculated means of using the Perrin equation (equation 4.13). The probability density function refers to a continuous distribution of a variable. The fluorescence lifetime τ and steady-state anisotropy r are considered to be random, independent and continuous variables. Therefore, the joint distribution for independent variables analysis will be applied here to solve the $pdf(\theta)$.

We have seen that rearranging the Perrin equation, equation 4.13, the rotational correlation time θ is given as follows:

$$\theta = \frac{\tau}{\frac{r_0}{r} - 1} \tag{4.27}$$

The pdf of the two independent variables follows in this case a normalised Gaussian

function, such as:

$$f(\tau) = \frac{1}{\sqrt{2\pi\sigma_\tau^2}} e^{-\frac{(\tau-\mu_\tau)^2}{2\sigma_\tau^2}} \tag{4.28}$$

$$f(r) = \frac{1}{\sqrt{2\pi\sigma_r^2}} e^{-\frac{(r-\mu_r)^2}{2\sigma_r^2}} \tag{4.29}$$

The cumulative distribution of θ will be given as the integration of its probability density function pdf, dependent on τ and r:

$$F(\theta) = F(\tau, r) = \iint_{-\infty}^{\theta} f(\tau, r)\, d\tau\, dr \tag{4.30}$$

From the Perrin equation (4.13), the variable τ is expressed as a function of r and θ and the determinant of the Jacobian of this transformation is introduced in equation 4.30.

$$\tau = \theta(r_0/r - 1) \tag{4.31}$$

$$F(\theta) = \int_{-\infty}^{+\infty} \int_{-\infty}^{\theta} f(\theta(r_0/r-1), y) J(\theta, r)\, d\theta\, dr \tag{4.32}$$

The determinant of the Jacobian is calculated:

$$J(\theta, r) = \begin{vmatrix} \frac{\partial\tau}{\partial\theta} & \frac{\partial\tau}{\partial r} \\ \frac{\partial r}{\partial\theta} & \frac{\partial r}{\partial r} \end{vmatrix} = \begin{vmatrix} \frac{r_0}{r} - 1 & \frac{r_0\tau}{(\tau+\theta)^2} - \frac{r_0\theta}{r^2} \\ 0 & 1 \end{vmatrix} = \frac{r_0}{r} - 1 \tag{4.33}$$

Equation 4.33 is rewritten as follows:

$$F(\theta) = \int_{-\infty}^{+\infty} \int_{-\infty}^{\theta} f(\theta(r_0/r-1), r)(r_0/r-1)\, d\theta\, dr \tag{4.34}$$

By deriving the cumulative probability distribution $F(\theta)$ (equation 4.34) with respect to θ, the probability distribution function $f(\theta)$ is given by:

$$f(\theta) = \frac{dF(\theta)}{d\theta} = \int_{-\infty}^{+\infty} \int_{-\infty}^{\theta} f(\theta(r_0/r-1), r)(r_0/r-1)\, dr \tag{4.35}$$

If two random variables x and y are independent, the joint cumulative distribution satisfies:

$$F(x,y) = F(x)F(y) \tag{4.36}$$

where F is the cumulative probability distribution.

Similarly, two continuous random variables are independent if:

$$f(x,y) = f(x)f(y) \tag{4.37}$$

where f is the probability density function pdf.

Applying equation 4.37, equation 4.35 is modified as follows:

$$f(\theta) = \int_{-\infty}^{+\infty} f(\theta(r_0/r-1))f(r)(r_0/r-1)\,dr \tag{4.38}$$

The explicit probability density functions of τ and r (equations 4.28 and 4.29) are introduced in equation 4.38:

$$f(\theta) = \int_{-\infty}^{+\infty} \frac{1}{\sqrt{2\pi\sigma_\tau^2}} e^{-\frac{\left(\theta\left(\frac{r_0}{r}-1\right)-\mu_\tau\right)^2}{2\sigma_\tau^2}} \frac{1}{\sqrt{2\pi\sigma_r^2}} e^{-\frac{(r-\mu_r)^2}{2\sigma_r^2}} (r_0/r-1)\,dr \tag{4.39}$$

Equation 4.39 shows that the rotational correlation time distribution is given by a combination of a Gaussian and a non-Gaussian function. However, as finding a solution of this integral is not trivial, the problem will be approached in the next section from a numerical point of view.

4.4.1.2 Numerical Approach

Simulation of Fluorescence Lifetime & Steady-State Anisotropy Distributions

Rotational correlation time distributions were simulated by defining a set of Gaussian distributions for the fluorescence lifetime and the steady-state anisotropy in

MATLAB and by applying equation 4.14. The initial anisotropy r_0 was set to 0.4. Each Gaussian distribution for τ and r was built up with 512×512 data points, simulating usual experimental images taken in the laboratory, with the same number of pixels. Normal distributions of r, with a mean value μ ranging from 0.1 to 0.3 and with a standard deviation σ going from 0.005 to 0.1, were generated. Three different mean values for the fluorescence lifetime distributions and three different standard deviations per parameter were defined: 3.7 (± 0,001, 0.001, 0.1), 10 (± 0.001, 0.1, 1) and 100 (± 0.1, 1, 10) ns. So for each $\tau \pm sd(\tau)$, the rotational correlation time distribution was calculated from all the combinations of $r \pm sd(r)$.

Mode & Skewness Distribution

The magnitude of the maximum θ within the rotational correlation time distribution was obtained by computing its mode, which finds the most sampled value within the distribution.

The asymmetry of the θ distribution around its mean was investigated by calculating its skewness (SK). If the skewness is positive, it means the data are spread out more to the right of the mean than to the left. If the skewness is negative, the data are spread out more to the left. The skewness of a perfectly symmetric distribution is zero. The skewness expression used in this work was the following:

$$SK = \frac{\frac{1}{n}\sum_{i=1}^{n}(x_i-\mu)^3}{\left(\sqrt{\frac{1}{n}\sum_{i=1}^{n}(x_i-\mu)^2}\right)^3} \tag{4.40}$$

where x is the data of the distribution, μ is the mean value of x and n accounts for the number of data points.

A skewness SK of 0 means that the distribution can be considered to be normal or symmetric. If $SK > 1$ or $SK < -1$, the distribution is considered to be highly

skewed. If - $1 < SK < -0.5$ or $0.5 < SK < 1$, the distribution is moderately skewed, and if - $0.5 < SK < 0.5$, the distribution is approximately symmetric.

Equation 4.40 relies on the mean value of the distribution. Large rotational correlation time values off the general trend were discarded from the distribution when the denominator of equation 4.14 gets close to 0. The criteria applied for setting the histogram range was stopping the distribution when the number of events at a certain θ was smaller or equal to 1% the registered number of events at the peak position. This is analogous to consider a normal distribution with a standard deviation close to 3σ.

4.4.2 Results & Discussion

All the results presented in the upcoming subsections correspond to simulated data.

4.4.2.1 Evolution of the Rotational Correlation Time Distribution with the Steady-State Anisotropy Standard Deviation

An example of how the rotational correlation time distribution θ evolves with $sd(r)$ is presented in this subsection. This is given by Figure 4.10A, where the rotational correlation time θ histogram is plotted for a range of steady-state standard deviations $sd(r)$.

A clear distinction between θ histograms corresponding to the first and last cases ($sd(r)$ = 0.005 and 0.1) are presented in Figure 4.10B and C, along their rotational correlation time maps. From both plots, it can be observed that:

1. The magnitude of θ increases with $sd(r)$ across the image.

2. The θ histogram evolves from a Gaussian distribution for low $sd(r)$ to a non-Gaussian distribution for high $sd(r)$.

For the given example, the r normal distribution was defined around r = 0.3 and the fluorescence lifetime was defined as a Gaussian distribution with μ = 3.7

ns and σ = 0.1 ns. The initial anisotropy was set to r_0 = 0.4. Similar plots, with varying τ and r normal distributions are presented in Appendix C.

Considering a single value for the initial anisotropy r_0 is supported by the low experimental uncertainties found for this parameter in *Section* 4.3.3.3 (Table 4.2). Therefore, we do not expect any significant change in the rotational correlation time distribution if a normal distribution for this parameter is defined. Nevertheless, this is verified by defining a normal distribution for r_0, with μ = 0.38 and σ = 0.02, and comparing the resultant rotational correlation time distributions with the ones obtained when r_0 is set to 0.4. The results are presented in Appendix D.

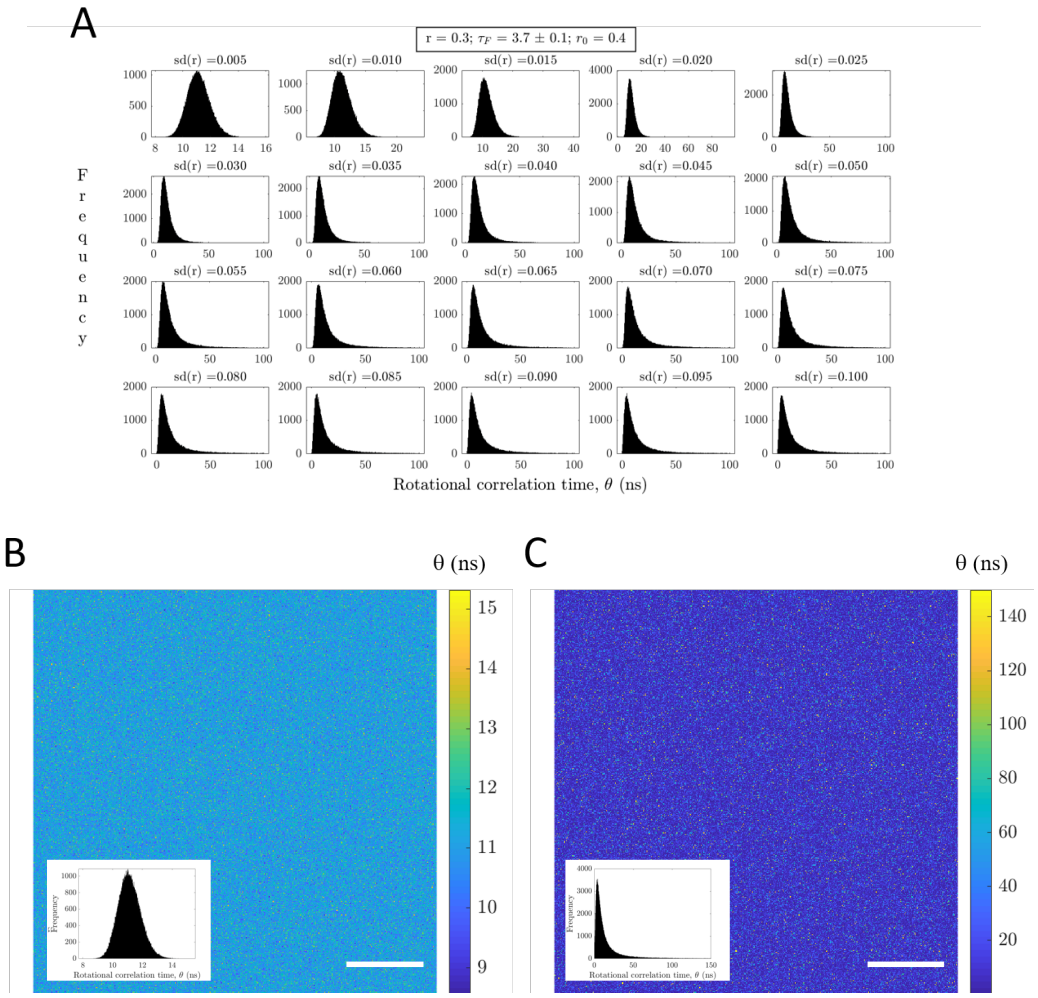

Figure 4.10: (A) Evolution of the rotational correlation time distribution with $sd(r)$ for r = 0.3, τ = 3.7 ± 0.1 ns and r_0 = 0.4. Rotational correlation time maps and histograms for (B) $sd(r)$ = 0.005 and (C) $sd(r)$ = 0.1. The map scale bars correspond to 25 pixels.

A detailed numerical analysis of the impact of the different Perrin equation parameters on the rotational correlation time distribution will be conducted in the following sections.

4.4.2.2 Mode Dependence with the Fluorescence Lifetime Standard Deviation

From Figure 4.10A, one can state with confidence that the θ distribution depends on $sd(r)$, as its histogram evolution with this parameter is evident. In order to assess how the peak position of these distributions changes with $sd(r)$ and assess the impact of $sd(\tau)$ on it, θ_{max} (mode) is calculated for each θ distribution. Three different cases with τ = 3.7 ns are considered: $sd(\tau)$ = 0.1, 0.01 and 0.001 ns. The steady-state anisotropy r is set to 0.1 and the initial anisotropy r_0 to 0.4. This is presented in Figure 4.11A, where the mode of θ is plotted against the steady-state anisotropy standard deviation $sd(r)$.

For all the $sd(\tau)$ cases, the maximum θ decreases with $sd(r)$, which has a clear impact on the magnitude and shape of the θ distribution. The three data sets are fitted with a linear model, from where the gradients are extracted: - 9.48, - 8.87 and - 9.10 ns, for sd(τ) = 0.1, 0.01 and 0.001 ns, respectively. No correlation of the gradient fit with sd(τ) is observed. Therefore, it can be concluded that for a specific τ, r and r_0, the magnitude of $sd(\tau)$ does not have any impact on the peak position of the rotational correlation time θ distribution. The same data analysis was undertaken for different fluorescence lifetimes and standard deviations: 10 $\pm$ 0.01, 0.1, 1 ns and 100 $\pm$ 0.1, 1, 10 ns (Appendix E).

4.4.2.3 Mode Dependence with the Steady-State Anisotropy

The dependence of the peak position of the rotational correlation time distribution θ_{max} with r was also investigated. Three different cases for r were taken into consideration: 0.1, 0.2 and 0.3. For this example, θ was set to 3.7 $\pm$ 0.1 ns and r_0 to

0.4. The magnitude of θ_{max} per r case was plotted against $sd(r)$ (Figure 4.11B), showing a progressive decrease of θ_{max} with $sd(r)$.

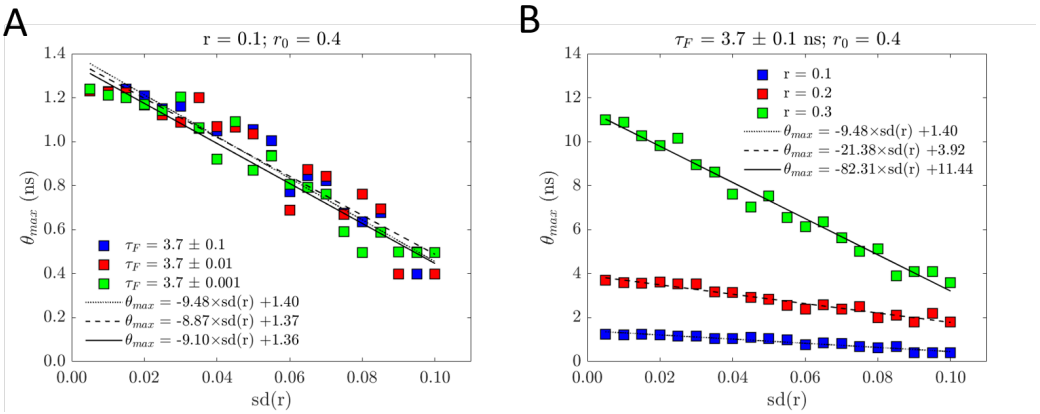

Figure 4.11: Dependence of the maximum value (θ_{max}) of the rotational correlation time distribution with $sd(r)$ (A) for a fixed r and varying τ and sd(τ), and (B) for a fixed τ and sd(τ) and varying r. All the data sets are fitted with a linear approximation.

The steepest slope of decrease of theta with increasing $sd(r)$ was found at $r = 0.3$. At $r = 0.1$, θ was nearly constant, independent of $sd(r)$. The data was fitted by linear regression, giving progressively shallower slope with increasing r. For $r = 0.3$, $r = 0.2$, and $r = 0.1$, the slopes of the linear regression model were -82.31 ns, -21.38 ns, and -9.48 ns, respectively. Therefore, the gradient of the fit was correlated with the steady-state anisotropy r, which indicates the change in the peak position with $sd(r)$ is more evident for high values of r. Also, the magnitude of θ_{max} increased with r, as predicted by the Perrin equation (equation 4.13). The highest intercept for the r = 0.3 data was a clear indication of this. Therefore, the intercepts increased with r: 11.44 ns, 3.92 ns and 1.40 ns for r = 0.3, 0.2 and 0.1, respectively. A similar data analysis with alike results was undertaken for τ = 10 $\pm$ 0.1 ns and 100 $\pm$ 0.1 ns (Appendix F).

4.4.2.4 Rotational Correlation Time Distribution Mode Map

The mode of the rotational correlation time distribution per r, $sd(r)$, τ and sd(τ) is investigated in this subsection.

In Figure 4.12, an array of r and $sd(r)$, ranging from 0.10 and 0.005 to 0.30 and 0.01, respectively, is defined. Three different fluorescence lifetimes with three varying standard deviations are selected (3.7 $\pm$ 0.001, 0.01, 0.1 ns, 10 $\pm$ 0.01, 0.1, 1 ns and 100 $\pm$ 0.1, 1, 10 ns) and the corresponding rotational correlation time distribution calculated. From each distribution, the maximum θ is computed and plotted. Each row corresponds to one fluorescence lifetime τ and different $sd(\tau)$ are located in different columns. The initial anisotropy r_0 is 0.4. For each plot of

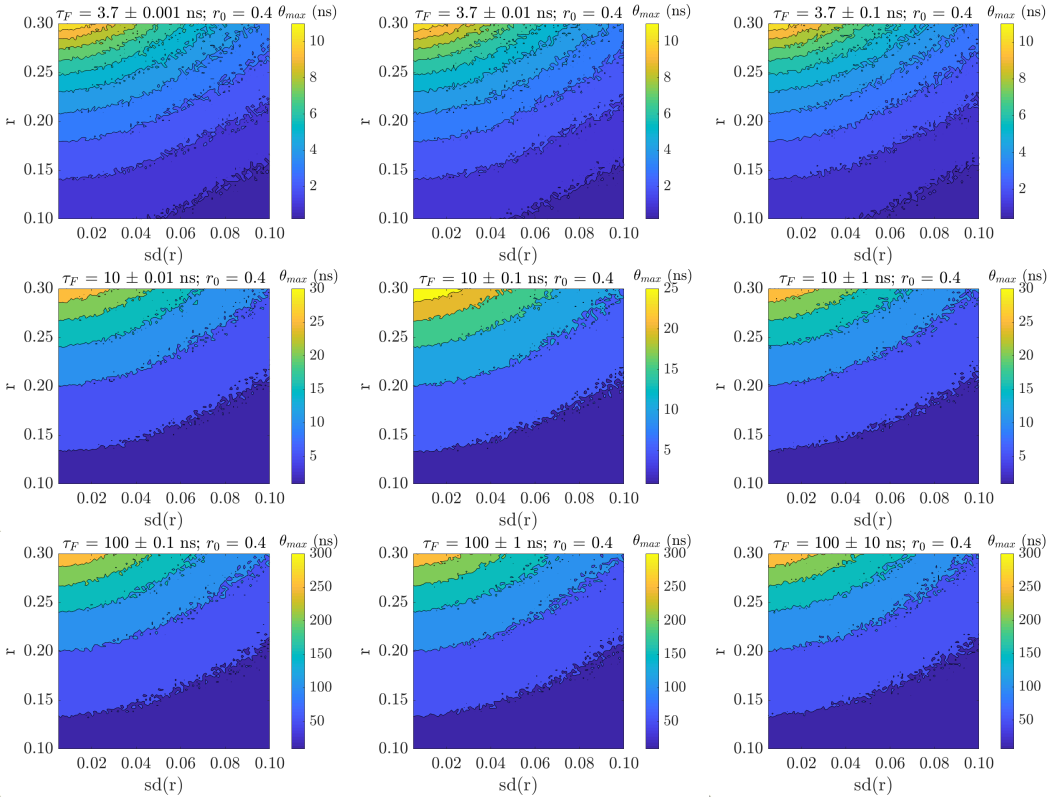

Figure 4.12: Rotational correlation time distribution mode per r, $sd(r)$ and $\tau \pm sd(\tau)$.

Figure 4.12, an increase in the θ_{max} is observed in a diagonal trend, from high $sd(r)$ and low r to low $sd(r)$ and high r values. The magnitude of θ_{max} scales up with the fluorescence lifetime, in good agreement with the Perrin equation (equation 4.13). The plots of each individual row can be considered as almost identical, where the $sd(\tau)$ does not modify the final outcome, such as it was discussed in the previous section (*Section* 4.4.2.2).

4.4.2.5 Skewness Map of the Rotational Correlation Time Distribution

The study of how far a distribution deviates from normal is undertaken by calculating the skewness SK of such distribution. This was applied to the θ distributions per r, $sd(r)$, τ and $sd(\tau)$.

A similar array of r and $sd(r)$ as described in *Section* 4.4.2.4 was generated and the skewness of the resultant θ distributions was calculated according to equation 4.40. The results are presented in Figure 4.13 and classified by fluorescence and standard deviation lifetimes. For all the τ cases, the SK of the θ distribution

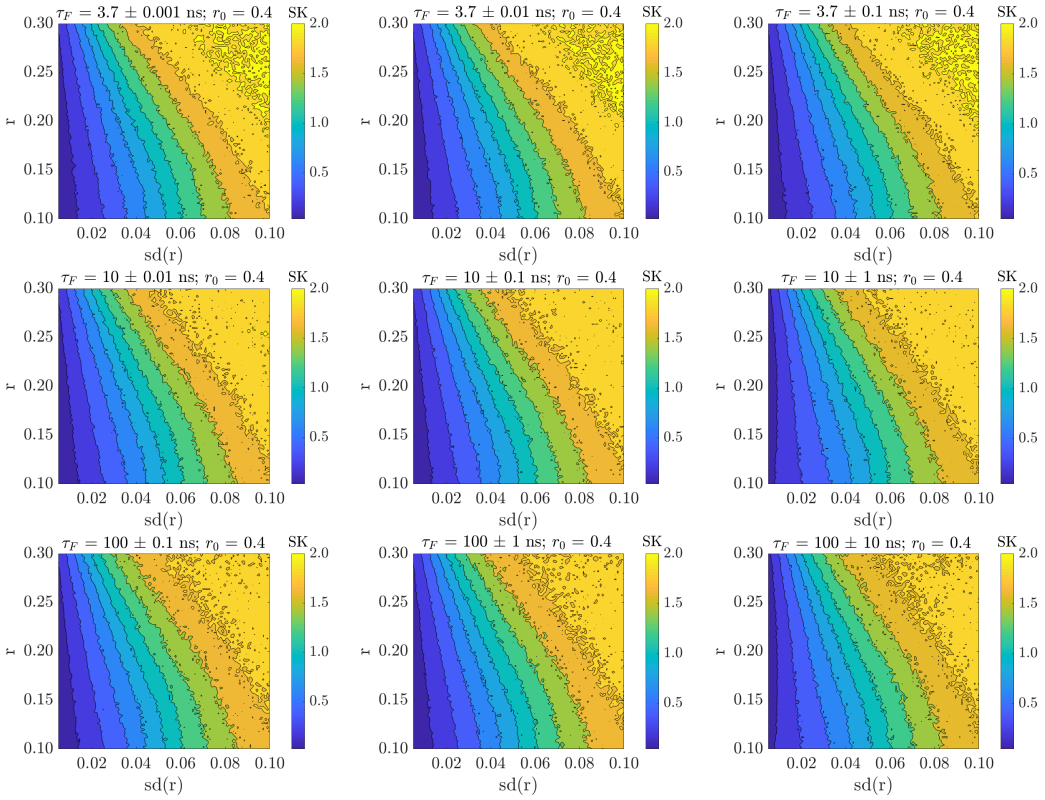

Figure 4.13: Rotational correlation time distribution skewness SK per r, $sd(r)$ and $\tau \pm sd(\tau)$.

over $sd(r)$ increases with a slower rate for small values of r, where in contrast for higher values of r the SK magnitude achieves higher levels, for the same $sd(r)$. This indicates that the θ distribution evolves faster from a normal to a highly skewed dis-

tribution for high r values. Also, for the same fluorescence lifetime τ, a change in sd(τ) does not modify the *SK* trend or it is almost negligible. If the *SK* of the θ distribution is compared across the three fluorescence lifetimes τ, a decrease on magnitude of *SK* is observed at high r and $sd(r)$ when τ increases. This is indicated by the yellow dots located at the high r and $sd(r)$ region of the first row of plots of Figure 4.13 (lowest τ) and the lack of them at the last row of plots of Figure 4.13 (highest τ). This yields an increase in the *SK* bands magnitude at high $sd(r)$ when τ is larger.

4.5 Summary & Conclusion

This chapter was split in two different sections:

1. *Section* 4.3: 'Estimation of the Rotational Correlation Time Uncertainty from a Single Decay'

2. *Section* 4.4: 'Rotational Correlation Time Distribution from an Image'

1. An expression for the uncertainty of the rotational correlation time (equation 4.21) was derived and applied in order to investigate which boundary conditions should be established to optimise the uncertainty of θ. This was done making use of a standard propagation of uncertainties of the parameters θ and r and the Perrin equation for a freely rotating probe. The simulated data revealed that the minimum θ uncertainty is located at $\theta = \tau$ [288]. However, if the number of time channels k is too low, the minimum θ is located at $\theta \leq \tau$ with an increase on its uncertainty. For these cases, a higher time resolution is needed in order to measure with high accuracy the rotational correlation time θ of a probe that rotates fast(er) in comparison to the lifetime τ of its excited state. Equation 4.21 allows the user to estimate how many photons N are necessary to obtain a desired accuracy for θ, where τ, θ and r_0 are known or must be estimated a priori. The theoretical expression for the fluorescence lifetime standard deviation was validated by comparison of its outcome with

some experimental data with varying N. Once an agreement between theory and experiment was shown, this equation was introduced with confidence in the expression derived in this chapter for *sd(θ)*. The experimental time-resolved fluorescence anisotropy fit parameter θ and its uncertainty were calculated for varying N regions and *sd(θ)/θ* was compared with its theoretical equivalence (equation 4.21). A good agreement between theory and experiment was shown, and the importance of measuring a G-factor equal to 1 or very close to 1 in order to correctly apply the derived equation, was highlighted.

Since the initial goal of this section was to figure out how many photons are needed for time-resolved fluorescence anisotropy measurements, we present in the following table a real example of GFP in water, with the fluorescence lifetime τ = 2.5 ns, the rotational correlation time θ = 16 ns, the initial steady-state anisotropy r_0 = 0.4, the number of time channels k = 1024, the experimental time window T = 50 ns and the G-factor G = 1. The number of photons N is isolated from equation 4.22 and the results for different rotational correlation time accuracies are as follows:

Table 4.4: Calculation of the number of photons N needed to achieve the different θ accuracies in time-resolved fluorescence anisotropy.

θ accuracy (%)	**N (photons)**
1	$\simeq 4 \times 10^6$
5	$\simeq 1.6 \times 10^5$
10	$\simeq 4 \times 10^4$
20	$\simeq 10^4$
50	$\simeq 1.6 \times 10^3$

2. The rotational correlation time distribution of a probe freely rotating in an isotropic and homogeneous solution was studied. Although, an analytical expression for the probability density function of θ was presented in this work, a numerical approach was applied for simplicity. The analytically derived equation 4.39 states that the *pdf(θ)* is a combination of a Gaussian and a non-Gaussian distribution. From a numerical point of view, simulated data showed that the θ distribu-

tion evolved from a Gaussian to a non-Gaussian distribution when the steady-state anisotropy standard deviation $sd(r)$ increased. Also, its peak position (mode) was demonstrated to vary with r, $sd(r)$ and the fluorescence lifetime τ, but no change in the θ distribution mode was noticeable by varying the $sd(\tau)$ of a certain τ. The mode was shown to scale up with r and τ, while decreasing with $sd(r)$. The skewness studies suggested that at low r and $sd(r)$ values the θ distribution is minimally skewed, while at high r and $sd(r)$ values, the pdf(θ) increases its skewness. This transition between low and high skewness SK occurred in a faster rate for low r values. The fluorescence lifetime and its standard deviation seemed to have no significant impact on the $pdf(\theta)$ skewness. For all these examples, only positive and zero values for SK were found, indication of a right-located tail on the θ distribution.

Overall, this work was able to successfully address the two scientific questions that had been asked in the *Motivation* section.

Chapter 5

Conclusions and future directions

Exploring the stretched exponential decay model as a FRET indicator for EGFP dimers

As protein dimerisation triggers many biological processes, such as cell signalling, the investigation of this phenomenon was the subject of the second chapter of this thesis. The disruption of the transmembrane protein Coxsackievirus and Adenovirus Receptor (CAR) dimers tagged with GFP was studied after infection with the adenovirus Ad5 Fibre-knob (Ad5FK) in Human Bronchial Epithelial Cells (HBEC). For this purpose, two EGFP standards, monomer and dimer, in buffer/glycerol solutions were first characterised via fluorescence microscopy techniques and simulation tools. The main objective consisted of comparing these two EGFP standards with the response measured in cells to conclude with quantitative information about the number of proteins CAR.

The fluorescence lifetime of each EGFP construct per buffer/glycerol solution was correlated with its environmental refractive index according to the Strickler-Berg relationship. Almost identical fluorescence lifetime values were reported for both EGFP constructs in the same environmental conditions. However, a very small increase in the fluorescence lifetime of the EGFP dimer in comparison to the EGFP monomer was observed and related to the presence of the other EGFP monomer and the flexible linker that holds the two proteins together. Experimental time-

resolved fluorescence anisotropy measurements showed with high clarity the difference between EGFP constructs via the observation of the beginning of the decay. While the EGFP monomer anisotropy decays were successfully fitted with a single-exponential model, the EGFP dimer anisotropy decays needed additional parameters for a proper fit. Two models were proposed for the fit: stretched exponential and bi-exponential. The stretched exponential model was shown to fit best the EGFP dimer anisotropy data, where the anisotropy depolarisation is assumed to be exclusively due to homo-FRET. The bi-exponential model was automatically discarded for the interpretation of the anisotropy data, as the results extracted from this model stated that the EGFP dimer experienced a quicker tumbling in comparison to the EGFP monomer, which makes no sense since its gyration radius is larger. When the EGFP dimer solutions were investigated via spectrally resolved steady-state fluorescence anisotropy measurements, a decrease in homo-FRET near the red-edge of the excitation spectrum was detected, consistent with the suppression of FRET at that position. The lateral mobility of the two EGFP constructs was assessed via FRAP, where a slower mobility was associated to the EGFP dimer in comparison to the monomer construct. With the molecular dynamic (MD) simulations, the FRET energy efficiency between proteins was calculated via the extraction of the distance between EGFPs and their relative orientation. The FRET energy efficiency calculated from the MD simulations was compared with the experimental data, which presented a good agreement with the results extracted from the application of the stretched exponential model to the experimental anisotropy data. Simulated time-resolved anisotropy decays were also generated for both EGFP constructs, where rotational Brownian motion is the only cause of anisotropy depolarisation. The results revealed that, in the absence of FRET, each monomer of the EGFP dimer construct tumbles approximately twice as slowly as the EGFP monomer construct. Moreover, the experimental and simulated rotational correlation times of the EGFP monomer were shown to be in excellent agreement. Overall, two EGFP constructs

(monomer and dimer) were characterised and clearly distinguished through experimental techniques and simulation tools.

After the characterisation of these two EGFP standards, the disruption of the CAR-GFP dimers was investigated via time-resolved and steady-state fluorescence anisotropy. Treated cells with the adenovirus Ad5FK were fixed after three and 20 minutes of the adenovirus uptake by the cell. The fluorescence lifetime associated with the 20-minute treated cells was found to be almost identical to the control's, where the three-minute treated cells presented the highest fluorescence lifetime response. If the GFP fluorescence lifetime is exclusively correlated with the environmental refractive index, then the results may be interpreted as a relocation of the CAR proteins to their original position after the dimer disruption by the adenovirus. Consistent results were given by time-resolved and steady-state fluorescence anisotropy. The time-resolved fluorescence anisotropy data was fitted with two models: hindered rotation and stretched exponential. The FRET energy efficiency calculated from the application of the stretched exponential model to the anisotropy data was shown to be in good agreement with the fluorescence lifetime and the steady-state fluorescence anisotropy results.

A continuation of the work presented in *Chapter* 2, in regards to the two EGFP standards, involves further investigation of the effect of the environmental refractive index on the integral overlap between excitation and emission spectra via the extinction coefficient of the molecule. This may explain why the molecule concentration is not consistent across the varying refractive index solutions. Another parameter involved in the molecule concentration is the dipole orientation between proteins, given by κ^2. Although we expect this value to remain constant across the varying refractive index and viscosity solutions, it may be worthwhile investigating its behaviour via further MD and/or Monte Carlo simulations. It may also be interesting to make solution mixtures using a different solvent in combination with

PBS(X1). The rotational correlation time of the EGFP dimer could be investigated and compared with the experimental results presented in *Chapter* 2 at comparable refractive index/viscosity values. This may give some insight about the effect of the solvent on the protein dynamics.

The ultimate goal of *Chapter* 2 consisted of the study of protein dimerisation in physiological conditions. Therefore, the next step would consist of tracking the disruption of CAR dimers via the adenovirus Ad5FK in live cells through time-resolved fluorescence anisotropy. In order to compare the response measured from the two EGFP standards and the response obtained from the GFP-CAR samples, the two EGFP standards need to be measured in a similar environment/structure. For this reason, a more fair comparison may consist of preparing some homogeneates and measure the anisotropy response of the two EGFP standards to directly compare with the results found in live cells.

Development of a Multi-Modal Confocal Fluorescence Microscopy Technique based on Time-Correlated Single Photon Counting

The third chapter of this thesis presents the development of a multi-modal confocal fluorescence microscopy setup based on time-correlated single photon counting (TCSPC), named F^3. The main advantage of this setup is the amount of information that is collected from the sample, taking full advantage of the limited photon budget. The techniques that conform this setup are: Fluorescence lifetime imaging (FLIM), time-resolved fluorescence anisotropy imaging (tr-FAIM) and fluorescence recovery after photobleaching (FRAP). A series of fluorescence parameters are measured in a single experiment and information about the probe's environment is gained. The setup was successfully calibrated with five solutions of rhodamine 6G in glycerol/water and applied to single lipid bilayers (SLBs) with

the environmentally-sensitive dye di-4-ANEPPDHQ. As an imaging setup, F^3 was able to generate FLIM, steady-state anisotropy, steady-state anisotropy standard deviation, total intensity and rotational correlation time maps for each sample. The grainy nature of the rotational correlation times maps was associated with the difficulty of performing accurate anisotropy fits in the presence of high noise levels and the binning effect.

The rhodamine 6G hydrodynamic radius ($R_{h,F^3,rot}$ = 0.3963 $\pm$ 0.0821 nm) was calculated combining the rotational and translational information, without any a priori knowledge about the viscosity. The results obtained in this work were in good agreement with the previously reported in literature. As discussed in *Chapter* 3, the anisotropic nature of the SLB did not permit the combination of the rotational (related to micro-viscosity) and translational (associated with macro-viscosity) information to calculate the hydrodynamic radius of di-4-ANEPPDHQ. Macro- and micro-viscosities were shown to differ by more than one order of magnitude and the low values extracted for the translational diffusion coefficient ($D_{t,exp} = 0.15 \pm 0.06\ \mu m^2/s$) were related to the interaction of the lipids with the substrate, which may slow down the lateral mobility of the probe. Another explanation for the mismatch between the two viscosities may lie in the fact that the probe, sitting between the lipids, is able to rotate locally (θ = 2.36 $\pm$ 0.26 ns) at a different speed in comparison to its lateral mobility, where the probe finds as an opposition the lipids conforming the cell membrane. The low calculated rotational correlation time reinforces the theory of the location of the probe in the outer leaflet of the membrane, providing the dye high rotational mobility. This is consistent with the obtained lipid packing (S^2 = 0.44 $\pm$ 0.03). Fluorescence lifetime information was also extracted, where an average value of 2.10 $\pm$ 0.06 ns was reported. Useful information can be extracted from this fluorescence parameter. Fluorescence lifetime reports for instance on the membrane hydration. A probe's fluorescence lifetime re-

duction may be an indication of water quenching, and thus high levels of hydration within the cell membrane. Moreover, an increase in the number of water molecules surrounding the probe may suggest an incomplete insertion of the dye within the cell membrane, consistent with the interpretation of the anisotropy data.

Future work on the topic presented in *Chapter* 3 may consist of a further study of the interaction between the glass surface and the membrane. Via molecular dynamic (MD) simulations one should be able to assess the lateral mobility of the dye di-4-ANEPPDHQ within the cell membrane at varying distances between the solid support and the lipid bilayer. To ensure about the experimental methodology and data analysis approach, other popular model membranes with other dyes can be measured, such as the dye laurdan in DOPC giant unilamellar vesicles (GUVs). This would enable the direct comparison with findings reported by literature. Lastly, F^3 may be explored with other model membranes and dyes to probe different types of micro-environments with order parameters, such as membrane curvature, charge, hydration, fluidity, etc. Temperature-controlled measurements could also be acquired for this purpose and to investigate the model membrane transition points.

Investigation of the Rotational Correlation Time Uncertainty and Distribution from Time-Resolved Fluorescence Anisotropy Data

On the one hand, an expression for the uncertainty of the rotational correlation time $\Delta\theta$ was derived in *Chapter* 4. This expression permitted the investigation of the boundary conditions that should be established to optimise the uncertainty associated with the rotational correlation time via simulated data. Within the main findings, we can highlight the following: in the great majority of the cases the optimal rotational correlation time was found at $\theta = \tau$, such as established by Weber [288], and the time resolution given by the number of channels k was shown

to act as a threshold in the optimisation of the rotational correlation time uncertainty. The derived expression for $\Delta\theta$ was applied to experimental data and was demonstrated to highly correlate with the simulated data. On the other hand, the distribution of the rotational correlation time across an homogeneous image was investigated through simulated data. This was mainly driven by the experimental observation of a non-Gaussian distribution for this parameter, θ. For this purpose, an analytical expression for its distribution was derived, where the fluorescence lifetime and steady-state anisotropy distributions were defined as Gaussian functions. Due to its non-trivial solution, the problem was approached numerically. The main conclusion of this study attributed a high dependence of the skewness of the rotational correlation time histogram on the uncertainty of the steady-state anisotropy distribution. The skewness of the rotational correlation time was found to increase with the uncertainty associated with the steady-state anisotropy and to remain almost invariant with any change in the fluorescence lifetime or its uncertainty. Thus, we demonstrated that the distribution of the rotational correlation time can present a Gaussian or non-Gaussian distribution, strongly dependent on the steady-state anisotropy uncertainty.

A possible continuation of this work would consist of establishing a frame of reference that helped the user to know the collection time for the parallel and perpendicular intensity decays to achieve the desired rotational correlation time uncertainty. Different factors should be taken into account: laser repetition rate, laser power, time window, time resolution, objective NA, dimensions of field of view if the sample is scanned, etc. In regards to the rotational correlation time distribution, simulated and experimental data should be compared with a change in the steady-state anisotropy uncertainty distribution via varying the number of photons collected per image pixel.

Appendix A

Single Lipid Bilayers Preparation

1. Materials

    - Dipalmitoylphosphatidylcholine (DOPC) Lipid Solution in Chloroform
    - Fluorescence dye (Di-4-ANEPPDHQ) solution in Dimethyl Sulfoxide (DMSO) or methanol
    - Deionized water
    - SLBs buffer
    - Glass substrate and cover slip
    - Extrusion set (Avanti Mini Extruder)
    - Pipettes
    - Desiccator
    - Sonicator Bath
    - Plasma Cleaner
    - Glass spherical flask and vial

2. Protocol

    (a) Single Lipid Bilayers (SLB) Buffer Preparation

i. The buffer solution was made as previously described [290]. For the elaboration of the buffer we used the following concentrations: 100 mM NaCl (Sodium Chloride), 20 mM of N-2-hydroxyethylpiperazine-N-2-ethanesulfonic acid (HEPES), and 2 mM $CaCl_2$ (Calcium Chloride). Measure 290 mg of NaCl, 238 mg of HEPES, and 11.1 mg of $CaCl_2$ using a high precision digital scale and add to 50 mL of purified water in a conical bottom tube. The calcium ions facilitate the adhesion of the SUVs onto the coverslip in the last stages of the SLB preparation.

ii. As a preservative, Sodium Azide (NaN_3) is used. 15 μL of 0.5 M NaN_3 are added.

iii. The solution's pH is adjusted to 7.4 with a pH meter, by adding NaOH. Prior calibration is required.

iv. Ensure all solids have readily dissolved in the purified water by placing conical bottom tube on vortex mixer. The buffer solution should be kept refrigerated.

(b) Small Unilamellar Vesicles (SUVs) Preparation

i. DOPC (Molar mass: 734 g/mol) was the phospholipid used to prepare the lipid bilayer solution. The lipids should be stored at -20°C.

ii. 10 mg of DOPC are added into 1 mL of chloroform by using a small glass vial that has been previously washed with chloroform. The final lipid concentration is 13.6 mM.

iii. Add 100 μL of this mixture to the spherical flask. Make a stock solution of the dye di-4-ANEPPDHQ at 5 mM in DMSO. Add 2 μL of the dye solution to the lipid one. In this way, the ratio between the dye and the lipid is 1/50.

iv. Evaporate the chloroform of the solution by rotating the flask under

very gentle nitrogen flow. The dried lipid films should form on the walls of the glass vial.

v. To ensure that the solvent has been completely removed, dry the lipid films overnight in vacuum conditions (in a desiccator) to prevent the sample from oxidising.

vi. The stock lipid vesicle solution used is typically 1 mM. Therefore, and additional 1 ml of SLB buffer is added to the solution. This yields to a final concentration of the stock lipid vesicle solution of 1.36 mM. Sonication (minimum: 1 hour) is performed in order to achieve complete dilution. The sonication lasts till the lipid films are totally resuspended and the solution is cloudy.

vii. To reduce the size of the SUVs to 100 nm diameter, load the solution into an extrusion syringe and extrude 10 times through a 100 nm nucleopore track-etch membrane, guarded between two filter supports. After extrusion, the solution should be clear.

   A. To assemble the extruder apparatus, prewet the two filter supports in buffer and place them on each of the two Teflon blocks. Prewet the nucleopore membrane and center it on one of the two blocks, ensuring that the inner part is intact. With the two Teflon blocks facing each other and the membrane held between them, seal the system using the hex nut.

   B. Place the empty syringe on the one end of the extruder and the filled one on the other. Gently push the filled syringe until it is completely empty and its contents have transferred into the other syringe. Repeat this process 10 times, with the final extrusion filling the initially empty syringe.

   C. The SUV solution should be stored at 4°C and used within one

week.

(c) Glass cover slip Preparation

i. To ensure that the glass cover slips are clean, sonicate with ethanol and dry them using gentle nitrogen flow.

ii. Spread substrates on a petri dish without touching each other or overlapping and place it on the flat surface inside the tube of the plasma cleaner. Treat both sides of the substrates with air plasma for two minutes per side.

(d) Supported Lipid Bilayers (SLBs) Formation

i. Place an orange squared sticker onto the back of a petri dish as a reference and immediately after you affix the substrate on top of it. Glue a black rubber ring on its surface using vacuum grease.

ii. Add 270 μL of the buffer solution to the treated substrate and 30 μL of the SLB solution (1:9 dilution) such that it covers the entire surface enclosed by the rubber ring. Incubate for 30 minutes (optional: in a moisture box). DOPC can be incubated at room temperature.

iii. After incubation, wash the SLB by pipetting the buffer solution up and down at least three times while adding fresh buffer after every wash. It is crucial that the surface of the substrate never completely dries or has gaps in its surface otherwise the SLB structures will be destroyed. For that reason it is also important to not touch the surface of the glass substrate with the pipette. Finally the coverslip is placed on top of the black rubber ring which contains the final lipid labelled solution.

Appendix B

Dependence of Rotational Correlation Time Uncertainty with Time Resolution: Cross Sections

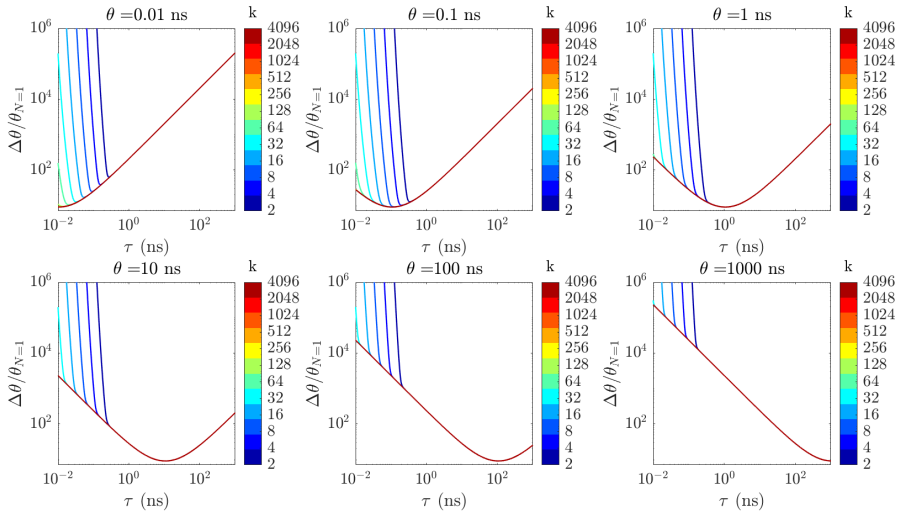

Figure B.1: Dependence of minimum $\Delta\theta/\theta_{N=1}$ with τ and k for a fixed θ and time window T. This example is given for T = 10 ns.

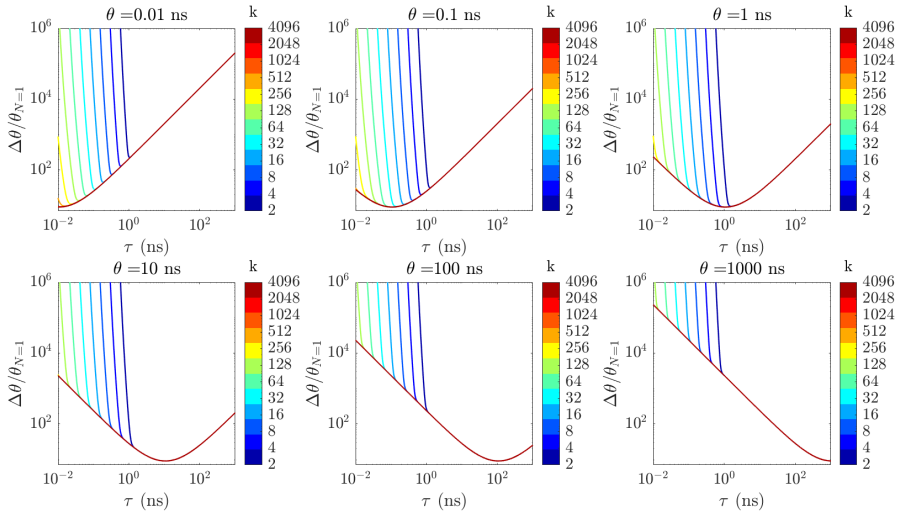

Figure B.2: Dependence of minimum $\Delta\theta/\theta_{N=1}$ with τ and k for a fixed θ and time window T. This example is given for T = 50 ns.

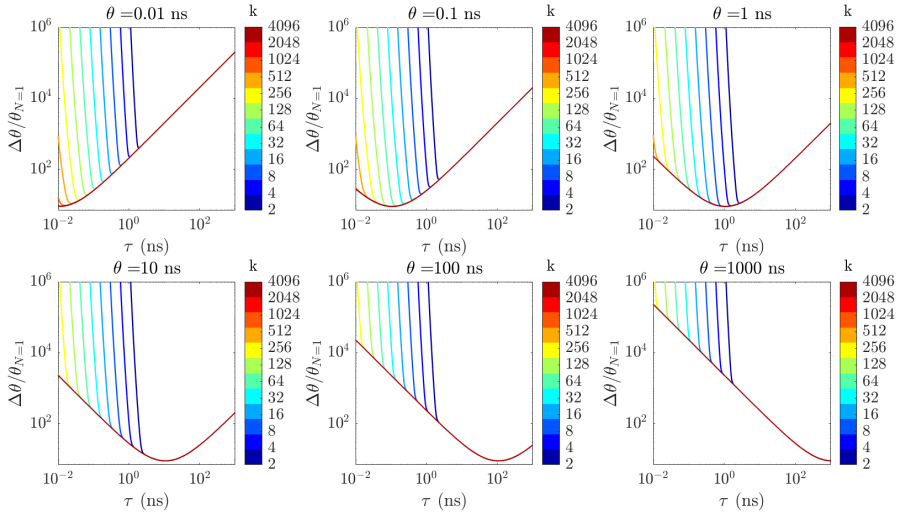

Figure B.3: Dependence of minimum $\Delta\theta/\theta_{N=1}$ with τ and k for a fixed θ and time window T. This example is given for T = 100 ns.

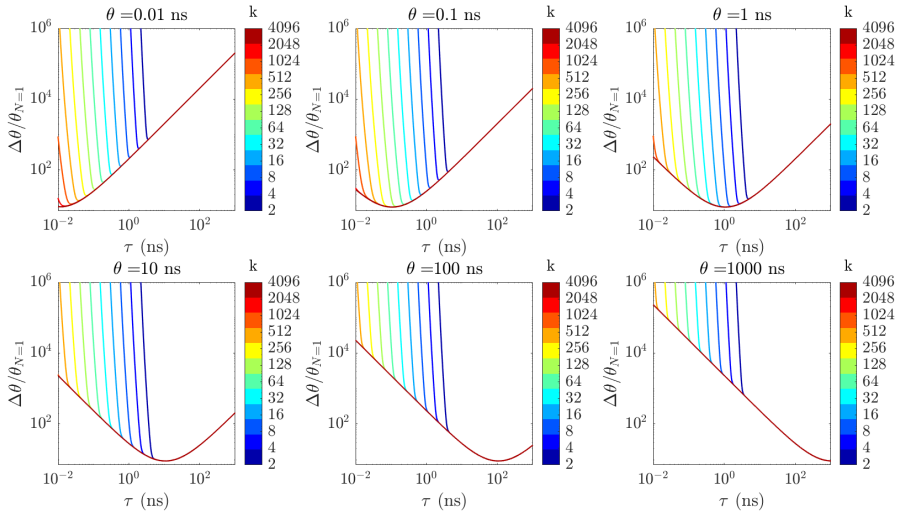

Figure B.4: Dependence of minimum $\Delta\theta/\theta_{N=1}$ with τ and k for a fixed θ and time window T. This example is given for T = 200 ns.

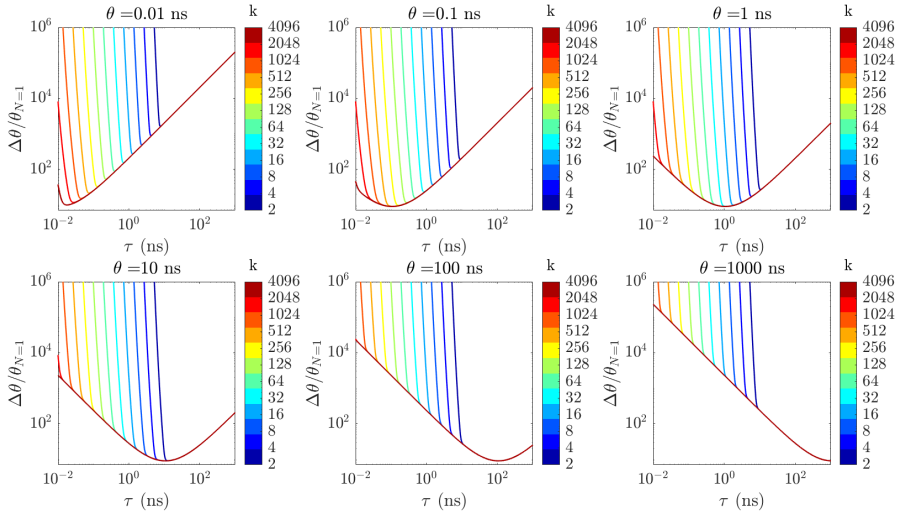

Figure B.5: Dependence of minimum $\Delta\theta/\theta_{N=1}$ with τ and k for a fixed θ and time window T. This example is given for T = 500 ns.

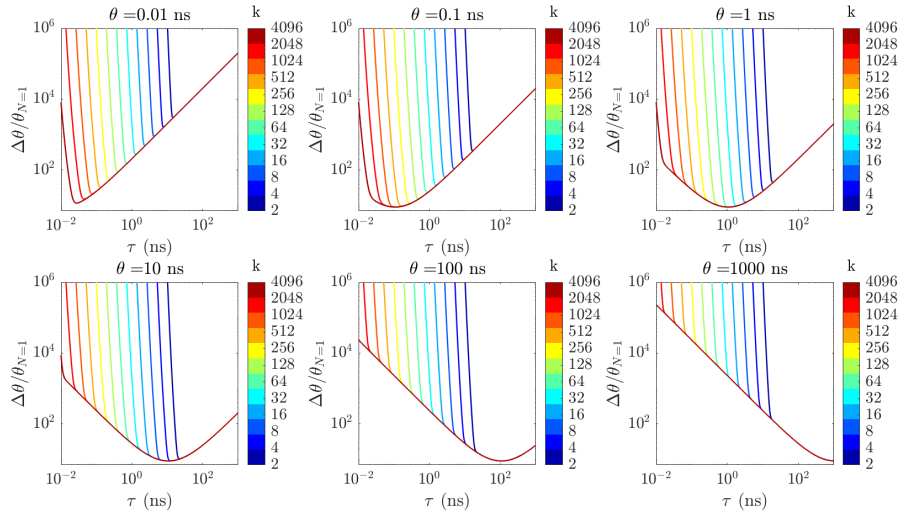

Figure B.6: Dependence of minimum $\Delta\theta/\theta_{N=1}$ with τ and k for a fixed θ and time window T. This example is given for T = 1000 ns.

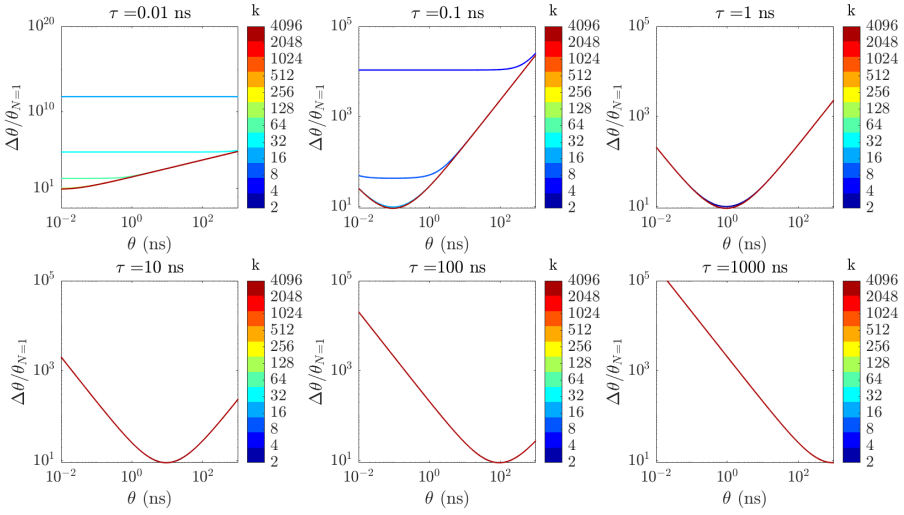

Figure B.7: Dependence of minimum $\Delta\theta/\theta_{N=1}$ with θ and k for a fixed τ and time window T. This example is given for T = 10 ns.

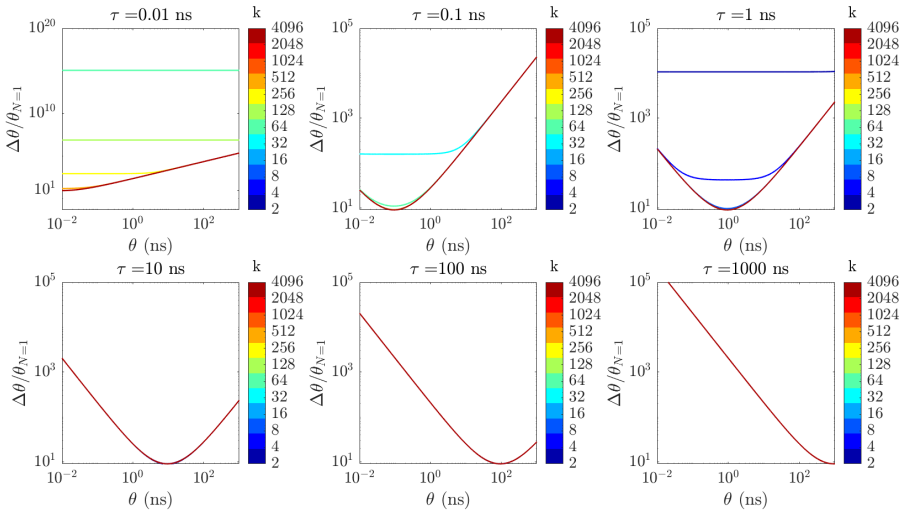

Figure B.8: Dependence of minimum $\Delta\theta/\theta_{N=1}$ with θ and k for a fixed τ and time window T. This example is given for T = 50 ns.

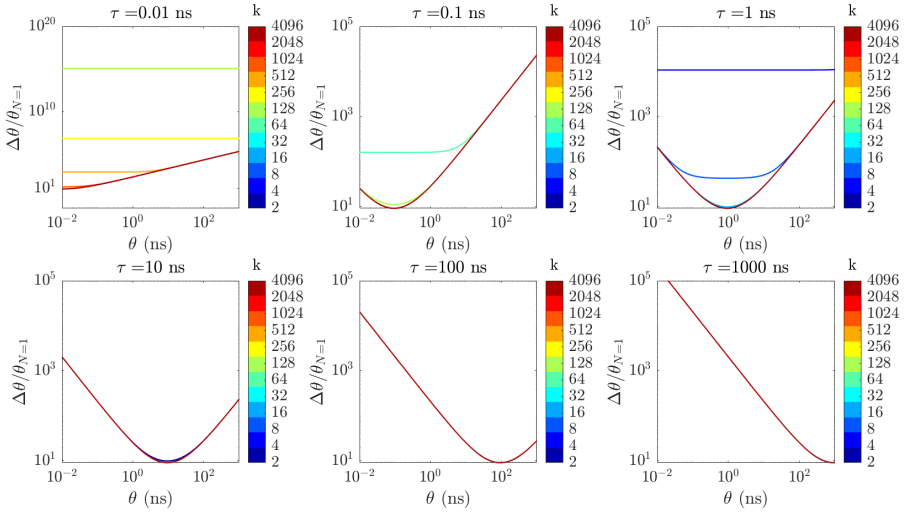

Figure B.9: Dependence of minimum $\Delta\theta/\theta_{N=1}$ with θ and k for a fixed τ and time window T. This example is given for T = 100 ns.

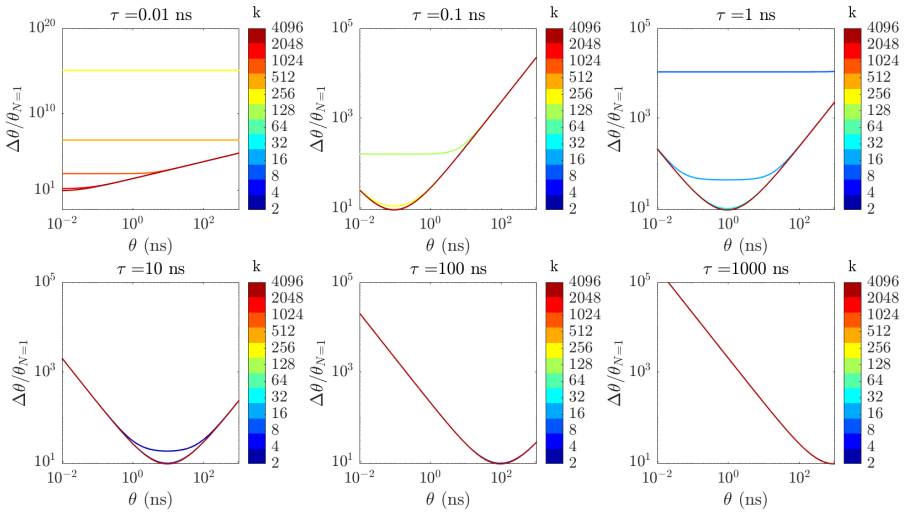

Figure B.10: Dependence of minimum $\Delta\theta/\theta_{N=1}$ with θ and k for a fixed τ and time window T. This example is given for T = 200 ns.

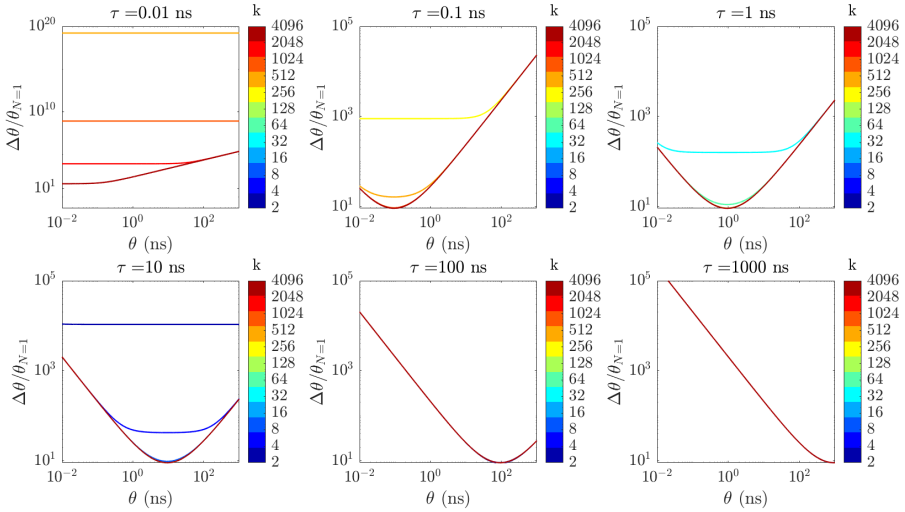

Figure B.11: Dependence of minimum $\Delta\theta/\theta_{N=1}$ with θ and k for a fixed τ and time window T. This example is given for T = 500 ns.

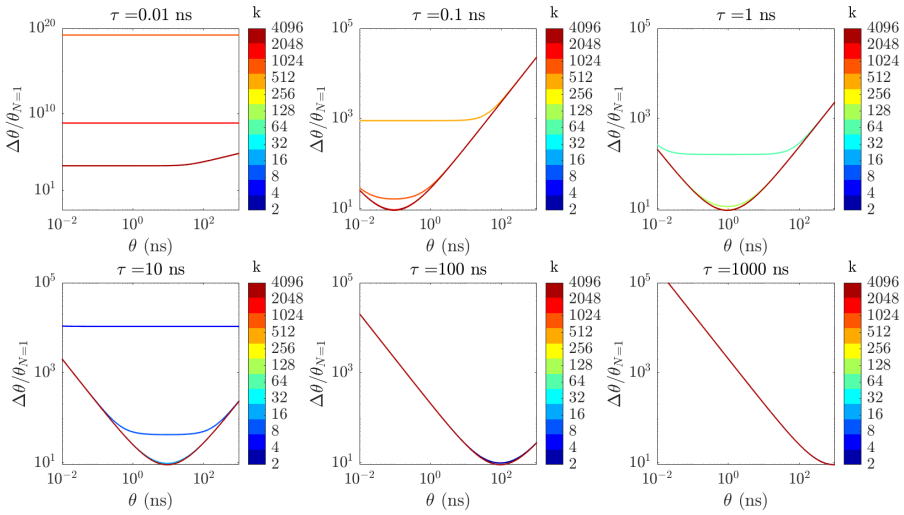

Figure B.12: Dependence of minimum $\Delta\theta/\theta_{N=1}$ with θ and k for a fixed τ and time window T. This example is given for T = 1000 ns.

Appendix C

Evolution of the Rotational Correlation Time Distribution with the Steady-State Anisotropy Standard Deviation

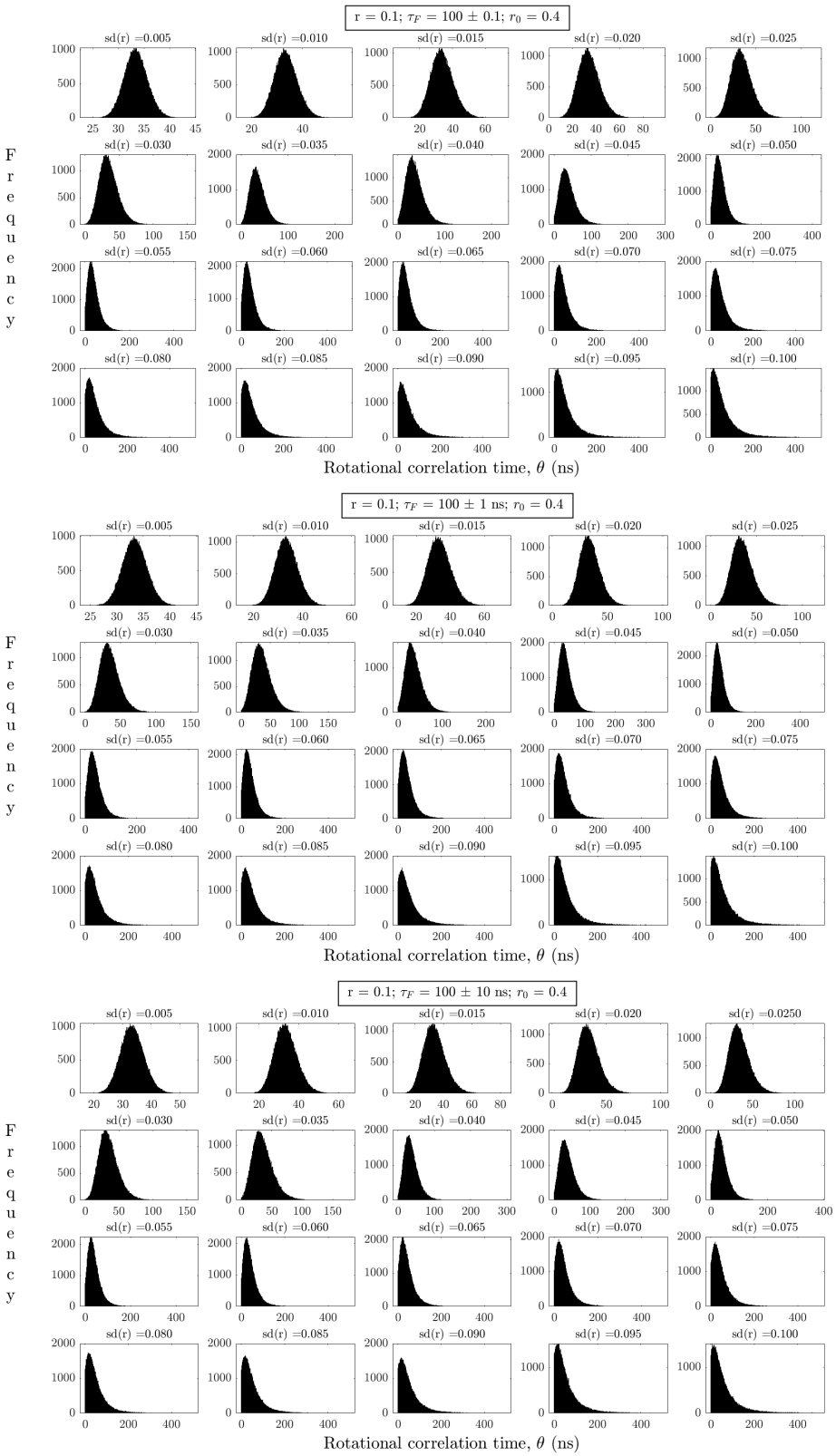

Figure C.1: Evolution of the rotational correlation time distribution with $sd(r)$ for τ = 100 ± (a) 0.1, (b) 1 and (c) 10 ns. The initial anisotropy r_0 is set to 0.4.

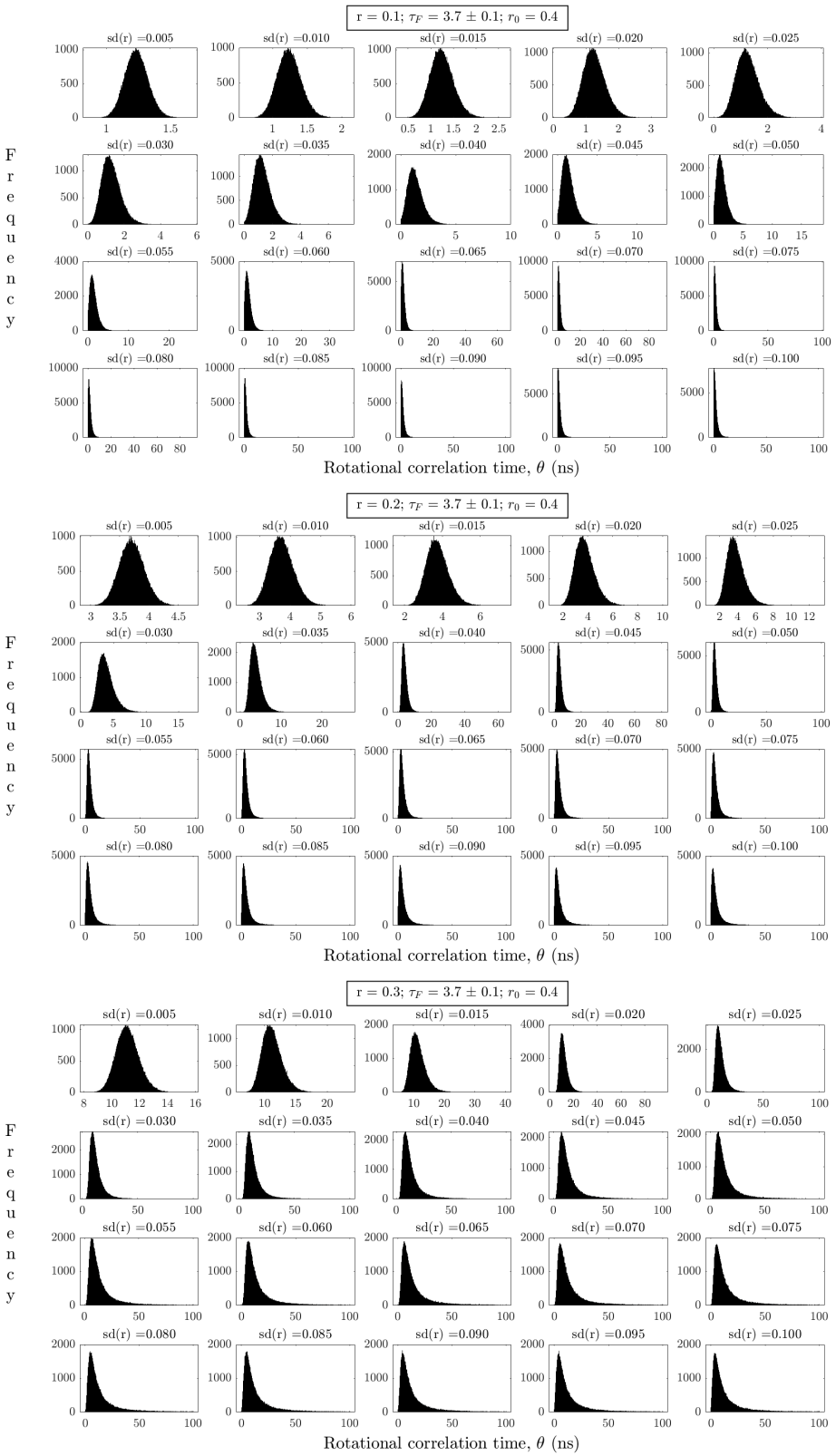

Figure C.2: Evolution of the rotational correlation time distribution with $sd(r)$ for τ = 3.7 ± 0.1 ns and for three different steady-state anisotropy values: (a) r = 0.1, (b) r = 0.2 and (c) r = 0.3. The initial anisotropy r_0 is set to 0.4.

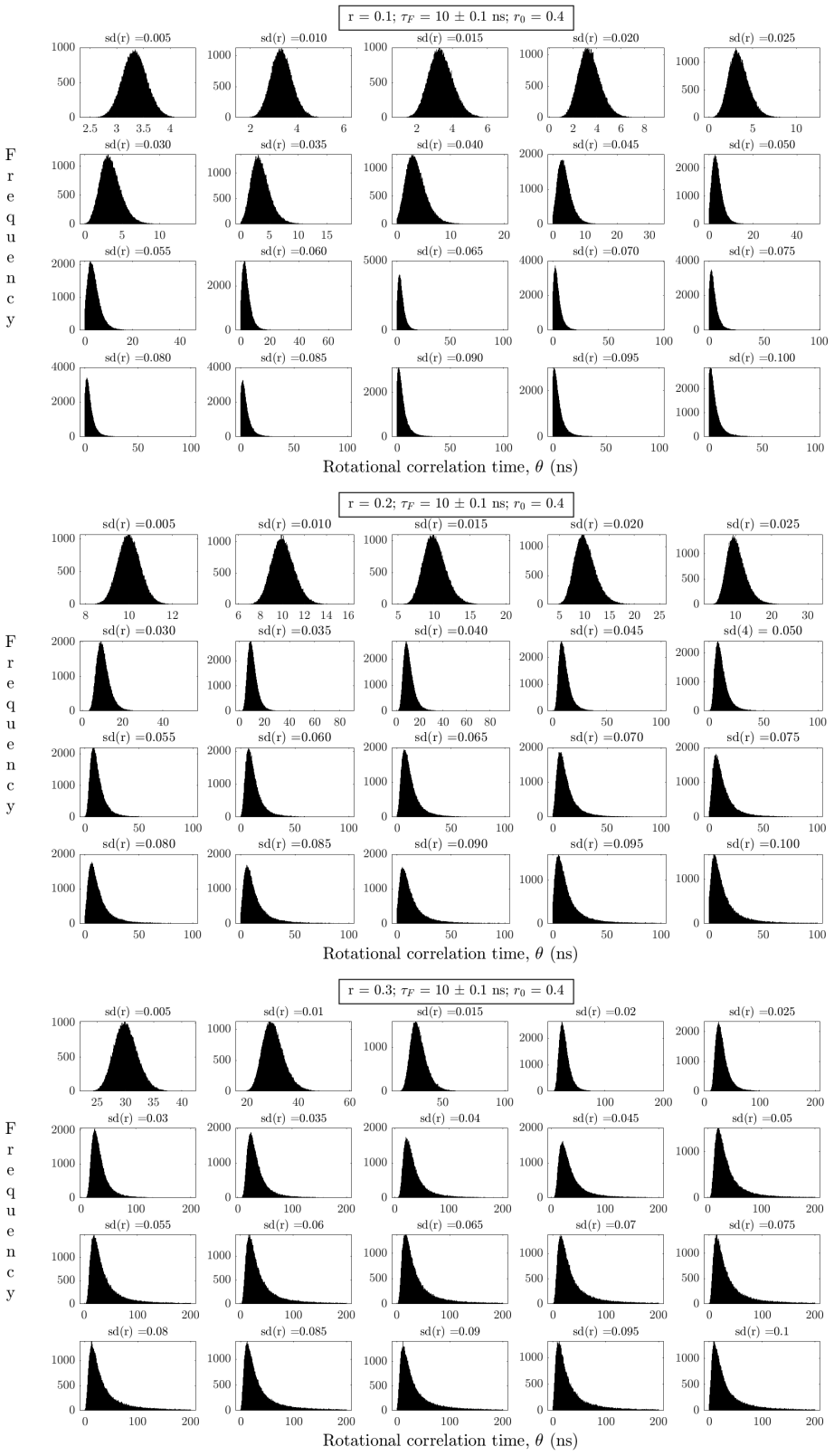

Figure C.3: Evolution of the rotational correlation time distribution with $sd(r)$ for τ = 100 ± 0.1 ns and for three different steady-state anisotropy values: (a) r = 0.1, (b) r = 0.2 and (c) r = 0.3. The initial anisotropy r_0 is set to 0.4.

Appendix D

Evolution of the Rotational Correlation Time Distribution with the Steady-State Anisotropy Standard Deviation for a r_0 Normal Distribution

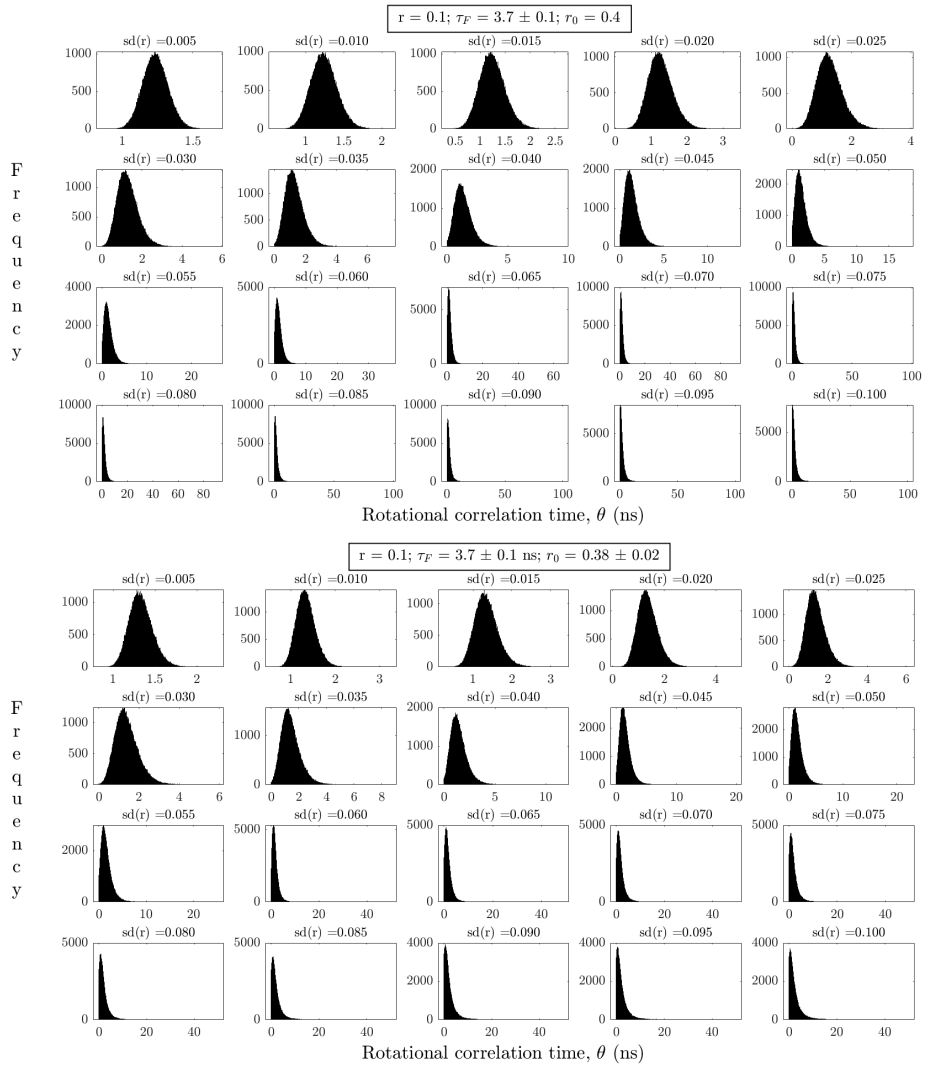

Figure D.1: Evolution of the rotational correlation time distribution with $sd(r)$ for τ = 3.7 ± 0.1 ns and r = 0.1. The initial anisotropy r_0 is set to (a) 0.4 and (b) 0.38 ± 0.02.

Appendix E

Mode Dependence with the Fluorescence Lifetime Standard Deviation

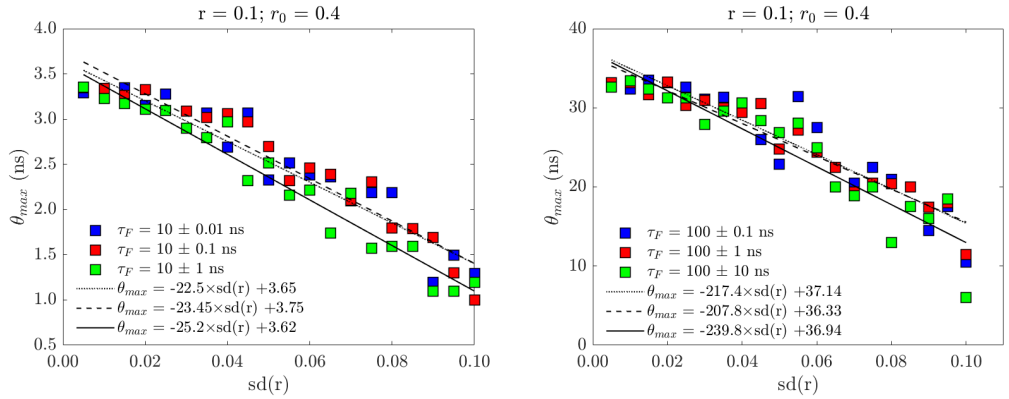

Figure E.1: Dependence of the maximum value (θ_{max}) of the rotational correlation time distribution with $sd(r)$ for r = 0.1 and r_0 = 0.4. Varying fluorescence lifetimes and standard deviations are applied: (a) τ = 10 $\pm$ 0.01, 0.1 and 1 ns, and (b) τ = 100 $\pm$ 0.1, 1 and 10 ns.

Appendix F

Mode Dependence with the Steady-State Anisotropy

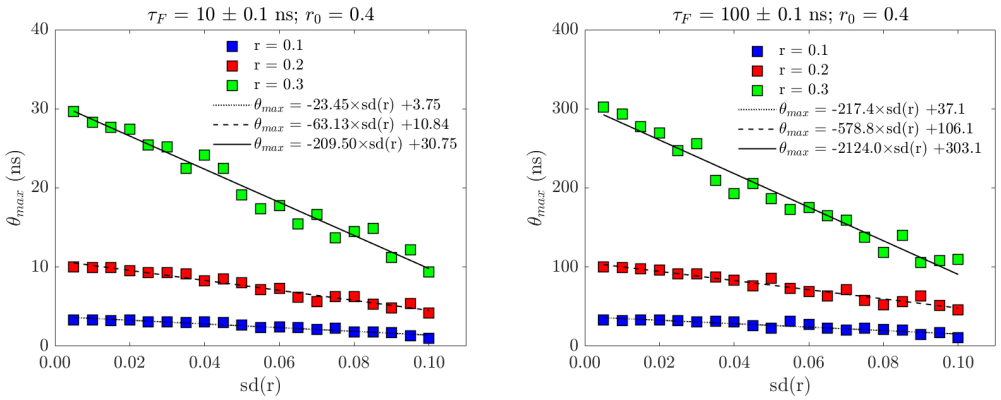

Figure F.1: Dependence of the maximum value (θ_{max}) of the rotational correlation time distribution with $sd(r)$ for r = 0.1, 0.2 and 0.3. The fluorescence lifetime is: (a) τ = 10 ± 0.1 ns and (b) τ = 100 ± 0.1 ns. The initial anisotropy r_0 is equal to 0.4

Bibliography

[1] M. J. Sanderson, I. Smith, I. Parker, and M. D. Bootman, "Fluorescence microscopy Michael," *Cold Spring Harbor Protocols*, vol. 10, no. 10, pp. 1–36, 2014.

[2] J. R. McIntosh, "Electron microscopy of cells: a new beginning for a new century," *Journal of Cell Biology*, vol. 153, no. 6, pp. 25–32, 2001.

[3] S. A. Galdeen and A. J. North, *Live cell fluorescence microscopy techniques*, pp. 205–222. Humana Press, 2011.

[4] E. Abbe, "Ueber einen neuen Beleuchtungsapparat am Mikroskop," *Archiv für mikroskopische Anatomie*, vol. 9, no. 1, pp. 469–480, 1873.

[5] S. W. Hell and J. Wichmann, "Breaking the diffraction resolution limit by stimulated emission: stimulated-emission-depletion fluorescence microscopy," *Opt. Lett.*, vol. 19, no. 11, pp. 780–782, 1994.

[6] T. A. Klar and S. W. Hell, "Subdiffraction resolution in far-field fluorescence microscopy," *Opt. Lett.*, vol. 24, no. 14, pp. 954–956, 1999.

[7] M. G. Gustafsson, "Surpassing the lateral resolution limit by a factor of two using structured illumination microscopy," *Journal of Microscopy*, vol. 198, no. 2, pp. 82–87, 2000.

[8] M. G. Gustafsson, L. Shao, P. M. Carlton, C. J. Wang, I. N. Golubovskaya, W. Z. Cande, D. A. Agard, and J. W. Sedat, "Three-dimensional resolution doubling in wide-field fluorescence microscopy by structured illumination," *Biophysical Journal*, vol. 94, no. 12, pp. 4957–4970, 2008.

[9] L. Schermelleh, P. M. Carlton, S. Haase, L. Shao, L. Winoto, P. Kner, B. Burke, M. C. Cardoso, D. A. Agard, M. G. L. Gustafsson, H. Leonhardt, and J. W. Sedat, "Subdiffraction multicolor imaging of the nuclear periphery with 3D structured illumination microscopy," *Science*, vol. 320, no. 5881, pp. 1332–1336, 2008.

[10] M. Bates, B. Huang, G. T. Dempsey, and X. Zhuang, "Multicolor super-resolution imaging with photo-switchable fluorescent probes," *Science*, vol. 317, no. 5845, pp. 1749–1753, 2007.

[11] S. T. Hess, T. P. Girirajan, and M. D. Mason, "Ultra-high resolution imaging by fluorescence photoactivation localization microscopy," *Biophysical Journal*, vol. 91, no. 11, pp. 4258–4272, 2006.

[12] C. J. Szymanski, H. Yi, J. L. Liu, E. R. Wright, and C. K. Payne, *Imaging intracellular quantum dots: fluorescence microscopy and transmission electron microscopy*, pp. 21–33. Humana Press, 2013.

[13] M. Green, P. Howes, C. Berry, O. Argyros, and M. Thanou, "Simple conjugated polymer nanoparticles as biological labels," *Proceedings of the Royal Society A: Mathematical, Physical and Engineering Sciences*, vol. 465, no. 2109, pp. 2751–2759, 2009.

[14] K. Thorn, "Genetically encoded fluorescent tags," *Molecular Biology of the Cell*, vol. 28, no. 7, pp. 848–857, 2017.

[15] J. McGinty, N. P. Galletly, C. Dunsby, I. Munro, D. S. Elson, J. Requejo-Isidro, P. Cohen, R. Ahmad, A. Forsyth, A. V. Thillainayagam, M. A. A. Neil, P. M. W. French, and G. W. Stamp, "Wide-field fluorescence lifetime imaging of cancer," *Biomedical Optics Express*, vol. 1, no. 2, p. 627, 2010.

[16] K. Maxwell and G. N. Johnson, "Chlorophyll fluorescence-a practical guide," *Journal of experimental botany*, vol. 51, no. 345, pp. 659–668, 2000.

[17] Y. Yuanlong, Y. Yanming, L. Fuming, L. Yufen, and M. Paozhong, "Characteristic autofluorescence for cancer diagnosis and its origin," *Lasers in Surgery and Medicine*, vol. 7, no. 6, pp. 528–532, 1987.

[18] A. Balasubramaniam, R. Sriraman, P. Sindhuja, K. Mohideen, R. Parameswar, and K. Muhamed Haris, "Autofluorescence based diagnostic techniques for oral cancer," *Journal of Pharmacy And Bioallied Sciences*, vol. 7, no. 6, pp. 374–377, 2015.

[19] B. Valeur, *Molecular fluorescence: principles and applications*. Wiley-VCH, 1st ed., 2001.

[20] J. R. Lakowicz, *Principles of fluorescence spectroscopy*. 2006.

[21] W. E. Moerner and L. Kador, "Optical detection and spectroscopy of single molecules in a solid," *Physical Review Letters*, vol. 62, no. 21, pp. 2535–2538, 1989.

[22] M. Kasha, "Characterization of electronic transitions in complex molecules," *Discuss. Faraday Soc.*, vol. 9, pp. 14–19, 1950.

[23] G. G. Stokes, "On the change of refrangibility of light," *The Royal Society*, vol. 142, 1852.

[24] J. R. Albani, "New insights in the interpretation of tryptophan fluorescence," *Journal of Fluorescence*, vol. 17, no. 4, pp. 406–417, 2007.

[25] S. J. Strickler and R. A. Berg, "Relationship between absorption intensity and Fluorescence Lifetime of molecules," *The Journal of Chemical Physics*, vol. 37, no. 4, pp. 814–822, 1962.

[26] J. Olmsted, "Effect of refractive index on molecular radiative lifetimes," *Chemical Physics Letters*, vol. 38, no. 2, pp. 287 – 292, 1976.

[27] R. A. Lampert, S. R. Meech, J. Metcalfe, D. Phillips, and A. P. Schaap, "The refractive index correction to the radiative rate constant in fluorescence lifetime measurements," *Chemical Physics Letters*, vol. 94, no. 2, pp. 137 – 140, 1983.

[28] D. Toptygin, R. S. Savtchenko, N. D. Meadow, S. Roseman, and L. Brand, "Effect of the solvent refractive index on the excited-state lifetime of a single tryptophan residue in a protein," *The Journal of Physical Chemistry B*, vol. 106, no. 14, pp. 3724–3734, 2002.

[29] K. Suhling, J. Siegel, D. Phillips, P. M. W. French, S. Leveque-Fort, S. E. D. Webb, and D. M. Davis, "Imaging the environment of green fluorescent protein," *Biophysical Journal*, vol. 83, no. 6, pp. 3589–3595, 2002.

[30] A. Pillonnet, P. Fleury, A. I. Chizhik, A. M. Chizhik, D. Amans, G. Ledoux, F. Kulzer, A. J. Meixner, and C. Dujardin, "Local refractive index probed via the fluorescence decay of semiconductor quantum dots," *Optical Society of America*, vol. 20, no. 3, pp. 4310–4315, 2012.

[31] A. A. Istratov and O. F. Vyvenko, "Exponential analysis in physical phenomena," *Review of Scientific Instruments*, vol. 70, no. 2, pp. 1233–1257, 1999.

[32] H. Lossau, A. Kummer, R. Heinecke, F. Pöllinger-Dammer, C. Kompa, G. Bieser, T. Jonsson, C. M. Silva, M. M. Yang, D. C. Youvan, and M. E. Michel-Beyerle, "Time-resolved spectroscopy of wild-type and mutant

green fluorescent proteins reveals excited state deprotonation consistent with fluorophore-protein interactions," *Chemical Physics*, vol. 213, no. 1, pp. 1 – 16, 1996.

[33] M. Chattoraj, B. A. King, G. U. Bublitz, and S. G. Boxer, "Ultra-fast excited state dynamics in green fluorescent protein: multiple states and proton transfer," *Proceedings of the National Academy of Sciences*, vol. 93, no. 16, pp. 8362–8367, 1996.

[34] U. Haupts, S. Maiti, P. Schwille, and W. W. Webb, "Dynamics of fluorescence fluctuations in green fluorescent protein observed by fluorescence correlation spectroscopy," *Proceedings of the National Academy of Sciences*, vol. 95, no. 23, pp. 13573–13578, 1998.

[35] T. M. H. Creemers, A. J. Lock, V. Subramaniam, T. M. Jovin, and S. Völker, "Photophysics and optical switching in green fluorescent protein mutants," *Proceedings of the National Academy of Sciences*, vol. 97, no. 7, pp. 2974–2978, 2000.

[36] W. Becker, *Advanced time-correlated single photon counting techniques*. Springer-Verlag Berlin Heidelberg, 1 ed., 2005.

[37] K. Kinosita, S. Kawato, and A. Ikegami, "A theory of fluorescence polarization decay in membranes," *Biophysical Journal*, vol. 20, no. 3, pp. 289 – 305, 1977.

[38] G. Lipari and A. Szabo, "Effect of librational motion on fluorescence depolarization and nuclear magnetic resonance relaxation in macromolecules and membranes.," *Biophysical Journal*, vol. 30, no. 3, pp. 489–506, 1980.

[39] G. Saffman and M. Delbrock, "Brownian motion in biological membranes," vol. 72, no. 8, pp. 3111–3113, 1975.

[40] V. Devauges, D. R. Matthews, J. Aluko, J. Nedbal, J. A. Levitt, S. P. Poland, O. Coban, G. Weitsman, J. Monypenny, T. Ng, and S. M. Ameer-Beg, "Steady-state acceptor fluorescence anisotropy imaging under evanescent excitation for visualisation of FRET at the plasma membrane," *PLoS ONE*, vol. 9, no. 10, 2014.

[41] A. N. Bader, E. G. Hofman, J. Voortman, P. M. Van Bergen En Henegouwen, and H. C. Gerritsen, "Homo-FRET imaging enables quantification of protein cluster sizes with subcellular resolution," *Biophysical Journal*, vol. 97, no. 9, pp. 2613–2622, 2009.

[42] P. Weber, M. Wagner, and H. Schneckenburger, "Fluorescence imaging of membrane dynamics in living cells," *Journal of Biomedical Optics*, vol. 15, no. 4, p. 046017, 2010.

[43] T. Forster, "10th spiers memorial lecture. Transfer mechanisms of electronic excitation," *Discuss. Faraday Soc.*, vol. 27, pp. 7–17, 1959.

[44] S. C. Warren, A. Margineanu, M. Katan, C. Dunsby, and P. M. French, "Homo-FRET based biosensors and their application to multiplexed imaging of signalling events in live cells," *International Journal of Molecular Sciences*, vol. 16, no. 7, pp. 14695–14716, 2015.

[45] L. W. Runnels and S. F. Scarlata, "Theory and application of fluorescence homotransfer to melittin oligomerization," *Biophysical Journal*, vol. 69, no. 4, pp. 1569–1583, 1995.

[46] V. M. Agranovich and M. D. Galanin, "Electron-excitation energy transfer in condensed media," *Moscow Izdatel Nauka*, 1978.

[47] T. Förster, "Zwischenmolekulare Energiewanderung und Fluoreszenz," *Annalen der Physik*, vol. 437, no. 1-2, pp. 55–75, 1948.

[48] T. Förster, "Experimentelle und theoretische Untersuchung des zwischenmolekularen Übergangs von Elektronenanregungsenergie," *Zeitschrift fur Naturforschung - Section A Journal of Physical Sciences*, vol. 4, no. 5, pp. 321–327, 1949.

[49] E. Gratton, "Fluorescence lifetime imaging for the two-photon microscope: time-domain and frequency-domain methods," *Journal of Biomedical Optics*, vol. 8, no. 3, p. 381, 2003.

[50] J. Philip and K. Carlsson, "Theoretical investigation of the signal-to-noise ratio in fluorescence lifetime imaging," *J. Opt. Soc. Am. A*, vol. 20, no. 2, pp. 368–379, 2003.

[51] A. Esposito, H. C. Gerritsen, and F. S. Wouters, "Optimizing frequency-domain fluorescence lifetime sensing for high-throughput applications: photon economy and acquisition speed," *Journal of the Optical Society of America A*, vol. 24, no. 10, p. 3261, 2007.

[52] H. C. Gerritsen, M. A. H. Asselbergs, A. V. Agronskaia, and W. G. J. H. M. Van Sark, "Fluorescence lifetime imaging in scanning microscopes: acquisition speed, photon economy and lifetime resolution," *Journal of Microscopy*, vol. 206, no. 3, pp. 218–224, 2002.

[53] Q. Zhao, I. T. Young, and J. G. S. de Jong, "Photon budget analysis for fluorescence lifetime imaging microscopy," *Journal of Biomedical Optics*, vol. 16, no. 8, p. 086007, 2011.

[54] D. Phillips and D. V. O'Connor, *Time-correlated single photon counting*. Academic Press, 1984.

[55] W. Becker, "The bh TCSPC technique: Introduction." `https://www.becker-hickl.com/wp-content/uploads/2019/01/bh-TCSPC-Introduction.pdf`, 2019.

[56] R. Z. Bachrach, "A photon counting apparatus for kinetic and spectral measurements," *Review of Scientific Instruments*, vol. 43, no. 5, pp. 734–737, 1972.

[57] T. Binkert, H. P. Tschanz, and P. E. Zinsli, "The measurement of fluorescence decay curves with the single-photon counting method and the evaluation of rate parameters," *Journal of Luminescence*, vol. 5, no. 3, pp. 187 – 217, 1972.

[58] C. Lewis, W. R. Ware, L. J. Doemeny, and T. L. Nemzek, "The measurement of short-lived fluorescence decay using the single photon counting method," *Review of Scientific Instruments*, vol. 44, no. 2, pp. 107–114, 1973.

[59] L. M. Hirvonen, Z. Petrášek, A. Beeby, and K. Suhling, "Sub-μs time resolution in wide-field time-correlated single photon counting microscopy obtained from the photon event phosphor decay," *New Journal of Physics*, vol. 17, 2015.

[60] K. Suhling, L. M. Hirvonen, J. A. Levitt, P.-H. Chung, C. L. Tregidgo, A. Le Marois, D. A. Rusakov, K. Zheng, S. Ameer-Beg, S. P. Poland, S. P. Pereira Coelho, R. Henderson, and N. Krstajić, "Fluorescence lifetime imaging (FLIM): basic concepts and some recent developments," *Medical Photonics*, vol. 27, pp. 3–40, 2015.

[61] C. Tregidgo, J. A. Levitt, and K. Suhling, "Effect of refractive index on the fluorescence lifetime of green fluorescent protein," *Journal of Biomedical Optics*, vol. 13, no. 3, p. 31218, 2008.

[62] H.-J. van Manen, P. Verkuijlen, P. Wittendorp, V. Subramaniam, T. K. van den Berg, D. Roos, and C. Otto, "Refractive index sensing of green fluorescent proteins in living cells using fluorescence lifetime imaging microscopy," 2008.

[63] A. Pliss, L. Zhao, T. Y. Ohulchanskyy, J. Qu, and P. N. Prasad, "Fluorescence lifetime of fluorescent proteins as an intracellular environment probe sensing the cell cycle progression," *ACS Chemical Biology*, vol. 7, no. 8, pp. 1385–1392, 2012.

[64] M. K. Kuimova, G. Yahioglu, J. A. Levitt, and K. Suhling, "Molecular rotor measures viscosity of live cells via fluorescence lifetime imaging," *Journal of the American Chemical Society*, vol. 130, no. 21, pp. 6672–6673, 2008.

[65] R. Sanders, A. Draaijer, H. C. Gerritsen, P. M. Houpt, and Y. K. Levine, "Quantitative pH imaging in cells using confocal fluorescence lifetime imaging microscopy," *Analytical Biochemistry*, vol. 227, no. 2, pp. 302–308, 1995.

[66] M. K. Kuimova, G. Yahioglu, and P. R. Ogilby, "Singlet oxygen in a cell: spatially dependent lifetimes and quenching rate constants," *Journal of the American Chemical Society*, vol. 131, no. 1, pp. 332–340, 2009.

[67] C. Biskup and T. Gensch, *Fluorescence lifetime imaging of ions in biological tissues in L Marcu, PMW French PMW, DS Elson, editors, fluorescence lifetime spectroscopy and imaging - principles and applications in biomedical diagnostics: CRC Press*, pp. 497–534. 2014.

[68] R. M. Clegg, "Chapter 1 Förster resonance energy transfer — FRET what is it, why do it, and how it's done," in *FRET and FLIM techniques*, vol. 33 of *Laboratory Techniques in Biochemistry and Molecular Biology*, pp. 1–57, Elsevier, 2009.

[69] S. S. Vogel, C. Thaler, and S. V. Koushik, "Fanciful FRET," *Science's STKE : signal transduction knowledge environment*, vol. 2006, no. 331, p. re2, 2006.

[70] E. A. Jares-Erijman and T. M. Jovin, "Imaging molecular interactions in living cells by FRET microscopy," *Current Opinion in Chemical Biology*, vol. 10, no. 5, pp. 409–416, 2006.

[71] R. B. Sekar and A. Periasamy, "Fluorescence resonance energy transfer (FRET) microscopy imaging of live cell protein localizations," *The Journal of Cell Biology*, vol. 160, no. 5, pp. 629–633, 2003.

[72] D. W. Piston and G.-J. Kremers, "Fluorescent protein FRET: the good, the bad and the ugly," *Trends in Biochemical Sciences*, vol. 32, no. 9, pp. 407–414, 2007.

[73] M. T. Stöckl and A. Herrmann, "Detection of lipid domains in model and cell membranes by fluorescence lifetime imaging microscopy," *Biochimica et Biophysica Acta (BBA) - Biomembranes*, vol. 1798, no. 7, pp. 1444–1456, 2010.

[74] J. A. Levitt, D. R. Matthews, S. M. Ameer-Beg, and K. Suhling, "Fluorescence lifetime and polarization-resolved imaging in cell biology," *Current Opinion in Biotechnology*, vol. 20, no. 1, pp. 28–36, 2009.

[75] S. Rajoria, L. Zhao, X. Intes, and M. Barroso, "FLIM-FRET for cancer applications," vol. 3, no. 2, pp. 144–161, 2014.

[76] S. Weidtkamp-Peters and Y. Stahl, *The use of FRET/FLIM to study proteins interacting with plant receptor kinases*, pp. 163–175. Springer New York, 2017.

[77] A. P. Savitsky, A. L. Rusanov, V. V. Zherdeva, T. V. Gorodnicheva, M. G. Khrenova, and A. V. Nemukhin, "FLIM-FRET imaging of caspase-3 activity

in live cells using pair of red fluorescent proteins," *Theranostics*, vol. 2, no. 2, pp. 215–226, 2012.

[78] A. H. A. Clayton, Q. S. Hanley, D. J. Arndt-Jovin, V. Subramaniam, and T. M. Jovin, "Dynamic fluorescence anisotropy imaging microscopy in the frequency domain (rFLIM)," *Biophysical Journal*, vol. 83, no. 3, pp. 1631–1649, 2002.

[79] I. Gautier, M. Tramier, C. Durieux, J. Coppey, R. B. Pansu, J. C. Nicolas, K. Kemnitz, and M. Coppey-Moisan, "Homo-FRET microscopy in living cells to measure monomer-dimer transition of GFP-tagged proteins," *Biophysical Journal*, vol. 80, no. 6, pp. 3000–3008, 2001.

[80] R. Varma and S. Mayor, "GPI-anchored proteins are organized in submicron domains at the cell surface," *Nature*, vol. 394, no. 6695, pp. 798–801, 1998.

[81] P. Sharma, R. Varma, R. C. Sarasij, Ira, K. Gousset, G. Krishnamoorthy, M. Rao, and S. Mayor, "Nanoscale organization of multiple GPI-anchored proteins in living cell membranes," *Cell*, vol. 116, no. 4, pp. 577–589, 2004.

[82] A. M. Melo, A. Fedorov, M. Prieto, and A. Coutinho, "Exploring homo-FRET to quantify the oligomer stoichiometry of membrane-bound proteins involved in a cooperative partition equilibrium," *Physical Chemistry Chemical Physics: PCCP*, vol. 16, no. 34, pp. 18105–18117, 2014.

[83] R. Peters, J. Peters, K. H. Tews, and W. Bähr, "A microfluorimetric study of translational diffusion in erythrocyte membranes," *Biochimica et Biophysica Acta (BBA) - Biomembranes*, vol. 367, no. 3, pp. 282–294, 1974.

[84] D. Axelrod, D. E. Koppel, J. Schlessinger, E. Elson, and W. W. Webb, "Mobility measurement by analysis of fluorescence photobleaching recovery kinetics," *Biophysical Journal*, vol. 16, no. 9, pp. 1055–1069, 1976.

[85] J. Lippincott-Schwartz, E. Snapp, and A. Kenworthy, "Studying protein dynamics in living cells," *Nature Reviews. Molecular Cell Biology*, vol. 2, no. 6, pp. 444–456, 2001.

[86] H. Deschout, K. Raemdonck, J. Demeester, S. C. De Smedt, and K. Braeckmans, "FRAP in pharmaceutical research: practical guidelines and applications in drug delivery," *Pharmaceutical Research*, vol. 31, no. 2, pp. 255–270, 2014.

[87] N. W. Goehring, D. Chowdhury, A. A. Hyman, and S. W. Grill, "FRAP analysis of membrane-associated proteins: lateral diffusion and membrane-cytoplasmic exchange," *Biophysical Journal*, vol. 99, no. 8, pp. 2443–2452, 2010.

[88] F. Pincet, V. Adrien, R. Yang, J. Delacotte, J. E. Rothman, W. Urbach, and D. Tareste, "FRAP to characterize molecular diffusion and interaction in various membrane environments," *PLoS ONE*, vol. 11, no. 7, pp. 1–19, 2016.

[89] R. Machan, Y. H. Foo, and T. Wohland, "On the equivalence of FCS and FRAP: simultaneous lipid membrane measurements," *Biophysical Journal*, vol. 111, no. 1, pp. 152–161, 2016.

[90] J. Yguerabide, J. A. Schmidt, and E. E. Yguerabide, "Lateral mobility in membranes as detected by fluorescence recovery after photobleaching," vol. 39, pp. 69–75, 1982.

[91] S. Seiffert and W. Oppermann, "Systematic evaluation of FRAP experiments performed in a confocal laser scanning microscope," *Journal of Microscopy*, vol. 220, no. 1, pp. 20–30, 2005.

[92] D. Blumenthal, L. Goldstien, M. Edidin, and L. A. Gheber, "Universal approach to FRAP analysis of arbitrary bleaching patterns," *Scientific Reports*, vol. 5, no. 1, p. 11655, 2015.

[93] D. M. Soumpasis, "Theoretical analysis of fluorescence photobleaching recovery experiments," *Biophysical Journal*, vol. 41, no. 1, pp. 95–97, 1983.

[94] P. Jönsson, M. P. Jonsson, J. O. Tegenfeldt, and F. Höök, "A method improving the accuracy of fluorescence recovery after photobleaching analysis," *Biophysical Journal*, vol. 95, no. 11, pp. 5334–5348, 2008.

[95] H. Deschout, J. Hagman, S. Fransson, J. Jonasson, M. Rudemo, N. Loren, and K. Braeckmans, "Straightforward FRAP for quantitative diffusion measurements with a laser scanning microscope," *Optics Express*, vol. 18, no. 22, pp. 22886–22905, 2010.

[96] M. Kang, C. A. Day, A. K. Kenworthy, and E. DiBenedetto, "Simplified equation to extract diffusion coefficients from confocal FRAP data," *Traffic*, vol. 13, no. 12, pp. 1589–1600, 2012.

[97] R. Xiong, R. E. Vandenbroucke, K. Broos, T. Brans, E. V. Wonterghem, C. Libert, J. Demeester, S. C. D. Smedt, and K. Braeckmans, "Sizing nanomaterials in bio-fluids by CFRAP enables protein aggregation measurements and diagnosis of bio-barrier permeability," *Nature Communications*, no. 7, p. 12982, 2016.

[98] D. E. Koppel, "Fluorescence redistribution after photobleaching. A new multipoint analysis of membrane translational dynamics," *Biophysical Journal*, vol. 28, no. 2, pp. 281–291, 1979.

[99] P. Wedekind, U. Kubitscheck, and R. Peters, "Scanning microphotolysis: a new photobleaching technique based on fast intensity modulation of a

scanned laser beam and confocal imaging," *Journal of Microscopy*, vol. 176, no. 1, pp. 23–33, 1994.

[100] L. S. Cutts, P. A. Roberts, J. Adler, M. C. Davies, and C. D. Melia, "Determination of localized diffusion coefficients in gels using confocal scanning laser microscopy," *Journal of Microscopy*, vol. 180, no. 2, pp. 131–139, 1995.

[101] K. Braeckmans, L. Peeters, N. N. Sanders, S. C. De Smedt, and J. Demeester, "Three-dimensional fluorescence recovery after photobleaching with the confocal scanning laser microscope," *Biophysical Journal*, vol. 85, no. 4, pp. 2240–2252, 2003.

[102] M. Kang, C. A. Day, K. Drake, A. K. Kenworthy, and E. DiBenedetto, "A generalization of theory for two-dimensional fluorescence recovery after photobleaching applicable to confocal laser scanning microscopes," *Biophysical Journal*, vol. 97, no. 5, pp. 1501–1511, 2009.

[103] D. Mazza, K. Braeckmans, F. Cella, I. Testa, D. Vercauteren, J. Demeester, S. S. De Smedt, and A. Diaspro, "A new FRAP/FRAPa method for three-dimensional diffusion measurements based on multiphoton excitation microscopy," *Biophysical Journal*, vol. 95, no. 7, pp. 3457–3469, 2008.

[104] S. Seiffert and W. Oppermann, "Systematic evaluation of FRAP experiments performed in a confocal laser scanning microscope," *Journal of Microscopy*, vol. 220, no. 1, pp. 20–30.

[105] G. I. Hauser, S. Seiffert, and W. Oppermann, "Systematic evaluation of FRAP experiments performed in a confocal laser scanning microscope - Part II: multiple diffusion processes," *Journal of Microscopy*, vol. 230, no. 3, pp. 353–362.

[106] E. L. Elson, "Fluorescence correlation spectroscopy measures molecular transport in cells," *Traffic (Copenhagen, Denmark)*, vol. 2, no. 11, pp. 789–796, 2001.

[107] B. L. Sprague, R. L. Pego, D. A. Stavreva, and J. G. McNally, "Analysis of binding reactions by fluorescence recovery after photobleaching," *Biophysical journal*, vol. 86, no. 6, pp. 3473–95, 2004.

[108] M. Liu, M. Jia, H. Pan, L. Li, M. Chang, H. Ren, F. Argoul, S. Zhang, and J. Xu, "Instrument response standard in time-resolved fluorescence spectroscopy at visible wavelength: quenched fluorescein sodium," *Applied spectroscopy*, vol. 68, no. 5, pp. 577–583, 2014.

[109] M. Koshioka, K. Sasaki, and H. Masuhara, "Time-dependent fluorescence depolarization analysis in three-dimensional microspectroscopy," *Applied Spectroscopy*, vol. 49, no. 2, pp. 224–228, 1995.

[110] J. J. Fisz, "Fluorescence polarization spectroscopy at combined high-aperture excitation and detection: application to one-photon-excitation fluorescence microscopy," *Journal of Physical Chemistry A*, vol. 111, no. 35, pp. 8606–8621, 2007.

[111] S. C. Warren, A. Margineanu, D. Alibhai, D. J. Kelly, C. Talbot, Y. Alexandrov, I. Munro, M. Katan, C. Dunsby, and P. M. W. French, "Rapid global fitting of large fluorescence lifetime imaging microscopy datasets," *PLoS ONE*, vol. 8, no. 8, 2013.

[112] S. Pelet, M. J. R. Previte, L. H. Laiho, and P. T. C. So, "A fast global fitting algorithm for fluorescence lifetime imaging microscopy based on image segmentation," *Biophys J*, vol. 87, no. 4, pp. 2807–2817, 2004.

[113] P. J. Verveer, A. Squire, and P. I. H. Bastiaens, "Global analysis of fluorescence lifetime imaging microscopy data," *Biophysical Journal*, vol. 78, no. 4, pp. 2127–2137, 2000.

[114] S.-c. Liao, Y. Sun, and U. Coskun, "FLIM analysis using the phasor plots," *ISS Technical Note*, no. 0, pp. 1–13, 2014.

[115] M. A. Digman, V. R. Caiolfa, M. Zamai, and E. Gratton, "The phasor approach to fluorescence lifetime imaging analysis," *Biophysical Journal*, vol. 94, no. 2, pp. L14–L16, 2008.

[116] A. Le Marois, S. Labouesse, K. Suhling, and R. Heintzmann, "Noise-corrected principal component analysis of fluorescence lifetime imaging data," *Journal of Biophotonics*, vol. 10, no. 9, pp. 1124–1133, 2017.

[117] R. Esposito, G. Mensitieri, and S. de Nicola, "Improved maximum entropy method for the analysis of fluorescence spectroscopy data: evaluating zero-time shift and assessing its effect on the determination of fluorescence lifetimes," *Analyst*, vol. 140, pp. 8138–8147, 2015.

[118] E. G. Novikov, V. V. Skakun, J. W. Borst, and A. J. W. G. Visser, "Maximum entropy analysis of polarized fluorescence decay of (E)GFP in aqueous solution," *Methods and Applications in Fluorescence*, vol. 6, no. 1, 2018.

[119] S. C. Warren, *Development and application of multiplexed fluorescence imaging to chemotaxis signalling pathways*. PhD thesis, Imperial College London, 2014.

[120] V. V. Anh, "Nonlinear least squares and maximum likelihood estimation of a heteroscedastic regression model," *Stochastic Processes and their Applications*, vol. 29, no. 2, pp. 317–333, 1988.

[121] M. Maus, M. Cotlet, J. Hofkens, T. Gensch, F. C. De Schryver, J. Schaffer, and C. A. M. Seidel, "An experimental comparison of the maximum likelihood estimation and nonlinear least-squares fluorescence lifetime analysis of single molecules," *Analytical Chemistry*, vol. 73, no. 9, pp. 2078–2086, 2001.

[122] T. Hauschild and M. Jentschel, "Comparison of maximum likelihood estimation and chi-square statistics applied to counting experiments," vol. 457, no. 1-2, pp. 384–401, 2001.

[123] J. Kim and J. Seok, "Statistical properties of amplitude and decay parameter estimators for fluorescence lifetime imaging," *Optics Express*, vol. 21, no. 5, p. 6061, 2013.

[124] P. Barber, "Help for time-resolved analysis TRI2 version 2.4." `http://users.ox.ac.uk/~atdgroup/technicalnotes/Time20resolved20analysis20help.pdf`, 2010.

[125] M. I. Rowley, A. C. C. Coolen, B. Vojnovic, and P. R. Barber, "Estimation, decay model selection and instrument response determination for low-intensity FLIM imaging," pp. 1–28, 2016.

[126] M. I. Rowley, P. R. Barber, A. C. C. Coolen, and B. Vojnovic, "Bayesian analysis of fluorescence lifetime imaging data," in *Multiphoton Microscopy in the Biomedical Sciences XI* (A. Periasamy, K. König, and P. T. C. So, eds.), vol. 7903, pp. 339 – 350, International Society for Optics and Photonics, SPIE, 2011.

[127] P. Kapusta, R. Erdmann, U. Ortmann, and M. Wahl. `https://www.picoquant.com/images/uploads/page/files/7345/technote_ft100_anisotropy.pdf`.

[128] K. A. Lidke, B. Rieger, D. S. Lidke, and T. M. Jovin, "The role of photon statistics in fluorescence anisotropy imaging," *IEEE Trans. Img. Proc.*, vol. 14, no. 9, pp. 1237–1245, 2005.

[129] C. Kappel and R. Eils, "Fluorescence recovery after photobleaching with the Leica TCS SP2," *Cancer Research*, no. 18, 2004.

[130] E. D. Siggia, J. Lippincott-schwartz, and S. Bekiranov, "Diffusion in inhomogeneous media: theory and simulations applied to whole cell photobleach recovery," *Biophysical Journal*, vol. 79, no. 4, pp. 1761–1770, 2000.

[131] E. L. Snapp, N. Altan, and J. Lippincott-Schwartz, "Measuring protein mobility by photobleaching GFP chimeras in living cells," *Current Protocols in Cell Biology*, vol. 19, no. 1, pp. 21.1.1–21.1.24, 2003.

[132] H. Deschout, J. Hagman, S. Fransson, J. Jonasson, M. Rudemo, N. Lorén, and K. Braeckmans, "Straightforward FRAP for quantitative diffusion measurements with a laser scanning microscope," *Optics Express*, vol. 18, no. 22, pp. 22886–22905, 2010.

[133] M. Weiss, "Challenges and artifacts in quantitative photobleaching experiments," *Traffic*, vol. 5, no. 9, pp. 662–671, 2004.

[134] T. T. Tsay and K. A. Jacobson, "Spatial Fourier analysis of video photobleaching measurements. Principles and optimization," *Biophysical journal*, vol. 60, no. 2, pp. 360–368, 1991.

[135] D. A. Berk, F. Yuan, M. Leunig, and R. K. Jain, "Fluorescence photobleaching with spatial Fourier analysis: measurement of diffusion in light-scattering media," *Biophysical journal*, vol. 65, no. 6, pp. 2428–36, 1993.

[136] M. Peter, S. M. Ameer-Beg, M. K. Hughes, M. D. Keppler, S. Prag, M. Marsh, B. Vojnovic, and T. Ng, "Multiphoton-FLIM quantification of

the EGFP-mRFP1 FRET pair for localization of membrane receptor-kinase interactions," *Biophysical Journal*, vol. 88, no. 2, pp. 1224–1237, 2005.

[137] H. W. Ai, K. L. Hazelwood, M. W. Davidson, and R. E. Campbell, "Fluorescent protein FRET pairs for ratiometric imaging of dual biosensors," *Nature Methods*, vol. 5, no. 5, pp. 401–403, 2008.

[138] J. Schwarz, H. J Leopold, R. Leighton, R. C. Miller, C. P. Aplin, A. J. Boersma, A. A. Heikal, and E. D. Sheets, "Macromolecular crowding effects on energy transfer efficiency and donor-acceptor distance of hetero-FRET sensors using time-resolved fluorescence," *Methods and applications in fluorescence*, vol. 7, no. 2, p. 025002, 2019.

[139] A. N. Bader, E. G. Hofman, P. M. P. van Bergen en Henegouwen, and H. C. Gerritsen, "Imaging of protein cluster sizes by means of confocal time-gated fluorescence anisotropy microscopy," *Optics Express*, vol. 15, no. 11, p. 6934, 2007.

[140] E. K. Yeow and A. H. Clayton, "Enumeration of oligomerization states of membrane proteins in living cells by homo-FRET spectroscopy and microscopy: theory and application," *Biophysical Journal*, vol. 92, no. 9, pp. 3098–3104, 2007.

[141] J.-c. Cossec, V. Devauges, C. Marquer, S. Le, C. Potier, E. Fort, K. Suhling, and S. Le, "Homodimerization of amyloid precursor protein at the plasma membrane : a homoFRET study by time-resolved fluorescence anisotropy imaging," vol. 7, no. 9, 2012.

[142] T. A. Nguyen, P. Sarkar, J. V. Veetil, S. V. Koushik, and S. S. Vogel, "Fluorescence polarization and fluctuation analysis monitors subunit proximity, stoichiometry, and protein complex hydrodynamics," *PLoS ONE*, vol. 7, no. 5, 2012.

[143] T. A. Nguyen, H. L. Puhl, A. K. Pham, and S. S. Vogel, "Auto-FPFA: an automated microscope for characterizing genetically encoded biosensors," *Scientific Reports*, vol. 8, no. 1, pp. 1–17, 2018.

[144] J. Berrout, E. Kyriakopoulou, L. Moparthi, A. S. Hogea, L. Berrout, C. Ivan, M. Lorger, J. Boyle, C. Peers, S. Muench, J. E. Gomez, X. Hu, C. Hurst, T. Hall, S. Umamaheswaran, L. Wesley, M. Gagea, M. Shires, I. Manfield, M. A. Knowles, S. Davies, K. Suhling, Y. Teijeiro-Gonzalez, N. Carragher, K. Macleod, N. J. Abbott, G. A. Calin, N. Gamper, P. M. Zygmunt, and Z. Timsah, "TRPA1-FGFR2 binding event is a regulatory oncogenic driver modulated by miRNA-142-3p," *Nature Communications*, vol. 8, no. 1, 2017.

[145] D. Llères, J. James, S. Swift, D. G. Norman, and A. I. Lamond, "Quantitative analysis of chromatin compaction in living cells using FLIM-FRET," *Journal of Cell Biology*, vol. 187, no. 4, pp. 481–496, 2009.

[146] A. S. Belmont, S. Dietzel, A. C. Nye, Y. G. Strukov, and T. Tumbar, "Large-scale chromatin structure and function," *Current Opinion in Cell Biology*, vol. 11, no. 3, pp. 307–311, 1999.

[147] K. Luger and J. C. Hansen, "Nucleosome and chromatin fiber dynamics," *Current Opinion in Structural Biology*, vol. 15, no. 2, pp. 188–196, 2005.

[148] N. S. Caron, L. N. Munsie, J. W. Keillor, and R. Truant, "Using FLIM-FRET to measure conformational changes of transglutaminase type 2 in live cells," *PLoS ONE*, vol. 7, no. 8, 2012.

[149] T. Ng, D. Shima, A. Squire, P. I. Bastiaens, S. Gschmeissner, M. J. Humphries, and P. J. Parker, "PKCα regulates β1 integrin-dependent cell motility through association and control of integrin traffic," *EMBO Journal*, vol. 18, no. 14, pp. 3909–3923, 1999.

[150] I. Ziomkiewicz, A. Loman, R. Klement, C. Fritsch, A. S. Klymchenko, G. Bunt, T. M. Jovin, and D. J. Arndt-Jovin, "Dynamic conformational transitions of the EGF receptor in living mammalian cells determined by FRET and fluorescence lifetime imaging microscopy," *Cytometry Part A*, vol. 83, no. 9, pp. 794–805, 2013.

[151] B. J. Bacskai, J. Skoch, G. A. Hickey, R. Allen, and B. T. Hyman, "Fluorescence resonance energy transfer determinations using multiphoton fluorescence lifetime imaging microscopy to characterize amyloid-beta plaques," *Journal of Biomedical Optics*, vol. 8, no. 3, p. 368, 2003.

[152] M. Elangovan, R. N. Day, and A. Periasamy, "Nanosecond fluorescence resonance energy transfer-fluorescence lifetime imaging microscopy to localize the protein interactions in a single living cell," *Journal of Microscopy*, vol. 205, no. 1, pp. 3–14, 2002.

[153] Y. Chen, J. D. Mills, and A. Periasamy, "Protein localization in living cells and tissues using FRET and FLIM," *Differentiation*, vol. 71, no. 9-10, pp. 528–541, 2003.

[154] R. Y. Tsien, "The green fluorescent protein," *Annual Review of Biochemistry*, vol. 67, no. 1, pp. 509–544, 1998.

[155] F. H. Johnson, O. Shimomura, Y. Saiga, L. C. Gershman, G. T. Reynolds, and J. R. Waters, "Quantum efficiency of cypridina luminescence, with a note on that of aequorea," *Journal of Cellular and Comparative Physiology*, vol. 60, no. 1, pp. 85–103, 1962.

[156] J. G. Morin and J. W. Hastings, "Energy transfer in a bioluminescent system," *Journal of Cellular Physiology*, vol. 77, no. 3, pp. 313–318.

[157] R. Heim, D. C. Prasher, and R. Y. Tsien, "Wavelength mutations and post-translational autoxidation of green fluorescent protein," *Proceedings of the National Academy of Sciences*, vol. 91, no. 26, pp. 12501–12504, 1994.

[158] M. Cotlet, J. Hofkens, M. Maus, T. Gensch, M. Van der Auweraer, J. Michiels, G. Dirix, M. Van Guyse, J. Vanderleyden, A. J. W. G. Visser, and F. C. De Schryver, "Excited-state dynamics in the enhanced green fluorescent protein mutant probed by picosecond time-resolved single photon counting spectroscopy," *The Journal of Physical Chemistry B*, vol. 105, no. 21, pp. 4999–5006, 2001.

[159] M. Ormö, A. B. Cubitt, K. Kallio, L. A. Gross, R. Y. Tsien, and S. J. Remington, "Crystal structure of the aequorea bictoria green fluorescent protein," *Science*, vol. 273, no. 5280, pp. 1392–1395, 1996.

[160] J. T. Weber, "Green fluorescent protein: properties, applications, and protocols. 2nd edition edited by M. Chalfie (Columbia University) and S. R. Kain (Agilent Technologies). Wiley-Interscience, Hoboken," *Journal of Natural Products*, vol. 70, no. 1, pp. 141–141, 2007.

[161] M. Zimmer, "Green fluorescent protein (GFP): applications, structure, and related photophysical behavior," *Chemical Reviews*, vol. 102, no. 3, pp. 759–782, 2002. PMID: 11890756.

[162] A. J. W. G. Visser, A. H. Westphal, V. V. Skakun, and J. W. Borst, "GFP as potential cellular viscosimeter," *Methods and Applications in Fluorescence*, vol. 4, no. 3, p. 035002, 2016.

[163] J. S. Donner, S. A. Thompson, M. P. Kreuzer, G. Baffou, and R. Quidant, "Mapping intracellular temperature using green fluorescent protein," *Nano Letters*, vol. 12, no. 4, pp. 2107–2111, 2012. PMID: 22394124.

[164] E. N. Bodunov and M. N. Berberan-Santos, "Stretched exponential kinetics of the luminescence concentration depolarization and penetration depth of molecules in a medium," *Optics and Spectroscopy (English translation of Optika i Spektroskopiya)*, vol. 119, no. 1, pp. 22–28, 2015.

[165] M. N. Berberan-Santos and B. Valeur, "Fluorescence depolarization by electronic energy transfer in donor–acceptor pairs of like and unlike chromophores," *The Journal of Chemical Physics*, vol. 95, no. 11, pp. 8048–8055, 1991.

[166] D. L. Huber, D. S. Hamilton, and B. Barnett, "Time-dependent effects in fluorescent line narrowing," *Physical Review B*, vol. 16, no. 10, pp. 4642–4650, 1977.

[167] C. J. Cohen, J. T. C. Shieh, R. J. Pickles, T. Okegawa, J.-T. Hsieh, and J. M. Bergelson, "The coxsackievirus and adenovirus receptor is a transmembrane component of the tight junction," *Proceedings of the National Academy of Sciences*, vol. 98, no. 26, pp. 15191–15196, 2001.

[168] K. J. D. A. Excoffon, A. Hruska-Hageman, M. Klotz, G. L. Traver, and J. Zabner, "A role for the PDZ-binding domain of the coxsackie B virus and adenovirus receptor (CAR) in cell adhesion and growth," *Journal of Cell Science*, vol. 117, no. 19, pp. 4401–4409, 2004.

[169] Z. Chen, Q. Wang, J. Sun, A. Gu, M. Jin, Z. Shen, Z. Qiu, J. Wang, X. Wang, Z. Zhan, and J.-W. Li, "Expression of the coxsackie and adenovirus receptor in human lung cancers," *Tumor Biology*, vol. 34, no. 1, pp. 17–24, 2013.

[170] R. Pike, E. Ortiz-Zapater, B. Lumicisi, G. Santis, and M. Parsons, "KIF22 coordinates CAR and EGFR dynamics to promote cancer cell proliferation," *Science Signaling*, vol. 11, no. 515, 2018.

[171] H. Schmitz, C. Barmeyer, M. Fromm, N. Runkel, H.-D. Foss, C. J. Bentzel, E.-O. Riecken, and J.-D. Schulzke, "Altered tight junction structure contributes to the impaired epithelial barrier function in ulcerative colitis," *Gastroenterology*, vol. 116, no. 2, pp. 301 – 309, 1999.

[172] C. B. Coyne and J. M. Bergelson, "CAR: A virus receptor within the tight junction," *Advanced Drug Delivery Reviews*, vol. 57, no. 6, pp. 869 – 882, 2005.

[173] C. Farmer, P. E. Morton, M. Snippe, G. Santis, and M. Parsons, "Coxsackie adenovirus receptor (CAR) regulates integrin function through activation of p44/42 MAPK," *Experimental Cell Research*, vol. 315, no. 15, pp. 2637 – 2647, 2009.

[174] C. Demaison, K. Parsley, G. Brouns, M. Scherr, K. Battmer, C. Kinnon, M. Grez, and A. J. Thrasher, "High-level transduction and gene expression in hematopoietic repopulating cells using a human imunodeficiency virus type 1-based lentiviral vector containing an internal spleen focus forming virus promoter," *Human Gene Therapy*, vol. 13, no. 7, pp. 803–813, 2002.

[175] I. Kirby, E. Davison, A. J. Beavil, C. P. C. Soh, T. J. Wickham, P. W. Roelvink, I. Kovesdi, B. J. Sutton, and G. Santis, "Mutations in the DG loop of adenovirus type 5 fiber knob protein abolish high-affinity binding to its cellular receptor CAR," *Journal of Virology*, vol. 73, no. 11, pp. 9508–9514, 1999.

[176] P. E. Morton, A. Hicks, T. Nastos, G. Santis, and M. Parsons, "CAR regulates epithelial cell junction stability through control of E-cadherin trafficking," *Scientific Reports*, vol. 3, pp. 1–13, 2013.

[177] F. Tanaka and N. Mataga, "Dynamic depolarization of interacting fluorophores. Effect of internal rotation and energy transfer," *Biophysical Journal*, vol. 39, pp. 129–140, 1982.

[178] J. Timmermans, "Physico-chemical constants of pure organic compounds," *Elsevier*, vol. 39, no. 11, pp. 651–651, 1950.

[179] J. A. Levitt, P. Chung, M. K. Kuimova, G. Yahioglu, Y. Wang, J. Qu, and K. Suhling, "Fluorescence anisotropy of molecular rotors," *ChemPhysChem*, vol. 12, no. 3, pp. 662–672, 2011.

[180] J. Hunt, A. H. Keeble, R. E. Dale, M. K. Corbett, R. L. Beavil, J. Levitt, M. J. Swann, K. Suhling, S. Ameer-Beg, B. J. Sutton, and A. J. Beavil, "A fluorescent biosensor reveals conformational changes in human immunoglobulin E Fc: implications for mechanisms of receptor binding, inhibition, and allergen recognition," *Journal of Biological Chemistry*, vol. 287, no. 21, pp. 17459–17470, 2012.

[181] G. F. Schröder, U. Alexiev, and H. Grubmüller, "Simulation of fluorescence anisotropy experiments: Probing protein dynamics," *Biophysical Journal*, vol. 89, no. 6, pp. 3757 – 3770, 2005.

[182] P. Košovan, Z. Limpouchová, and K. Procházka, "Molecular dynamics simulation of time-resolved fluorescence anisotropy decays from labeled polyelectrolyte chains," *Macromolecules*, vol. 39, pp. 3458–3465, 2006.

[183] R. Best, H. Hofmann, D. Nettels, and B. Schuler, "Quantitative interpretation of fret experiments via molecular simulation: force field and validation," *Biophysical Journal*, vol. 108, no. 11, pp. 2721 – 2731, 2015.

[184] O. Mancini, T. Wellbrock, O. J. Rolinski, K. Kubiak-Ossowska, and P. A. Mulheran, "Probing beta amyloid aggregation using fluorescence anisotropy:

experiments and simulation," *Physical Chemistry Chemical Physics: PCCP*, vol. 20, no. 6, pp. 4216–4225, 2018.

[185] W. L. Jorgensen, J. Chandrasekhar, J. D. Madura, R. W. Impey, and M. L. Klein, "Comparison of simple potential functions for simulating liquid water," *The Journal of Chemical Physics*, vol. 79, pp. 926–935, 1983.

[186] M. A. González and J. L. F. Abascal, "The shear viscosity of rigid water models," *The Journal of Chemical Physics*, vol. 132, no. 9, p. 096101, 2010.

[187] Y. Song and L. L. Dai, "The shear viscosities of common water models by non-equilibrium molecular dynamics simulations," *Molecular Simulation*, vol. 36, no. 7-8, pp. 560–567, 2010.

[188] M. A. Uskova, J.-W. Borst, M. A. Hink, A. van Hoek, A. Schots, N. L. Klyachko, and A. J. Visser, "Fluorescence dynamics of green fluorescent protein in aot reversed micelles," *Biophysical Chemistry*, vol. 87, no. 1, pp. 73 – 84, 2000.

[189] A. Heikal, S. Hess, and W. Webb, "Multiphoton molecular spectroscopy and excited-state dynamics of enhanced green fluorescent protein (EGFP): acid-base specificity," *Chemical Physics*, vol. 274, no. 1, pp. 37–55, 2001.

[190] N.-S. Cheng, "Formula for the viscosity of a glycerolâˆ'water mixture," *Industrial & Engineering Chemistry Research*, vol. 47, no. 9, pp. 3285–3288, 2008.

[191] M. A. Hink, R. A. Griep, J. W. Borst, A. van Hoek, M. H. M. Eppink, A. Schots, and A. J. W. G. Visser, "Structural dynamics of green fluorescent protein alone and fused with a single chain fv protein," *Journal of Biological Chemistry*, vol. 275, no. 23, pp. 17556–17560, 2000.

[192] D. Bhunia, R. Chowdhury, K. Bhattacharyya, and S. Ghosh, "Fluorescence fluctuation of an antigen–antibody complex: circular dichroism, FCS and smFRET of enhanced GFP and its antibody," *Phys. Chem. Chem. Phys.*, vol. 17, pp. 25250–25259, 2015.

[193] P.-H. Chung, C. Tregidgo, and K. Suhling, "Determining a fluorophore's transition dipole moment from fluorescence lifetime measurements in solvents of varying refractive index," *Methods and Applications in Fluorescence*, vol. 4, no. 4, p. 045001, 2016.

[194] S. Hirayama and D. Phillips, "Correction for refractive index in the comparison of radiative lifetimes in vapour and solution phases," *Journal of Photochemistry*, vol. 12, no. 2, pp. 139 – 145, 1980.

[195] D. Toptygin, "Effects of the solvent refractive index and its dispersion on the radiative decay rate and extinction coefficient of a fluorescent solute," *Journal of Fluorescence*, vol. 13, no. 3, pp. 201–219, 2003.

[196] R. Dale, J. Eisinger, and W. Blumberg, "The orientational freedom of molecular probes. the orientation factor in intramolecular energy transfer," *Biophysical Journal*, vol. 26, no. 2, pp. 161 – 193, 1979.

[197] I. Z. Steinberg, E. Haas, and E. Katchalski-Katzir, *Long-range nonradiative transfer of electronic excitation energy*, pp. 411–450. Springer US, 1983.

[198] B. van der Meer, M. Raymer, S. Wagoner, R. Hackney, J. Beechem, and E. Gratton, "Designing matrix models for fluorescence energy transfer between moving donors and acceptors," *Biophysical Journal*, vol. 64, no. 4, pp. 1243 – 1263, 1993.

[199] Z. Hillel and C.-W. Wu, "Statistical interpretation of fluorescence energy transfer measurements in macromolecular systems," *Biochemistry*, vol. 15, no. 10, pp. 2105–2113, 1976.

[200] S. S. Vogel, T. A. Nguyen, B. W. van der Meer, and P. S. Blank, "The impact of heterogeneity and dark acceptor states on FRET: implications for using fluorescent protein donors and acceptors," *PLoS ONE*, vol. 7, no. 11, pp. 1–14, 2012.

[201] J. A. Levitt, P. E. Morton, G. O. Fruhwirth, G. Santis, P. Chung, M. Parsons, and K. Suhling, "Simultaneous FRAP, FLIM and FAIM for measurements of protein mobility and interaction in living cells," *Biomedical Optics Express*, vol. 6, no. 10, pp. 3842–3854, 2015.

[202] J. W. Borst and A. J. W. G. Visser, "Fluorescence Lifetime Imaging Microscopy in life sciences," *Measurement Science and Technology*, vol. 21, no. 10, p. 102002, 2010.

[203] W. Becker, "Fluorescence lifetime imaging – techniques and applications," *Journal of Microscopy*, vol. 247, no. 2, pp. 119–136, 2012.

[204] X. Michalet, O. H. W. Siegmund, J. V. Vallerga, P. Jelinsky, J. E. Millaud, and S. Weiss, "Detectors for single-molecule fluorescence imaging and spectroscopy," *Journal of Modern Optics*, vol. 54, no. 2-3, pp. 239–281, 2007.

[205] F. Festy, S. M. Ameer-Beg, T. Ng, and K. Suhling, "Imaging proteins in vivo using fluorescence lifetime microscopy," *Molecular Biosystems*, vol. 3, no. 6, pp. 381–391, 2007.

[206] W. Becker, A. Bergmann, M. A. Hink, K. Konig, K. Benndorf, and C. Biskup, "Fluorescence lifetime imaging by time-correlated single-photon counting," *Microscopy Research and Technique*, vol. 63, no. 1, pp. 58–66, 2004.

[207] P. I. Bastiaens and A. Squire, "Fluorescence lifetime imaging microscopy: spatial resolution of biochemical processes in the cell," *Trends in Cell Biology*, vol. 9, no. 2, pp. 48–52, 1999.

[208] K. Suhling, P. M. W. French, and D. Phillips, "Time-resolved fluorescence microscopy," *Photochemical & Photobiological Sciences*, vol. 4, no. 1, pp. 13–22, 2005.

[209] M. Y. Berezin and S. Achilefu, "Fluorescence lifetime measurements and biological imaging," *Chemical Reviews*, vol. 110, no. 5, pp. 2641–2684, 2010.

[210] K. Suhling, J. Siegel, P. M. P. Lanigan, S. Lévêque-Fort, S. E. D. Webb, D. Phillips, D. M. Davis, and P. M. W. French, "Time-resolved fluorescence anisotropy imaging applied to live cells," *Optics Letters*, vol. 29, no. 6, pp. 584–586, 2004.

[211] J. Siegel, K. Suhling, P. M. W. French, D. Phillips, D. M. Davis, S. E. D. Webb, Y. Sabharwal, and S. Levequefort, "Wide-field time-resolved fluorescence anisotropy imaging (TR-FAIM): imaging the rotational mobility of a fluorophore," *Review of Scientific Instruments*, vol. 74, no. 1, pp. 182–192, 2003.

[212] Q. Zhao, I. T. Young, and J. G. Sander de Jong, "Photon budget analysis for fluorescence lifetime imaging microscopy," *Journal of Biomedical Optics*, vol. 16, no. 8, p. 086007, 2011.

[213] D. R. Matthews, G. O. Fruhwirth, G. Weitsman, L. M. Carlin, E. Ofo, M. Keppler, P. R. Barber, I. D. C. Tullis, B. Vojnovic, T. Ng, and S. M. Ameer-Beg, "A multi-functional imaging approach to high-content protein interaction screening," *PLoS ONE*, vol. 7, no. 4, p. 16, 2012.

[214] Y. Zhou, J. M. Dickenson, and Q. S. Hanley, "Imaging lifetime and anisotropy spectra in the frequency domain," *Journal of Microscopy*, vol. 234, no. 1, pp. 80–88, 2009.

[215] D. R. James, D. R. Demmer, R. P. Steer, and R. E. Verrall, "Fluorescence lifetime quenching and anisotropy studies of ribonuclease T1," *Biochemistry*, vol. 24, no. 20, pp. 5517–5526, 1985.

[216] M. J. Roberti, T. M. Jovin, and E. Jares-Erijman, "Confocal fluorescence anisotropy and FRAP Imaging of α-Synuclein amyloid aggregates in living cells," *PLoS ONE*, vol. 6, no. 8, pp. 1–7, 2011.

[217] Y. Teijeiro-Gonzalez, A. L. Marois, A. M. Economou, L. M. Hirvonen, J. A. Levitt, A. J. Beavil, R. L. Beavil, A. Crnjar, C. Molteni, E. Ortiz-Zapater, M. Parsons, and K. Suhling, "Fluorescence recovery after photobleaching (FRAP) with simultaneous fluorescence lifetime and time-resolved fluorescence anisotropy imaging (FLIM and tr-FAIM)," in *Three-Dimensional and Multidimensional Microscopy: Image Acquisition and Processing XXVI* (T. G. Brown and T. Wilson, eds.), vol. 10883, pp. 1 – 11, International Society for Optics and Photonics, SPIE, 2019.

[218] N. Chaffey, "Molecular biology of the cell," *Annals of Botany*, vol. 91, no. 3, pp. 401–401, 2003.

[219] "Chapter 2 - cell membranes," in *Medical Cell Biology (Third Edition)* (S. R. Goodman, ed.), pp. 27 – 57, Academic Press, third edition ed., 2008.

[220] D. E. Warnock, C. Roberts, M. S. Lutz, W. A. Blackburn, W. W. J. Young, and J. U. Baenziger, "Determination of plasma membrane lipid mass and composition in cultured Chinese hamster ovary cells using high gradient magnetic affinity chromatography," *The Journal of biological chemistry*, vol. 268, no. 14, pp. 10145–10153, 1993.

[221] Z. S. e. a. Lodish H, Berk A, "Chapter biomembranes: structural organization and basic functions," in *Molecular Cell Biology*, 4th ed., 2000.

[222] S. J. Singer and G. L. Nicolson, "The fluid mosaic model of the structure of cell membranes," *Science*, vol. 175, no. 4023, pp. 720–731, 1972.

[223] Z. Korade and A. K. Kenworthy, "Lipid rafts, cholesterol, and the brain," *Neuropharmacology*, vol. 55, no. 8, pp. 1265 – 1273, 2008.

[224] L. J. Pike, "The challenge of lipid rafts," *Journal of Lipid Research*, vol. 50, no. Supplement, pp. S323–S328, 2009.

[225] R. P. Richter, R. Bérat, and A. R. Brisson, "Formation of solid-supported lipid bilayers: an integrated view," *Langmuir*, vol. 22, no. 8, pp. 3497–3505, 2006.

[226] A. S. Ulrich, M. Sami, and A. Watts, "Hydration of dopc bilayers by differential scanning calorimetry," *Biochimica et Biophysica Acta (BBA) - Biomembranes*, vol. 1191, no. 1, pp. 225 – 230, 1994.

[227] A. Obaid, L. Loew, J. Wuskell, and B. Salzberg, "Novel naphthylstyryl-pyridinium potentiometric dyes offer advantages for neural network analysis," *Journal of Neuroscience Methods*, vol. 134, no. 2, pp. 179 – 190, 2004.

[228] L. Jin, A. C. Millard, J. P. Wuskell, H. A. Clark, and L. M. Loew, "Cholesterol-enriched lipid domains can be visualized by di-4-ANEPPDHQ with linear and nonlinear optics," *Biophysical Journal*, vol. 89, no. 1, pp. 4–6, 2005.

[229] L. Jin, A. C. Millard, J. P. Wuskell, X. Dong, D. Wu, H. A. Clark, and L. M. Loew, "Characterization and application of a new optical probe for membrane lipid domains," *Biophysical Journal*, vol. 90, no. 7, pp. 2563–2575, 2006.

[230] E. Sezgin, T. Sadowski, and K. Simons, "Measuring lipid packing of model and cellular membranes with environment sensitive probes," *Langmuir*, vol. 30, no. 27, pp. 8160–8166, 2014.

[231] E. Sezgin, F. Schneider, V. Zilles, I. Urbančič, E. Garcia, D. Waithe, A. S. Klymchenko, and C. Eggeling, "Polarity-sensitive probes for superresolution stimulated emission depletion microscopy," *Biophysical Journal*, vol. 113, no. 6, pp. 1321 – 1330, 2017.

[232] D. M. Jameson, "Gregorio Weber, 1916-1997: A fluorescent lifetime," *Biophysical Journal*, vol. 75, no. 1, pp. 419–421, 1998.

[233] W. Yu, P. T. C. So, T. French, and E. Gratton, "Fluorescence generalized polarization of cell membranes: a two-photon scanning microscopy approach," *Biophysical Journal*, vol. 70, pp. 626–636, 1996.

[234] Y. Niko, P. Didier, Y. Mely, G. Konishi, and A. S. Klymchenko, "Bright and photostable push-pull pyrene dye visualizes lipid order variation between plasma and intracellular membranes," *Nature Publishing Group*, pp. 1–9, 2016.

[235] A. S. Klymchenko, "Solvatochromic and Fluorogenic Dyes as Environment-Sensitive Probes: Design and Biological Applications," *Accounts of Chemical Research*, vol. 50, no. 2, pp. 366–375, 2017.

[236] D. M. Owen, P. M. P. Lanigan, C. Dunsby, I. Munro, D. Grant, M. A. A. Neil, P. M. W. French, and A. I. Magee, "Fluorescence lifetime imaging provides enhanced contrast when imaging the phase-sensitive dye di-4-ANEPPDHQ in model membranes and live cells," pp. 80–82, 2006.

[237] J. M. Kwiatek, D. M. Owen, A. Abu-Siniyeh, P. Yan, L. M. Loew, and K. Gaus, "Characterization of a new series of fluorescent probes for imaging membrane order," *PLoS ONE*, vol. 8, no. 2, pp. 1–7, 2013.

[238] V. Kilin, O. Glushonkov, L. Herdly, A. Klymchenko, L. Richert, and Y. Mely, "Fluorescence lifetime imaging of membrane lipid order with a ratiometric fluorescent probe," *Biophysical Journal*, vol. 108, no. 10, pp. 2521 – 2531, 2015.

[239] A. L. Marois, D. M. Owen, and K. Suhling, "Investigating cell membrane structure and dynamics with TCSPC-FLIM," in *Multiphoton Microscopy in the Biomedical Sciences XV* (A. Periasamy, P. T. C. So, and K. König, eds.), vol. 9329, pp. 319 – 325, International Society for Optics and Photonics, SPIE, 2015.

[240] H. B. B. Steele, M. J. Sydor, D. S. Anderson, A. Holian, and J. B. A. Ross, "Using time-resolved fluorescence anisotropy of di-4-ANEPPDHQ and F2N12S to analyze lipid packing dynamics in model systems," *Journal of Fluorescence*, vol. 29, no. 2, pp. 347–352, 2019.

[241] A. Honigmann, C. Walter, F. Erdmann, C. Eggeling, and R. Wagner, "Characterization of horizontal lipid bilayers as a model system to study lipid phase separation," *Biophysical Journal*, vol. 98, no. 12, pp. 2886–2894, 2010.

[242] L. F. Aguilar, J. A. Pino, M. A. Soto-Arriaza, F. J. Cuevas, S. Sánchez, and C. P. Sotomayor, "Differential dynamic and structural behavior of lipid-cholesterol domains in model membranes," *PLoS ONE*, vol. 7, no. 6, pp. 1–13, 2012.

[243] G. Rayan, J. E. Guet, N. Taulier, F. Pincet, and W. Urbach, "Recent applications of fluorescence recovery after photobleaching (FRAP) to membrane bio-macromolecules," *Sensors*, vol. 10, pp. 5927–5948, 2010.

[244] B. Y. E. Gorter, "On bimolecular layers of lipids on the chromo- cytes of the blood," *Journal of Experimental Medicine*, vol. 41, no. 4, pp. 439–443, 1925.

[245] S. Ladha, A. R. Mackie, L. J. Harvey, D. C. Clark, E. J. Lea, M. Brullemans, and H. Duclohier, "Lateral diffusion in planar lipid bilayers: a fluorescence recovery after photobleaching investigation of its modulation by lipid composition, cholesterol, or alamethicin content and divalent cations," *Biophysical Journal*, vol. 71, no. 3, pp. 1364–1373, 1996.

[246] M. Wagner and L. Tamm, "Tethered polymer-supported planar lipid bilayers for reconstitution of integral membrane proteins: silane-polyethyleneglycol-lipid as a cushion and covalent linker," *Biophysical Journal*, vol. 79, pp. 1400–1414, 2000.

[247] R. Macháň and M. Hof, "Lipid diffusion in planar membranes investigated by fluorescence correlation spectroscopy," *Biochimica et Biophysica Acta - Biomembranes*, vol. 1798, no. 7, pp. 1377–1391, 2010.

[248] L. K. Tamm and H. M. McConnell, "Supported phospholipid bilayers," *Biophysical Journal*, vol. 47, no. 1, pp. 105–113, 1985.

[249] S. J. Johnson, T. M. Bayerl, D. C. McDermott, G. W. Adam, A. R. Rennie, R. K. Thomas, and E. Sackmann, "Structure of an adsorbed dimyristoylphosphatidylcholine bilayer measured with specular reflection of neutrons," *Biophysical Journal*, vol. 59, no. 2, pp. 289–294, 1991.

[250] P. Hinterdorfer, G. Baber, and L. K. Tamm, "Reconstitution of membrane fusion sites," *J. Biol. Chem.*, vol. 269, no. 32, pp. 20360–20368, 1994.

[251] J. Salafsky, J. T. Groves, and S. G. Boxer, "Architecture and function of membrane proteins in planar supported bilayers: a study with photosynthetic reaction centers," *Biochemistry*, vol. 35, no. 47, pp. 14773–14781, 1996.

[252] M. Hetzer, S. Heinz, S. Grage, and T. M. Bayerl, "Asymmetric molecular friction in supported phospholipid bilayers revealed by NMR measurements of lipid diffusion," *Langmuir*, vol. 14, no. 5, pp. 982–984, 2002.

[253] C. Scomparin, S. Lecuyer, M. Ferreira, T. Charitat, and B. Tinland, "Diffusion in supported lipid bilayers: influence of substrate and preparation technique on the internal dynamics," *European Physical Journal E*, vol. 28, no. 2, pp. 211–220, 2009.

[254] L. Renner, T. Pompe, C. Werner, T. Osaki, S. Chiantia, and P. Schwille, "Supported lipid bilayers on spacious and pH-responsive polymer cushions with varied hydrophilicity," *Journal of Physical Chemistry B*, vol. 112, no. 20, pp. 6373–6378, 2008.

[255] A. Benda, M. Beneš, V. Mareček, A. Lhotský, W. T. Hermens, and M. Hof, "How to determine diffusion coefficients in planar phospholipid systems by confocal fluorescence correlation spectroscopy," *Langmuir*, vol. 19, no. 10, pp. 4120–4126, 2003.

[256] S. Chiantia, J. Ries, and P. Schwille, "Fluorescence correlation spectroscopy in membrane structure elucidation," *Biochimica et Biophysica Acta (BBA) - Biomembranes*, vol. 1788, no. 1, pp. 225 – 233, 2009.

[257] M. Jan Akhunzada, B. Chandramouli, N. Bhattacharjee, S. Macchi, F. Cardarelli, and G. Brancato, "The role of Tat peptide self-aggregation in membrane pore stabilization: insights from a computational study," *Physical Chemistry Chemical Physics*, vol. 19, no. 40, pp. 27603–27610, 2017.

[258] S. Macchi, R. Nifosì, G. Signore, S. Di Pietro, C. Boccardi, F. D'Autilia, F. Beltram, and F. Cardarelli, "Self-aggregation propensity of the Tat peptide revealed by UV-Vis, NMR and MD analyses," *Physical Chemistry Chemical Physics*, vol. 19, no. 35, pp. 23910–23914, 2017.

[259] M. Jan Akhunzada, F. D'Autilia, B. Chandramouli, N. Bhattacharjee, A. Catte, R. Di Rienzo, F. Cardarelli, and G. Brancato, "Interplay between lipid lateral diffusion, dye concentration and membrane permeability unveiled by a combined spectroscopic and computational study of a model lipid bilayer," *Scientific Reports*, vol. 9, no. 1, pp. 1–12, 2019.

[260] G. J. Schütz, H. Schindler, and T. Schmidt, "Single-molecule microscopy on model membranes reveals anomalous diffusion," *Biophysical Journal*, vol. 73, no. 2, pp. 1073–1080, 1997.

[261] T. Dertinger, I. Von Der Hocht, A. Benda, M. Hof, and J. Enderlein, "Surface sticking and lateral diffusion of lipids in supported bilayers," *Langmuir*, vol. 22, no. 22, pp. 9339–9344, 2006.

[262] A. Sharonov, R. Bandichhor, K. Burgess, A. D. Petrescu, F. Schroeder, A. B. Kier, and R. M. Hochstrasser, "Lipid diffusion from single molecules of a labeled protein undergoing dynamic association with giant unilamellar vesicles and supported bilayers," *Langmuir*, vol. 24, no. 3, pp. 844–850, 2008.

[263] S. Chiantia, J. Ries, N. Kahya, and P. Schwille, "Combined AFM and two-focus SFCS study of raft-exhibiting model membranes," *ChemPhysChem*, vol. 7, no. 11, pp. 2409–2418, 2006.

[264] S. Chiantia, N. Kahya, J. Ries, and P. Schwille, "Effects of ceramide on liquid-ordered domains investigated by simultaneous AFM and FCS," vol. 90, pp. 4500–4508, 2006.

[265] D. R. Lide, *CRC Handbook of Chemistry and Physics*. CRC PRESS, 85th ed., 2005.

[266] A. J. Cross and G. R. Fleming, "Analysis of time-resolved fluorescence anisotropy decays," *Biophysical Journal*, vol. 46, no. 1, pp. 45–56, 1984.

[267] D. Magde, G. E. Rojas, and P. G. Seybold, "Solvent dependence of the fluorescence lifetimes of xanthene dyes," *Photochemistry and Photobiology*, vol. 70, no. 5, pp. 737–744, 1999.

[268] P. A. Anfinrud, D. E. Hart, J. F. Hedstrom, and W. S. Struve, "Fluorescence depolarization of rhodamine 6G in glycerol: a photon-counting test of three-dimensional excitation transport theory," *The Journal of Physical Chemistry*, vol. 90, no. 11, pp. 2374–2379, 1986.

[269] A. Bain, P. Chandna, G. Butcher, and J. Bryant, "Picosecond polarized fluorescence studies of anisotropic fluid media. II. Experimental studies of molecular order and motion in jet aligned rhodamine 6G and resorufin solutions," *The Journal of Chemical Physics*, vol. 112, pp. 10435–10449, 2000.

[270] C. B. Müller, A. Loman, V. Pacheco, F. Koberling, D. Willbold, W. Richtering, and J. Enderlein, "Precise measurement of diffusion by multi-color dual-focus fluorescence correlation spectroscopy," *EPL (Europhysics Letters)*, vol. 83, no. 4, 2008.

[271] P.-O. Gendron, F. Avaltroni, and K. J. Wilkinson, "Diffusion coefficients of several rhodamine derivatives as determined by pulsed field gradient-nuclear magnetic resonance and fluorescence correlation spectroscopy," *Journal of Fluorescence*, vol. 18, no. 6, pp. 1093–1101, 2008.

[272] Y. Ma, A. Benda, J. Kwiatek, D. M. Owen, and K. Gaus, "Time-resolved laurdan fluorescence reveals insights into membrane viscosity and hydration levels," *Biophysical Journal*, vol. 115, no. 8, pp. 1498–1508, 2018.

[273] V. V. Shynkar, A. S. Klymchenko, C. Kunzelmann, G. Duportail, C. D. Muller, A. P. Demchenko, J. M. Freyssinet, and Y. Mely, "Fluorescent biomembrane probe for ratiometric detection of apoptosis," *Journal of the American Chemical Society*, vol. 129, no. 7, pp. 2187–2193, 2007.

[274] Unsay, Joseph D and Cosentino, Katia and García-Sáez, Ana J, "Atomic force microscopy imaging and force spectroscopy of supported lipid bilayers," *Journal of Visualized Experiments*, pp. 1–9, 2015.

[275] Z. Lv, S. Banerjee, K. Zagorski, and Y. L. Lyubchenko, *Supported Lipid Bilayers for Atomic Force Microscopy Studies*, pp. 129–143. Springer New York, 2018.

[276] O. Golfetto, E. Hinde, and E. Gratton, "Laurdan fluorescence lifetime discriminates cholesterol content from changes in fluidity in living cell membranes," *Biophysical Journal*, vol. 104, no. 6, pp. 1238–1247, 2013.

[277] J. Sýkora, P. Jurkiewicz, R. M. Epand, R. Kraayenhof, M. Langner, and M. Hof, "Influence of the curvature on the water structure in the headgroup region of phospholipid bilayer studied by the solvent relaxation technique," *Chemistry and Physics of Lipids*, vol. 135, no. 2, pp. 213–221, 2005.

[278] Y. L. Zhang, J. A. Frangos, and M. Chachisvilis, "Laurdan fluorescence senses mechanical strain in the lipid bilayer membrane," *Biochemical and Biophysical Research Communications*, vol. 347, no. 3, pp. 838–841, 2006.

[279] A. P. B. and G. Sheela K., "Image denoising techniques - an overview," *IOSR Journal of Electronics and Communication Engineering*, vol. 11, no. 1, pp. 78–84, 2016.

[280] W. Feller, *An Introduction to Probability Theory and Its Applications*, vol. 1. Biometrika Trust, 3rd ed., 1968.

[281] P. R. Bevington, D. K. Robinson, and G. Bunce, "Data reduction and error analysis for the Physical Sciences, 2nd ed.," *American Journal of Physics*, vol. 61, no. 8, pp. 766–767, 1993.

[282] K. Malte and W. Jürgen, "How many photons are necessary for fluorescence-lifetime measurements?," *Chemical Physics Letters*, vol. 200, no. 1, pp. 199 – 204, 1992.

[283] D. F. Eaton, F. C. De Schryver, M. A. Winnik, M. Ameloot, N. Boens, C. Colombano, J. Demas, A. R. Holzwarth, H. Kokubun, N. Mataga, J. Lofroth, D. Phillips, B. Valeur, and I. Yamazaki, "International union of pure and applied chemistry organic chemistry division commission on photochemistry* Recommended methods for fluorescence decay analysis," *National Representatives: H.-D. Becker (Sweden); T. BBrczes (Hungary); F. C. de Schryver (Belgium); E. Fanghanel (GDR); E. Fischer (Israel); B. Holmstrom (Sweden I. Micic (Yugoslavia); P. Natarajan (India Korea*, vol. 62, no. 0, pp. 1631–1648, 1990.

[284] S. Baker and R. D. Cousins, "Clarification of the use of chi-square and likelihood functions in fits to histograms," *Nuclear Instruments and Methods in Physics Research*, vol. 221, no. 2, pp. 437 – 442, 1984.

[285] J. Siegel, K. Suhling, P. M. W. French, D. Phillips, D. M. Davis, S. E. D. Webb, Y. Sabharwal, and S. Levequefort, "Wide-field time-resolved fluorescence anisotropy imaging (tr-FAIM): imaging the rotational mobility of a fluorophore," *Review of Scientific Instruments*, vol. 74, no. 1, pp. 182–192, 2003.

[286] P. Hall and B. Selinger, "Better estimates of exponential decay parameters," *Journal of Physical Chemistry*, vol. 85, no. 20, pp. 2941–2946, 1981.

[287] H. P. Good, A. J. Kallir, and U. P. Wild, "Comparison of fluorescence lifetime fitting techniques," *Journal of Physical Chemistry*, vol. 88, no. 22, pp. 5435–5441, 1984.

[288] G. Weber, "Polarization of the fluorescence of macromolecules. II. Fluorescent," *The Biochemical Journal*, vol. 51, no. 2, pp. 155–167, 1952.

[289] G. Nishimura and M. Tamura, "Artefacts in the analysis of temporal response functions measured by photon counting," *Physics in Medicine and Biology*, vol. 50, no. 6, pp. 1327–1342, 2005.

[290] Y. Keiji and O. Toshio, "Phase separation in lipid bilayer membranes induced by intermixing at a boundary of two phases with different components," *Chemistry and Physics of Lipids*, vol. 191, pp. 147 – 152, 2015.